

Universidade Federal de Minas Gerais  
Instituto de Ciências Exatas  
Departamento de Química

Juliana Cecília de Mendonça Silva

PROPRIEDADES QUÍMICAS DA ARSENOPIRITA, ADSORÇÃO DE AGENTES  
LIXIVIANTES E SEU MECANISMO DE OXIDAÇÃO A PARTIR DE CÁLCULOS DFT

Belo Horizonte  
2016

UFMG/ICEx/DQ. 1.161<sup>a</sup>

T. 522<sup>a</sup>

Juliana Cecília de Mendonça Silva

PROPRIEDADES QUÍMICAS DA ARSENOPIRITA, ADSORÇÃO DE AGENTES  
LIXIVANTES E SEU MECANISMO DE OXIDAÇÃO A PARTIR DE CÁLCULOS DFT

Tese apresentada ao Departamento de  
Química do Instituto de Ciências Exatas da  
Universidade Federal de Minas Gerais  
como requisito parcial para obtenção do  
grau de Doutor em Ciências – Química

Belo Horizonte

2016

S586p Silva, Juliana Cecília de Mendonça  
2016 Propriedades químicas da arsenopirita, adsorção de  
T agentes lixiviantes e seu mecanismo de oxidação a  
partir de cálculos DFT [manuscrito] / Juliana Cecília  
de Mendonça Silva. 2016.  
[xv], 148 f. : il.

Orientador: Hélio Anderson Duarte.

Coorientador: Heitor Avelino de Abreu.

Tese (doutorado) - Universidade Federal de Minas  
Gerais - Departamento de Química.

Inclui bibliografia.

1. Físico-Química - Teses 2. Sulfetos - Teses 3.  
Resíduos - Teses 4. Minas - Drenagem - Teses 5.  
Oxidação - Teses 6. Funcionais de densidade - Teses 7.  
Adsorção - Teses I. Duarte, Hélio Anderson, Orientador  
II. Abreu, Heitor Avelino de, Coorientador III.  
Título.

CDU 043

**"Propriedades Químicas da Arsenopirita, Adsorção de Agentes Lixivantes e seu Mecanismo de Oxidação a partir de Cálculos DFT"**

**Juliana Cecília de Mendonça Silva**

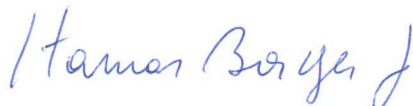
Tese aprovada pela banca examinadora constituída pelos Professores:



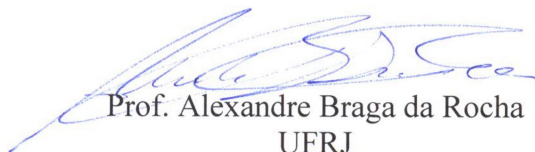
Prof. Hélio Anderson Duarte - Orientador  
UFMG



Prof. Heitor Avelino de Abreu - Coorientador  
UFMG



Prof. Itamar Borges Júnior  
IME



Prof. Alexandre Braga da Rocha  
UFRJ



Prof. Willian Ricardo Rocha  
UFMG



Prof. Gilson de Freitas Silva  
UFMG

Belo Horizonte, 19 de julho de 2016.

Esta tese foi orientada pelo  
Prof. Dr. Hélio Anderson Duarte e  
coorientada pelo Prof. Dr. Heitor Avelino de Abreu

Aos meus pais Júlio e Luciene e ao  
meu namorado Daniel

“A bit of science distances one from God, but much science  
nears one to Him. The more I study nature, the more I stand  
amazed at the work of the Creator.”

Louis Pasteur

## Agradecimentos

A Deus, por ter me criado, sempre me amado e sustentado. A Nossa Senhora e meu anjo da guarda por sempre me protegerem e guiarem.

Aos meus pais, Júlio e Luciene, pelo amor, carinho e suporte em todos os momentos.

Ao meu namorado, Daniel, que foi o melhor presente do meu doutorado e me ajudou tanto no final da tese.

Aos meus orientadores, professor Hélio e Heitor, pela oportunidade de fazer o doutorado e sua orientação.

Aos amigos do grupo GPQIT, Antônio, Aline, Mirele, Egon, Maicon, Fernando, Paulo, Guilherme, Mateus e Jessyca e àqueles que fizeram parte do grupo, Maurício, Cláudio e Angel, pela amizade, auxílio e boas discussões.

Ao professor Thomas Heine e seu grupo pela oportunidade de estudar por um período de um ano na Alemanha. E a todos os amigos que fiz nesse país, especialmente Vladimir, Darka, Martin, Augusto, Aga, Rossalba, Wenqing, Bärbel, Heike, Christine, Clarisse e Bernd.

Às Gen, Sâmara, Cynthia, Cássia, Rebeca, Suzana e Sara, às focolarinas, Walnete, Nives, Eli, Rosa, Lílian, Fabiana, Cíntia, Tes e Vanessa, e aos membros do Movimento dos Focolares de Belo Horizonte e da Alemanha, além dos amigos June e Jim Gladden, que também contribuíram para essa tese com suas orações.

A todos os meus amigos e familiares. Aos meus avós *in memoriam*.

Aos professores, colegas e funcionários do Departamento de Química da UFMG. Em especial às secretárias de pós-graduação Paulete e Fernanda, ao bibliotecário Sérgio e ao porteiro Luís pela gentileza e solicitude.

Aos órgãos CNPq, FAPEMIG, CAPES e INCT-Acqua pelo fomento de nossa pesquisa.

## Contents

Abbreviation list.....	vii
List of Figures .....	viii
List of Tables .....	xiii
Resumo .....	xiv
Abstract.....	xv
1 Introduction.....	1
1.1 Sulfide Minerals.....	1
1.2 Crystal Structure of Sulfides.....	5
1.3 Arsenopyrite and Acid Rock Drainage.....	8
1.4 Arsenopyrite and the Chemical Reactivity of Sulfides .....	10
1.5 References.....	15
2 Methodology .....	20
2.1 Density Functional Theory (DFT).....	20
2.2 Plane Waves (PW) .....	25
2.3 Pseudopotentials.....	27
2.4 Quantum Theory of Atoms in Molecules (QTAIM) .....	29
2.5 Electron Localization Function (ELF) .....	32
2.6 Nudged Elastic Band (NEB).....	33
2.7 Computational Aspects of the Arsenopyrite Calculations .....	36
2.8 Final Considerations .....	40
2.9 References.....	41
3 Structural, Mechanical and Electronical Properties of Arsenopyrite and its Surfaces. ...	44
3.1 Arsenopyrite Structure.....	44
3.2 Electronic Structure of Arsenopyrite .....	50
3.3 Topological Analysis of the Electron Density. ....	54
3.4 Arsenopyrite Surfaces .....	60
3.5 Final Considerations .....	70
3.6 References.....	71
4 Adsorption of Leaching Agents on Arsenopyrite .....	75

4.1	Water Adsorption on Arsenopyrite Surface.....	76
4.1.1	Water adsorption on (101) Surface .....	76
4.1.2	Water adsorption on (001) Surface .....	82
4.2	Adsorption of HCl .....	95
1.6	Adsorption of H <sub>2</sub> SO <sub>4</sub> .....	97
4.3	Final Considerations .....	108
4.4	References:.....	109
5	Oxidation of Arsenopyrite .....	111
5.1	Adsorption of Oxygen .....	112
5.2	Adsorption of Oxygen and Water .....	126
5.3	Oxidation Reaction .....	130
5.4	Final Considerations .....	137
5.5	References.....	137
6	Concluding Remarks and Perspectives.....	139
6.1	References.....	143
7	Curriculum Vitae.....	145

## Abbreviation list

AFM (Atomic Force Microscopy)  
AMD (Acid Mine Drainage)  
ARD (Acid Rock Drainage)  
BB (bidentate binuclear)  
BCP (Bond Critical Point)  
BM (bidentate mononuclear)  
BSSE (Basis Set Superposition Error)  
CCP (Cage Critical Point)  
CI (Climbing Image)  
CPMD (Car-Parrinello Molecular Dynamics)  
DFT (Density Functional Theory)  
DOS (Density of States)  
ELF (Electron Localization Function)  
EXAFS (Extended X-ray Absorption Fine Structure)  
GGA (Generalized Gradient Approximation)  
HF (Hartree-Fock)  
LDA (Local Density Approximation)  
LEED (Low Energy Electron Diffraction)  
MEP (Minimum Energy Path)  
MB (Monodentate binuclear)  
MM (monodentate mononuclear)  
NCP (Nuclear Critical Point)  
NEB (Nudged Elastic Band)  
PES (Potential Energy Surface)  
PW (Plane Waves)  
QTAIM (Quantum Theory of Atoms in Molecules)  
RCP (ring critical point)  
STM (Scanning Tunneling Microscopy)  
TS (Transition State)  
hTST (harmonic Transition State Theory)  
WHO (World Health Organization)  
XANES (X-ray Absorption Near-Edge Structure)  
XC (Exchange and Correlation)  
XPS (X-ray Photoelectron Spectroscopy)

## List of Figures

Figure 1.1: Rio Tinto in Spain .....	2
Figure 1.2: Sulfide mineral samples. ....	4
Figure 1.3: Unit cell of pyrite. ....	6
Figure 1.4: Unit cell of chalcopyrite.....	6
Figure 1.5: Unit cell of arsenopyrite.....	7
Figure 1.6: a) The As–S dianions coordinated octahedrally to Fe; b) neighboring octahedra share an edge. ....	8
Figure 1.7: Eh-pH diagram for Arsenopyrite.....	11
Figure 1.8: Pyrite oxidation mechanism. ....	14
Figure 2.1: Representation of the construction of a pseudo wave function $\phi(r)$ and its respective pseudopotential $V^{ps}(r)$ from the wave function $\psi(r)$ and the Coulomb potential $V^{Coul}(r)$ . ....	28
Figure 2.2: a) Map of the trajectory vector $\nabla\rho(r)$ for ethylene; b) Map of the trajectory vector $\nabla\rho(r)$ showing the atomic interaction line. ....	31
Figure 2.3: Scheme of a minimum energy path found by the NEB method.....	35
Figure 2.4: a) Convergence test for the cutoff energy $E_{cut}$ . b) Calculation time as a function of the cutoff energy. ....	37
Figure 2.5: a) K-points mesh convergence test.....	38
Figure 2.6: Magnetization test of bulk arsenopyrite.....	40
Figure 3.1: Arsenopyrite monoclinic unit cell used in bulk calculations. a) view along $a$ axis; b) view along $b$ axis.....	44
Figure 3.2: Structure of sulfides: a) pyrite; b) marcasite; c) loellingite; d) arsenopyrite. The filled circles represent the cations and the open ones the anions. From reference [9]. ....	47
Figure 3.3: Molecular orbital diagram of the Fe–Fe bond [9]. ....	47
Figure 3.4: Path through K-space for band structure calculation for a monoclinic cell suggested in reference [18]. ....	50
Figure 3.5: Band structure calculated for arsenopyrite.....	51
Figure 3.6: Total and projected DOS of the atoms of arsenopyrite plotted using a Gaussian width of 0.005 Ry.....	52
Figure 3.7: Total and projected DOS over the atomic orbitals of arsenopyrite plotted using a Gaussian width of 0.005 Ry.....	52
Figure 3.8: DOS projected over iron $d$ orbitals plotted using a Gaussian width of 0.005 Ry.....	53

Figure 3.9: a) As–S dianions octahedrally coordinated to Fe. b) Neighbor octahedrons sharing one edge. Yellow atoms are sulfur, purple are arsenic and brown are iron.....	53
Figure 3.10: Electron density map of the arsenopyrite (010) plane. Brown balls are iron atoms.	54
Figure 3.11: Bond critical points (BCP) in green, Ring critical points (RCP) in blue, and Cage critical points (CCP) in pink for arsenopyrite QTAIM analysis. Atoms in brown are iron, in yellow are sulfur and in purple are arsenic. ....	56
Figure 3.12: a) Bond critical points and b) Ring critical points in detail. Yellow atoms are sulfur, purple are arsenic and brown are iron.....	57
Figure 3.13: ELF of arsenopyrite As–S bond. brown is iron, purple is arsenic and yellow is sulfur. ....	58
Figure 3.14: ELF of the arsenopyrite (010) plane. Iron atoms are represented by brown spheres. ....	58
Figure 3.15: Surface Types according to Tasker. Adapted from [39]. ....	61
Figure 3.16: Arsenopyrite cleavage planes. Iron is in brown, sulfur in yellow and arsenic in purple. Miller indices are based on the $P2_1/c$ symmetry. ....	62
Figure 3.17: Arsenopyrite cleavage surfaces used to perform the calculations. Iron is in brown, sulfur in yellow and arsenic in purple. Miller indices are based on the $P2_1/c$ symmetry. ....	64
Figure 3.18: Optimized arsenopyrite surfaces (after relaxation). Iron is in brown, sulfur in yellow and arsenic in purple. Miller indices are based on the $P2_1/c$ symmetry.....	64
Figure 3.19: Top view of surfaces: a) (001); b) (100); c) (010). Brown is iron, purple is arsenic and yellow is sulfur.....	66
Figure 3.20: Projected DOS over the atoms of the surfaces: a) (001); b) (010); c) (100) plotted using a Gaussian width of 0.005 Ry. ....	68
Figure 3.21: (001) surface energy as a function of the number of layers $n$ in the slab.....	69
Figure 3.22: Projected DOS of Arsenopyrite (001) surface calculated using spin-polarization....	70
Figure 4.1: Arsenopyrite (101) surface. a) Side view and b) Top view. Brown is iron, purple is arsenic and yellow is sulfur. ....	77
Figure 4.2: DOS projected over the (101) surface atoms. ....	77
Figure 4.3: Adsorption of a water molecule to the iron site on arsenopyrite (101) surface. a) Side view and b) Top view. Brown is iron, purple is arsenic, yellow is sulfur, red is oxygen and white hydrogen. ....	78
Figure 4.4: Dissociative adsorption of a water molecule on arsenopyrite (101) surface. a) Side view and b) Top view. Brown is iron, purple is arsenic, yellow is sulfur, red is oxygen and white hydrogen. ....	79
Figure 4.5: Adsorption of a water molecule to the arsenic site on arsenopyrite (101) surface. a) Side view and b) Top view. Brown is iron, purple is arsenic, yellow is sulfur, red is oxygen and white hydrogen.....	79

Figure 4.6: Adsorption of a water molecule to the sulfur site on arsenopyrite (101) surface. a) Side view and b) Top view. Brown is iron, purple is arsenic, yellow is sulfur, red is oxygen and white hydrogen.....	80
Figure 4.7: Adsorption of a water molecule to two neighbor arsenic atoms on arsenopyrite (101) surface. a) Side view and b) Top view. Brown is iron, purple is arsenic, yellow is sulfur, red is oxygen and white hydrogen.....	81
Figure 4.8: Adsorption of a water molecule to two neighbor sulfur atoms on arsenopyrite (101) surface. a) Side view and b) Top view. Brown is iron, purple is arsenic, yellow is sulfur, red is oxygen and white hydrogen.....	81
Figure 4.9: Adsorption of a water molecule to two neighbor arsenic and sulfur atoms on arsenopyrite (101) surface. a) Side view and b) Top view. Brown is iron, purple is arsenic, yellow is sulfur, red is oxygen and white hydrogen. ....	82
Figure 4.10: Arsenopyrite (001) surface: a) top view; b) side view. ....	83
Figure 4.11: First layer of atoms in arsenopyrite (001) surface showing the two different Fe sites: Fe1, more exposed, and Fe2, less exposed. a) top view; b) side view. ....	83
Figure 4.12: Adsorption of one water molecule on two different Fe sites on the (001) arsenopyrite surface: a) Fe1 top view; b) Fe1 side view; c) Fe2 top view; Fe2 side view. Yellow atoms are sulfur, purple are arsenic, brown are iron, red are oxygen and white are hydrogen.....	85
Figure 4.13: Adsorption of one water molecule on Fe sites on (100), (110) and (101) arsenopyrite surfaces: a) (100) top view; b) (100) side view; c) (110) top view; d) (110) side view; e) (101) top view; (101) side view. Yellow atoms are sulfur, purple are arsenic, brown are iron, red are oxygen and white are hydrogen. ....	87
Figure 4.14: Adsorption of one water molecule on the As and S sites of (001) arsenopyrite surface: a) and b) As site; c) and d) As and S sites; e) and f) S site. Yellow atoms are sulfur, purple are arsenic, brown are iron, red are oxygen and white are hydrogen.....	88
Figure 4.15: Dissociative adsorption of one water molecule, in which the OH group bounds to an Fe1 site and the H atom bounds to a) As and c) S. Yellow atoms are sulfur, purple are arsenic, brown are iron, red are oxygen and white are hydrogen. ....	90
Figure 4.16 Dissociative adsorption of one water molecule, in which the OH group bounds to an Fe1 site and the H atom bounds to an As atom. Yellow atoms are sulfur, purple are arsenic, brown are iron, red are oxygen and white are hydrogen.....	91
Figure 4.17: Dissociative adsorption of one water molecule, in which the OH group bounds to a Fe1 site and the H atom bounds to a S atom. Yellow atoms are sulfur, purple are arsenic, brown are iron, red are oxygen and white are hydrogen.....	92
Figure 4.18: Dissociative adsorption of one water molecule, in which the OH group bounds to a Fe2 site and the H atom bounds to a As atom. Yellow atoms are sulfur, purple are arsenic, brown are iron, red are oxygen and white are hydrogen.....	93
Figure 4.19: Optimized structure of 8 water molecules adsorbed on arsenopyrite (001) surface forming two solvation layers. Yellow atoms are sulfur, purple are arsenic, brown are iron, red are oxygen and white are hydrogen.....	94

Figure 4.20: Optimized structure of 4 water molecules adsorbed on arsenopyrite (001) surface. Yellow atoms are sulfur, purple are arsenic, brown are iron, red are oxygen and white are hydrogen. ....	94
Figure 4.21: Dissociative adsorption of HCl on arsenopyrite (001) surface: a), b) on Fe1 and S sites c), d) on Fe1 and As sites. Yellow atoms are sulfur, purple are arsenic, brown are iron, green are chlorine and white are hydrogen. ....	96
Figure 4.22: Figure 9: Dissociative adsorption of HCl on Fe2 site of arsenopyrite (001) surface. Yellow atoms are sulfur, purple are arsenic, brown are iron, green are chlorine and white are hydrogen. ....	97
Figure 4.23: Most stable structures for adsorption of H <sub>2</sub> SO <sub>4</sub> on arsenopyrite (001) surface: a),b) H <sub>2</sub> SO <sub>4</sub> MM; c),d) H <sup>+</sup> , HSO <sub>4</sub> <sup>-</sup> BB, e), f) 2H <sup>+</sup> , SO <sub>4</sub> <sup>2-</sup> BB on Fe sites; g), h) 2H <sup>+</sup> , SO <sub>4</sub> <sup>2-</sup> BB on Fe and As sites. Yellow atoms are sulfur, purple are arsenic, brown are iron, red are oxygen and white are hydrogen. ....	100
Figure 4.24: Adsorption of H <sub>2</sub> SO <sub>4</sub> on arsenopyrite (001) surface: a), b) 2H <sup>+</sup> , SO <sub>4</sub> <sup>2-</sup> BM; c), d) H <sup>+</sup> , HSO <sub>4</sub> <sup>-</sup> MM. Yellow atoms are sulfur, purple are arsenic, brown are iron, red are oxygen and white are hydrogen. ....	101
Figure 4.25: Adsorption of H <sub>2</sub> SO <sub>4</sub> on Fe and As atom of arsenopyrite (001) surface: a), b) 2H <sup>+</sup> , SO <sub>4</sub> <sup>2-</sup> ; c), d) H <sup>+</sup> , HSO <sub>4</sub> <sup>-</sup> . Yellow atoms are sulfur, purple are arsenic, brown are iron, red are oxygen and white are hydrogen.....	102
Figure 4.26: Figure S7: Adsorption of HSO <sub>4</sub> <sup>-</sup> on Fe and S atom of arsenopyrite (001) surface: a), b) S1; c), d) S2. Yellow atoms are sulfur, purple are arsenic, brown are iron, red are oxygen and white are hydrogen. ....	103
Figure 4.27: Adsorption of H <sub>2</sub> SO <sub>4</sub> on arsenopyrite (001) surface: a), b) SO <sub>4</sub> <sup>2-</sup> BB; c),d) HSO <sub>4</sub> <sup>-</sup> MM. Yellow atoms are sulfur, purple are arsenic, brown are iron, red are oxygen and white are hydrogen. ....	104
Figure 4.28: Adsorption of H <sub>2</sub> O on pyrite (001) surface. a),b) molecular adsorption; c),d) dissociate adsorption. Yellow atoms are sulfur, brown are iron, red are oxygen and white are hydrogen. ....	106
Figure 4.29: Dissociative adsorption of HCl on pyrite (001) surface. Yellow atoms are sulfur, brown are iron, green are chlorine and white are hydrogen.....	106
Figure 4.30: Adsorption of H <sub>2</sub> SO <sub>4</sub> on pyrite (001) surface: a), b) H <sub>2</sub> SO <sub>4</sub> , c), d) H <sup>+</sup> , HSO <sub>4</sub> <sup>-</sup> e), f) 2H <sup>+</sup> , SO <sub>4</sub> <sup>2-</sup> . Yellow atoms are sulfur, brown are iron, red are oxygen and white are hydrogen.....	107
Figure 5.1: First layer of atoms of the arsenopyrite (001) surface showing the different Fe sites: Fe1 and Fe3, more exposed, and Fe2 and Fe4, less exposed.....	113
Figure 5.2: End-on adsorption of O <sub>2</sub> on the (001) arsenopyrite surface .....	114
Figure 5.3: Side-on adsorption of O <sub>2</sub> on the (001) arsenopyrite surface.....	116
Figure 5.4: Dissociative adsorption of O <sub>2</sub> on the arsenopyrite (001) surface: a) Fe1 and As sites top view, b) Fe1 and As sites side view; c) Fe2 and Fe3 sites top view, d) Fe2 and Fe3 sites side view .....	117

Figure 5.5: Dissociative adsorption of O <sub>2</sub> on the arsenopyrite (001) surface: a) Fe1 and Fe2 sites top view, b) Fe1 and Fe2 sites side view; c) Fe2 and Fe3 sites top view, d) Fe2 and Fe3 sites side view; e) Fe3 and Fe4 sites top view, f) Fe3 and Fe4 sites side view; g) Fe4 and Fe1 sites top view, h) Fe4 and Fe1 sites side view .....	119
Figure 5.6: Dissociative adsorption of O <sub>2</sub> on the arsenopyrite (001) surface: a) Fe1 and Fe2 sites top view, b) Fe1 and Fe2 sites side view; c) Fe2 and Fe3 sites top view, d) Fe2 and Fe3 sites side view.....	120
Figure 5.7: Dissociative adsorption of O <sub>2</sub> on the arsenopyrite (001) surface: a) Fe1 and Fe4 sites top view, b) Fe1 and Fe4 sites side view; c) equivalent Fe3 sites top view, d) equivalent Fe3 sites side view; e) Fe3 and Fe4 sites top view, f) Fe3 and Fe4 sites side view .....	121
Figure 5.8: Dissociative adsorption of O <sub>2</sub> on the arsenopyrite (001) surface on As atoms. ....	122
Figure 5.9: Dissociative adsorption of O <sub>2</sub> on the arsenopyrite (001) surface on S atoms .....	123
Figure 5.10: Dissociation of the O <sub>2</sub> molecule on the arsenopyrite (001) surface.....	125
Figure 5.11: Energy barrier graph for the O <sub>2</sub> dissociation on the arsenopyrite (001) surface. ...	125
Figure 5.12: Co-adsorption of water and dissociated oxygen to the arsenopyrite (001) surface. ....	127
Figure 5.13: Co-adsorption of water and oxygen end-on to the arsenopyrite (001) surface. ....	128
Figure 5.14: Substitution of one water molecule for an O <sub>2</sub> molecule on the arsenopyrite (001) surface.....	129
Figure 5.15: Substitution of two water molecules for an O <sub>2</sub> molecule on the arsenopyrite (001) surface.....	129
Figure 5.16: Proposed oxidation reaction for the arsenopyrite (001) surface.....	131
Figure 5.17: Minimum Energy Paths for the H donation reactions in the oxidation of arsenopyrite.. ..	132
Figure 5.18: OH groups bound to S atoms in the oxidation reaction of the arsenopyrite (001) surface.....	133
Figure 5.19: Migration of the OH group from an Fe atom to an As atom on the arsenopyrite surface.....	134
Figure 5.20: Reaction steps for the formation of AsO <sub>4</sub> <sup>3-</sup> on the FeAsS (001) surface. ....	136
Figure 6.1: Adsorption of Fe(H <sub>2</sub> O) <sub>4</sub> <sup>3+</sup> on the FeAsS (001) surface.. ..	143

## List of Tables

Table 2.1: Total energy variation with respect to the cutoff energy for the XC functionals PBE and PW91.....	37
Table 2.2: K-points mesh test for two XC functionals: PBE and PW91.....	39
Table 3.1: Interatomic distances for arsenopyrite bulk.....	45
Table 3.2: Crystallographic data of bulk arsenopyrite.....	46
Table 3.3: Critical points in QTAIM analysis.....	55
Table 3.4: Atomic charges in AIM analysis.....	59
Table 3.5: Calculated and experimental bulk moduli for arsenopyrite, marcasite and pyrite.....	60
Table 3.6: Surfaces correspondence in C <sub>2</sub> /d and P2 <sub>1</sub> /c unit cells.....	61
Table 3.7: Surface energies and coordination numbers of surface atoms of different arsenopyrite surfaces.....	63
Table 3.8: Comparison of Arsenopyrite and Pyrite's surface energies.....	67
Table 4.1: Atomic distances on arsenopyrite (001) surface as effect of water adsorption.....	85
Table 4.2: Dissociative adsorption of water on arsenopyrite surface.....	90
Table 4.3: Adsorption Energy of water calculated for different sulfide surfaces.....	95
Table 4.4: Atomic distances on arsenopyrite (001) surface as effect of HCl adsorption.....	97
Table 4.5: Adsorption energies of aqueous H <sub>2</sub> SO <sub>4</sub> species in different positions on arsenopyrite (001) surface in kcal mol <sup>-1</sup> .....	99
Table 4.6: Atomic distances on arsenopyrite (001) surface as effect of H <sub>2</sub> SO <sub>4</sub> adsorption.....	99
Table 4.7: Dissociative adsorption of SO <sub>4</sub> <sup>2-</sup> and HSO <sub>4</sub> <sup>-</sup> on arsenopyrite surface.....	99
Table 4.8: Adsorption Energy of leaching agents calculated for different sulfide surfaces.....	105
Table 5.1: O–O distances calculated for different O <sub>2</sub> bond types.....	114
Table 5.2: Adsorption energies and M–O distances for the O <sub>2</sub> adsorption on the arsenopyrite (001) surface.....	123
Table 5.3: Atomic distances on the arsenopyrite (001) surface as effect of oxygen adsorption.....	126
Table 5.4: Adsorption energies and Fe–O distances in O <sub>2</sub> and H <sub>2</sub> O adsorption on the arsenopyrite (001) surface.....	128
Table 5.5: pK <sub>a</sub> and standard electrochemical potentials for arsenic and sulfur aqueous species.....	136

## Resumo

Os sulfetos minerais, dentre os quais a arsenopirita, estão comumente presentes em rejeitos de mineração e são responsáveis pela drenagem ácida de rocha (DAR). Nesse fenômeno, o mineral sofre oxidação em contato com oxigênio e água e produz um líquido contendo ácido e metais pesados capaz de contaminar o ambiente. A mitigação do problema da DAR e o desenvolvimento de contramedidas são facilitados pela compreensão de seu mecanismo. Por isso o conhecimento do processo de oxidação de sulfetos é muito importante, especialmente da arsenopirita, que, além da DAR, também libera o elemento tóxico arsênio em sua oxidação. Esse processo ainda não é completamente compreendido, pois as reações envolvidas são muito complexas, o que leva a uma falta de consenso na literatura. Nesse contexto, cálculos de primeiros princípios podem contribuir para o entendimento e interpretação dos dados experimentais e na elucidação do mecanismo de reação ao nível molecular.

Nesta tese foram investigadas por cálculos DFT as propriedades estruturais, eletrônicas e mecânicas da arsenopirita, suas ligações químicas e suas superfícies de clivagem, além da adsorção de agentes lixiviantes e seu mecanismo de oxidação. Evidências mostrando que não há ligação Fe–Fe na arsenopirita e que a ligação As–S possui forte caráter covalente foram fornecidas. Também foi mostrado que essa forte ligação As–S é improvável de ser quebrada durante a formação da superfície. As clivagens preferenciais são previstas de ocorrer nos planos (001), (010) e (100). A superfície (001) é a que apresenta menor energia de formação e possui propriedades magnéticas. A adsorção de água sobre essa superfície é mais favorável na forma molecular e sobre os sítios de Fe mais expostos. O ácido clorídrico favorece a adsorção dissociativa e o ácido sulfúrico tem preferência pela forma molecular monodentada, enquanto o bissulfato se adsorve em coordenação bidentada binuclear. A adsorção de oxigênio sobre o sítio de Fe é bastante favorável, principalmente de forma dissociativa, quando é formada uma ponte Fe–O–As. Nesse processo tanto os átomos de Fe quanto de As são oxidados. A co-adsorção de oxigênio e água sobre a superfície também é estável. Um mecanismo de oxidação da arsenopirita foi proposto em que o oxigênio se adsorve sobre a superfície e recebe átomos de H de moléculas de água, que reduzem novamente o Fe. Nesse mecanismo, o arsênio é o elemento que se oxida preferencialmente, o que explica os dados experimentais disponíveis. Cálculos para a pirita também foram realizados para comparar com a arsenopirita, com o objetivo de prover uma compreensão significativa sobre ambos os sistemas.

**Palavras chave:** sulfetos, arsenopirita, drenagem ácida de rocha, oxidação, QTAIM, DFT.

## **Abstract – Chemical Properties of Arsenopyrite, Adsorption of Leaching Agents and its Oxidation Mechanism from DFT Calculations**

Sulfide minerals, among them arsenopyrite, are commonly present in mining tailings and are responsible for acid rock drainage (ARD). In this phenomenon, the mineral undergoes oxidation in contact with oxygen and water and produces a liquid containing acid and heavy metals capable of contaminating the environment. Mitigation of the ARD problem and the development of countermeasures are facilitated by understanding its mechanism. Therefore the knowledge of the sulfides oxidation process is very important, especially of arsenopyrite, which, in addition to ARD, also releases the toxic element arsenic by its oxidation. This process is not yet completely understood, since the reactions involved are very complex, which leads to a lack of consensus in the literature. In this context, first principle calculations can contribute to the understanding and interpretation of the experimental data in the elucidation of the reaction mechanism at a molecular level.

In this thesis, the structural, electronic and mechanical properties of arsenopyrite, its chemical bonds and its surfaces cleavage, as well as the adsorption of leaching agents and its oxidation mechanism have been investigated by DFT calculations. Evidences showing that there is no Fe–Fe bond in arsenopyrite and that the As–S bond has strong covalent character have been provided. It has been also shown that this strong As–S bond is unlikely to be broken during the surface formation. The preferential cleavages are predicted to occur in the planes (001), (010) and (100). The (001) surface is the one that presents the lowest surface energy, and has magnetic properties. The adsorption of water on this surface is most favorable in molecular form on the most exposed Fe sites. Hydrochloric acid favors dissociative adsorption and sulfuric acid prefers the molecular monodentate adsorption form, while bisulfate adsorbs in bidentate binuclear coordination. The adsorption of sulfate is predicted to be not favored. The adsorption of oxygen on the Fe site is very favorable, especially dissociatively, when a Fe–O–As bridge is formed. In this process, both Fe and As atoms are oxidized. The co-adsorption of oxygen and water on the surface is also stable. An oxidation mechanism for arsenopyrite has been proposed, in which the oxygen is adsorbed to the surface and receives H atoms from water molecules, which again reduces the Fe. In the proposed mechanism, arsenic is the element that preferentially oxidizes, which explains the available experimental data. Calculations for pyrite have also been performed and compared with arsenopyrite, aiming to provide significant insights about both systems.

**Key words:** sulfides, arsenopyrite, acid rock drainage, oxidation, QTAIM, DFT.

# 1 Introduction

## 1.1 Sulfide Minerals

Sulfide minerals are considered the most important group of minerals of the earth's crust [1] for being the main natural sources of non-ferrous metals, such as copper, zinc and lead. These metals are softer acids that easily bind to the soft base  $S^{2-}$ , while harder acids, such as iron, aluminum and chromium, prefer to form oxides. The definition of sulfide mineral is very wide due to the great number of existing compounds and their different properties. However, it can be said that they are natural binary or ternary crystalline sulfur compounds or their synthetic analogues [2]. Although there are hundreds of known sulfide minerals, most of them are secondary minerals and only six exist in abundance to form rocks: pyrite ( $FeS_2$ ), pyrrhotite ( $Fe_{1-x}S_2$ ), galena ( $PbS$ ), sphalerite ( $ZnS$ ), chalcopyrite ( $CuFeS_2$ ) and chalcocite ( $Cu_2S$ ) [1].

The metal sulfides – sulfides that have metals in their composition – have aroused the interest of the scientific community due to their potential applications as semiconductor materials. The use of these minerals in solar cells [3-5], solid batteries [6] and catalysis [7] has also been investigated.

Another interest in the study of sulfides came from the discovery of living organisms in hydrothermal systems on the ocean floor, whose metabolic pathway is chemosynthetic instead of photosynthetic [1]. These organisms use the surface of sulfide minerals as a catalyst for the synthesis of complex molecules necessary for life, which raised a theory of the origin of life from sulfide minerals [8, 9]. In fact, acetic acid has been synthesized from carbon monoxide (CO) and methanethiol ( $CH_3SH$ ) on sulfide surfaces [10] in conditions similar to the primitive terrestrial atmosphere, which is thought to have existed prior to the origin of life.

Despite the industrial potential of sulfide minerals, a great reason to currently study them is the environmental problem caused by oxidation and dissolution of these compounds resulting from acid mine drainage (AMD), or the more general term, acid rock drainage (ARD). Because metals such as gold and copper are found associated with sulfide rocks, ARD occurs mainly during the industrial extraction of

these ores. In this process, the sulfides present in mining tailings, in contact with oxygen and environmental water, oxidize producing sulfuric acid. The generated solution acts as a leaching agent, in other words, as a mixture that solubilizes the solid constituent mineral, producing a liquid containing dissolved metals and sulfuric acid, which can contaminate soil and aquifers [11].

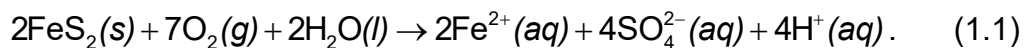
ARD is a spontaneous process that arises whenever a sulfide rock is exposed to the atmosphere and moisture, without special conditions. A classic example is the ARD that occurs in Rio Tinto, a river in Spain (Figure 1.1) which received this name because of its red color. Along the river there is a large deposit of pyrite, with a pH of the order of 2 and high concentrations of heavy metals. The ARD process in this region is lasting for about 50 centuries, since mining activities started there. The extreme local conditions pointed to environmental studies that simulate what might be found on planet Mars [12]. But the crucial cause of ARD is anthropogenic, mainly due to mining activity, which aggravates the problem because of the amount of sulfides exposed to the atmosphere [11]. For this reason, it is a concern for the state of Minas Gerais, Brazil, due to the intense mining activity in its territory, where a serious mining accident happened in the town of Mariana in 2015 with huge social, economic and environmental impacts.



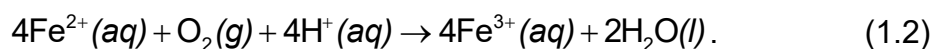
Figure 1.1: Rio Tinto in Spain, where acid rock drainage occurs for centuries [13].

Acid rock drainage can be accelerated in the presence of microorganisms of the species *Acidithiobacillus ferrooxidans*, *Acidithiobacillus thiooxidans* and *Leptospirillum ferrooxidans* [14], and this is difficult to control because each mine has different characteristics. There is no standard treatment and costs can be enormous [11]. In the United States, the costs for the mining industry to treat ARD are more than a million dollars a day [15] and around US\$100 billion has been or will be spent in ARD remediation in the whole world [14]. The separation of pyrite from other economically important minerals by flotation and leaching methods also generates costs for the mining industry [15], which explains the interest in its study.

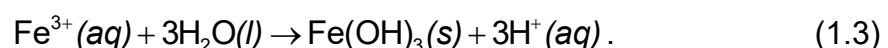
Pyrite ( $\text{FeS}_2$ ) is the most geologically important, widespread and abundant sulfide on Earth. For this reason, it is the one that contributes the most to ARD. Other sulfides reported to also cause ARD are pyrrhotite, bornite, arsenopyrite, enargite, tetrahedrite, realgar, orpiment, stibnite, sphalerite, galena, chalcopyrite and covellite [16]. The name pyrite has Greek origin and means *fire*, probably due to the sparks it produces when struck against steel. It is popularly known as "fool's gold" because of its typical golden glow. This mineral has little economic value, but is often associated with more valuable minerals, as sphalerite, chalcopyrite, galena and gold [15]. It is used as a raw material in industrial production of sulfuric acid and as iron ore only in places where iron oxides are not available [17]. When exposed to oxygen and water, pyrite is oxidized to form sulfuric acid:



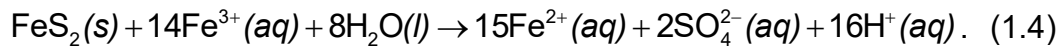
If the environmental conditions are sufficiently oxidizing, the ferrous ion will oxidize to a ferric ion:



In pH between 2.3 and 3.5, the ferric ion will precipitate as  $\text{Fe}(\text{OH})_3$ , leaving the medium even more acidic:



The  $\text{Fe}^{3+}$  ions that do not precipitate in the reaction of equation 1.3 can oxidize pyrite again:



Chalcopyrite ( $\text{CuFeS}_2$ ) is another sulfide that also contributes to ARD, though economically important, because it is the main source of copper in the world. Copper is a metal widely used in the electric industry, electronics and construction [18]. Obtaining metallic copper from the ore is traditionally made by a pyrometallurgical route, wherein the mineral is concentrated, then smelted in an oxidizing atmosphere and, at last, copper is reduced by electrolysis [19]. However, when the concentration of copper in the ore is low, the hydrometallurgical route is applied. In this process, a low-cost chemical agent is used as a leaching agent to extract the  $\text{Cu}^{2+}$  ion in ore piles, followed by electrochemical reduction thereof to metallic copper [19]. The problem of the hydrometallurgical route is the low leaching kinetics. The reaction stops at a certain point, which complicates its industrial use, and several attempts were made to explain this phenomenon [20].

Arsenopyrite ( $\text{FeAsS}$ ) is the most common arsenic mineral in nature, and it can be found in many ore deposits. Because of its association with rocks containing gold, silver, copper and lead [17] and its little economic importance [21], arsenopyrite is a mineral commonly present in mining waste of these metals [22]. Although stable under reducing conditions, this mineral also generates acid rock drainage. An aggravating aspect is the release of arsenic – a toxic element – to the environment, whose mechanism is still not completely understood.

Figure 1.2 shows a picture of each of the sulfides described above.

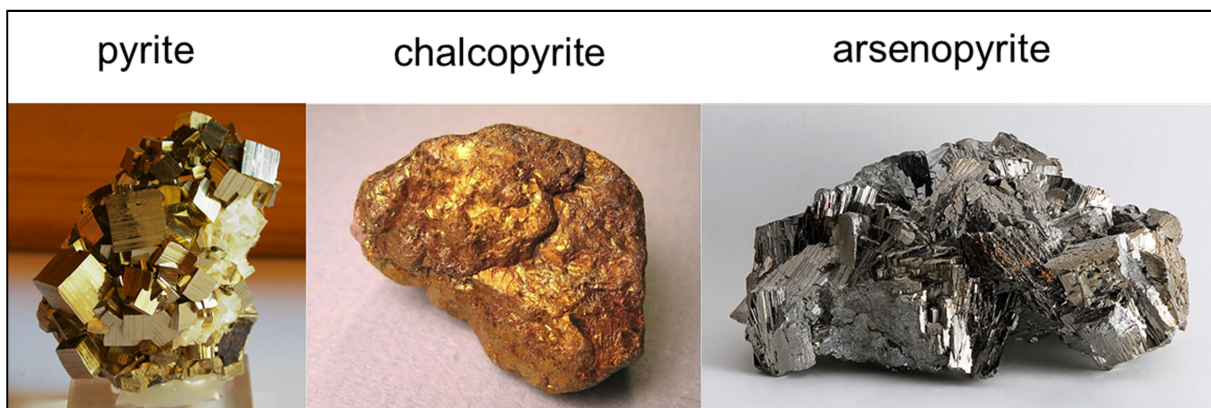


Figure 1.2: Sulfide mineral samples. Photos taken from references [23-25].

## 1.2 Crystal Structure of Sulfides

The crystal structures of all common and many rare sulfide minerals are well known. They range from the simple crystal structure of salt, such as PbS, or structures involving anion-anion bonds, as CuS, to complex structures where there is uncertainty about the occupation sites and oxidation states of the atoms, as in tetrahedrites, economically important minerals [26] for being a source of copper and silver [27]. The electric and magnetic properties of these minerals are also more diverse than in any other group, ranging from diamagnetic insulators (ZnS), diamagnetic semiconductors (PbS), antiferromagnetic semiconductors (CuFeS<sub>2</sub>), to antiferromagnetic and ferromagnetic conductors (Fe<sub>7</sub>S<sub>8</sub> and Fe<sub>9</sub>S<sub>10</sub>) [26]. Therefore these materials can have a nonzero electron density located between the cations and anions, forming chemical bonds, as well as delocalized electronic states, which makes describing the chemical bonds a challenging task [26]. Pauling [28] has observed that many sulfides have mostly covalent bonds, with a small ionic character. Moreover, it is common to observe deviations in the stoichiometric composition of sulfides, defects, impurities and association with other minerals.

Pyrite was one of the first solids analyzed by X-ray diffraction. It crystallizes in a cubic face-centered structure with space group  $Pa\bar{3}$ , in a structure similar to NaCl, as shown in Figure 1.3, exchanging Na<sup>+</sup> with Fe<sup>2+</sup> and Cl<sup>-</sup> for the center of the S–S bond in S<sub>2</sub><sup>2-</sup>. The orientation of the S–S dimers in dumbbell shape is respectively parallel to the four diagonals of the cell body [29]. The sulfur atoms are coordinated to a S atom and three Fe atoms in a tetrahedral way, while the iron atoms are octahedrally coordinated to six S atoms. The unit cell of pyrite contains 4 FeS<sub>2</sub> formulas and it is a diamagnetic semiconductor [30]. It has poor preferential cleavage on the (100) and (110) surfaces [31]. It may also exist in the polymorphic form of marcasite, which is less stable by  $1.0 \pm 0.5$  kcal mol<sup>-1</sup> [32].

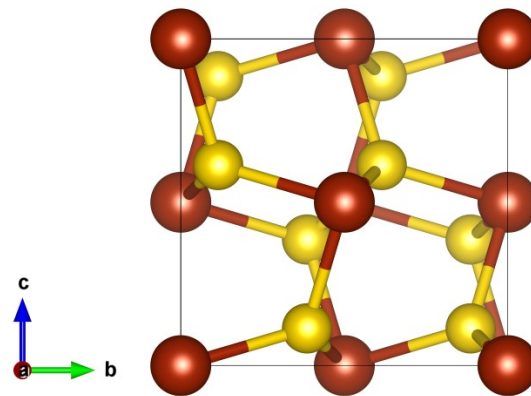


Figure 1.3: Unit cell of pyrite. The iron atoms are in brown color and the sulfur atoms in yellow.

Chalcopyrite crystallizes in a tetragonal system, with space group  $I\bar{4}2d$  and 4  $\text{CuFeS}_2$  formulas per unit cell, as shown in Figure 1.4. Each metal atom is coordinated to four sulfur atoms forming a tetrahedron, whereas the sulfur atoms are bonded to two iron and two copper atoms also in tetrahedral shape. In chalcopyrite the oxidation states of the atoms are  $(\text{Cu}^{1+})(\text{Fe}^{3+})(\text{S}_2^{2-})$  [33]. The solid is an antiferromagnetic semiconductor with alternating atomic layers of iron atoms with spin density up and down along the  $c$  direction [29]. Chalcopyrite has no preferred cleavage plane [31, 34].

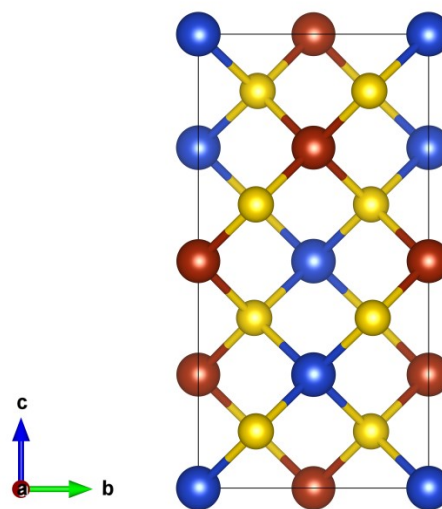


Figure 1.4: Unit cell of chalcopyrite. The iron atoms are shown in brown, the copper atoms in blue, and the sulfur atoms in yellow.

Arsenopyrite has a monoclinic unit cell belonging to the space group  $P2_1/c$  derived from marcasite (orthorhombic  $\text{FeS}_2$ ) [17] with 4  $\text{FeAsS}$  formulas per unit cell, as shown in Figure 1.5a-b. However, a refinement of the structure of arsenopyrite in the space group  $C2_1/d$  has also been performed [35], in a pseudo-orthorhombic unit cell as shown in Figure 1.5c. Nevertheless the first refinement, in the  $P2_1/c$  group, seems to be preferred by most authors [17, 36, 37]. Its structure contains arsenic and sulfur dianions ( $\text{As-S}$ ) in the shape of dumbbells coordinated to iron in an octahedral way (Figure 1.6a). The adjacent octahedra in a row share one edge and their coordinations are related to each other by an inversion operation. This results in alternating short and long distances between cations (Figure 1.6b).

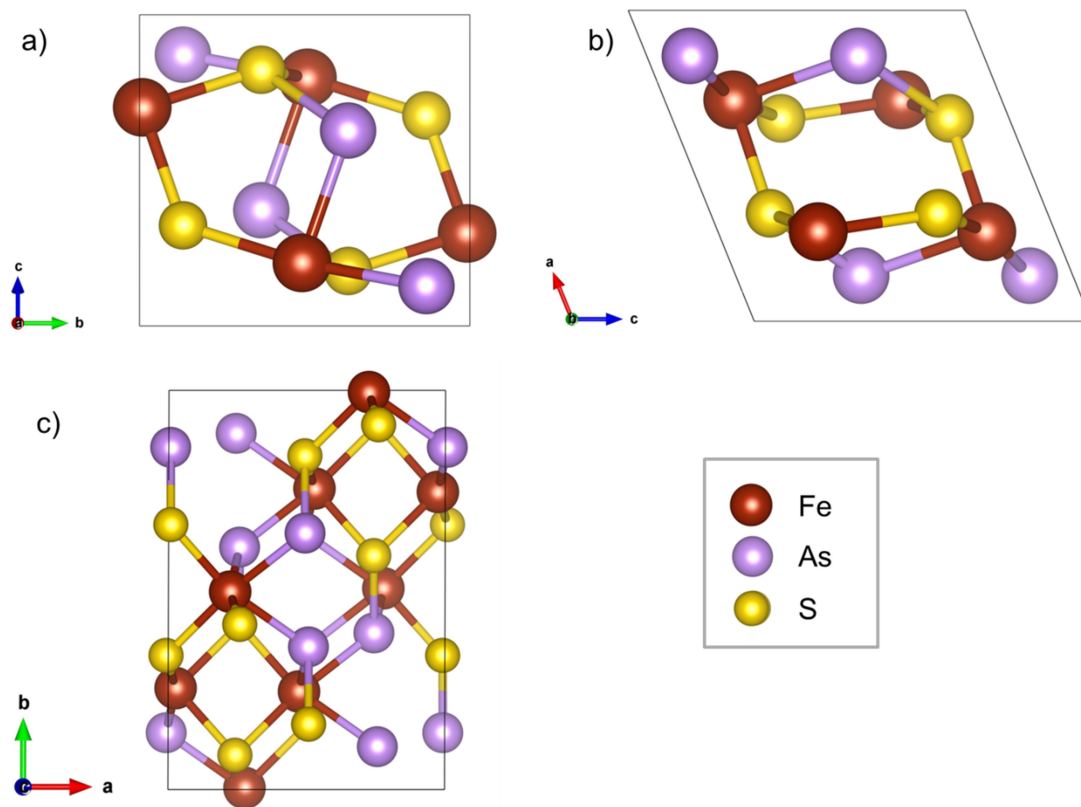


Figure 1.5: Unit cell of arsenopyrite. a) view along *a* axis of the monoclinic cell; b) view along *b* axis of the monoclinic cell; c) view along *c* axis of the pseudo-orthorhombic cell.

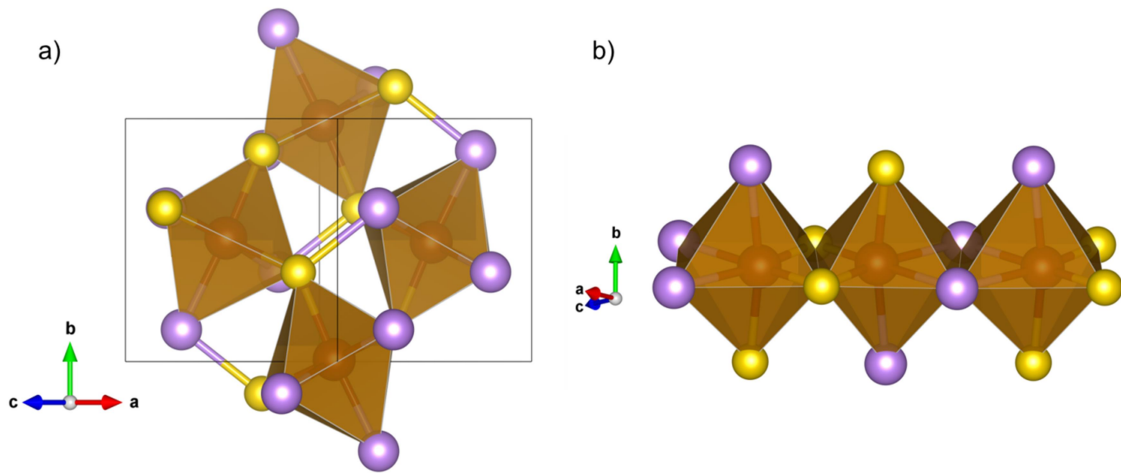


Figure 1.6: a) The As–S dianions coordinated octahedrally to Fe; b) neighboring octahedra share an edge. The iron atoms are in brown color, the arsenic atoms in purple, and the sulfur atoms in yellow.

Natural arsenopyrite has a composition ranging from  $\text{FeAs}_{0.9}\text{S}_{1.1}$  to  $\text{FeAs}_{1.1}\text{S}_{0.9}$  [36]. It is a diamagnetic semiconductor mineral [30]. About the cleavage plane, the literature informations do not agree with each other and vary among the (100) [38], (001) [39], (101) [17, 40] and (110) [27, 41] planes. Many of the published studies do not clearly define which unit cell was used as a reference, creating ambiguities in the definition of a preferential cleavage plane. Therefore, there may be discrepancies due to two different unit cells, since the cleavage plane changes accordingly.

### 1.3 Arsenopyrite and Acid Rock Drainage

In atmospheric conditions, arsenopyrite is a stable phase in reducing environments, but it is oxidized in the presence of common oxidants, such as ferric ion ( $\text{Fe}^{3+}$ ) and dissolved oxygen in aqueous media [22]. Under these conditions, the oxidation of arsenopyrite has slow kinetics, which can be catalyzed by microorganisms present in the environment [22]. Its oxidation by weathering effects releases the chemical species  $\text{H}_2\text{SO}_4$ ,  $\text{H}_3\text{AsO}_3$  and  $\text{H}_3\text{AsO}_4$  [21] to the environment. These generated species are a problem because they contain arsenic and because the acid produced in the oxidation reaction increases the dissolution of heavy metals into groundwater and acidifies aquifers. Arsenic is toxic to plants and animals, so its

release, as a result of arsenopyrite oxidation, increases environmental risk and can become a public health problem [42]. For this reason, understanding the kinetics and dissolution mechanisms of this mineral in different conditions is extremely important in environmental, social and economic ways [42].

Arsenic is a ubiquitous element found naturally in the atmosphere, soil, rocks, natural waters and organisms. However anthropogenic activity such as mining, fossil fuel burning, and the use of arsenic as a pesticide and herbicide in the past, besides its current use in wood preservation, can increase its availability in the environment [43]. Arsenic is often found in penta- and trivalent states, in which arsenite, As(III), is more toxic, more soluble and more mobile than arsenate, As(V) [44]. To humans, the toxicity of As(III) is related to its irreversible complexation with sulfhydryl (R-SH) groups present in enzymes and aminoacids, while As(V) competes with phosphate ions, interrupting the phosphorylation process [45]. Arsenate is more abundant under oxidizing conditions, while arsenite is prevalent in a reducing environment [42].

A study in the scope of INCT-Acqua investigated the possibility of contamination by arsenic in a community close to the mining area in the Brazilian town of Paracatu/MG [46]. The amount of As present in air, water, soil/dust and food was measured and, considering all sources, the calculated risk associated with arsenic exposure to the population was 0.44  $\mu\text{g}/\text{kg}/\text{day}$  for adults. The maximum dose established by the WHO ( $\text{BMDL}_{0.5}$ ) is 3  $\mu\text{g}/\text{kg}/\text{day}$ , higher than the dose found in Paracatu. Still the environmental risks of mining waste cannot be neglected, requiring chemical procedures to immobilize arsenic and mitigate environmental problems.

In the gold mine Cuiabá, located in the town of Sabará/MG, arsenopyrite present in the sulfide concentrate is volatilized in the form of arsenic trioxide ( $\text{As}_2\text{O}_3$ ) in the calcination process, then As is adsorbed to water in the gas scrubbers and finally removed by coprecipitation/adsorption with the addition of oxide or iron salts and lime [47]. The waste of this process is arranged in tailings dams located near the metallurgical plant.

In North America the most common techniques for prevention and correction of ARD are grouped into passive, active and bacterial [48]. Passive techniques include wetlands, limestone drains, water covers and natural geochemical/biological processes. In wetlands, a dilution of the waste is made, then the heavy metals are removed by filtration and the waste is placed on marshes, where they are gradually

degraded. Subsequently, anaerobic and aerobic processes naturally neutralize the water. Limestone drains are a series of tubes containing lime that neutralizes the acid drainage while the liquid flows within them. Water covers serve as a barrier to atmospheric oxygen, slowing down the oxidation process. In natural processes, the waste is dumped into water bodies containing limestone and a high buffering capacity that is able to neutralize it. Oxide minerals present in the system can avoid ARD because they are able to receive  $H^+$ , buffering the medium and slowing down the oxidation reaction [49]. In this case, tests are necessary to measure the ecological sensitivity of the environment. Active methods involve investments into technology and require the addition of bases, followed by a separation of solids and liquids to remove metal hydroxides and finally the disposal of the sludge. These processes are expensive and involve products that may require additional cleaning. Lastly, the use of bacteria and algae capable of decomposing sulfides has been the best solution from an economic and environmental point of view, but it is not always technically applicable [48].

Although there is no general pattern to predict ARD, the procedures commonly used in engineering do not deviate from Morin and Hutt's wheel [14]. They are procedures done in practice in the field and laboratory, but the knowledge about sulfides oxidation mechanism is still scarce. This comprehension allows the definition of more efficient and effective processes to reduce the environmental problem of ARD, as well as the costs of waste treatment. This understanding is highly enriched from the study of the chemical reactivity of the sulfide surfaces, a subject which has been given attention to in the literature in recent years [50-52].

#### ***1.4 Arsenopyrite and the Chemical Reactivity of Sulfides***

As a wide range of different oxidation states is possible for metals and sulfur, sulfide minerals are very reactive. In contact with aqueous solutions, the chemistry of sulfide surfaces is controlled by the pH and the reduction potential. In Figure 1.7 the Pourbaix diagram for arsenopyrite is shown. Chemical species in contact with water survive in the range between the dashed lines. The dashed box in the middle

presents near-surface conditions. It indicates that arsenopyrite can be oxidized when exposed to the atmosphere.

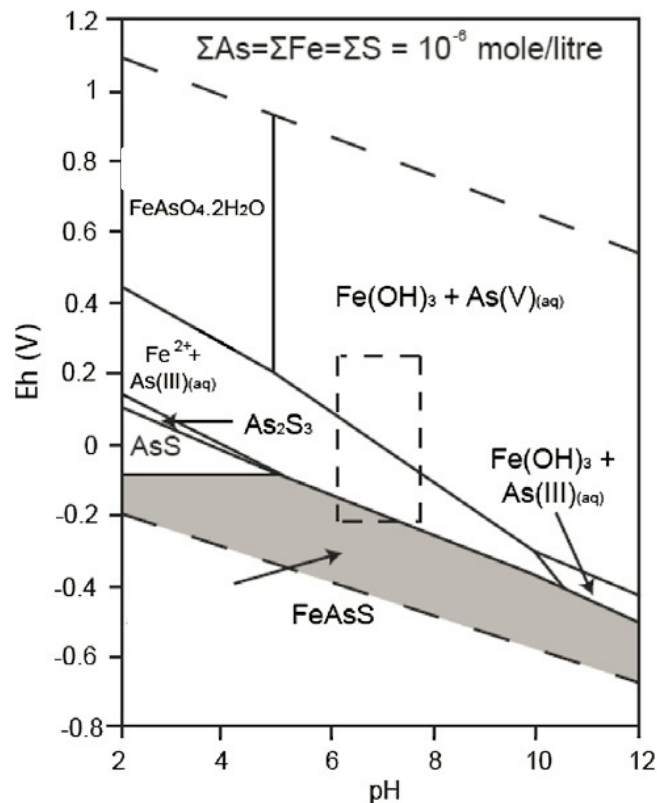


Figure 1.7: Eh-pH diagram for Arsenopyrite. Reference [22] adapted from [53].

Experimental researches use techniques such as LEED (Low Energy Electron Diffraction), Infra-Red Spectroscopy, XPS (X-ray Photoelectron Spectroscopy) and Auger Spectroscopy, besides Cyclic Voltammetry and other methods, to study the chemical composition and reactivity of surfaces [1, 52]. In particular the use of high-intensity photon sources, together with synchrotron radiation, has increased the sensitivity of analysis regarding surfaces and the spatial resolution of existing techniques. The use of synchrotron radiation allowed for extending the application of X-ray Absorption Spectroscopy techniques such as EXAFS (Extended X-ray Absorption Fine Structure) and XANES (X-ray Absorption Near-Edge Structure), which can be used to investigate the environment of surface atoms of a particulate sample in contact with a fluid at a molecular scale [31].

Microscopy techniques are also used, such as Scanning Tunneling Microscopy (STM) and Atomic Force Microscopy (AFM), which allow for an "observation" of the surface atoms, as well as *in situ* monitoring of gases and fluids

reactions on a surface in real time [31]. However, these techniques cannot always reach only the surface atoms. In the LEED technique, for example, electrons can penetrate between 5 and 20 Å into the surface [31], in XPS, about six atomic monolayers for Fe analysis and 15 layers for As analysis [54], and in Auger Spectroscopy about 10 Å [55]. To get a molecular point of view of the reaction, precisely on the surface atoms, it is possible to combine experimental results with results obtained by computer simulation [56-58], in particular Density Functional Theory (DFT) methods. The increased computing capacity and the improvement of numerical methods and computer programs made systems such as sulfide minerals accessible for numerical calculations. Theoretical methods help in understanding the geometry of both solid and surface, and also its electronic, electrical and mechanical properties.

In order to understand the mechanism of chalcopyrite leaching, many experimental [59-62] and theoretical [34, 63-66] studies have been published. Also pyrite has been widely investigated by both experimental [15, 50, 67, 68] and theoretical [50, 69-74] techniques, besides two theoretical works about arsenic incorporation into pyrite [75, 76]. About arsenopyrite, there are several studies in the literature concerning the products formed in its oxidation in different media [21, 22, 38, 77-81] and one theoretical study about the electronic characteristic of arsenopyrite (110) surface [41]. But since the natural samples used in these studies may vary in composition and the solutions formed in the process are too complex, as well as the reactions involved, the results found for products, kinetics and mechanism of arsenopyrite oxidation are not always in agreement, and a lack of consensus is observed [22].

Buckley and Walker [77], as well as Mikhlin *et al.* [81], suggested a depletion in Fe and As on arsenopyrite surface after acid treatment. Costa *et al.* [82] observed elemental S when arsenopyrite was reacted in acid. However Richardson and Vaughan [55] found the opposite: a surface enriched in Fe and As after reaction with H<sub>2</sub>SO<sub>4</sub>. Nesbitt and Muir [79] reported the absence of S on arsenopyrite surface reacted in acidic mine waste water. Nesbitt *et al.* [21] and Schaufuss *et al.* [83] found a preferential enrichment of arsenic as As-oxides on the overlayer of oxidized arsenopyrite due to diffusion of this atom from the bulk. In aqueous solution this layer can be leached. Corkhill *et al.* [38] observed the species Fe(III)-OH, As(III)-O, As(V)-O, thiosulfate and sulfate for arsenopyrite reacted in H<sub>2</sub>SO<sub>4</sub>. They also

observed that As is the most rapidly oxidized element under these conditions. Nesbitt *et al.* [21] and Schaufuss *et al.* [83] agreed that As is more readily oxidized than Fe, and S, while McKibben *et al.*'s [84] results show that Fe is dissolved quicker than As. Walker *et al.* [85] proposed that the rate-determining step of the oxidation reaction in FeAsS is the attachment of oxygen from water to As and S species, while Corkhill *et al.* [22] suggested that it could be the transference of electrons to the oxidant agent. Nesbitt *et al.* [21] also observed the same type of chemical species in air-oxidation and water-oxidation of arsenopyrite, however greater proportions of oxide species were found by water-oxidation, especially S-oxides, which indicates that the oxidation process is more intense in this medium. McKibben *et al.* [84] found that arsenopyrite dissolution is three to four times faster than pyrite and Blanchard *et al.* [76] noticed that the presence of arsenic in pyrite could accelerate its dissolution, and consequently the ARD.

The observed differences might originate from the variety of media the studies have been performed in. Therefore, more information about arsenopyrite and its chemical reactivity is necessary. In this context, first-principles calculations emerge as a tool providing information about the surface reactivity of arsenopyrite and insights about its oxidation mechanism. One advantage of theoretical studies is that the results can be carried out in more controlled situations than what can be done experimentally. The understanding of the kinetics and the mechanism of dissolution of this material in different conditions is essential for assessing the stability of the arsenic-containing tailings and the development of more efficient processes to control its remobilization with great environmental, social and economic consequences.

A proposed mechanism for the oxidation reaction of pyrite was studied by Sit and coworkers using the DFT method [73]. In this study, the proposed mechanism starts at the dissociative adsorption of O<sub>2</sub> on two adjacent Fe atoms on the (100) surface of pyrite, forming the species Fe<sup>4+</sup>=O<sup>2-</sup>. Simultaneously, an incoming water molecule interacts with the adsorbed oxygen by a hydrogen bond. In a second step, the water molecule transfers both hydrogens to each adsorbed oxygen, forming Fe<sup>3+</sup>-OH<sup>-</sup>, while the oxygen stemmed from water adsorbs to a sulfur atom, oxidizing it. A second water molecule is added and again donates both hydrogens to the OH groups, forming adsorbed water on Fe, and the remaining oxygen binds to sulfur. The water molecules are desorbed, a new oxygen molecule adsorbs dissociatively,

and the reaction repeats until the surface S is completely oxidized to  $\text{SO}_4^{2-}$  and all proposed steps are energetically favorable. Yet another proposed mechanism, possibly more favorable, was made by Duarte *et al.* [52], which takes into account the formation of more common chemical species and is diagrammed in Figure 1.8. For the other sulfides, there is no theoretical study in the literature considering the oxidation mechanism.

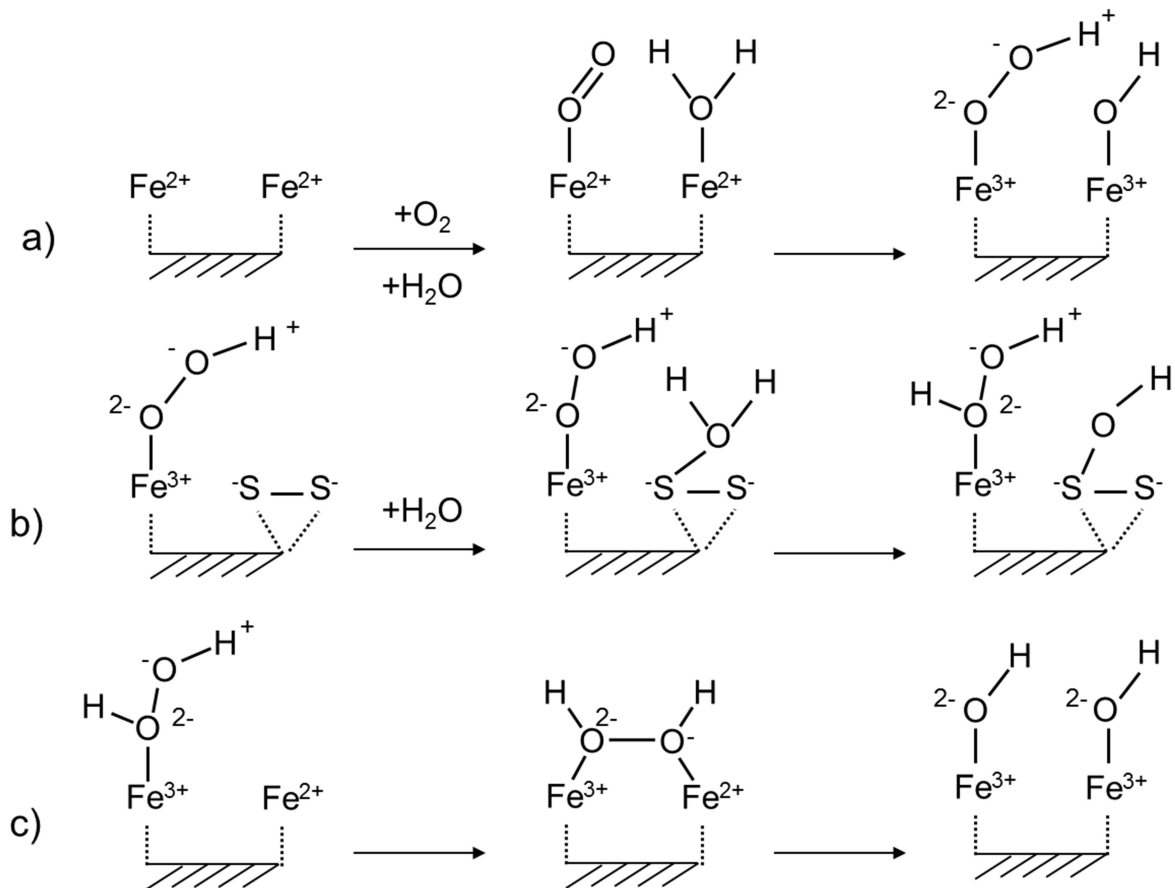


Figure 1.8: Pyrite oxidation mechanism. From reference [52].

Studies of the arsenopyrite oxidation mechanism are still relatively scarce. Aspects such as the effect of arsenic in the arsenopyrite structure and its influence on the chemical reactivity of this mineral have not yet been answered. The structure of the surface and its interaction with leaching agents, such as water, cations and anions as well as acids are not understood. The objective of this work is to fill this gap of information, aiming to contribute to understand the oxidation mechanism of arsenopyrite at a molecular level. It has been a consensus that without understanding this process at a molecular level it will be difficult to have a

breakthrough in this field and to envisage more efficient strategies to mitigate the ARD in the mining regions rich in arsenopyrite.

In the next chapter, the fundamentals of the methodology used in this work are reviewed. The following chapters will be concerned with the structure and electronic properties of arsenopyrite and its cleavage surfaces and with the adsorption of water and other leaching agents. A proposal for the oxidation mechanism in the presence of oxygen and water is presented. In the final considerations, we highlight the main achievements and the perspectives of the field. We advance that the oxidation mechanism is closely related to the pyrite oxidation mechanism which we have also investigated [74].

## 1.5 References

1. Vaughan, D.J., *Sulfide Mineralogy and Geochemistry: Introduction and Overview*. Reviews in Mineralogy and Geochemistry, 2006. **61**(1): p. 147.
2. Vaughan, D.J. and J.R. Craig, *Mineral chemistry of metal sulfides*. Cambridge earth science series. 1978, Cambridge Eng. ; New York: Cambridge University Press.
3. Ennaoui, A., et al., *Photoactive Synthetic Polycrystalline Pyrite (FeS<sub>2</sub>)* Journal of the Electrochemical Society, 1985. **132**(7): p. 1579-1582.
4. Ennaoui, A., et al., *Photoelectrochemistry of Highly Quantum Efficient Single-Crystalline n-FeS<sub>2</sub> (Pyrite)*. Journal of the Electrochemical Society, 1986. **133**(1): p. 97-106.
5. Ennaoui, A. and H. Tributsch, *Iron sulphide solar cells*. Solar Cells, 1984. **13**(2): p. 197-200.
6. Wang, S.S. and R.N. Seefurth, *Electrochemical Studies of FeS<sub>2</sub> Electrodes in Various Sulfide-Containing Molten Salts*. Journal of The Electrochemical Society, 1987. **134**(3): p. 530-535.
7. Cody, G.D., et al., *Assaying the catalytic potential of transition metal sulfides for abiotic carbon fixation*. Geochimica et Cosmochimica Acta, 2004. **68**(10): p. 2185-2196.
8. Wächtershäuser, G., *Before enzymes and templates: theory of surface metabolism*. Microbiological Reviews, 1988. **52**(4): p. 452-484.
9. Russell, M.J., A.J. Hall, and A.P. Gize, *Pyrite and the origin of life*. Nature, 1990. **344**(6265): p. 387-387.
10. Huber, C. and G. Wächtershäuser, *Activated Acetic Acid by Carbon Fixation on (Fe,Ni)S Under Primordial Conditions*. Science, 1997. **276**(5310): p. 245-247.
11. Akcil, A. and S. Koldas, *Acid Mine Drainage (AMD): causes, treatment and case studies*. Journal of Cleaner Production, 2006. **14**(12-13): p. 1139-1145.

12. Fernández-Remolar, D.C., et al., *The Río Tinto Basin, Spain: Mineralogy, sedimentary geobiology, and implications for interpretation of outcrop rocks at Meridiani Planum, Mars*. *Earth and Planetary Science Letters*, 2005. **240**(1): p. 149-167.
13. 02/14/2014]; Available from: <http://upload.wikimedia.org/wikipedia/commons/thumb/9/91/Riotintoagua.jpg/200px-Riotintoagua.jpg>.
14. Parbhakar-Fox, A. and B.G. Lottermoser, *A critical review of acid rock drainage prediction methods and practices*. *Minerals Engineering*, 2015. **82**: p. 107-124.
15. Chandra, A.P. and A.R. Gerson, *The mechanisms of pyrite oxidation and leaching: A fundamental perspective*. *Surface Science Reports*, 2010. **65**(9): p. 293-315.
16. *The Environmental Geochemistry of Mineral Deposits*. Part A: Processes, Techniques, and Health Issues Part B: Case Studies and Research Topics, ed. G.S. Plumlee, M.J. Logsdon, and L.F. Filipek. 1996: Society of Economic Geologists. 588.
17. Klein, C., C.S. Hurlbut, and J.D. Dana, *Manual of mineralogy : (after James D. Dana)*. 21st ed. 1999, New York: J. Wiley.
18. *Informações e Análises da Economia Mineral Brasileira* Available from: <http://www.ibram.org.br/sites/1300/1382/00001145.pdf>.
19. Davenport, W.G., et al., *Extractive Metallurgy of Copper*. 2002: Elsevier Science.
20. Córdoba, E.M., et al., *Leaching of chalcopyrite with ferric ion. Part I: General aspects*. *Hydrometallurgy*, 2008. **93**(3-4): p. 81-87.
21. Nesbitt, H.W., I.J. Muir, and A.R. Prarr, *Oxidation of arsenopyrite by air and air-saturated, distilled water, and implications for mechanism of oxidation*. *Geochimica et Cosmochimica Acta*, 1995. **59**(9): p. 1773-1786.
22. Corkhill, C.L. and D.J. Vaughan, *Arsenopyrite oxidation – A review*. *Applied Geochemistry*, 2009. **24**(12): p. 2342-2361.
23. SHB. 01/03/2014]; Available from: <http://www.mineral-s.com/imagenes/pirita5-8599.gif>.
24. Weller, R. 2009 01/03/2014]; Available from: <http://skywalker.cochise.edu/wellerr/mineral/chalcopyrite/6chalcopyrite98.jpg>.
25. Harrison, J. 2009 01/03/2014]; Available from: [http://upload.wikimedia.org/wikipedia/commons/thumb/c/c4/Arsenopyrite%2C\\_Panasqueira\\_Mine%2C\\_Portugal.jpg/800px-Arsenopyrite%2C\\_Panasqueira\\_Mine%2C\\_Portugal.jpg](http://upload.wikimedia.org/wikipedia/commons/thumb/c/c4/Arsenopyrite%2C_Panasqueira_Mine%2C_Portugal.jpg/800px-Arsenopyrite%2C_Panasqueira_Mine%2C_Portugal.jpg).
26. Vaughan, D.J., U. Becker, and K. Wright, *Sulphide mineral surfaces: theory and experiment*. *International Journal of Mineral Processing*, 1997. **51**(1-4): p. 1-14.
27. Dana, E.S. and W.E. Ford, *A Text-book of Mineralogy: With an Extended Treatise on Crystallography and Physical Mineralogy*. 4 ed. 1966, New York: Wiley.
28. Pauling, L., *Crystallography and Chemical Bonding in Sulfide Minerals*. *Mineralogical Society of America Special Paper*, 1970. **3**: p. 125-131.
29. Von Oertzen, G.U., S.L. Harmer, and W.M. Skinner, *XPS and ab initio calculation of surface states of sulfide minerals: pyrite, chalcopyrite and molybdenite*. *Molecular Simulation*, 2006. **32**(15): p. 1207-1212.
30. Pearce, C.I., R.A.D. Patrick, and D.J. Vaughan, *Electrical and Magnetic Properties of Sulfides*. *Reviews in Mineralogy and Geochemistry*, 2006. **61**(1): p. 127-180.
31. Rosso, K.M., *Sulfide Mineral Surfaces*. *Reviews in Mineralogy and Geochemistry*, 2006. **61**(1): p. 505-556.

32. Chase, M.W., et al., *Janaf Thermochemical Tables - 3rd Edition* .2. Journal of Physical and Chemical Reference Data, 1985. **14**: p. 927-1856.
33. Mikhlin, Y.L., et al., *Spectroscopic and electrochemical characterization of the surface layers of chalcopyrite (CuFeS<sub>2</sub>) reacted in acidic solutions*. Applied Surface Science, 2004. **225**(1-4): p. 395-409.
34. de Oliveira, C., et al., *Reconstruction of the Chalcopyrite Surfaces—A DFT Study*. The Journal of Physical Chemistry C, 2012. **116**(10): p. 6357-6366.
35. Fues, H., et al., *Crystal-Structure Refinement and Electron-Microscopy of Arsenopyrite*. Zeitschrift Fur Kristallographie, 1987. **179**(1-4): p. 335-346.
36. Morimoto, N. and L.A. Clark, *Arsenopyrite Crystal-Chemical Relations*. American Mineralogist, 1961. **46**(11-2): p. 1448-1469.
37. Bindi, L., et al., *Stoichiometric Arsenopyrite, FeAsS, from La Roche-Balve Quarry, Loire-Atlantique, France: Crystal Structure and Mossbauer Study*. The Canadian Mineralogist, 2012. **50**(2): p. 471-479.
38. Corkhill, C.L., et al., *The oxidative dissolution of arsenopyrite (FeAsS) and enargite (Cu<sub>3</sub>AsS<sub>4</sub>) by Leptospirillum ferrooxidans*. Geochimica et Cosmochimica Acta, 2008. **72**(23): p. 5616-5633.
39. Ford, M. and C.C. Ferguson, *Cleavage Strain in the Variscan Fold Belt, County Cork, Ireland, Estimated from Stretched Arsenopyrite Rosettes*. Journal of Structural Geology, 1985. **7**(2): p. 217-223.
40. Wolff, G.A. and J.D. Broder, *Cleavage and the Identification of Minerals*. American Mineralogist, 1960. **45**(11-2): p. 1230-1242.
41. Corkhill, C.L., M.C. Warren, and D.J. Vaughan, *Investigation of the electronic and geometric structures of the (110) surfaces of arsenopyrite (FeAsS) and enargite (Cu<sub>3</sub>AsS<sub>4</sub>)*. Mineralogical Magazine, 2011. **75**(1): p. 45-63.
42. Cheng, H.F., et al., *Geochemical processes controlling fate and transport of arsenic in acid mine drainage (AMD) and natural systems*. Journal of Hazardous Materials, 2009. **165**(1-3): p. 13-26.
43. Smedley, P.L. and D.G. Kinniburgh, *A review of the source, behaviour and distribution of arsenic in natural waters*. Applied Geochemistry, 2002. **17**(5): p. 517-568.
44. Mandal, B.K. and K.T. Suzuki, *Arsenic round the world: a review*. Talanta, 2002. **58**(1): p. 201-235.
45. Ladeira, A.C.Q., et al., *Chemical speciation and its importance for the mineral extraction processes and environmental remediation*. Cadernos Temáticos de Química Nova na Escola, 2014. **8**: p. 18-23.
46. Ciminelli, V.S.T., et al., *Annual Activity Report*. 2012, INCT - Acqua: Belo Horizonte. p. 30-34.
47. Pantuzzo, F.L. and V.S.T. Ciminelli, *Arsenic association and stability in long-term disposed arsenic residues*. Water Research, 2010. **44**(19): p. 5631-5640.
48. Hilson, G. and B. Murck, *Progress toward pollution prevention and waste minimization in the North American gold mining industry*. Journal of Cleaner Production, 2001. **9**(5): p. 405-415.
49. Brough, C.P., et al., *The process mineralogy of mine wastes*. Minerals Engineering, 2013. **52**: p. 125-135.
50. Murphy, R. and D.R. Strongin, *Surface reactivity of pyrite and related sulfides*. Surface Science Reports, 2009. **64**(1): p. 1-45.

51. Chen, J.-h., et al., *DFT calculation on relaxation and electronic structure of sulfide minerals surfaces in presence of H<sub>2</sub>O molecule*. Journal of Central South University, 2014. **21**(10): p. 3945-3954.
52. de Lima, G.F., H. Avelino de Abreu, and H. Anderson Duarte, *Chapter 6 Surface reactivity of the sulfide minerals*, in *Chemical Modelling: Volume 10*. 2014, The Royal Society of Chemistry. p. 153-182.
53. Craw, D., D. Falconer, and J.H. Youngson, *Environmental arsenopyrite stability and dissolution: theory, experiment, and field observations*. Chemical Geology, 2003. **199**(1–2): p. 71-82.
54. Jones, R.A. and H.W. Nesbitt, *XPS evidence for Fe and As oxidation states and electronic states in loellingite (FeAs<sub>2</sub>)*. American Mineralogist, 2002. **87**(11-12): p. 1692-1698.
55. Richardson, S. and D.J. Vaughan, *Arsenopyrite - a Spectroscopic Investigation of Altered Surfaces*. Mineralogical Magazine, 1989. **53**(370): p. 223-229.
56. Ladeira, A.C.Q., et al., *Mechanism of anion retention from EXAFS and density functional calculations: arsenic (V) adsorbed on gibbsite*. Geochimica et Cosmochimica Acta, 2001. **65**(8): p. 1211-1217.
57. Teixeira, M.C., et al., *Raman spectroscopy and DFT calculations of As(III) complexation with a cysteine-rich biomaterial*. Journal of Colloid and Interface Science, 2007. **315**(1): p. 128-134.
58. Duarte, G., et al., *As(III) immobilization on gibbsite: Investigation of the complexation mechanism by combining EXAFS analyses and DFT calculations*. Geochimica et Cosmochimica Acta, 2012. **83**: p. 205-216.
59. Munoz, P.B., J.D. Miller, and M.E. Wadsworth, *Reaction mechanism for the acid ferric sulfate leaching of chalcopyrite*. Metallurgical Transactions B, 1979. **10**(2): p. 149-158.
60. Parker, A., et al., *An X-ray photoelectron spectroscopy study of the mechanism of oxidative dissolution of chalcopyrite*. Hydrometallurgy, 2003. **71**(1–2): p. 265-276.
61. Hackl, R.P., et al., *Passivation of chalcopyrite during oxidative leaching in sulfate media*. Hydrometallurgy, 1995. **39**(1–3): p. 25-48.
62. Baláž, P., et al., *Combined chemical and bacterial leaching of ultrafine ground chalcopyrite*. Hydrometallurgy, 1996. **42**(2): p. 237-244.
63. Edelbro, R., Å. Sandström, and J. Paul, *Full potential calculations on the electron bandstructures of Sphalerite, Pyrite and Chalcopyrite*. Applied Surface Science, 2003. **206**(1–4): p. 300-313.
64. de Oliveira, C. and H.A. Duarte, *Disulphide and metal sulphide formation on the reconstructed (001) surface of chalcopyrite: A DFT study*. Applied Surface Science, 2010. **257**(4): p. 1319-1324.
65. de Lima, G.F., et al., *Water Adsorption on the Reconstructed (001) Chalcopyrite Surfaces*. The Journal of Physical Chemistry C, 2011. **115**(21): p. 10709-10717.
66. de Lima, G.F., et al., *Sulfuric and hydrochloric acid adsorption on the reconstructed sulfur terminated (001) chalcopyrite surface*. International Journal of Quantum Chemistry, 2012. **112**(19): p. 3216-3222.
67. Savage, K.S., D. Stefan, and S.W. Lehner, *Impurities and heterogeneity in pyrite: Influences on electrical properties and oxidation products*. Applied Geochemistry, 2008. **23**(2): p. 103-120.

68. Rimstidt, J.D. and D.J. Vaughan, *Pyrite oxidation: A state-of-the-art assessment of the reaction mechanism*. *Geochimica et Cosmochimica Acta*, 2003. **67**(5): p. 873-880.
69. Hung, A., et al., *Density-functional theory studies of pyrite FeS<sub>2</sub>(100) and (110) surfaces*. *Surface Science*, 2002. **513**(3): p. 511-524.
70. Hung, A., et al., *Density-functional theory studies of pyrite FeS<sub>2</sub> (111) and (210) surfaces*. *Surface Science*, 2002. **520**(1-2): p. 111-119.
71. Stirling, A., M. Bernasconi, and M. Parrinello, *Ab initio simulation of water interaction with the (100) surface of pyrite*. *Journal of Chemical Physics*, 2003. **118**(19): p. 8917-8926.
72. Stirling, A., M. Bernasconi, and M. Parrinello, *Defective pyrite (100) surface: An ab initio study*. *Physical Review B*, 2007. **75**(16): p. 165406.
73. Sit, P.H.L., M.H. Cohen, and A. Selloni, *Interaction of Oxygen and Water with the (100) Surface of Pyrite: Mechanism of Sulfur Oxidation*. *Journal of Physical Chemistry Letters*, 2012. **3**(17): p. 2409-2414.
74. Dos Santos, E.C., J.C. de Mendonça Silva, and H.A. Duarte, *Pyrite Oxidation Mechanism by Oxygen in Aqueous Medium*. *The Journal of Physical Chemistry C*, 2016. **120**(5): p. 2760-2768.
75. Reich, M. and U. Becker, *First-principles calculations of the thermodynamic mixing properties of arsenic incorporation into pyrite and marcasite*. *Chemical Geology*, 2006. **225**(3-4): p. 278-290.
76. Blanchard, M., et al., *Arsenic incorporation into FeS<sub>2</sub> pyrite and its influence on dissolution: A DFT study*. *Geochimica et Cosmochimica Acta*, 2007. **71**(3): p. 624-630.
77. Buckley, A.N. and G.W. Walker, *The Surface-Composition of Arsenopyrite Exposed to Oxidizing Environments*. *Applied Surface Science*, 1988. **35**(2): p. 227-240.
78. Fernandez, P.G., H.G. Linge, and M.W. Wadsley, *Oxidation of arsenopyrite (FeAsS) in acid .1. Reactivity of arsenopyrite*. *Journal of Applied Electrochemistry*, 1996. **26**(6): p. 575-583.
79. Nesbitt, H.W. and I.J. Muir, *Oxidation states and speciation of secondary products on pyrite and arsenopyrite reacted with mine waste waters and air*. *Mineralogy and Petrology*, 1998. **62**(1-2): p. 123-144.
80. Almeida, C.M.V.B. and B.F. Giannetti, *Electrochemical study of arsenopyrite weathering*. *Physical Chemistry Chemical Physics*, 2003. **5**(3): p. 604-610.
81. Mikhlin, Y.L., A.S. Romanchenko, and I.P. Asanov, *Oxidation of arsenopyrite and deposition of gold on the oxidized surfaces: A scanning probe microscopy, tunneling spectroscopy and XPS study*. *Geochimica et Cosmochimica Acta*, 2006. **70**(19): p. 4874-4888.
82. Costa, M.C., A.M. Botelho do Rego, and L.M. Abrantes, *Characterization of a natural and an electro-oxidized arsenopyrite: a study on electrochemical and X-ray photoelectron spectroscopy*. *International Journal of Mineral Processing*, 2002. **65**(2): p. 83-108.
83. Schaufuss, A.G., et al., *Reactivity of surface sites on fractured arsenopyrite (FeAsS) toward oxygen*. *American Mineralogist*, 2000. **85**(11-12): p. 1754-1766.
84. McKibben, M.A., B.A. Tallant, and J.K. del Angel, *Kinetics of inorganic arsenopyrite oxidation in acidic aqueous solutions*. *Applied Geochemistry*, 2008. **23**(2): p. 121-135.
85. Walker, F.P., M.E. Schreiber, and J.D. Rimstidt, *Kinetics of arsenopyrite oxidative dissolution by oxygen*. *Geochimica et Cosmochimica Acta*, 2006. **70**(7): p. 1668-1676.

## 2 Methodology

In this chapter the main theoretical concepts and methodologies used in this work are presented. Not all details of the theoretical concepts and the mathematical and computational implementation of the methods used are covered. Further discussion can be found in the cited references.

### 2.1 *Density Functional Theory (DFT)*

Density Functional Theory (DFT) has become an alternative to *ab initio* methods – Hartree-Fock (HF) and post-HF (perturbation methods, coupled-cluster and configuration interaction) – for calculating the electronic structure of solid and molecular systems in the last decades [1]. The great advantage of DFT is the lower computational cost when compared to the usual theoretical methods including electron correlation. Therefore DFT is nowadays the most used method to investigate solids and surfaces, which often requires the simulation of many atoms with a large number of electrons.

DFT uses the electron density,  $\rho(r)$ , as the basic variable in the description of an electronic system. This practice was first performed in the early twentieth century by Drude [2, 3], who applied the kinetic theory of gases to treat metals. His theory describes the electrons of a metal as a homogeneous electron gas to study the thermal and electrical conduction. From this idea, other models have been developed, such as the Thomas-Fermi model [4, 5], which uses statistical arguments to calculate the system energy functional based on the electron density. In the following, Dirac [6] improved this model to include the exchange energy. However, only after the publication of the theorems of Hohenberg and Kohn [7] in 1964, DFT was recognized as an exact theory and the use of the electron density as the basic variable was legitimized. The first Hohenberg and Kohn theorem states that the external potential to which the electrons are subjected is a single functional of  $\rho(r)$ , plus an additive constant, that is, the electron density of a system determines the external potential and the number of electrons,  $N$ , which can be calculated through equation

$$\int \rho(r) dr = N. \quad (2.1)$$

By determining the number of electrons in a system from  $\rho(r)$ , one can also find the external potential in which the electrons move and consequently the Hamiltonian of the system. As the energy can be calculated by the Hamiltonian, it is determined by the electron density. The electronic ground state energy  $E_0$  is a functional of the electron density of the ground state:

$$E_0 = E_0[\rho_0]. \quad (2.2)$$

The second theorem of Hohenberg and Kohn follows the energy variational principle, in which the total energy of a system, calculated from an approximate electron density, will always be greater than or equal to the exact energy. Therefore, the electron density that describes the system is the one that minimizes the energy  $E_0$ . The ground state energy is then calculated using electron density functionals that contain the electronic interactions, according to

$$E_0[\rho_0] = T[\rho_0] + V_{ne}[\rho_0] + V_{ee}[\rho_0], \quad (2.3)$$

where  $T$  is the kinetic energy,  $V_{ne}$  is the energy related to the electron-nucleus interaction and  $V_{ee}$  is the electron-electron interaction. The latter term is composed of terms for the Coulomb interaction, exchange interaction and electron correlation.

The following year, in 1965, Kohn and Sham [8] developed a methodology that allows the DFT calculations, proposing a method to get around the problem of having to use an exact electron density functional for the kinetic energy. According to the interpretation of Levy [9], the Kohn-Sham method uses a reference system in which the electrons do not interact with each other and have the same electron density as the actual system. In this way, the residual part of the kinetic energy, which differs from the real system, is also included in the exchange and correlation functional.

The Hamiltonian of the reference system can be written according to:

$$\hat{H} = -\frac{1}{2}\nabla^2 + V_{ef}(r), \quad (2.4)$$

where the first term on the right is the kinetic energy operator and the second one the effective potential. Then the Schrödinger equation for one electron can be formulated as

$$\left(-\frac{1}{2}\nabla^2 + V_{ef}\right)\psi_i^{KS}(r) = \varepsilon_i\psi_i^{KS}(r). \quad (2.5)$$

Here,  $\psi_i^{KS}(r)$  is the wave function for each electron  $i$  in the position  $r$ , and  $\varepsilon_i$  is the respective eigenvalue of the wave function. The electron density of the reference system can be calculated according to equation 2.6, where  $N$  is the number of electrons in the system:

$$\rho(r) = \sum_i^N |\psi_i^{KS}(r)|^2. \quad (2.6)$$

The effective potential is calculated according to:

$$V_{ef}(r) = V(r) + \int \frac{\rho(r_1)}{|r - r_1|} dr + V_{xc}(r), \quad (2.7)$$

where  $V(r)$  is the external potential due to nuclear charges. The second term corresponds to the Coulomb potential and the last term to the exchange and correlation potential, defined by

$$V_{xc}(r) = \frac{\delta E_{xc}[\rho]}{\delta \rho}. \quad (2.8)$$

As the effective potential depends on the electron density, which is obtained by equations 2.5 and 2.6, to solve all the equations above, known as the Kohn-Sham equations, it is necessary to perform a self-consistent procedure similar to the HF method. In practice, an initial electron density is defined, which is used to calculate

the effective potential, and then equation 2.5 is solved to find a new set of  $\Psi_i(r)$ , with which a new density  $\rho(r)$  is found by equation 2.6 and the procedure is repeated until convergence. The total energy can be determined through

$$E = \sum \varepsilon_i - \frac{1}{2} \int \frac{\rho(r_1)\rho(r_2)}{|r_1 - r_2|} dr_1 dr_2 + E_{xc}[\rho] - \int \rho(r)V_{xc}(r)dr. \quad (2.9)$$

As well as the calculation of energy and the electron density of the system, the Kohn-Sham method enables the calculation of all other system properties. Through the theorems of Hohenberg and Kohn, it was proved that there is an exact electron density functional that permits the calculation of the system energy. However, this functional is unknown because its calculation requires the determination of the exchange and correlation (XC) potential, whose analytical expression is unknown. For this reason, the exchange and correlation functionals commonly used are derivative from approximations that tend to provide the most accurate results possible.

The Local Density Approximation (LDA) functional is based on the theory of the homogeneous electron gas, in which the exchange and correlation energy of a system with electron density  $\rho(r)$  is considered to be equal to the exchange and correlation energy of a homogeneous electron gas with the same electron density. As the electron density in real systems is not homogeneous, it was proposed to include the electron density gradient  $\nabla\rho(r)$  in the exchange-correlation functional. The set of these more elaborate functionals is called Generalized Gradient Approximation (GGA). Other types of functionals developed are hybrids functionals, which include part of the exact exchange energy of the Hartree-Fock method in the DFT exchange-correlation functional, besides meta-GGA functionals, which extend the expansion of the generalized gradient to second order derivatives (Laplacians).

Electronic structure calculations based on DFT describe reasonably well complex systems such as solids and surfaces. In the case of solids, usually a huge number of atoms is necessary for a good description of the system. This can be overcome by considering the inherent symmetry features of solids in order to decrease the computer effort and the number of atoms explicitly treated. A crystal can be described by a minimum set of lattice points, the unit cell, which is repeated

periodically in space to describe the whole crystal. Thus corresponding lattice points from different unit cells are geometrically equivalent and are related by a lattice translation operation (translational invariance). Note that there may exist further symmetry operations that relate different lattice points within the unit cell itself. Because of this characteristic, the potential energy of the solid system has the same periodicity of the lattice, according to

$$V(r+R)=V(r), \quad (2.10)$$

where  $R$  is the translation vector that leads from one unit cell to the next. Under these conditions the Bloch theorem states that every electronic wave function  $\psi_k(r)$  can be written as the product of a plane wave function ( $e^{ik \cdot r}$ ) with wave vector  $k$  and another function that has the same periodicity as the lattice ( $u_k(r)$ ), expressed in

$$\psi_k(r) = e^{ik \cdot r} u_k(r), \quad (2.11)$$

where

$$u_k(r+R) = u_k(r). \quad (2.12)$$

The wave vector  $k$  classifies the eigenvalues and eigenfunctions of the mono-electronic states in a periodic lattice. Bloch's theorem is interpreted as a boundary condition for the solutions of the Schrödinger equation in a periodic potential. This theorem changes the problem of calculating an infinite number of wave functions in a solid to the calculation of a finite number of wave functions in infinite  $k$  points. However, the wave functions in nearby  $k$  points will be very similar. So it is possible to represent the wave functions of a region in  $k$  space by functions at a single  $k$  point (discretization of  $k$  space).

In practice the  $k$  points sampling in the first Brillouin zone is used. The first Brillouin zone corresponds to the Wigner-Seitz cell in reciprocal space ( $k$  space), that is, the set of points that are closer to a specific lattice point than to any other point of the reciprocal lattice [10]. The Wigner-Seitz cell is a primitive cell, which means a unit cell with only one lattice point. Considering the structural and electronic

properties of this region is sufficient to characterize the whole crystal. Precise methods have been developed for the selection of electronic states in special  $k$  points, for example the method of Monkhorst-Pack [11]. The greater the number of  $k$  points chosen, the better can the calculation accuracy be expected, but the computational effort is increasing as well. Therefore the number of considered  $k$  points in each spatial direction should be carefully evaluated before starting a calculation of periodic systems.

## 2.2 Plane Waves (PW)

The solution to the Kohn-Sham equations can be obtained by an expansion of the wave function in a set of basis functions. In calculations of periodic systems, the periodic part of the wave function can be expanded using a basis set consisting of a discrete set of plane waves whose wave vectors  $G$  are vectors of the reciprocal crystal lattice [12].

$$u_k(r) = \sum_G c_{k,G} e^{iG \cdot r} . \quad (2.13)$$

In this way, each electronic wave function can be written as a sum of plane waves (PW),

$$\psi_k = \sum_G C_{k+G} e^{i(k+G) \cdot r} . \quad (2.14)$$

In agreement with this equation, for each  $k$  point, the wave function can be written as an infinite sum of  $G$  vectors, i.e., it would take an infinite set of plane waves for the expansion to be exact. However, plane waves related to large  $G$  values have small  $C_{k+G}$  coefficients and contribute little to the total sum, therefore it is possible to approximate the wave function by considering a finite number of expansion terms. It can be shown that the square of the sum  $k+G$  is related to the kinetic energy of a homogeneous electron gas,

$$E_{cin} = \frac{\hbar^2}{2m} |k + G|^2 \quad (2.15)$$

So the plane waves basis set may be truncated to include only the plane waves with less kinetic energy than a particular Energy cutoff. This procedure introduces an approximation error in the calculation of the total energy, which can be minimized by choosing an appropriate cutoff value. The higher this value is chosen, the greater the computational cost will be. Therefore, it is a crucial parameter that needs to be tested for convergence in relation to some system property before running the electronic structure calculations. It is worthwhile to remember that, while when using local basis sets the computational costs increase with the number of atoms, in the case of plane waves basis sets, the computational costs vary with the volume of the unit cell. In the case of surface studies, in which it is necessary to include a vacuum zone to create a surface, the costs are increased also in the direction perpendicular to the surface, although there are no atoms in the vacuum region.

Substituting equation 2.14 into equation 2.5 and integrating over  $r$ , yields the Kohn-Sham equation of the PW method [13],

$$\sum_{G'} \left| \frac{\hbar^2}{2m} |k + G|^2 \delta_{GG'} + V_{ion}(G - G') + V_H(G - G') + V_{xc}(G - G') \right| C_{i,k+G'} = \epsilon_i C_{i,k+G} \quad (2.16)$$

The first term is the kinetic energy, which is essentially a diagonal matrix. The remaining terms are the potentials arising from the effective potential:  $V_{ion}$  (electron-ion and ion-ion interaction),  $V_H$  (Hartree potential or electron-electron interaction) and  $V_{xc}$  (exchange and correlation potential). These terms can be expressed in terms of a Fourier transform,

$$V_{G-G'} = \int \hat{V}(r) e^{i(G-G')r} dV \quad (2.17)$$

The solution of equation 2.16 is obtained from the diagonalization of the Hamiltonian matrix, whose size is determined by the cutoff energy. If both the core and the valence electrons of the atoms are considered, the calculation of this matrix can become impractical because the region near the nucleus contains many

oscillations in the wave functions, which requires a lot of plane waves to be well described. But this problem can be overcome by the use of the pseudopotential approximation.

The use of the plane waves method has advantages in the treatment of periodic systems because of the fact that plane waves are not localized at the positions of the atoms, thus the basis expansion depends only on the cutoff energy. Also, the Hellman-Feynman theorem is valid, that relates the derivative of the total energy with respect to a parameter  $\lambda$  with the derivative of the Hamiltonian with respect to the same parameter. Thereby it facilitates the calculation of gradients in geometry optimization or molecular dynamic calculations. The study of metallic systems benefits from the fact that the plane waves are delocalized. Forming a basis set, they are also orthogonal and can take advantage of the Fourier transform, which is an important mathematical tool in the calculations regarding periodic systems, in addition to being free of basis set superposition error (BSSE). The disadvantages of the PW method are the need for many plane waves to describe systems like surfaces and occasionally the trouble when making a chemical interpretation of the system based on molecular orbitals.

### ***2.3 Pseudopotentials***

The use of pseudopotentials originated in 1959 with the work of Phillips and Kleinman [14], which established the theoretical basis for this method. As a very large number of plane wave functions would be necessary to expand the orbitals tightly bound to the core, where the wave functions oscillate rapidly, these functions can be replaced by pseudofunctions without knots in the core region, and the strong ionic potential by a softer potential, as shown in Figure 2.1. This procedure can be applied since many properties of solids, such as chemical bonds, depend only on the valence electrons, not on the core electrons.

Consider  $|\psi^{(v)}\rangle$  and  $|\psi^{(c)}\rangle$  as the eigenstates that describe the valence and core electrons, respectively. When the Hamiltonian operator acts on them, it

produces the eigenvalues  $\varepsilon^{(v)}$  and  $\varepsilon^{(c)}$  respectively. Let  $|\phi^{(v)}\rangle$  be a new set of valence state functions that relates to  $|\psi^{(v)}\rangle$  through,

$$|\psi^{(v)}\rangle = |\phi^{(v)}\rangle - \sum_c \langle \psi^{(c)} | \phi^{(v)} \rangle |\psi^{(c)}\rangle, \quad (2.18)$$

here the second term of the right side is a projection operator that removes the overlap of the valence states on the core states.

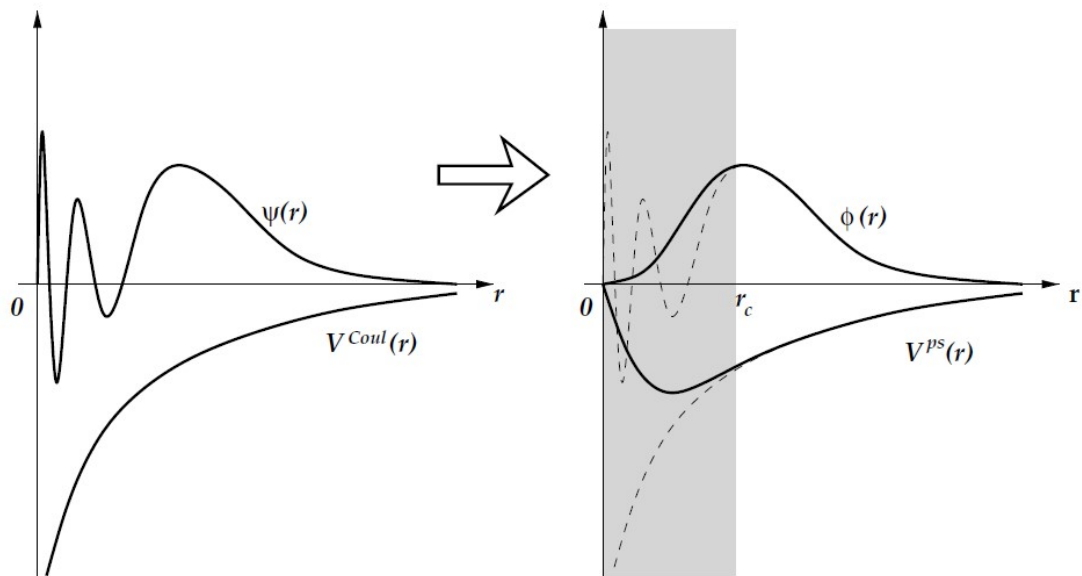


Figure 2.1: Representation of the construction of a pseudo wave function  $\phi(r)$  and its respective pseudopotential  $V^{ps}(r)$  from the wave function  $\psi(r)$  and the Coulomb potential  $V^{Coul}(r)$ .  $r_c$  is the cutoff radius from which the values of both functions correspond. From reference [15], page 76.

Applying the Hamiltonian operator on equation 2.18, we obtain

$$\hat{H}|\phi^{(v)}\rangle - \sum_c \langle \psi^{(c)} | \phi^{(v)} \rangle \hat{H}|\psi^{(c)}\rangle = \varepsilon^{(v)} \left[ |\phi^{(v)}\rangle - \sum_c \langle \psi^{(c)} | \phi^{(v)} \rangle |\psi^{(c)}\rangle \right]. \quad (2.19)$$

Rearranging equation 2.19 and remembering that  $\hat{H}|\psi^{(c)}\rangle = \varepsilon^{(c)}|\psi^{(c)}\rangle$ , one comes up to

$$\left[ \hat{H} + \sum_c (\varepsilon^{(v)} - \varepsilon^{(c)}) |\psi^{(c)}\rangle \langle \psi^{(c)}| \right] |\phi^{(v)}\rangle = \varepsilon^{(v)} |\phi^{(v)}\rangle. \quad (2.20)$$

Decomposing the Hamiltonian on the kinetic and potential energy contributions, we obtain the basic equation of the pseudopotential method,

$$\left[ -\frac{1}{2} \nabla^2 + \hat{V}^{PP} \right] |\phi^{(v)}\rangle = \varepsilon^{(v)} |\phi^{(v)}\rangle, \quad (2.21)$$

where

$$\hat{V}^{PP} = \hat{V} + \sum_c (\varepsilon^{(v)} - \varepsilon^{(c)}) |\psi^{(c)}\rangle \langle \psi^{(c)}|. \quad (2.22)$$

There are many pseudopotentials available in the literature, built with different methods. There are several ways to build a pseudopotential, but some basic points should be noted: the nature of the atom, the exchange and correlation potential employed, the system charge and the transferability of the pseudopotential. Therefore the ability of the pseudopotential to adequately describe the system should be carefully evaluated.

## 2.4 Quantum Theory of Atoms in Molecules (QTAIM)

Bader's Quantum Theory of Atoms in Molecules (QTAIM) [16, 17] proposes a topological analysis of the electron density, in which the atoms are distinguished by a division in the space of the total electron density of a system, called basin. Each critical point (CP) of the electron density is associated with a point in space, where the density gradient is zero,  $\nabla\rho(r)=0$ . In practice, the analysis begins by determining the critical points of the electron density. The density Laplacian  $\nabla^2\rho(r)$  of the critical points is constructed from the partial second derivatives, so it is essentially a measure for the curvature of the function in three dimensions. The

Laplacian of any scalar field indicates whether the point is a maximum, minimum or saddle point, thus characterizing the topology of the electron density.

For an arbitrary choice of coordinate axes in real space, the density Laplacian  $\partial^2\rho(\vec{r})/\partial\vec{r}^2$  is described by a 3×3 matrix, called the Hessian matrix.

$$\begin{pmatrix} \frac{\partial^2\rho}{\partial x^2} & \frac{\partial^2\rho}{\partial x\partial y} & \frac{\partial^2\rho}{\partial x\partial z} \\ \frac{\partial^2\rho}{\partial y\partial x} & \frac{\partial^2\rho}{\partial y^2} & \frac{\partial^2\rho}{\partial y\partial z} \\ \frac{\partial^2\rho}{\partial z\partial x} & \frac{\partial^2\rho}{\partial z\partial y} & \frac{\partial^2\rho}{\partial z^2} \end{pmatrix} \quad (2.23)$$

This matrix is real and symmetric, hence it can be diagonalized, and its eigenvalues ( $\lambda_1, \lambda_2, \lambda_3$ ) are real numbers that provide the curvature in the direction of the eigenvectors.

The critical points are classified according to the Hessian matrix into four types: 1) local maximum points, which represent all negative eigenvalues and where the atomic nuclei are localized (NCP: Nuclear Critical Point); 2) first order saddle points have two negative eigenvalues, defined as points of chemical bonds (BCP: Bond Critical Point); 3) second order saddle points, or ring points (RCP: Ring Critical Point) have one negative eigenvalue and are normally found between three atoms bound in a non-linear arrangement; and 4) local minimum points, or cage points (CCP: Cage critical point) which represent all positive eigenvalues and are found between four atoms bound in a 3D arrangement. The number of NCPs, BCPs, RCPS and CCPs are restricted according to the Morse relationship in the mathematical topological analysis as given by

$$NCP - BCP + RCP - CCP = 0 . \quad (2.24)$$

The eigenvectors associated with two negative eigenvalues define a two-dimensional surface generated by an infinite set of trajectories of  $\nabla\rho(r)$  that will end in a CP, called interatomic surface,  $S(r)$ , which separates the basins of two interacting atoms, as shown in Figure 2.2a. One NCP, together with the gradient

lines that have their source in the NCP, is an atomic basin and it is the most important area where there is a zero-flux condition, which means that in this region no trajectory of  $\nabla\rho(r)$  crosses  $S(r)$ . Atomic basins in solids are equivalent to polyhedra with curved edges and faces. Each face contains only one RCP and each edge is a CCP.

The eigenvector associated with a positive eigenvalue defines a single pair of trajectories of  $\nabla\rho(r)$  that originates in the CP and each one ends at the core of one of the neighboring atoms. This pair of trajectories defines a line in space where the electron density is maximum with respect to any neighboring line. This is called atomic interaction line, as shown in Figure 2.2b.

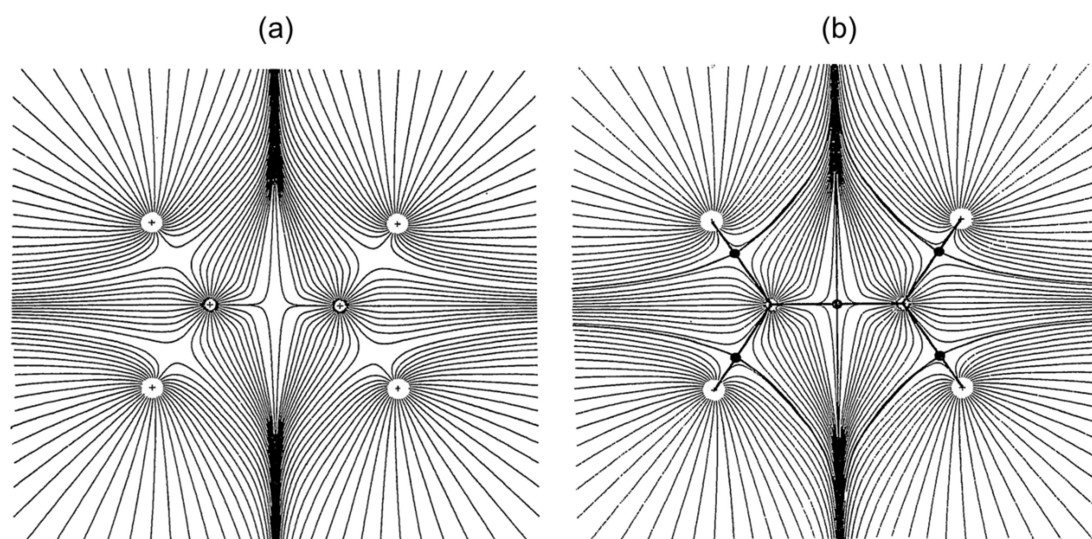


Figure 2.2: a) Map of the trajectory vector  $\nabla\rho(r)$  for ethylene; b) Map of the trajectory vector  $\nabla\rho(r)$  showing the atomic interaction line. Adapted from reference [17].

The primary importance of the QTAIM method for chemical analysis, besides atomic surface and dipole moment calculation, is to localize the bond critical points. According to Bader [18], the existence of a BCP in a point in space is a necessary and sufficient condition for two atoms to be bound to one another. The atomic interaction line, i.e., the line of maximum charge density connecting the nuclei, is called bond path in a bound system.

The formation of a bond path and its associated interatomic surface is the result of a competition between perpendicular compressions of  $\rho$  toward the bond path, which leads to a charge concentration or compression along this line, and the parallel expansion of  $\rho$  away from the surface, which leads to its separate concentration in each one of the atomic basins. The Laplacian  $\nabla^2\rho(r)$  determines which of the two competing effects is dominant, presenting a negative value when the scalar field is concentrated and a positive value when it is emptied.

When the Laplacian of a point is negative and large in magnitude, the density in this point is also high and the electronic charge is concentrated in the internuclear region as a result of the dominant perpendicular compression of  $\rho$  toward the bond path. The result is an electronic charge shared by two nuclei, characteristic of a covalent bond. In the cases of ionic bonding, hydrogen bonding and van der Waals interaction, the charge density has a relatively low value and a positive Laplacian. These interactions are dominated by charge depletion away from the interatomic surface in the direction of the nuclei, concentrating it in the basins of the neighboring atoms.

Bader's QTAIM analysis should be used in chemistry with care. Initially it must be clear that the theory has no predictive capability and enables to gain insights into the nature of the chemical bond from an observable quantity, which is the electron density. There are examples where chemical bond concepts of QTAIM do not apply, as to the study of He dimers encapsulated by fullerenes [19], in which up to five bond critical points have been found for each He atom. For more complex systems, it is difficult to predict if a bond path really indicates a chemical bond, or is merely an artifact of the topological analysis. Also Bader [20] has commented on these critics declaring that a bond path is "a Dirac observable, the measurable expectation value of a quantum mechanical operator", that goes beyond the restrictive concept of a chemical bond.

## **2.5 *Electron Localization Function (ELF)***

Another method that can be used in the study of chemical bonds is the Electron Localization Function (ELF) [21], introduced by Becke and Edgecombe [22]

in 1990. It allows for a topological analysis of the electron density of a non-polarized spin system. Mathematically, the ELF is defined as

$$ELF(\vec{r}) = \left[ 1 + \left( \frac{D(\vec{r})}{D^0(\vec{r})} \right)^2 \right]^{-1}, \quad (2.25)$$

where  $D^0(\vec{r})$  is the kinetic energy density of an uniform electron gas, given by

$$D^0(\vec{r}) = \frac{3}{5} (6\pi^2)^{2/3} \rho^{5/3}(\vec{r}), \quad (2.26)$$

and  $D(\vec{r})$  is the corresponding function given by

$$D(\vec{r}) = \tau(\vec{r}) - \frac{1}{4} \left( \frac{(\nabla \rho(\vec{r})^2)}{\rho(\vec{r})} \right). \quad (2.27)$$

Here  $\tau(\vec{r})$  and  $\rho(\vec{r})$  are the kinetic energy and the electron density, respectively. By definition, the values of  $ELF(\vec{r})$  range from 0 to 1. Values close to 1 mean that, in the vicinity of an electron, no other electron with the same spin is found, which occurs in bonding or lone pairs. Thus, in regions between two atoms where the ELF is close to 1, a covalent bond character is identified. Small values of ELF are typical in regions between two electron shells (Pauli principle). In the case of a homogeneous electron gas,  $D(\vec{r}) = D^0(\vec{r})$  and  $ELF = 0.5$  [23], which is interpreted as a metallic bond. This description completes the QTAIM theory in the way that it provides the location of the electron pairs, and if there is electron sharing.

## 2.6 Nudged Elastic Band (NEB)

An essential aspect in the study of chemical reactions is the identification of a reaction path in order to determine its rate. Since the movement of the atoms during a chemical reaction is a rare event, therefore much slower than the atomic

vibrations, it is not achievable by classical mechanics methods [24]. Hence other methods must be applied to investigate reaction rates. As long as the solids are tightly packed and the temperatures considered in the chemical reactions low compared to its melting point, the harmonic approximation of the Transition State Theory (hTST) can be used [24]. Therefore the search for a transition state (TS) becomes a search for the most relevant of the lowest saddle points in the potential energy surface (PES) [24].

The specific path in a reaction that provides the smallest increase in energy is called Minimum Energy Path (MEP) and the point of highest energy within this trajectory is called transition state (TS), thus it is the energy barrier to form a certain product in a chemical reaction. Many techniques have been developed to find reaction paths, such as methods that trace stepwise a path of slowest ascent or calculate normal modes of local harmonic approximations of the PES and then follow each of the normal modes until a saddle point is found. An algorithm commonly used for periodic systems is called Nudged Elastic Band (NEB) [24, 25]. This method is effective to find the MEP between an initial and final state of the process, building a set of images between the two extremes. It assumes that the nuclei movement controls the phase transformation and that the deformation of the cell vector follows the movement of the nuclei as an implicit function of the nuclear coordinates. To ensure the continuity of the path, spring interactions are added between adjacent images, mimicking an elastic band. An optimization of this band, minimizing the force of the images, takes the band to the MEP. A brief explanation of how the method works is given in the following.

The word “nudged” comes from an essential procedure in the NEB method, which is the use of a force projection to ensure that the spring forces do not interfere with the convergence of the elastic band and that the true force does not affect the distribution of images along the MEP. In order to do this, it is necessary to estimate the tangent to the path in each image to calculate the parallel and perpendicular projection of the forces. Only the perpendicular component of the true force and the parallel component of the spring force are included in the calculations. In this way the spring forces control only the spacing of the images, which avoids the problem of the true force causing the images to slide away from the high energy regions toward the minima.

If  $R_i$  is each of the  $N+1$  images in a NEB calculation, varying from  $R_0$  to  $R_N$ , the force acting on each image is the sum of the spring force along the local tangent and the true force perpendicular to the local tangent, which can be written as [24]:

$$\vec{F}_i = \vec{F}_i^s \Big|_{\parallel} - \vec{\nabla}E(\vec{R}_i) \Big|_{\perp}, \quad (2.28)$$

where the true force is

$$\vec{\nabla}E(\vec{R}_i) \Big|_{\perp} = \vec{\nabla}E(\vec{R}_i) - \vec{\nabla}E(\vec{R}_i) \cdot \hat{\tau}_i. \quad (2.29)$$

$E$  is the energy of the system as a function of the atomic coordinates and  $\tau_i$  is the normalized local tangent at image  $i$ . The spring force is given by

$$\vec{F}_i^s \Big|_{\parallel} = k (|R_{i+1} - R| - |R_i - R_{i-1}|) \hat{\tau}_i, \quad (2.30)$$

where  $k$  is the spring constant. The images are then adjusted to minimize the force by an optimization algorithm, such as the velocity Verlet [26], as shown in Figure 2.3.

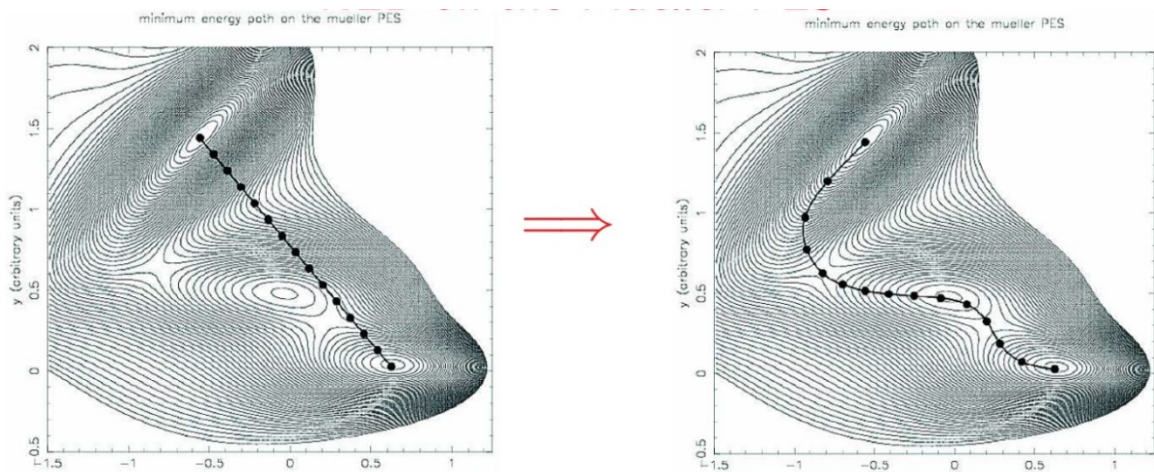


Figure 2.3: Scheme of a minimum energy path found by the NEB method. From reference [27].

In this method the transition state is obtained by interpolation between two images with the highest energy. To solve this problem, the climbing image method

(CI-NEB) introduces a small modification that improves the search for the transition state without increasing computational costs. After a few iterations, the maximum energy image  $i_{max}$  is found and the force on this image is not given by equation 2.28, but instead by

$$\vec{F}_{i_{max}} = -\vec{\nabla}E(\vec{R}_{i_{max}}) + 2\vec{\nabla}E(\vec{R}_{i_{max}}) \Big|_{\parallel} = -\vec{\nabla}E(\vec{R}_{i_{max}}) + 2\vec{\nabla}E(\vec{R}_{i_{max}}) \cdot \hat{\tau}_{i_{max}} \hat{\tau}_{i_{max}} . \quad (2.31)$$

In this way, the maximum energy image is not affected by the spring forces. Thus this image will converge to the saddle point, i.e., the transition state of the reaction.

The saddle point is the most important point along the MEP, therefore it must have a good resolution. In order to obtain better results for this point, it is important to have variable spring constants: stronger near the saddle point, and weaker in other regions. This allows a better determination of the tangent in the maximum energy image, and consequently a better description of the region close to the transition state. All the methods and variables must be carefully analyzed in a first-principle calculation in order to get the most appropriate description for the system of interest.

Computational details used in this work will be described below and along the results in the following chapters. The *Quantum ESPRESSO* software [28] was used in all steps of the calculations.

## 2.7 Computational Aspects of the Arsenopyrite Calculations

Tables 2.1 and 2.2 summarize the convergence tests performed for the cutoff energy  $E_{cut}$  and the  $\mathbf{K}$ -points mesh used for integration over the Brillouin zone. The convergence criterion used was the difference in total energy being less than  $10^{-3}$  Ry. The convergence test for the cutoff energy have been made with two pseudopotentials constructed using different DFT GGA XC functionals: PBE [29] and PW91 [30]. These exchange and correlation (XC) functionals have been widely used and provide results in excellent agreement with experimental data [31].

$E_{\text{cut}} = 60$  Ry is sufficient to ensure convergence in the third decimal place. A careful analysis of the data in Table 2.1 reveals that the XC functional PW91 converges faster than the PBE functional. Figure 2.4 shows the total energy and the calculation time as a function of  $E_{\text{cut}}$ . The choice of  $E_{\text{cut}}$  must take into account two aspects: accuracy and computational cost.

Table 2.1: Total energy variation with respect to the cutoff energy for the XC functionals PBE e PW91. Calculations were performed using a **K**-point mesh of  $4 \times 4 \times 4$ .

Energy cutoff	Total Energy/Ry	
	PBE	PW91
10	-1176.52746	-1222.33909
20	-1222.74509	-1241.02520
30	-1223.17074	-1241.11565
40	-1223.18078	-1241.11654
50	-1223.18524	-1241.11699
60	-1223.18811	-1241.11727
70	-1223.1907	-1241.11736
80	-1223.19075	-1241.11742
90	-1223.19216	-1241.11756

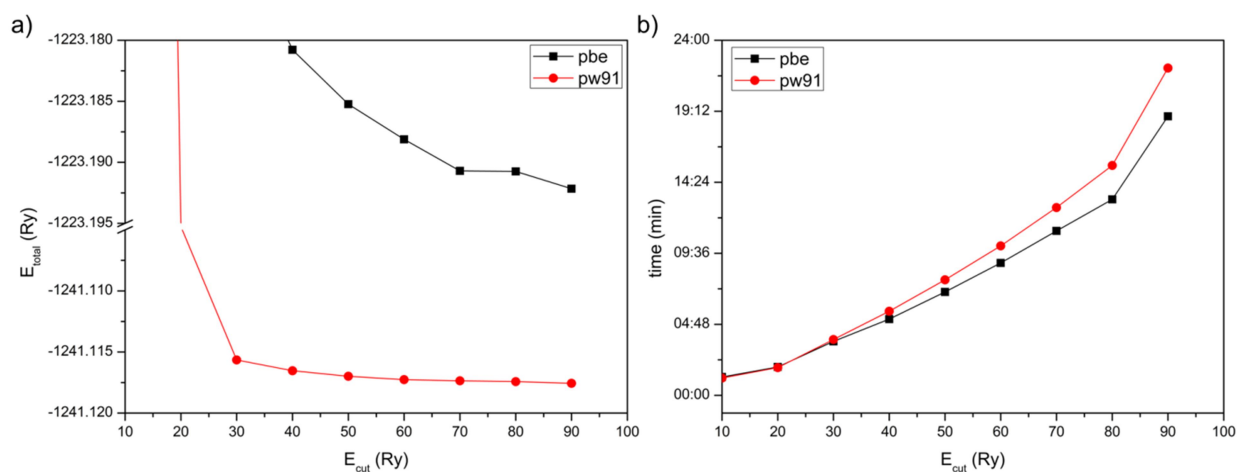


Figure 2.4: a) Convergence test for the cutoff energy  $E_{\text{cut}}$ . b) Calculation time as a function of the cutoff energy. Calculations were performed with a **K**-point mesh of  $4 \times 4 \times 4$  and parallelized to use 4 CPU cores.

The second test performed was of **K**-points sampling used to discretize the **K**-space. Figure 2.5 shows the dependence of the total energy and the computing time as a function of the **K**-points mesh, which are generally similar to the dependence on the cutoff energy (see Figure 2.4). In Table 2.2, the total energy as a function of the **K**-points mesh shape is presented. Convergence is observed for the 4×4×4 **K**-points mesh, as larger meshes do not decrease the total energy anymore. Accordingly, the 4x4x4 mesh was used in the following studies.

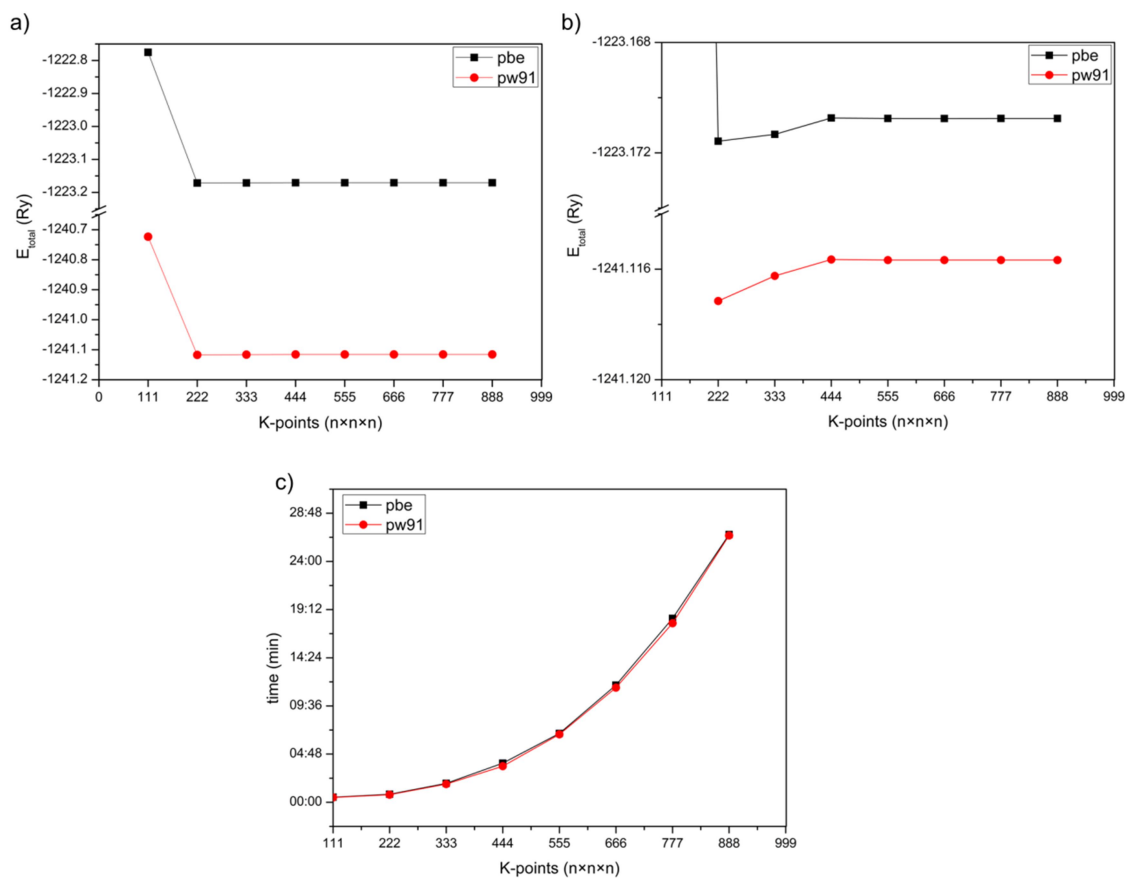


Figure 2.5: a) **K**-points mesh convergence test. b) **K**-points mesh convergence test zoom. c) Calculation time as function of the **K**-point mesh. Calculations were performed with a cutoff energy of 30 Ry.

Table 2.2: **K**-points mesh test for two XC functionals: PBE and PW91.  $E_{\text{cut}} = 30$  Ry.

<b>K</b> -points	Total Energy/Ry	
	PBE	PW91
111	-1222.77532	-1240.72323
222	-1223.17158	-1241.11715
333	-1223.17133	-1241.11625
444	-1223.17074	-1241.11565
555	-1223.17075	-1241.11567
666	-1223.17075	-1241.11567
777	-1223.17075	-1241.11567
888	-1223.17075	-1241.11567

Arsenopyrite (FeAsS) is a material in which the iron atom is in an oxidized state. Consequently, this ion in the arsenopyrite structure may exhibit unpaired electrons and therefore the material can be magnetic or have a nonzero local spin density at the iron atom.

Spin-polarized calculations for arsenopyrite have been performed in different combinations of spin compensated and non-compensated. In all the calculations, both the total and absolute magnetization obtained were  $0 \mu_B/\text{cell}$ . This suggests that arsenopyrite does not have magnetic properties. Calculations in which a total magnetization is imposed on the system, with values of 0, 2 and  $4 \mu_B/\text{cell}$ , have also been performed. The results are presented in Figure 2.6 and show that the system with zero magnetization has the lowest total energy. This result is in agreement with the literature, where arsenopyrite is classified as a diamagnetic mineral [32]. The coordination number of the iron atom is six, and the oxidation number is 2, so  $\text{Fe}^{2+}$  has a  $3d^6$  valence, in an octahedral field. According to the crystal field theory, the system must thus be diamagnetic.

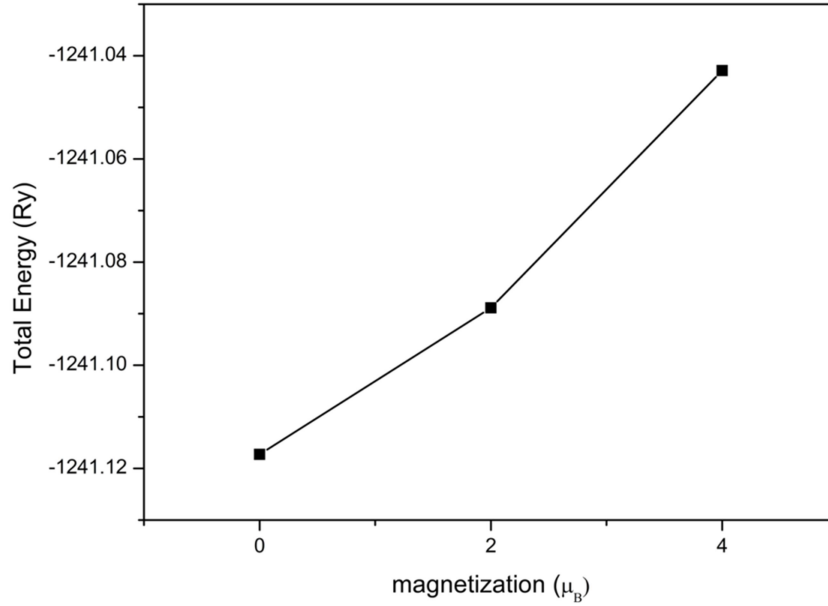


Figure 2.6: Magnetization test of bulk arsenopyrite.

The computational protocol used in the bulk calculations was: XC functional proposed by Perdew and Wang (PW91) [30]; core electrons described by ultrasoft pseudopotentials proposed by Vanderbilt [33], adopting the following valence configurations: Fe ( $3s^2 3p^6 3d^{6.5} 4s^1 4p^0$ ), As ( $4s^2 4p^3$ ) and S ( $3s^2 3p^4$ ) [34]. A kinetic energy cutoff of 60 Ry, a kinetic energy cutoff for the wavefunctions of 480 Ry, and a  $4 \times 4 \times 4$   $\mathbf{K}$ -point mesh have been used. A Marzari-Vanderbilt smearing [35] of 0.02 Ry for integration over the Brillouin zone of metals has been adopted. The Brillouin zone integration was based on the Monkhorst-Pack scheme [11]. The geometry optimizations were made using the method of Damped dynamics [36] with Parrinello-Rahman extended Lagrangian [37], maintaining a tolerance level of  $10^{-3}$  Ry Bohr $^{-1}$  for the convergence criterion. The positions of the atoms and the unit cell parameters have been optimized without any restrictions.

## 2.8 Final Considerations

In this chapter the fundamental aspects of the theoretical methods used in this work have been briefly described, reminding that these methods have been extensively tested and are used in many published works. For a deeper

understanding of DFT, there are up-to-date reviews available in the literature [38-41], as well as text books [42-44], dealing with a complete description of the method. About crystallographic and solid structures, we suggest the books of Ashcroft and Mermin [10] and Kittel [45]. On the implementation of DFT for solid state calculations, the suggestion for deepening are the books of Dovesi [46], Kaxiras [15], Vianna *et al.* [12], and Sholl and Steckel [43]. The paper of Giannozzi *et al.* [28] describes the details of the software *Quantum ESPRESSO*, in which many of these methods are implemented. For a complete study of QTAIM analysis, the book of Bader [17] is available. For NEB, we suggest the book chapter of Jónsson *et al.* [25] and the paper of Henkelman *et al.* [24] with explanations and examples of the method being applied, besides other papers where the method is improved [47-49].

## 2.9 References

1. Morgon, N.H. and K. Coutinho, *Métodos de Química Teórica e Modelagem Molecular*. 2007: Editora Livraria da Física.
2. Drude, P., *Zur Elektronentheorie der Metalle*. *Annalen der Physik*, 1900. **306**(3): p. 566-613.
3. Drude, P., *Zur Elektronentheorie der Metalle; II. Teil. Galvanomagnetische und thermomagnetische Effecte*. *Annalen der Physik*, 1900. **308**(11): p. 369-402.
4. Thomas, L.H., *The calculation of atomic fields*. *Mathematical Proceedings of the Cambridge Philosophical Society*, 1927. **23**(05): p. 542-548.
5. Fermi, E., *Un Metodo Statistico per la Determinazione di alcune Priorietà dell'Atomo*. *Rend. Accad. Naz. Lincei*, 1927. **6**: p. 602-607.
6. Dirac, P.A.M., *Note on Exchange Phenomena in the Thomas Atom*. *Mathematical Proceedings of the Cambridge Philosophical Society*, 1930. **26**(03): p. 376-385.
7. Hohenberg, P. and W. Kohn, *Inhomogeneous Electron Gas*. *Physical Review*, 1964. **136**(3B): p. B864-B871.
8. Kohn, W. and L.J. Sham, *Self-Consistent Equations Including Exchange and Correlation Effects*. *Physical Review*, 1965. **140**(4A): p. A1133-A1138.
9. Levy, M., *Universal variational functionals of electron densities, first-order density matrices, and natural spin-orbitals and solution of the  $v$ -representability problem*. *Proceedings of the National Academy of Sciences*, 1979. **76**(12): p. 6062-6065.
10. Ashcroft, N.W. and N.D. Mermin, *Solid state physics*. 1976: Saunders College.
11. Monkhorst, H.J. and J.D. Pack, *Special Points for Brillouin-Zone Integrations*. *Physical Review B*, 1976. **13**(12): p. 5188-5192.
12. Vianna, J.D.M., A. Fazzio, and S. Canuto, *Teoria quântica de moléculas e sólidos: simulação computacional*. 2004, São Paulo: Livraria da Física.

13. Payne, M.C., et al., *Iterative minimization techniques for ab initio total-energy calculations: molecular dynamics and conjugate gradients*. Reviews of Modern Physics, 1992. **64**(4): p. 1045-1097.
14. Phillips, J.C. and L. Kleinman, *New Method for Calculating Wave Functions in Crystals and Molecules*. Physical Review, 1959. **116**(2): p. 287-294.
15. Kaxiras, E., *Atomic and Electronic Structure of Solids*. 2003: Cambridge University Press.
16. Bader, R.F.W., *A quantum theory of molecular structure and its applications*. Chemical Reviews, 1991. **91**(5): p. 893-928.
17. Bader, R.F.W., *Atoms in Molecules: A Quantum Theory*. 1994: Oxford University Press, Incorporated.
18. Bader, R.F.W., *A Bond Path: A Universal Indicator of Bonded Interactions*. The Journal of Physical Chemistry A, 1998. **102**(37): p. 7314-7323.
19. Cerpa, E., et al., *Influence of Endohedral Confinement on the Electronic Interaction between He atoms: A He<sub>2</sub>@C<sub>20</sub>H<sub>20</sub> Case Study*. Chemistry – A European Journal, 2009. **15**(8): p. 1985-1990.
20. Bader, R.F.W., *Bond Paths Are Not Chemical Bonds*. The Journal of Physical Chemistry A, 2009. **113**(38): p. 10391-10396.
21. Savin, A., et al., *ELF: The electron localization function*. Angewandte Chemie-International Edition, 1997. **36**(17): p. 1809-1832.
22. Becke, A.D. and K.E. Edgecombe, *A Simple Measure of Electron Localization in Atomic and Molecular-Systems*. Journal of Chemical Physics, 1990. **92**(9): p. 5397-5403.
23. Savin, A., et al., *Electron Localization in Solid-State Structures of the Elements - the Diamond Structure*. Angewandte Chemie-International Edition, 1992. **31**(2): p. 187-188.
24. Henkelman, G., B.P. Uberuaga, and H. Jonsson, *A climbing image nudged elastic band method for finding saddle points and minimum energy paths*. Journal of Chemical Physics, 2000. **113**(22): p. 9901-9904.
25. JÓNSSON, H., G. MILLS, and K.W. JACOBSEN, *Nudged elastic band method for finding minimum energy paths of transitions*, in *Classical and Quantum Dynamics in Condensed Phase Simulations*. 2011, WORLD SCIENTIFIC. p. 385-404.
26. Verlet, L., *Computer "Experiments" on Classical Fluids. I. Thermodynamical Properties of Lennard-Jones Molecules*. Physical Review, 1967. **159**(1): p. 98-103.
27. Gironcoli, S.d., *Rare Events and Nudged Elastic Bands*. 2009: Santa Barbara.
28. Giannozzi, P., et al., *QUANTUM ESPRESSO: a modular and open-source software project for quantum simulations of materials*. Journal of Physics-Condensed Matter, 2009. **21**(39): p. 395502.
29. Perdew, J.P., K. Burke, and M. Ernzerhof, *Generalized gradient approximation made simple*. Physical Review Letters, 1996. **77**(18): p. 3865-3868.
30. Perdew, J.P. and Y. Wang, *Accurate and Simple Analytic Representation of the Electron-Gas Correlation-Energy*. Physical Review B, 1992. **45**(23): p. 13244-13249.
31. Janthon, P., et al., *Establishing the Accuracy of Broadly Used Density Functionals in Describing Bulk Properties of Transition Metals*. Journal of Chemical Theory and Computation, 2013. **9**(3): p. 1631-1640.
32. Vaughan, D.J., *Sulfide Mineralogy and Geochemistry: Introduction and Overview*. Reviews in Mineralogy and Geochemistry, 2006. **61**(1): p. 147.

33. Vanderbilt, D., *Soft Self-Consistent Pseudopotentials in a Generalized Eigenvalue Formalism*. Physical Review B, 1990. **41**(11): p. 7892-7895.
34. Available from: [http://www.quantum-espresso.org/wp-content/uploads/upf\\_files/Fe.pw91-sp-van\\_ak.UPF](http://www.quantum-espresso.org/wp-content/uploads/upf_files/Fe.pw91-sp-van_ak.UPF)
35. Marzari, N., et al., *Thermal Contraction and Disorder of the Al(110) Surface*. Physical Review Letters, 1999. **82**(16): p. 3296-3299.
36. Beeman, D., *Some Multistep Methods for Use in Molecular-Dynamics Calculations*. Journal of Computational Physics, 1976. **20**(2): p. 130-139.
37. Parrinello, M. and A. Rahman, *Polymorphic Transitions in Single-Crystals - a New Molecular-Dynamics Method*. Journal of Applied Physics, 1981. **52**(12): p. 7182-7190.
38. Cramer, C.J. and D.G. Truhlar, *Density functional theory for transition metals and transition metal chemistry*. Physical Chemistry Chemical Physics, 2009. **11**(46): p. 10757-10816.
39. Cohen, A.J., P. Mori-Sanchez, and W.T. Yang, *Challenges for Density Functional Theory*. Chemical Reviews, 2012. **112**(1): p. 289-320.
40. Ziegler, T. and J. Autschbach, *Theoretical methods of potential use for studies of inorganic reaction mechanisms*. Chemical Reviews, 2005. **105**(6): p. 2695-2722.
41. Chermette, H., *Density functional theory - A powerful tool for theoretical studies in coordination chemistry*. Coordination Chemistry Reviews, 1998. **178**: p. 699-721.
42. Cramer, C.J., *Essentials of Computational Chemistry: Theories and Models*. 2nd ed. 2004, West Sussex: John Wiley & Sons.
43. Sholl, D.S. and J.A. Steckel, *Density Functional Theory: A Practical Introduction*. Density Functional Theory. 2009, New Jersey: John Wiley & Sons, Inc.
44. Parr, R.G. and W. Yang, *Density-Functional Theory of Atoms and Molecules*. 1989, New York: Oxford University Press.
45. Kittel, C., *Introduction to solid state physics*. 2005: John Wiley & Sons.
46. Dovesi, R., et al., *Ab Initio Quantum Simulation in Solid State Chemistry*, in *Reviews in Computational Chemistry*. 2005, John Wiley & Sons, Inc. p. 1-125.
47. Henkelman, G. and H. Jónsson, *Improved tangent estimate in the nudged elastic band method for finding minimum energy paths and saddle points*. The Journal of Chemical Physics, 2000. **113**(22): p. 9978-9985.
48. Smidstrup, S., et al., *Improved initial guess for minimum energy path calculations*. The Journal of Chemical Physics, 2014. **140**(21): p. 214106.
49. Zarkevich, N.A. and D.D. Johnson, *Nudged-elastic band method with two climbing images: Finding transition states in complex energy landscapes a)*. The Journal of Chemical Physics, 2015. **142**(2): p. 024106.

### 3 Structural, Mechanical and Electrical Properties of Arsenopyrite and its Surfaces.

The results of the present chapter were published at the RSC *Advances*, 5: p. 2013-2023, **2015**.

To study the reactivity of the arsenopyrite surface using electronic structure calculations, it is necessary to define a suitable model for the calculation. The first step is a study of bulk arsenopyrite in order to determine an optimal set of parameters for the proposed model that best reproduces the properties of the real material. After this inevitable first step, it is necessary to choose a proper surface for the adsorption and oxidation studies (see Chapters 4 and 5). In this chapter, the reasoning behind the selection of the surface is presented.

The crystal structure of arsenopyrite obtained from X-ray diffraction technique of a monoclinic cell formed by 12 atoms [1], obtained from the ICSD database of crystal structures, is shown in Figure 3.1. This structure was used to carry out geometry optimization calculations and to validate the theoretical model.

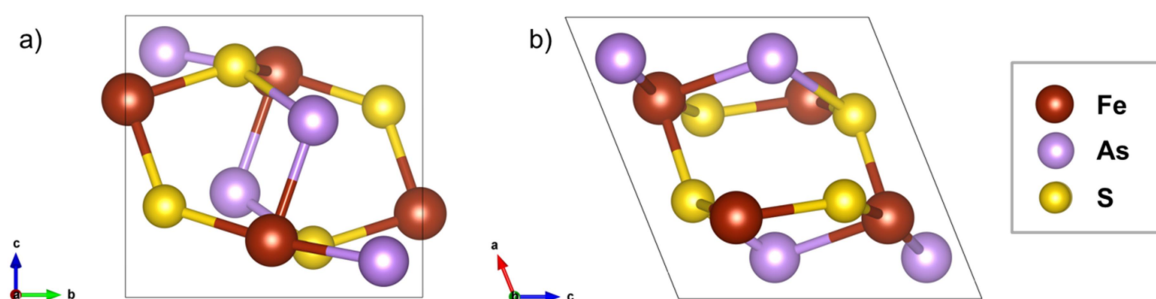


Figure 3.1: Arsenopyrite monoclinic unit cell used in bulk calculations. a) view along *a* axis; b) view along *b* axis.

#### 3.1 Arsenopyrite Structure

The interatomic distances calculated for arsenopyrite bulk are presented in Table 3.1 in comparison to available experimental values. The calculation results show a greater similarity to the experimental data of Bindi *et al.* [2] with a maximum of 2% difference, which are more recent and refer to a sample rich in As. It is

noteworthy that the experimental data are based on natural samples, that may be non-stoichiometric, and present defects, impurities or excesses of S [1] or As [2] compared to the ideal crystal. The sample studied by Fuess *et al.* [3] contained Co impurity and excess of S in relation to As in the following proportion:  $\text{Fe}_{0.87}\text{Co}_{0.13}\text{As}_{0.88}\text{S}_{1.12}$ .

The average Fe–S distance calculated is 2.203 Å, about 0.028 Å less than the average experimental value [2] and also less than the values calculated using similar methodologies for marcasite (orthorhombic  $\text{FeS}_2$ ) of 2.23 Å [4] and the one of chalcopyrite ( $\text{CuFeS}_2$ ) of 2.241 Å [5], as expected. The average Fe–As distance of 2.402 Å is 0.005 Å longer than the experimental value [2], and the As–S distance of 2.405 Å is 0.031 Å longer. The As–S bond length is also longer than the S–S distance calculated by Gudelli *et al.* [4] for marcasite (2.20 Å), which is expected due to the larger atomic radius of As. Gudelli *et al.* [4] also found only one Fe–Fe distance for marcasite (3.38 Å), polymorph of pyrite, an intermediate value between both distances found in the present work.

Table 3.1: Interatomic distances for arsenopyrite bulk. All values are in angstroms.

Reference	Short Fe–Fe	Long Fe–Fe	Fe–S	Fe–As	As–S
This work	2.668	3.765	2.190; 2.198; 2.222	2.380; 2.410; 2.415	2.405
Experimental (1961) [1]	2.82	3.62	2.22; 2.24; 2.25; 2.26; 2.26; 2.29	2.30; 2.32; 2.32; 2.38; 2.39; 2.41	2.33
Experimental (1987) [3]	2.922	3.627	2.239; 2.250; 2.257	2.336; 2.371; 2.375	2.346
Experimental (2012) [2]	2.734	3.741	2.229; 2.230; 2.233	2.370; 2.409; 2.412	2.374

The cell parameter results after optimization are shown on Table 3.2. They are in agreement with the experimental data and are closer to these data than the DFT/PBE/plane waves results of Corkhill *et al.* [6]. This indicates that the chosen arsenopyrite bulk model describes well its structural properties. The differences between lattice parameters did not exceed 0.022 Å, 0.33 degrees in  $\beta$  and 1.72 Å<sup>3</sup> in volume, compared to Bindi *et al.* [2].

Table 3.2: Crystallographic data of bulk arsenopyrite.

	a/Å	b/Å	c/Å	$\beta$ /°	Volume /Å <sup>3</sup>
This work	5.739	5.668	5.763	112.05	173.74
DFT/PBE [6]	5.61	5.56	5.63	111.67	164.20
Experimental (1961) [1]	5.744	5.675	5.785	112.17	174.50
Experimental (1987) [3]	5.741	5.649	5.756	110.59	174.73
Experimental (2012) [2]	5.761	5.684	5.767	111.72	175.46

Many studies have been performed comparing the structures of pyrite, marcasite, arsenopyrite and loellingite (FeAs<sub>2</sub>) to understand the differences between them and explain the reason of their stabilities. Hulliger and Mooser [7], as well as Pearson [8] and Nickel [9, 10], have used the ligand field theory to make a comparison between these structures. In the structure of pyrite the neighboring octahedra share only one corner, that keeps the iron atoms apart from one another. However in marcasite, arsenopyrite and loellingite, the octahedra share an edge, which allows a greater proximity between neighboring iron atoms and perhaps some interaction, as shown in Figure 3.2. Following this analysis, the authors say that the 6 iron *d* electrons do not participate in metal-sulfur bonds in marcasite. Extending this argument to arsenopyrite, keeping the pairs of bonding electrons and exchanging a S atom by an As one, which has one less valence electron, it was assumed that this electron would be taken from an iron *d* orbital. Thus, the iron atom would have 5 *d* electrons, therefore a +3 oxidation number.

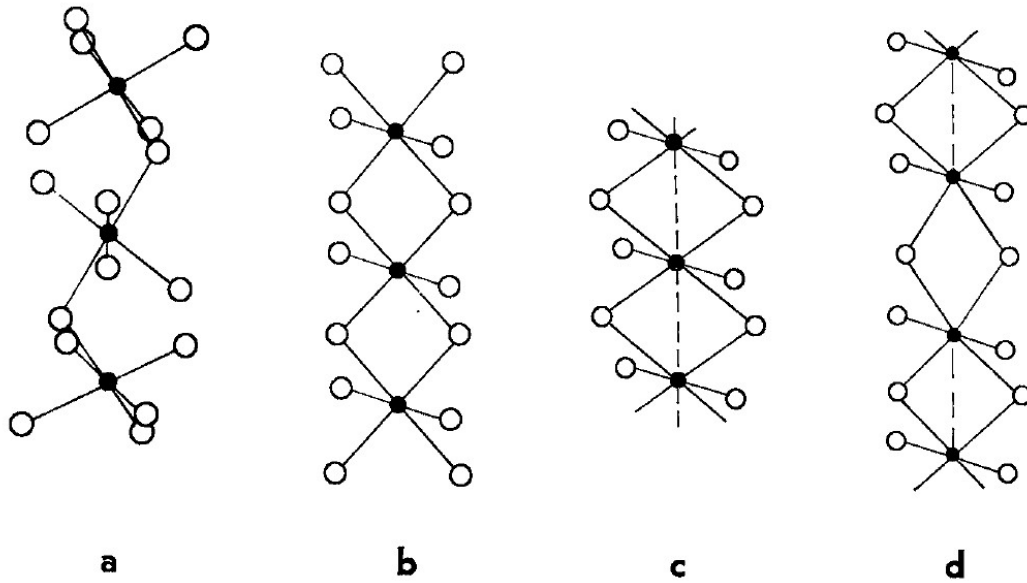


Figure 3.2: Structure of sulfides: a) pyrite; b) marcasite; c) loellingite; d) arsenopyrite. The filled circles represent the cations and the open ones the anions. From reference [9].

According to the ligand field theory, the degenerate iron  $d$  orbitals suffer a splitting in  $t_{2g}$  and  $e_g$  orbital types when the atom is in an octahedral environment. Knowing that all these sulfides have a low magnetic moment, Nickel [9] concluded that the iron atom must be in the low spin state, that is, all electrons occupying the  $t_{2g}$  orbitals. Because arsenopyrite is also diamagnetic and has 5  $d$  electrons in the iron atom, two neighboring iron atoms could bind to complete the occupation of the  $t_{2g}$  orbitals and this would give rise to two different Fe–Fe distances in arsenopyrite, as shown in Figure 3.3.

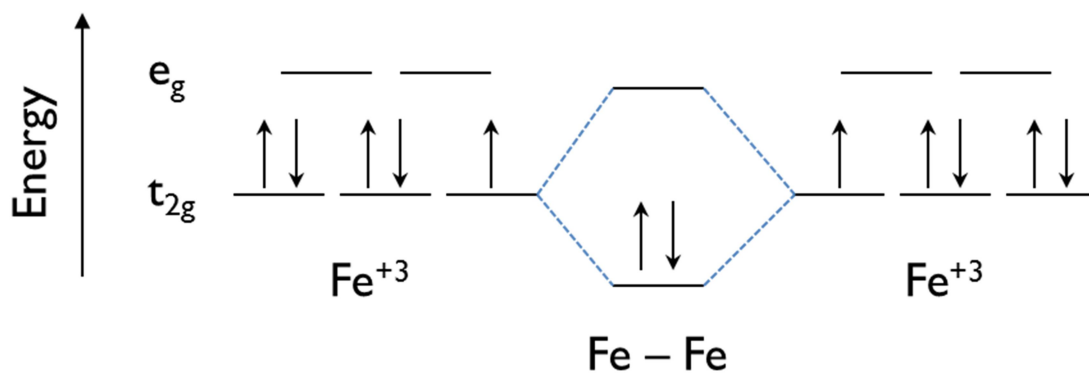


Figure 3.3: Molecular orbital diagram of the Fe–Fe bond [9].

Following this idea, marcasite would have repulsion between its iron neighbor atoms, that is, a longer distance between them, since they have occupied non-bonding  $t_{2g}$  orbitals. Loellingite, whose iron atoms have 4  $d$  electrons, would be diamagnetic if one of the  $t_{2g}$  orbitals had higher energy than the electron pairing energy, what would cease the repulsion between the iron atoms and, consequently have a shorter Fe–Fe distance. Pearson [8] named the structure of loellingite as compressed marcasite. One problem is to attribute an oxidation number of +4 to the iron atom in loellingite, which is only observed in specific biological reactions. Moreover, it does not explain the fact that the Fe–Fe distance in arsenopyrite is longer in the shared edge that contains the As atoms, instead of the one with the S atoms, which is the opposite of what happens in marcasite and loellingite.

Brostigen and Kjekshus [11] created bonding schemes to explain the differences between the three structure types (marcasite, arsenopyrite and loellingite) based on spatial orientation, energy level splitting and occupation of non-bonding  $d$  orbitals in the metal, which they called expansion model, and compared with experimental data. They argued that it is not necessary to introduce the Jahn-Teller effect to stabilize the structure of marcasite, as proposed by Hulliger and Mooser [7] and that the small axial ratios  $c/a$  and  $c/b$  in marcasite do not reflect a compressive force due to metal-metal bonding. Goodenough [12] criticized the previous arguments, proposing the splitting of Fe  $d$  orbitals into three groups: two that differ slightly in the energy of the  $t_{2g}$  orbitals and one that has high energy orbitals due to metal-metal interaction. His conclusion of the orbital analysis was that the distortions in the Fe–Fe distances of arsenopyrite in relation to marcasite are due to metal-anion interactions and not to metal-metal. Also, arsenopyrite represents an expansion rather than a compression of the marcasite structure, since there is a concentrated electron density in the separation region. However, Goodenough still considered the Fe oxidation state as different in the three compounds. Vaughan and Craig [13] criticized this assumption based on Mössbauer spectroscopy results showing that the iron atom has a low spin state in marcasite, arsenopyrite and loellingite.

Tossell and coworkers [14] considered the Fe atom in the divalent state and calculated the electronic structures of  $MA_2$  clusters by the SCF- $X_\alpha$ -SW method for the three compounds in question, besides others. Quantitative molecular orbital

calculations and qualitative perturbational molecular orbital arguments were used to interpret the spectra and the structure of different sulfides. They also concluded that the structure of these compounds is defined by the metal-dianion interaction and proposed an explanation for the different structures based on the analysis of the molecular orbitals occupation in different compounds. The problem of this study is that, as in Nickel's [9] analysis, they considered that the Fe–As–Fe bond angle, subtending the short Fe–Fe distance, is smaller than the Fe–S–Fe angle, subtending the long Fe–Fe distance, when the opposite occurs [2]. Figures 3.9b, page 53 and 3.12b, page 57, show this clearly. The reason for this misunderstanding is that in lollingite ( $\text{FeAs}_2$ ) the Fe–Fe distance is shorter than in marcasite ( $\text{FeS}_2$ ). Therefore it is curious that the opposite happens in arsenopyrite.

Schmokel and coworkers [15] carried out a detailed analysis of the experimental and theoretical electron density of pyrite and marcasite. They found that S–S bonds are more covalent and Fe–S bonds are weaker in pyrite compared to marcasite. This is explained based on the distribution of the *d*-orbital-like density difference between the two polymorphs.

XPS experiments carried out by Nesbitt *et al.* [16, 17] found that in both arsenopyrite and loellingite bulk, the Fe atoms have an oxidation state of +2, because the main peak of the spectrum corresponds to a binding energy very close to those in the spectrum of pyrite. They also suggested that As and S atoms are in a (-1) oxidation state in arsenopyrite, as well as the As atoms in loellingite. Mössbauer experiments of Bindi and coworkers [2] also corroborate this result, since they detected the iron atom in a divalent state, low-spin, and in an octahedral environment. Hence it is clear that the oxidation state of the atoms in arsenopyrite is  $\text{Fe}^{2+}\text{As}^-\text{S}^-$ . However the reason for the structural stability of this mineral is still uncertain. The knowledge about the nature of the chemical bonds in arsenopyrite can help solving this problem, especially concerning the hypothesis of a Fe–Fe bond, which still needs to be investigated.

### 3.2 Electronic Structure of Arsenopyrite

In order to better understand the electronic properties of arsenopyrite and also validate the bulk model, band structure calculations have been performed, in which the  $\mathbf{K}$ -points mesh has been expanded to  $8 \times 8 \times 8$  in order to improve the results. The band structure calculations were taken along the path through  $\mathbf{K}$ -space described in Figure 3.4, which was suggested by Setyawan *et al.* [18] for a monoclinic cell.

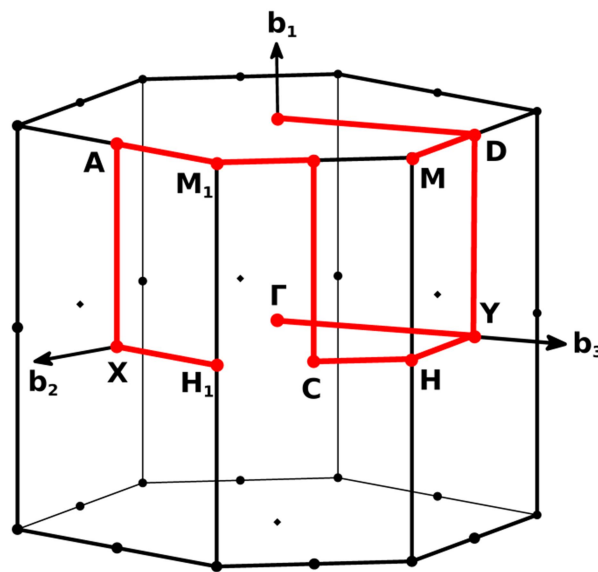


Figure 3.4: Path through  $\mathbf{K}$ -space for band structure calculation for a monoclinic cell suggested in reference [18].

The resulting band structure is shown in Figure 3.5. By its analysis, it is apparent that arsenopyrite is a semiconductor, which is in accordance to the literature [19]. There is an indirect band gap of 0.75 eV between the D and the  $\Gamma$  point, represented by the red vector in the figure. This band gap is about 0.07 eV smaller than the experimental value of 0.82 eV [20], as expected since it is known that the GGA XC functional underestimates the band gap due to the discontinuity of the derivative of the exchange and correlation potential with respect to the occupation number [21]. Experimental values for the band gap of pyrite range from 0.7 to 2.62 eV [4], but the most reliable results, between 0.9 and 0.95 eV, were obtained with photoconductivity measurements [22, 23]. Opahle and coworkers [24] found a value of 0.85 eV in a DFT/LDA-PZ calculation for pyrite, with a difference

from the experimental value similar to that found for arsenopyrite. Yet Gudelli *et al.* [4] calculated a band gap of 1.186 eV for pyrite and 1.603 eV for marcasite using the TBmBJ potential [21], which overestimates the band gap.

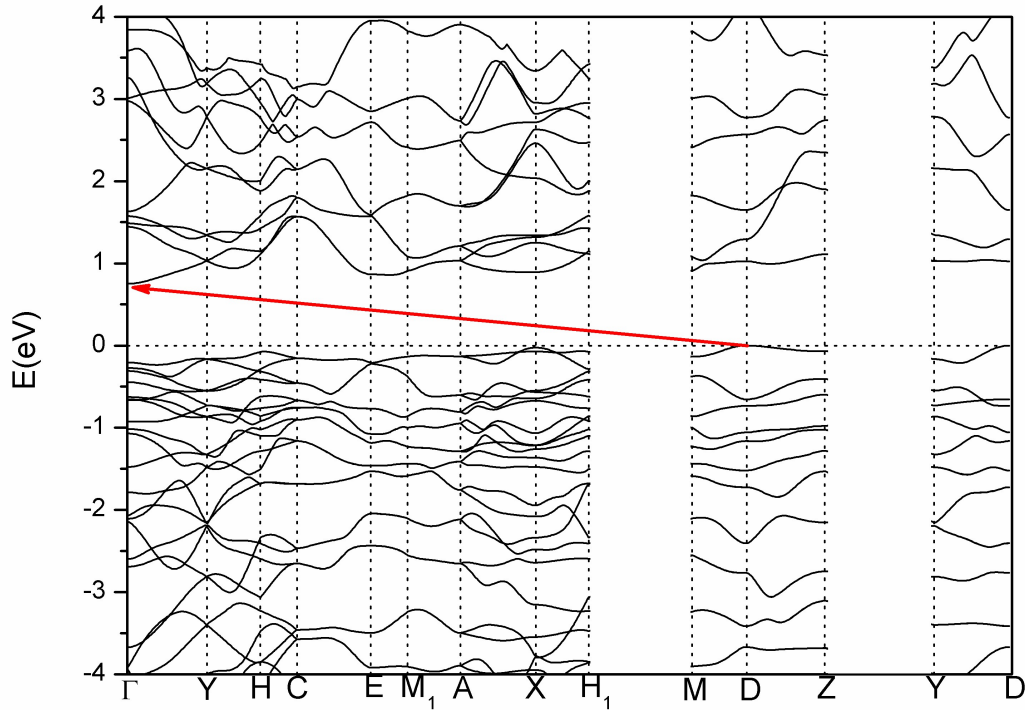


Figure 3.5: Band structure calculated for arsenopyrite.

The total density of states (DOS) and the DOS projected on the lattice sites of the different atomic species are shown in Figure 3.6. The DOS measures the quantity of electronic states per energy interval, which in solid systems is not discrete like in molecules, but continuous. The largest contribution to the DOS near the Fermi level, either in the valence or the conduction band, is received from the iron atoms, in particular the  $d$  orbitals of iron, as shown in Figure 3.7. According to the discussion of De Oliveira and Duarte [5], a dominating contribution of the iron atoms to the total DOS in both conduction band and valence band is consistent with the +2 oxidation state. The reason is that iron may oxidize, since it has electronic density in the valence band, as well as reduce, because electrons can be received in its electronic states in the conduction band. The DOS of the atoms As and S are similar close to the Fermi level, contributing equally to the conduction and valence bands. The integration over the valence band leads to a number of 108 electrons, as expected.

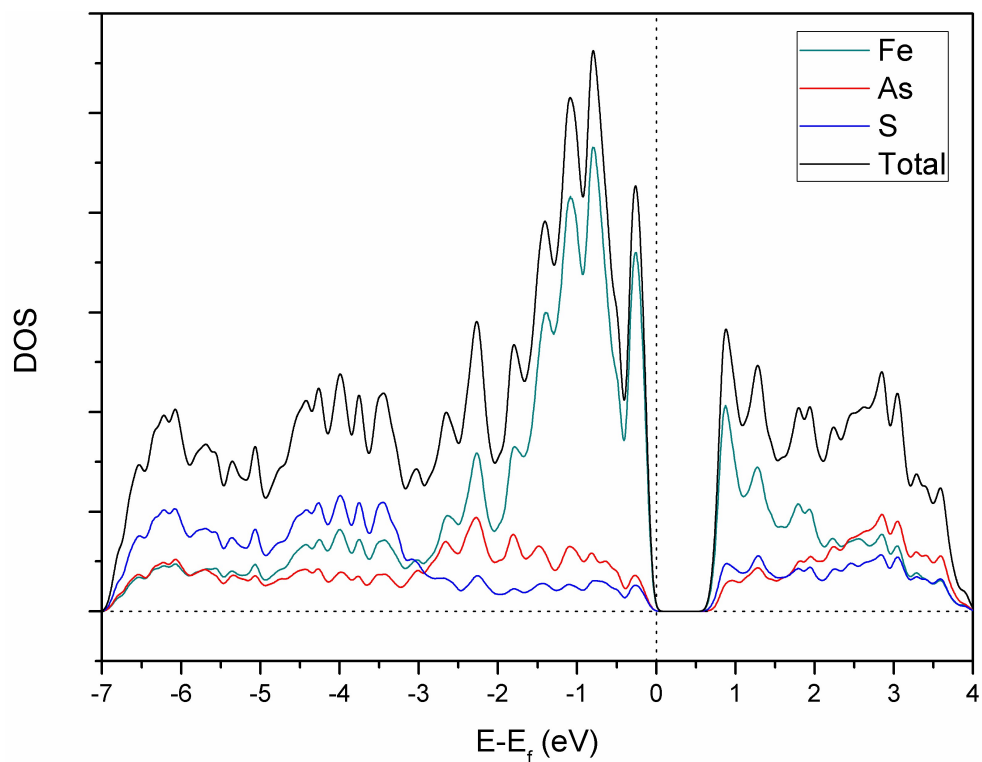


Figure 3.6: Total and projected DOS of the atoms of arsenopyrite plotted using a Gaussian width of 0.005 Ry.

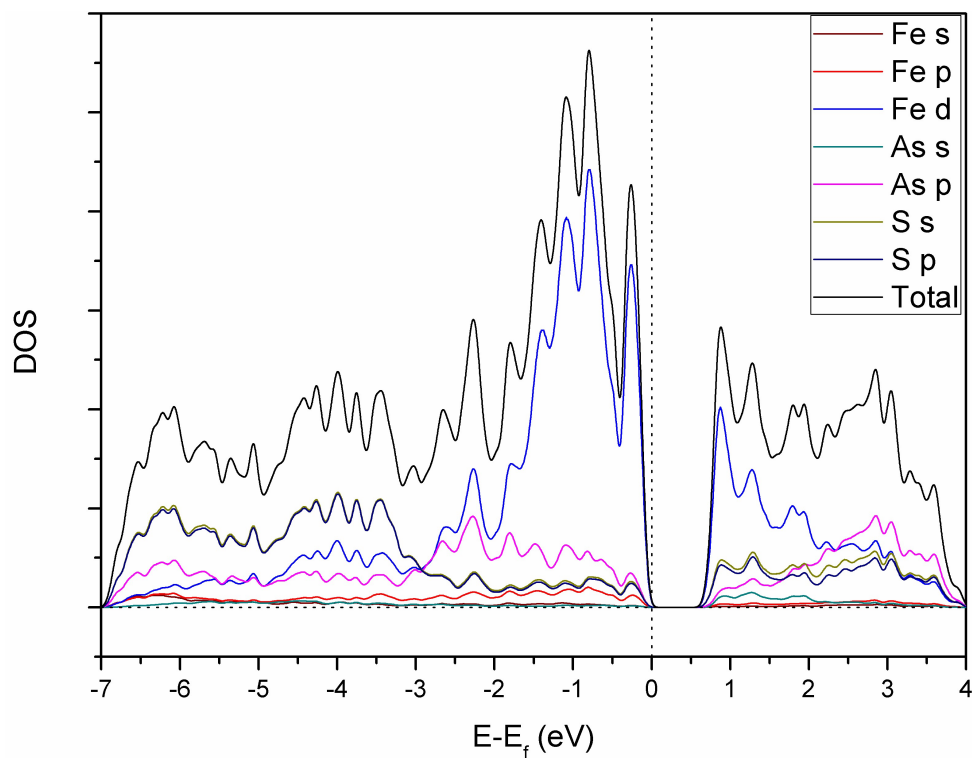


Figure 3.7: Total and projected DOS over the atomic orbitals of arsenopyrite plotted using a Gaussian width of 0.005 Ry.

The DOS projected at the  $d$  orbitals of iron is shown in Figure 3.8 and the position of the octahedrons of arsenopyrite in relation to the axes  $x$ ,  $y$  and  $z$  in Figure 3.9. One aspect to be pointed out is that the conduction band is more composed by  $d_{xz}$  orbitals, which are located in the (010) plane, where it was thought that there would be a bond between neighboring iron atoms, as shown in Figure 3.9b. Therefore there should be no chemical bond between these atoms. This argument is reinforced by the density map along the (010) plane (Figure 3.10) plotted with the software XCrySDen [25], which indicates that the electron density between two neighboring iron atoms is very tenuous.

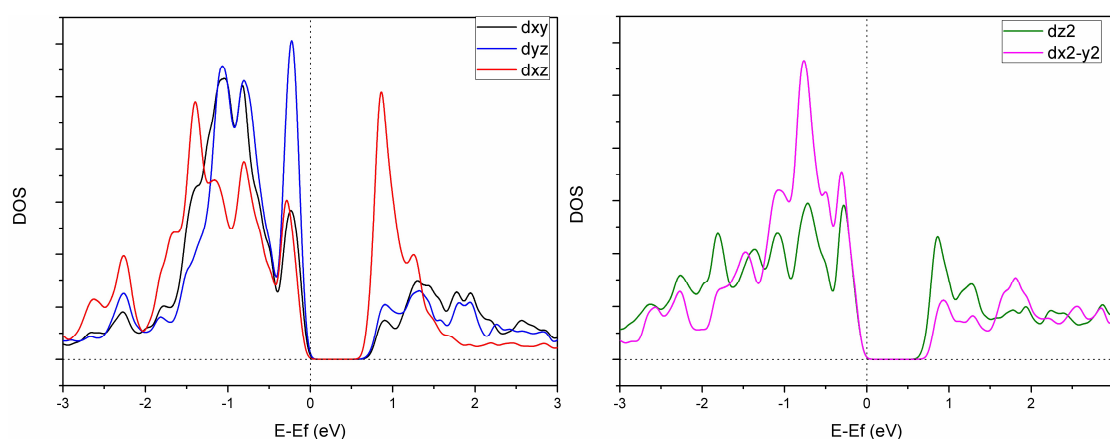


Figure 3.8: DOS projected over iron  $d$  orbitals plotted using a Gaussian width of 0.005 Ry.

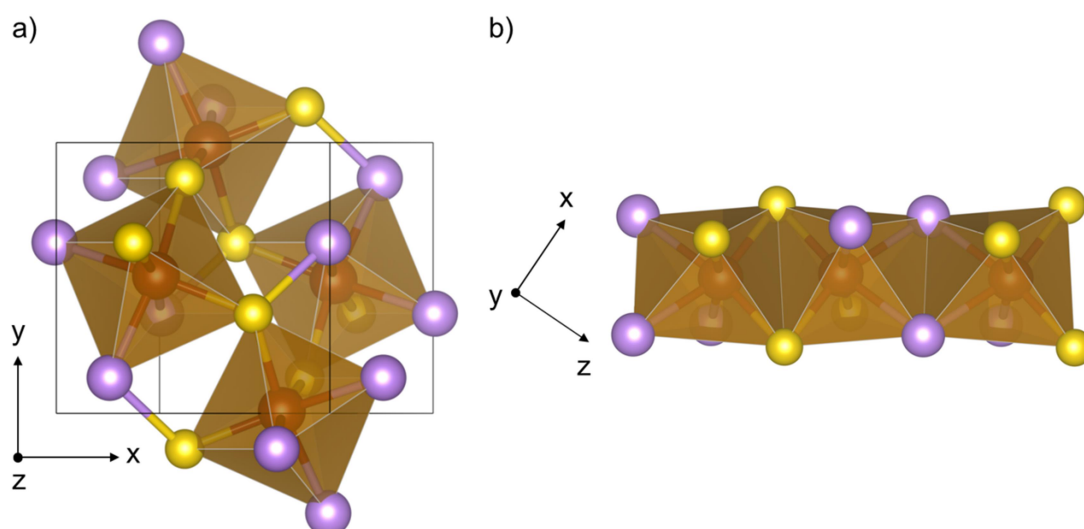


Figure 3.9: a) As-S dianions octahedrally coordinated to Fe. b) Neighbor octahedrons sharing one edge. Yellow atoms are sulfur, purple are arsenic and brown are iron.

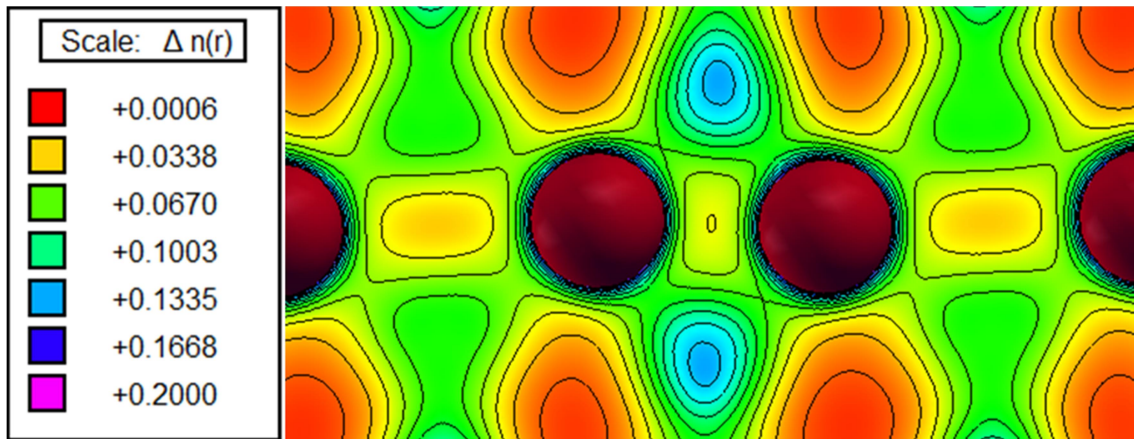


Figure 3.10: Electron density map of the arsenopyrite (010) plane. Brown balls are iron atoms.

### 3.3 Topological Analysis of the Electron Density.

An analysis of the electron density critical points based on the Quantum Theory of Atoms in Molecules (QTAIM) [26] has been carried out with the purpose of understanding the nature of the chemical bond in this solid. The topology of the electron density was explored and critical points were found and characterized by its Laplacian calculated numerically in a mesh of points. Therefore a  $\mathbf{K}$ -point mesh of  $12 \times 12 \times 12$  was used and a total of 90 critical points found, of which 24 were nonequivalent: three nuclear critical points (NCP), seven bond critical points (BCP), nine ring critical points (RCP) and five cage critical points (CCP). The position of the points is shown in Figure 3.11 and the respective data shown in Table 3.3. The Morse relationship ensures that  $n - b + r - c = 0$ , with  $n, c \geq 1$  and  $b, r \geq 3$  in the respective unit cell. This relationship is certified for the 24 nonequivalent critical points in the unit cell.

Table 3.3: Critical points in QTAIM analysis.

Critical points	$\rho(r_c)$ *	$\nabla^2\rho(r_c)$ **	Chemical meaning
Fe	6.2235	-73.0292	
As	0.5412	-18.0058	
S	0.3588	-10.8180	
b1	0.0721	0.0492	Fe-As
b2	0.0961	0.1501	Fe-S
b3	0.0733	0.0730	Fe-As
b4	0.0924	0.1996	Fe-S
b5	0.0725	0.0475	Fe-As
b6	0.0828	-0.0075	As-S
b7	0.0881	0.2232	Fe-S
r1	0.0326	0.0546	Fe...Fe long
r2	0.0430	0.0539	Fe...Fe short
r3	0.0145	0.0427	
r4	0.0109	0.0297	
r5	0.0145	0.0379	
r6	0.0151	0.0443	
r7	0.0174	0.0417	
r8	0.0162	0.0431	
r9	0.0078	0.0192	
c1	0.0119	0.0398	
c2	0.0081	0.0274	
c3	0.0101	0.0302	
c4	0.0078	0.0232	
c5	0.0078	0.0228	

\* Electron density and \*\* Laplacian of the electron density in atomic units.

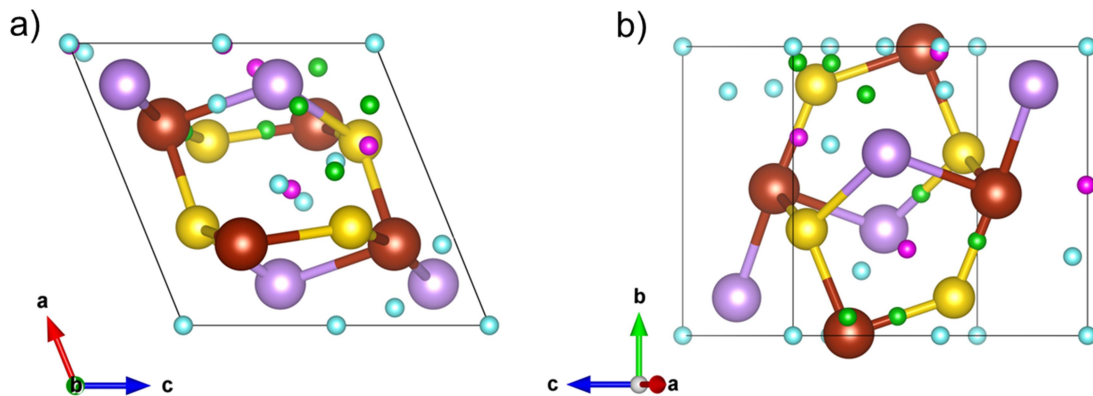


Figure 3.11: Bond critical points (BCP) in green, Ring critical points (RCP) in blue, and Cage critical points (CCP) in pink for arsenopyrite QTAIM analysis. Atoms in brown are iron, in yellow are sulfur and in purple are arsenic.

Concerning the Bond Critical Points, three are Fe–S bond, three are Fe–As bond and one is an As–S bond critical point, as shown in Figure 3.12a. The critical points involving Fe–S and Fe–As bonds have a positive Laplacian value, which indicates a bond with ionic character, although Schmokel *et al.* [15] have proposed that the Fe–S bonds in pyrite and marcasite have some covalent character due to Fe *d* orbitals mixing involved in this bond. The Fe–S BCP shows values of density and Laplacian (see Table 3.3) close to those of Gibbs *et al.* [27] for pyrite and marcasite calculated using DFT/LDA and localized basis sets and also close to the values published by Schmokel *et al.* [15] for the same minerals in a DFT/PBE study using multipole refinement. Aray *et al.* [28] found a value of 0.079 a.u. of density for the Fe–S BCP in pyrite and 0.13251 a.u. for the S–S BCP in DFT/PBE (FP-LAPW, full-potential linearized augmented plane-wave + local orbitals) calculations. The Fe–As BCP has density values smaller than the Fe–S BCP, indicating that the latter bond is stronger than the former. The Fe–S bond has more positive Laplacian values than the Fe–As bond, which indicates that the former has more ionic character than the latter. The As–S BCP has density of 0.0828 a.u. and a Laplacian value of -0.0075, which means that it has covalent character. Schmokel *et al.* [15] found similar results for density and Laplacian of the S–S BCP in pyrite and marcasite. The electron density and Laplacian of the S–S BCP in marcasite are 0.115 a.u. and -0.015 a.u., respectively, compared to the values of the same bond in pyrite of 0.126 a.u. and -0.043 a.u., respectively, indicating that this bond is stronger in pyrite than in

marcasite. This result is similar to the density of S–S BCP in covellite (0.135 a.u.) and its Laplacian (-0.079 a.u.) found by Morales-García [29] using a similar computational method. Comparing with our results for As–S BCP in arsenopyrite of 0.083 and -0.007 a.u. for density and Laplacian, respectively, it can be expected that the As–S bond in arsenopyrite is weaker than the S–S bond in pyrite, marcasite and covellite. However, analyzing the values shown in Table 3.3, the As–S bond is the strongest in arsenopyrite and, therefore, unlikely to break in surface cleavage.

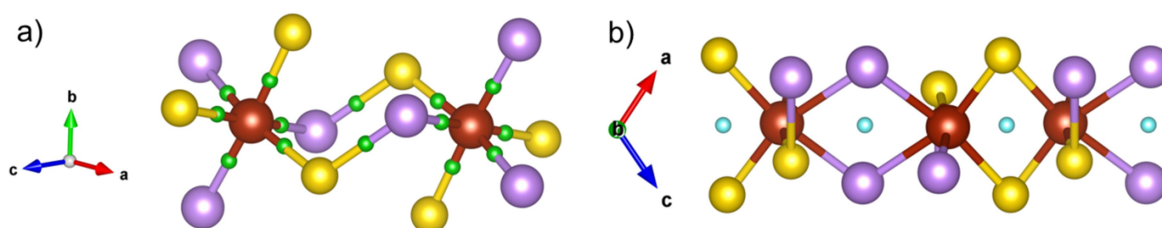


Figure 3.12: a) Bond critical points and b) Ring critical points in detail. Yellow atoms are sulfur, purple are arsenic and brown are iron.

To verify that the As–S bond is indeed covalent, a map of ELF (Electron Localization Function) has been generated (Figure 3.13). ELF is close to 1 in the region where electrons are localized, forming a covalent bond and around 0.5 in regions where the electrons are spread, that is, where the chemical bonds have a metallic character. In Figure 3.13 it is possible to see the pair of bonding electrons that share the electron cloud around the As and S atoms, which indicates the formation of a covalent bond.

No Bond Critical Point was found in the space between the iron atoms, only a Ring Critical Point, which is located in both types of shared edges of the neighboring octahedra: the one containing As atoms and the one containing S atoms (see Figure 3.12b). Although Pauling [30] has found complexes with a Fe–Fe bond up to 2.78 Å long, by our calculations, the hypothesis of a Fe–Fe bond is completely discarded. The values of density and Laplacian for the r1 and r2 RCPs corresponding to the Fe...Fe distances of 3.765 and 2.668 Å are very similar and the interaction of these atoms must have the same nature. The ELF map generated for the region between the iron atoms (Figure 3.14) shows a value of 0.25 in this region, which is not characteristic of a chemical bond.

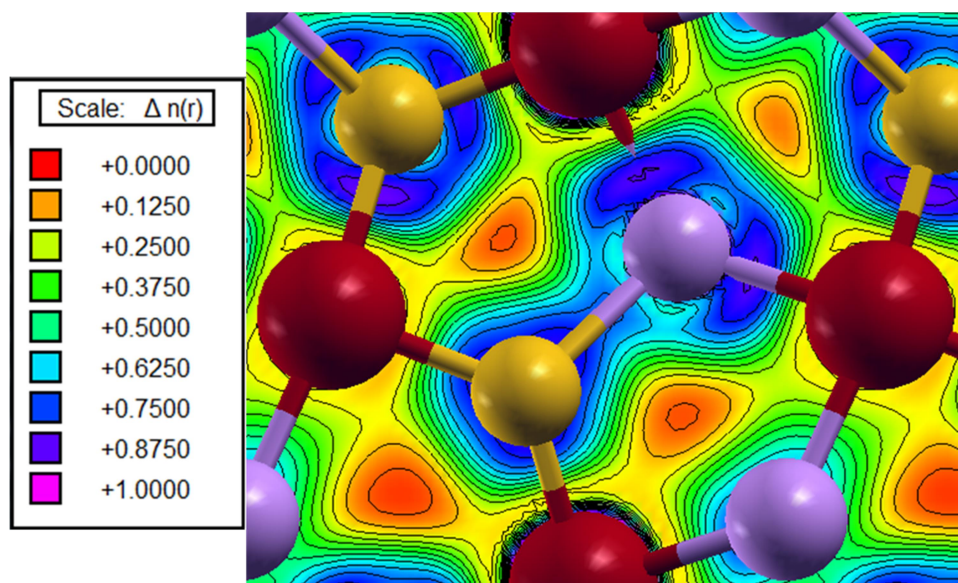


Figure 3.13: ELF of arsenopyrite As–S bond. brown is iron, purple is arsenic and yellow is sulfur.

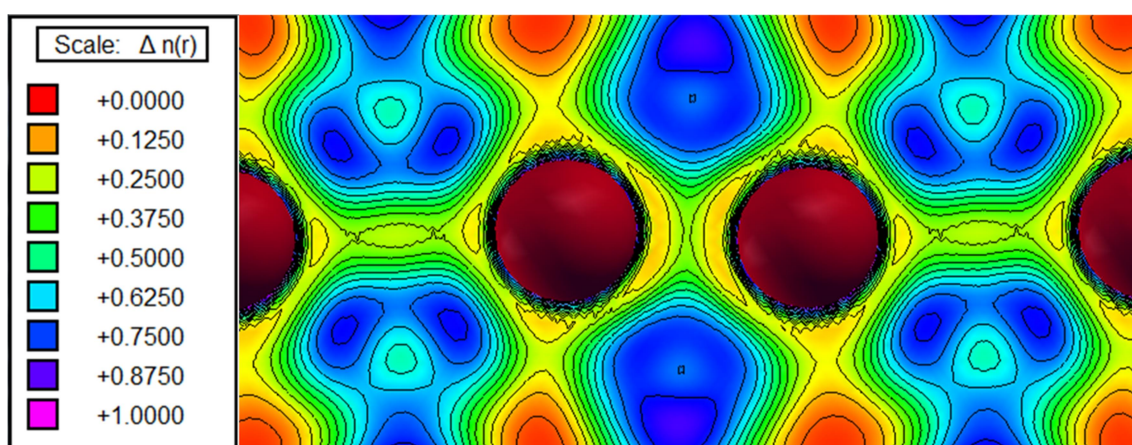


Figure 3.14: ELF of the arsenopyrite (010) plane. Iron atoms are represented by brown spheres.

The volumes and atomic charges calculated in QTAIM analysis are summarized in Table 3.4. There was no significant difference among the atoms of the same element. As can be seen, the calculated charge for the Fe atom is about twice that of As, being both positive, and the charge of the S atom negative. The positive charge on the As atom can be explained because this atom is less electronegative than the S atom in the  $\text{As-S}^{2-}$  anion, as also observed by Schaufuss and coworkers [31], that the electron density in the dimer is shifted to the S atom. The integration of the AsS basins lead to  $-0.41e$  and  $0.41e$  for the iron basin. This is

coherent with the formula  $\text{Fe}^{2+}(\text{AsS})^{2-}$ . The As and S atoms have the largest volumes, which means that these atoms dominate the crystal compressibility.

Table 3.4: Atomic charges in AIM analysis

Atoms	Charge	Volume (a. u.)	Pauling's electronegativity
Fe	0.41	69.9	1.83
As	0.18	112.9	2.18
S	-0.59	111.8	2.58
Total		1178.5	

The  $c$  parameter [32] can be used to evaluate how much the topological charge  $Q(\Omega)$  differs from the nominal oxidation state  $OS(\Omega)$ ,

$$c = \frac{1}{N} \sum_{\Omega=1}^N \frac{Q(\Omega)}{OS(\Omega)}, \quad (3.1)$$

indicating the ionicity degree of the crystal.

The closer to 1 the value of the  $c$  parameter is, the more ionic is the crystal, and the closer to zero, the more covalent. The value of  $c$  for arsenopyrite is 0.205, which indicates a solid with more covalent tendency than ionic.

The bulk modulus,  $B$ , measures the resistance of a material to a uniform compression. It is defined by

$$B = -V \frac{dP}{dV}, \quad (3.2)$$

where  $V$  is the volume and  $P$  the pressure. The bulk modulus of arsenopyrite was calculated and its value is presented and compared to other studies in Table 3.5. A value of 147.5 GPa was found, 15 GPa higher than the result obtained experimentally by Fan *et al.* [33] with X-ray diffraction in the pressure range from 0 to 9.6 GPa. However our result is closer to the one found by Gudelli *et al.* [4] for marcasite in PBE/plane waves calculations and to the one found by Chattopadhyay and Vonschning [34] using X-ray diffraction. It is also close to the values found for

pyrite using DFT calculations [35] and X-ray diffraction [36]. This shows that the method used in this work describes well not just each atom individually, but also the whole crystal structure.

Table 3.5: Calculated and experimental bulk moduli for arsenopyrite, marcasite and pyrite.

Compound	Bulk modulus (GPa)	Reference
Arsenopyrite	147.5	This work
Arsenopyrite	133	X-ray diffraction [33]
Marcasite	150.1	PBE/plane waves [4]
Marcasite	146.5	X-ray diffraction [34]
Pyrite	150	PAW/plane waves [35]
Pyrite	143	X-ray diffraction [36]

### 3.4 Arsenopyrite Surfaces

The crystal surfaces most commonly observed are those with low Miller indices, since they require less energy to be created [37]. Tasker [38] has classified the ionic or semi-ionic solid surfaces into three types based on the charge distribution along the planes parallel to the surface, as shown in Figure 3.15. In type I the layer is comprised of cations and anions with the same stoichiometry of the crystal, thus their charge is neutral. In type II, there are charged layers formed by cations or anions symmetrically arranged so that their charges cancel each other in total and the surface does not have a dipole moment. In type III there are alternately charged layers organized in a way that there is a dipole moment perpendicular to the surface.

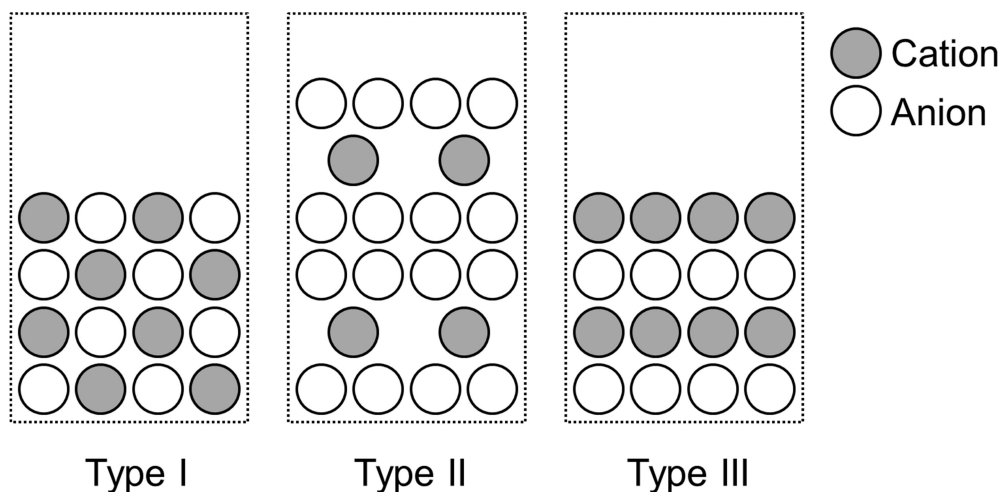


Figure 3.15: Surface Types according to Tasker. Adapted from [39].

The first two surface types are stable and undergo only minor changes in the direction normal to the surface, as a relaxation. However, type III is unstable and undergoes a drastic reconstruction to stabilize with chemical changes as breakage and formation of new bonds, which can also happen by adsorption of additional charge.

As for the preferential cleavage of arsenopyrite, there is no definitive conclusion in the literature, and the surfaces (100) [40], (001) [41], (101) [42, 43] and (110) [6, 44] were identified as the most favorable for cleavage by different authors. It is important to note that in some works the unit cell used to define the Miller indices was not clearly indicated, which may lead to misinterpretations. Table 3.6 shows the correspondence between the cleavage planes in cells  $C2_1/d$  and  $P2_1/c$ .

Table 3.6: Surfaces correspondence in  $C2_1/d$  and  $P2_1/c$  unit cells.

$C2_1/d$	$P2_1/c$
110	100
100	101
001	010
1-10	001
101	121
111	110
010	10-1

Several surfaces were created based on the optimized bulk  $P2_1/c$  cell to compare their energy. The planes are shown in Figure 3.16 and the generated surfaces in Figure 3.17, page 64. Some surfaces have two types of terminations; in this case, both have been calculated.

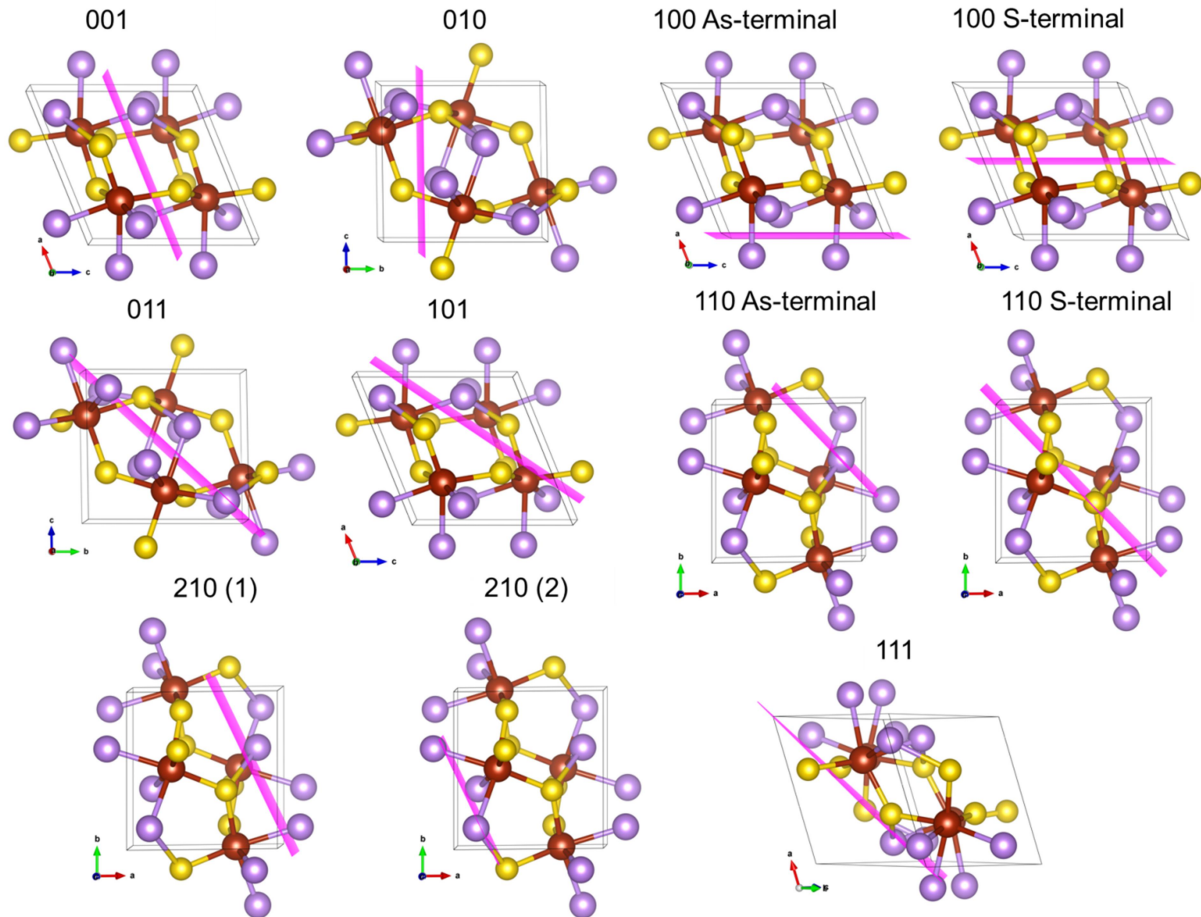


Figure 3.16: Arsenopyrite cleavage planes. Iron is in brown, sulfur in yellow and arsenic in purple. Miller indices are based on the  $P2_1/c$  symmetry.

All surfaces were created as type II of Tasker [38], which indicates that possibly there is no reconstruction of the surfaces, only relaxation. The surface energy was calculated as [36]

$$\Delta E_{surface}^n = \frac{(E^n - nE_{bulk})}{2A}, \quad (3.3)$$

where  $E^n$  is the energy of a n-layer slab,  $E_{bulk}$  is the energy of the unit cell which correspond to a single bulk layer, and  $A$  is the surface area. The cleavage energy  $E_{cleav}$  was calculated before the relaxation, in a single point calculation, and the surface energy  $E_{surf}$  was calculated after the relaxation. The results are shown in Table 3.7 together with the coordination number of each surface atom in the different cleavages. Figure 3.18, page 64, shows the structures after relaxation.

Table 3.7: Surface energies and coordination numbers of surface atoms of different arsenopyrite cleavage planes. Miller indices are based on the  $P2_1/c$  symmetry.  $E_{cleav}$  is the cleavage energy calculated before the relaxation and  $E_{surf}$  the surface energy calculated after the relaxation.

Surface	$E_{surf} / \text{J m}^{-2}$	$E_{cleav} / \text{J m}^{-2}$	Coordination Number		
			Fe	As	S
Bulk	-	-	6	4	4
001	1.05	1.23	5	3	3
010	1.06	1.28	5	3	3
100 As-terminal	1.07	1.21	5	3	4
100 S-terminal	1.09	1.35	5	4	4
011	1.30	1.50	5, 4	2	3
101	1.47	1.65	4	3	3
110 S-terminal	1.52	1.91	4	3	3, 2
110 As-terminal	1.57	1.93	4	3, 2	3
111	1.51	1.78	5	2	2
210 (1)	1.44	1.59	4, 3	3, 2	4, 3
210 (2)	1.78	2.29	4, 3	3, 1	2

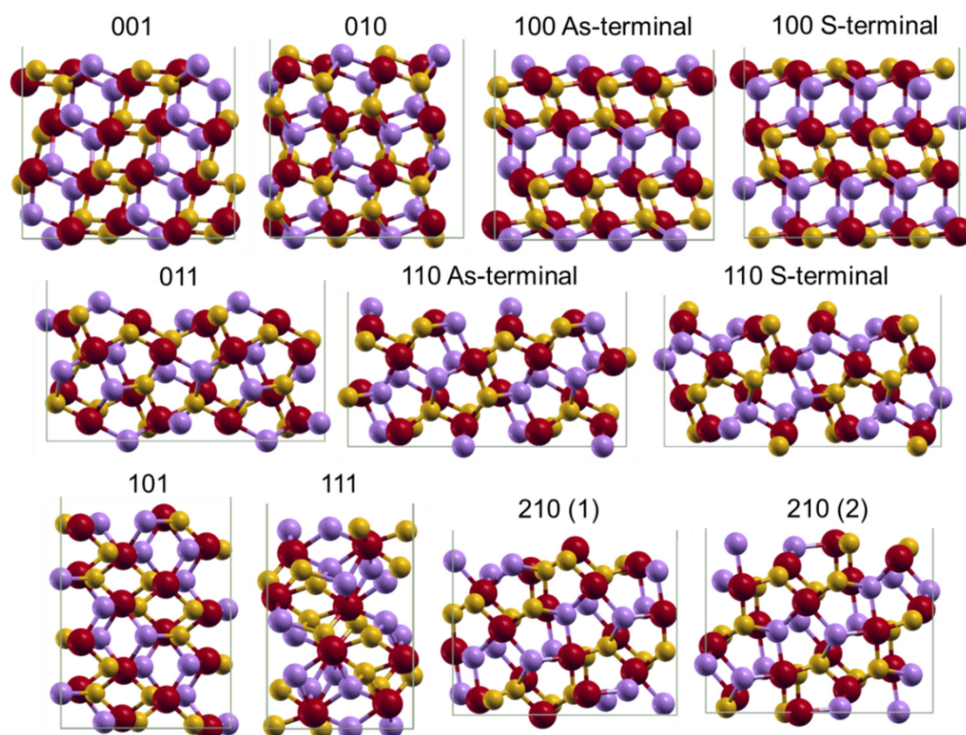


Figure 3.17: Arsenopyrite cleavage surfaces used to perform the calculations. Iron is in brown, sulfur in yellow and arsenic in purple. Miller indices are based on the  $P2_1/c$  symmetry.

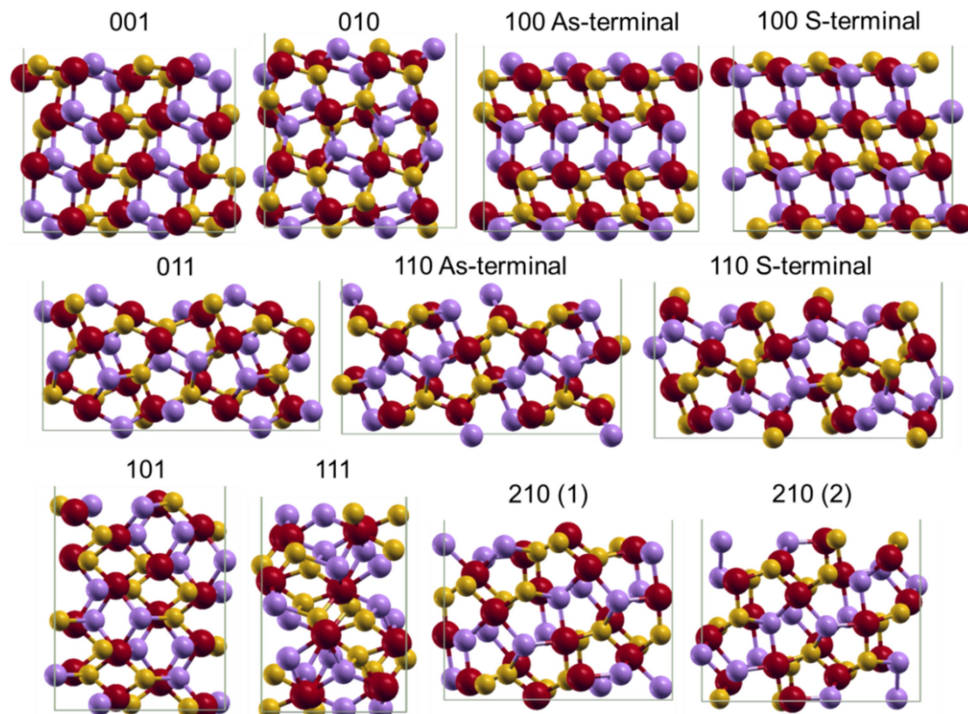


Figure 3.18: Optimized arsenopyrite surfaces (after relaxation). Iron is in brown, sulfur in yellow and arsenic in purple. Miller indices are based on the  $P2_1/c$  symmetry.

The atoms in the first layer of the surfaces moved more from their original positions in the bulk than the internal atoms. The greatest changes observed were 0.12 Å in a Fe–As bond on the (100) surface, 0.14 Å in a Fe–As bond on the (001) surface and 0.14 Å in the Fe–Fe distance on the (010) surface.

It is easy to see from Table 3.7 that the surface energy is related to the number of broken bonds in the cleavage. The planes (001), (010) and (100) are the most favorable with  $E_{\text{surf}}$  ranging from 1.05 to 1.09 J m<sup>-2</sup> and  $E_{\text{cleav}}$  from 1.21 to 1.35 Jm<sup>-2</sup>. A top view of these surfaces is shown in Figure 3.19. The (100) plane is more likely to cleave on the As-terminal surface. The surfaces (001) and (100) expose a similar terminal structure, but the (100) surface exposes more arsenic atoms, as can be observed in Figure 3.19, page 66. In these plans, no As–S bond is broken, as it was expected. They also agree with the observation of Schaufuss *et al.* [31] that As is the atom closest to the surface after cleavage of Fe–As bonds, except for the (100) S-terminal. Other plans have higher energies; hence their cleavage is less likely, although there is the possibility of twinning, which would help to fracture those plans. According to Klein *et al.* [42], twinning occurs on surfaces (100) and (001) of the P2<sub>1</sub>/c cell, while for Dana and Ford [44] it occurs on (110) and (101) surfaces.

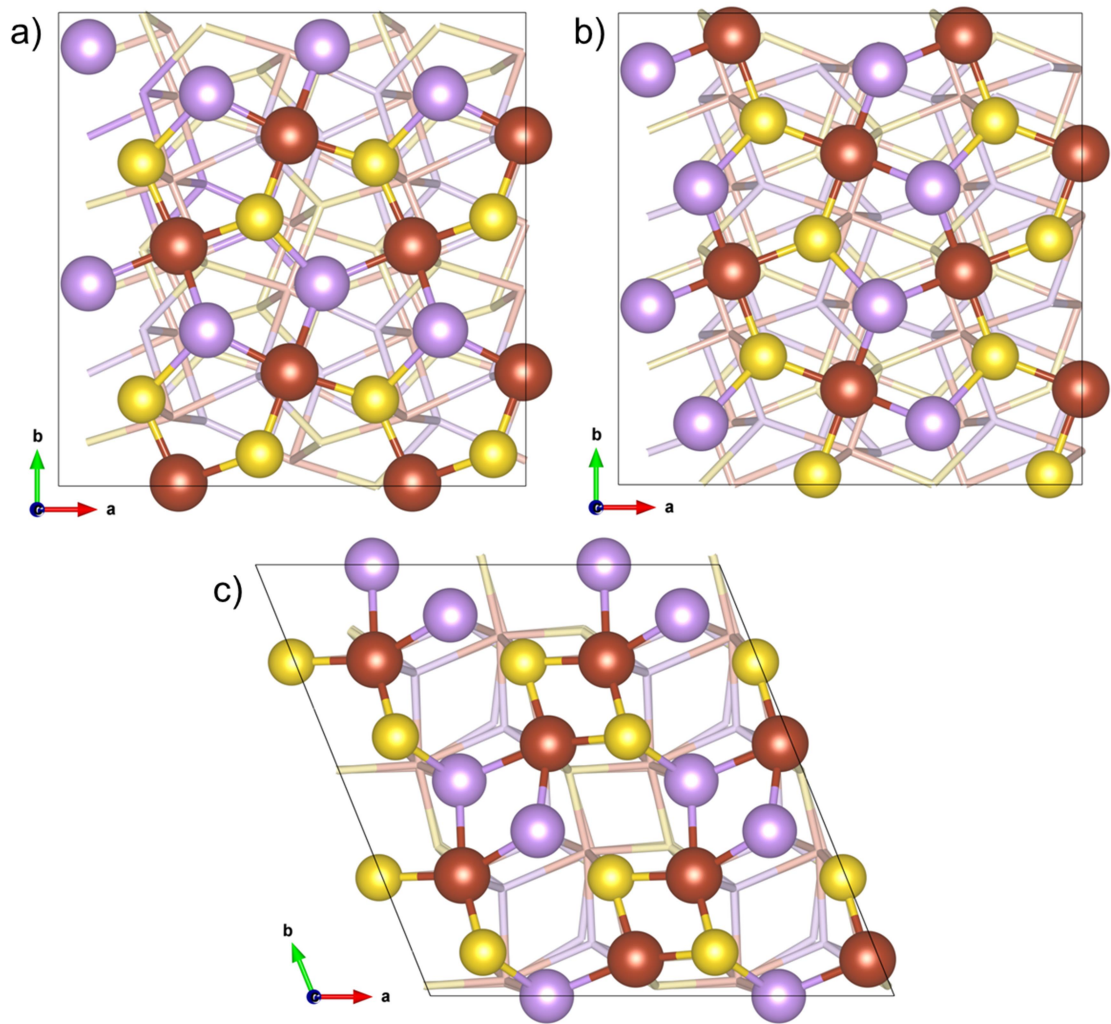


Figure 3.19: Top view of surfaces: a) (001); b) (100); c) (010). Brown is iron, purple is arsenic and yellow is sulfur.

Pyrite has a cubic unit cell, therefore the planes (100), (010) and (001) are equivalent and have often been used in studies of adsorption and oxidation of pyrite [47, 48]. Hung *et al.* [45, 46] studied (100), (110), (111) and (210) surfaces of pyrite by means of PBE/plane waves calculations. The results show the same tendency of arsenopyrite surface energies, except for the (100) surface cleavage energy of  $4.25 \text{ J m}^{-2}$ . Table 3.8 shows a comparison between the surface energies of arsenopyrite and pyrite. It is important to remember that these minerals have different structures and different unit cells, thus the bond breaking in the surface formation is different.

Table 3.8: Comparison of Arsenopyrite and Pyrite's surface energies. Miller indices are based on the  $P2_1/c$  symmetry.

Surface	Arsenopyrite		Pyrite [45, 46]	
	Surface Energy/J m <sup>-2</sup>	Cleavage Energy/J m <sup>-2</sup>	Surface Energy/J m <sup>-2</sup>	Cleavage Energy/J m <sup>-2</sup>
001	1.05	1.23		
010	1.06	1.28	1.06 <sup>3</sup>	4.25 <sup>3</sup>
100	1.07	1.21		
110 (S-terminal)	1.52	1.91	1.68	1.85
110 (As-terminal)	1.57	1.93	1.54 <sup>1</sup>	1.74 <sup>1</sup>
110 (1) <sup>2</sup>	1.76	2.08	-	-
110 (2) <sup>2</sup>	2.08	2.40	-	-
111	1.51	1.78	1.40	1.61
210	1.44	1.59	1.50	1.74

<sup>1</sup>Microfacetted (110) pyrite surface.

<sup>2</sup>Corkhill *et al.* [6].

<sup>3</sup>The (001), (010) and (100) pyrite surfaces are equivalent.

Corkhill *et al.* [6] also calculated the surface and cleavage energies of arsenopyrite (110) plane in two different terminations using PBE/plane waves. The models used by them (24 atoms, 5.65 Å × 7.91 Å × 16.9 Å cell) are four times smaller than the ones considered in the present work and do not have equal terminations on the top and bottom surfaces. Their estimated values of  $E_{\text{surf}}$  (1.76 and 2.08 Jm<sup>-2</sup>) and  $E_{\text{cleav}}$  (2.08 and 2.40 Jm<sup>-2</sup>), are higher than those achieved in this study (1.52, 1.57 Jm<sup>-2</sup>, 1.91, and 1.93 J m<sup>-2</sup>, respectively).

The DOS projected onto the surfaces atoms of (001), (010) and (100) planes are shown in Figure 3.20. Similarly to the bulk, the 3d Fe orbitals are dominant around the Fermi level, which means that nucleophilic or electrophilic interactions with adsorbents are most likely to occur on this atom. For all surfaces, the band gap that was present on the bulk almost disappeared, due to the formation of surface-bound electronic states with energy in the region between the valence and conduction band of the bulk semiconductor when the surface is created [49]. A

surface narrower band gap comparing to the bulk was also noticed by Dos Santos *et al.* when studying pyrite's surface [50].

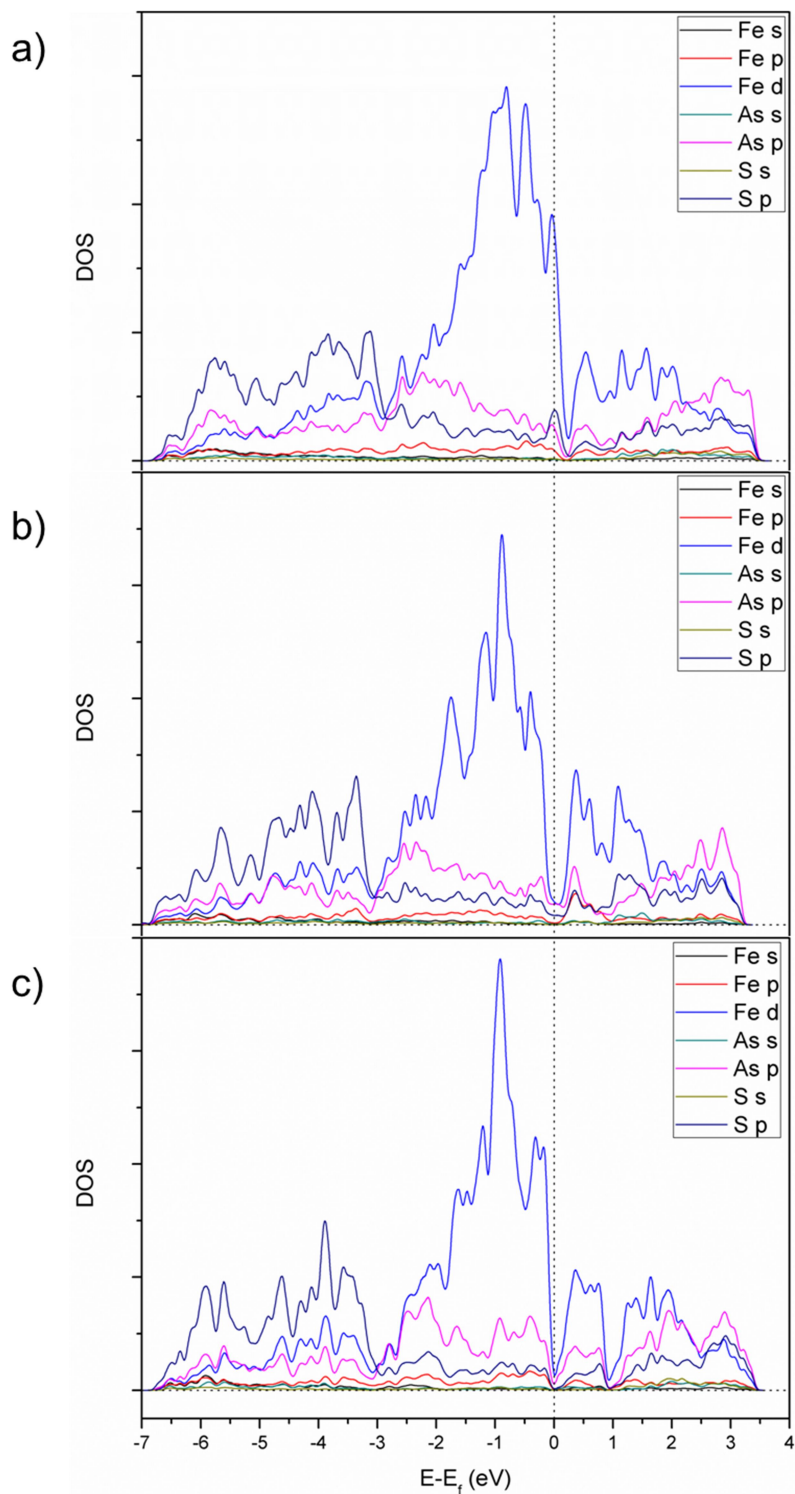


Figure 3.20: Projected DOS over the atoms of the surfaces: a) (001); b) (010); c) (100) plotted using a Gaussian width of 0.005 Ry.

Because it is the lowest energy surface and exposes Fe, As and S atoms, the (001) surface was chosen for the following stages of the study. The definition of an appropriate thickness of this slab surface was investigated to ensure there are no edge effects. We evaluated the surface energy varying the number of layers along the z axis according to equation 3.3, page 62. By the analysis of Figure 3.21, the number of 12 layers along the z axis was chosen, from which the energy converges within  $0.01 \text{ J m}^{-2}$ .

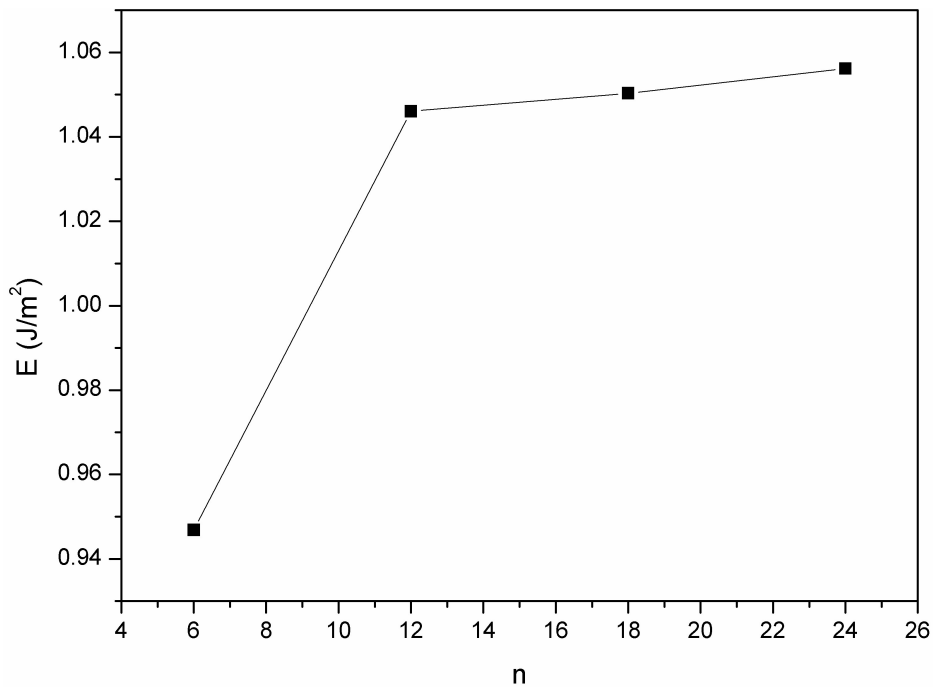


Figure 3.21: (001) surface energy as a function of the number of layers  $n$  in the slab.

Although our results show that FeAsS is a non-magnetic mineral, the formation of the (001) surface leads to occupied states across the Fermi level, as indicated by the calculated DOS of the surface in Figure 3.20a. The same surface structure was again optimized using spin-polarization on the surface Fe atoms in order to evaluate the magnetic behavior of the surface. Slight changes in the atomic positions have been observed, but the spin-polarization turned out to be necessary to correctly describe the DOS close to the Fermi level, as shown in Figure 3.22. This result is in agreement with the Stoner criterion [51], which once satisfied, the system evolves spontaneously towards maximum polarization. A total magnetization of  $-0.02 \mu_B$  and an absolute magnetization of  $21.4 \mu_B$  in the whole unit cell was

obtained, which corresponds to  $0.2 \mu_B$  per atom. At the surface most external Fe sites, the absolute magnetization was around  $1.3 \mu_B$ .

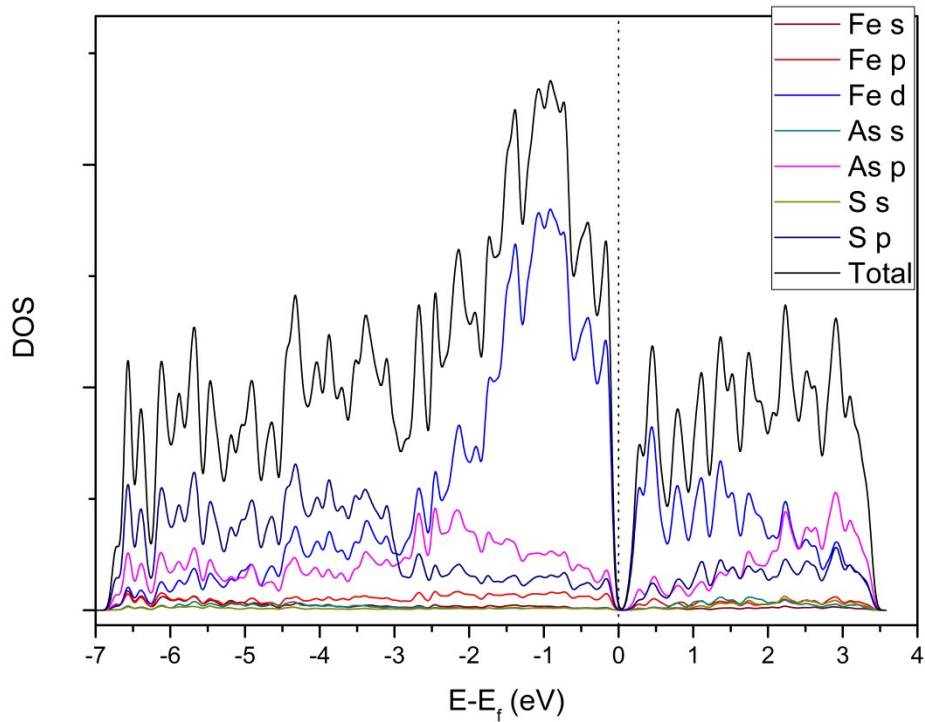


Figure 3.22: Projected DOS of Arsenopyrite (001) surface calculated using spin-polarization.

### 3.5 Final Considerations

Arsenopyrite ( $\text{FeAsS}$ ) is an important component in many mining tailings, which can be suitably disposed in dams to prevent remobilization of arsenic and acid rock drainage. Structural and electronic properties of arsenopyrite and its different cleavage surfaces have been investigated by the DFT/plane waves method. For the arsenopyrite bulk, the obtained structural parameters are in good agreement with experimental data and also with previous reported calculations. Bader's QTAIM analysis indicates that there is no Fe–Fe bond in arsenopyrite, only one ring critical point was found between the two iron atoms and the DOS indicates that the iron atom is in a divalent oxidation state. The As–S bond has covalent character and the

Fe–As and Fe–S bonds have ionic character. As in previously reported calculations of covellite [29] and pyrite [15], which concluded that S–S bond is unlikely to be broken, the breakage of the dianion As–S bond is unlikely in arsenopyrite surface cleavage, because it is the strongest bond in the structure. The system, as a whole, can be considered a covalent solid.

The cleavage and surface energies have been estimated for different arsenopyrite surfaces. The cleavage planes (001), (010) and (100) are considered the most favorable, with an average surface energy of  $1.07 \text{ J m}^{-2}$ . Perhaps the existence of various surfaces with similar formation energy justifies the lack of consensus about the cleavage plane of arsenopyrite in the literature. In these surfaces no As–S bond is broken and all three types of atoms, Fe, As and S are exposed on the surface. Thus, the surfaces (001), (010) and (100) are suitable for use in the investigation of the reactivity of arsenopyrite, wherein the (001) surface was chosen because it has the lowest energy and exposes all the atoms involved in the oxidation mechanism. The DOS projected onto the surface atoms shows that both the conduction and the valence band are composed mainly of iron *d* orbitals, indicating that this is the preferred site for adsorption. Hence, they must be involved in the initial steps of the arsenopyrite oxidation. The (001) surface presents some magnetic behavior, especially on the Fe surface sites. Therefore it must be calculated using spin-polarization.

### 3.6 References

1. Morimoto, N. and L.A. Clark, *Arsenopyrite Crystal-Chemical Relations*. American Mineralogist, 1961. **46**(11-2): p. 1448-1469.
2. Bindi, L., et al., *Stoichiometric Arsenopyrite, FeAsS, from La Roche-Balve Quarry, Loire-Atlantique, France: Crystal Structure and Mossbauer Study*. The Canadian Mineralogist, 2012. **50**(2): p. 471-479.
3. Fuess, H., et al., *Crystal-Structure Refinement and Electron-Microscopy of Arsenopyrite*. Zeitschrift Fur Kristallographie, 1987. **179**(1-4): p. 335-346.
4. Gudelli, V.K., et al., *Phase Stability and Thermoelectric Properties of the Mineral FeS<sub>2</sub>: An Ab Initio Study*. Journal of Physical Chemistry C, 2013. **117**(41): p. 21120-21131.

5. de Oliveira, C. and H.A. Duarte, *Disulphide and metal sulphide formation on the reconstructed (001) surface of chalcopyrite: A DFT study*. Applied Surface Science, 2010. **257**(4): p. 1319-1324.
6. Corkhill, C.L., M.C. Warren, and D.J. Vaughan, *Investigation of the electronic and geometric structures of the (110) surfaces of arsenopyrite (FeAsS) and enargite (Cu<sub>3</sub>AsS<sub>4</sub>)*. Mineralogical Magazine, 2011. **75**(1): p. 45-63.
7. Hulliger, F. and E. Mooser, *Semiconductivity in pyrite, marcasite and arsenopyrite phases*. Journal of Physics and Chemistry of Solids, 1965. **26**(2): p. 429-433.
8. Pearson, W.B., *Compounds with the marcasite structure*, in *Zeitschrift für Kristallographie - Crystalline Materials*. 1965. p. 449.
9. Nickel, E.H., *Structural stability of minerals with the pyrite, marcasite, arsenopyrite and lollingite structures*. The Canadian Mineralogist, 1968. **9**(3): p. 311-321.
10. Nickel, E.H., *The application of ligand-field concepts to an understanding of the structural stabilities and solid-solution limits of sulphides and related minerals*. Chemical Geology, 1970. **5**(4): p. 233-241.
11. Brostige, G. and A. Kjekshus, *Bonding Schemes for Compounds with Pyrite, Marcasite, and Arsenopyrite Type Structures*. Acta Chemica Scandinavica, 1970. **24**(8): p. 2993-3012.
12. Goodenou, J.B., *Energy-Bands in TX<sub>2</sub> Compounds with Pyrite, Marcasite, and Arsenopyrite Structures*. Journal of Solid State Chemistry, 1972. **5**(1): p. 144-152.
13. Vaughan, D.J. and J.R. Craig, *Mineral chemistry of metal sulfides*. Cambridge earth science series. 1978, Cambridge Eng. ; New York: Cambridge University Press.
14. Tossell, J.A., D.J. Vaughan, and J.K. Burdett, *Pyrite, marcasite, and arsenopyrite type minerals: Crystal chemical and structural principles*. Physics and Chemistry of Minerals, 1981. **7**(4): p. 177-184.
15. Schmokel, M.S., et al., *Atomic properties and chemical bonding in the pyrite and marcasite polymorphs of FeS<sub>2</sub>: a combined experimental and theoretical electron density study*. Chemical Science, 2014. **5**(4): p. 1408-1421.
16. Nesbitt, H.W., I.J. Muir, and A.R. Prarr, *Oxidation of arsenopyrite by air and air-saturated, distilled water, and implications for mechanism of oxidation*. Geochimica et Cosmochimica Acta, 1995. **59**(9): p. 1773-1786.
17. Jones, R.A. and H.W. Nesbitt, *XPS evidence for Fe and As oxidation states and electronic states in loellingite (FeAs<sub>2</sub>)*. American Mineralogist, 2002. **87**(11-12): p. 1692-1698.
18. Setyawan, W. and S. Curtarolo, *High-throughput electronic band structure calculations: Challenges and tools*. Computational Materials Science, 2010. **49**(2): p. 299-312.
19. Vaughan, D.J., *Sulfide Mineralogy and Geochemistry: Introduction and Overview*. Reviews in Mineralogy and Geochemistry, 2006. **61**(1): p. 147.
20. Almeida, C.M.V.B. and B.F. Giannetti, *Electrochemical study of arsenopyrite weathering*. Physical Chemistry Chemical Physics, 2003. **5**(3): p. 604-610.
21. Tran, F. and P. Blaha, *Accurate Band Gaps of Semiconductors and Insulators with a Semilocal Exchange-Correlation Potential*. Physical Review Letters, 2009. **102**(22): p. 226401.

22. Ferrer, I.J., et al., *About the band gap nature of FeS<sub>2</sub> as determined from optical and photoelectrochemical measurements*. Solid State Communications, 1990. **74**(9): p. 913-916.
23. Ennaoui, A., et al., *Iron disulfide for solar energy conversion*. Solar Energy Materials and Solar Cells, 1993. **29**(4): p. 289-370.
24. Opahle, I., K. Koepernik, and H. Eschrig, *Full-potential band-structure calculation of iron pyrite*. Physical Review B, 1999. **60**(20): p. 14035-14041.
25. Kokalj, A., *XCrySDen—a new program for displaying crystalline structures and electron densities*. Journal of Molecular Graphics and Modelling, 1999. **17**(3–4): p. 176-179.
26. Bader, R.F.W., *A quantum theory of molecular structure and its applications*. Chemical Reviews, 1991. **91**(5): p. 893-928.
27. Gibbs, G.V., et al., *Theoretical Electron Density Distributions for Fe- and Cu-Sulfide Earth Materials: A Connection between Bond Length, Bond Critical Point Properties, Local Energy Densities, and Bonded Interactions*. The Journal of Physical Chemistry B, 2007. **111**(8): p. 1923-1931.
28. Aray, Y., et al., *Correlation of the Topology of the Electron Density of Pyrite-Type Transition Metal Sulfides with Their Catalytic Activity in Hydrodesulfurization*. Angewandte Chemie International Edition, 2000. **39**(21): p. 3810-3813.
29. Morales-García, A., et al., *First-Principles Calculations and Electron Density Topological Analysis of Covellite (CuS)*. The Journal of Physical Chemistry A, 2014. **118**(31): p. 5823-5831.
30. Pauling, L., *Metal-Metal Bond Lengths in Complexes of Transition-Metals*. Proceedings of the National Academy of Sciences of the United States of America, 1976. **73**(12): p. 4290-4293.
31. Schaufuss, A.G., et al., *Reactivity of surface sites on fractured arsenopyrite (FeAsS) toward oxygen*. American Mineralogist, 2000. **85**(11-12): p. 1754-1766.
32. Mori-Sánchez, P., A.M. Pendás, and V. Luaña, *A Classification of Covalent, Ionic, and Metallic Solids Based on the Electron Density*. Journal of the American Chemical Society, 2002. **124**(49): p. 14721-14723.
33. Fan, D.W., et al., *X-ray diffraction study of arsenopyrite at high pressure*. Physics and Chemistry of Minerals, 2011. **38**(2): p. 95-99.
34. Chattopadhyay, T. and H.G. Vonscherner, *High pressure X-ray diffraction study on *p*-FeS<sub>2</sub>, *m*-FeS<sub>2</sub> and MnS<sub>2</sub> to 340 kbar: A possible high spin-low spin transition in MnS<sub>2</sub>*. Journal of Physics and Chemistry of Solids, 1985. **46**(1): p. 113-116.
35. Le Page, Y. and J.R. Rodgers, *Ab initio elasticity of FeS<sub>2</sub> pyrite from 0 to 135 GPa*. Physics and Chemistry of Minerals, 2005. **32**(8-9): p. 564-567.
36. Merkel, S., et al., *Equation of state, elasticity, and shear strength of pyrite under high pressure*. Physics and Chemistry of Minerals, 2002. **29**(1): p. 1-9.
37. Dovesi, R., et al., *Ab Initio Quantum Simulation in Solid State Chemistry*, in *Reviews in Computational Chemistry*. 2005, John Wiley & Sons, Inc. p. 1-125.
38. Tasker, P.W., *The stability of ionic crystal surfaces*. Journal of Physics C: Solid State Physics, 1979. **12**(22): p. 4977.
39. de Lima, G.F., *Reatividade Química da Superfície da Calcopirita e Mecanismo de Separação da Mistura Etanol-Água em Metal-Organic Frameworks*, in *Departamento de Química*. 2013, UFMG: Belo Horizonte.

40. Corkhill, C.L., et al., *The oxidative dissolution of arsenopyrite (FeAsS) and enargite (Cu<sub>3</sub>AsS<sub>4</sub>) by Leptospirillum ferrooxidans*. *Geochimica et Cosmochimica Acta*, 2008. **72**(23): p. 5616-5633.
41. Ford, M. and C.C. Ferguson, *Cleavage Strain in the Variscan Fold Belt, County Cork, Ireland, Estimated from Stretched Arsenopyrite Rosettes*. *Journal of Structural Geology*, 1985. **7**(2): p. 217-223.
42. Klein, C., C.S. Hurlbut, and J.D. Dana, *Manual of mineralogy : (after James D. Dana)*. 21st ed. 1999, New York: J. Wiley.
43. Wolff, G.A. and J.D. Broder, *Cleavage and the Identification of Minerals*. *American Mineralogist*, 1960. **45**(11-2): p. 1230-1242.
44. Dana, E.S. and W.E. Ford, *A Text-book of Mineralogy: With an Extended Treatise on Crystallography and Physical Mineralogy*. 4 ed. 1966, New York: Wiley.
45. Hung, A., et al., *Density-functional theory studies of pyrite FeS<sub>2</sub>(100) and (110) surfaces*. *Surface Science*, 2002. **513**(3): p. 511-524.
46. Hung, A., et al., *Density-functional theory studies of pyrite FeS<sub>2</sub> (111) and (210) surfaces*. *Surface Science*, 2002. **520**(1-2): p. 111-119.
47. Stirling, A., M. Bernasconi, and M. Parrinello, *Ab initio simulation of water interaction with the (100) surface of pyrite*. *Journal of Chemical Physics*, 2003. **118**(19): p. 8917-8926.
48. Sit, P.H.L., M.H. Cohen, and A. Selloni, *Interaction of Oxygen and Water with the (100) Surface of Pyrite: Mechanism of Sulfur Oxidation*. *Journal of Physical Chemistry Letters*, 2012. **3**(17): p. 2409-2414.
49. Kittel, C., *Introduction to solid state physics*. 2005: John Wiley & Sons.
50. Dos Santos, E.C., J.C. de Mendonça Silva, and H.A. Duarte, *Pyrite Oxidation Mechanism by Oxygen in Aqueous Medium*. *The Journal of Physical Chemistry C*, 2016. **120**(5): p. 2760-2768.
51. Stoner, E.C., *Collective Electron Ferromagnetism*. *Proceedings of the Royal Society of London A: Mathematical, Physical and Engineering Sciences*, 1938. **165**(922): p. 372-414.

## 4 Adsorption of Leaching Agents on Arsenopyrite

In natural environments, and especially in mining tailings, arsenopyrite surface is in contact with water, and the role of this molecule in the oxidation mechanism has not yet been investigated. The behavior of this mineral in aqueous medium is a step that must be investigated before any attempt to understand the mineral oxidation. In this context, first-principle calculations can contribute to the understanding of the arsenopyrite surface reactivity and allows a molecular study of the interaction surface/solution.

Pyrite, a similar sulfide mineral, has been extensively investigated by DFT/plane waves calculations, including the adsorption of water [1], H<sub>2</sub>S [2], and As(OH)<sub>3</sub> [3] on its surfaces, and its oxidation mechanism [4, 5]. Adsorption of water in different sulfides has also been investigated [6-8]. Chalcopyrite as well has been investigated about its surfaces and adsorption of leaching agents [9-12], showing that the adsorption of molecular water, chloride and sulfate is favorable on the (001) surface. However, to the best of our knowledge, no such study has been performed for arsenopyrite. Experimental studies focused on adsorption on arsenopyrite surface have also not been found. Therefore more information about the interaction of this mineral with leaching agents is necessary. For this reason the interaction of water and leaching agents such as HCl, and H<sub>2</sub>SO<sub>4</sub> with arsenopyrite surface was investigated in this work aiming to understand the behavior of this mineral surface in different media.

The parameters used previously for bulk calculations were kept in the surface, except for a cutoff energy of 30 Ry and a 2×2×1 **K**-point mesh sampling in order to reduce computational time in a larger system. All calculations were spin polarized on the iron surface atoms, except for the preliminary tests on (101) surface. A (2×2) unit cell slab model containing 96 atoms built from an optimized bulk structure was chosen for the surface, in order to avoid lateral interaction between the adsorbed molecules in the neighbor cells. A 15 Å of vacuum was applied to avoid interaction between slab layers. A slab with 12 atomic layers of thickness was used, since it has been shown in the last chapter that this assures the surface energy convergence within 0.01 J m<sup>-2</sup>. The slab was symmetric on top and bottom surfaces.

All adsorption energies were calculated using

$$\Delta E_{ads} = E_{sur+mol} - E_{sur} - E_{mol} \quad (4.1)$$

where  $\Delta E_{ads}$  is the adsorption energy,  $E_{sur+mol}$  is the total energy of the surface with the molecule adsorbed,  $E_{sur}$  is the total energy of the relaxed surface and  $E_{mol}$  is the total energy of the isolated molecule calculated in a box identical to the one used for the surface calculation.

## **4.1 Water Adsorption on Arsenopyrite Surface**

### **4.1.1 Water adsorption on (101) Surface**

In the early development of this project, the (101) surface was considered as the most favored in the cleavage of arsenopyrite [13, 14]. However, during the progress of this work, a more detailed analysis of the literature was carried out and it was observed that the determination of preferential cleavage was no consensus and, in some cases, the definition of the unit cell was not clearly defined in the studies [15-17]. Although this surface is not the preferred cleavage, preliminary results were obtained for it, which serve as a reference for more extensive investigations of other surfaces of arsenopyrite.

The process of arsenopyrite oxidation takes place in an aqueous medium. Therefore it is necessary to understand how its surface interacts with water. In this sense, we investigated the adsorption of a water molecule on the relaxed (101) surface. There are several possible adsorption sites on this surface (see Figure 4.1): two non-equivalent iron sites, one arsenic and one sulfur sites. The water molecule can also adsorb forming a bridge between two sulfur atoms, two arsenic or sulfur and arsenic atoms. According to the surface DOS, shown in Figure 4.2, the iron atom has empty states near the Fermi level capable of receiving electrons. That is, it is a Lewis acid site and, therefore, should be the preferred site for the adsorption of water. Recent theoretical studies of the interaction of water with chalcopyrite show that this site is preferential [10]. The remaining adsorption sites were also analyzed. These preliminary calculations were performed without spin-polarization, as it can be noticed by the DOS graph of Figure 4.2. In the last chapter a discussion about the

need of it was made and the new spin-polarized calculations performed for the adsorption of a water molecule in the next section will show the difference in results.

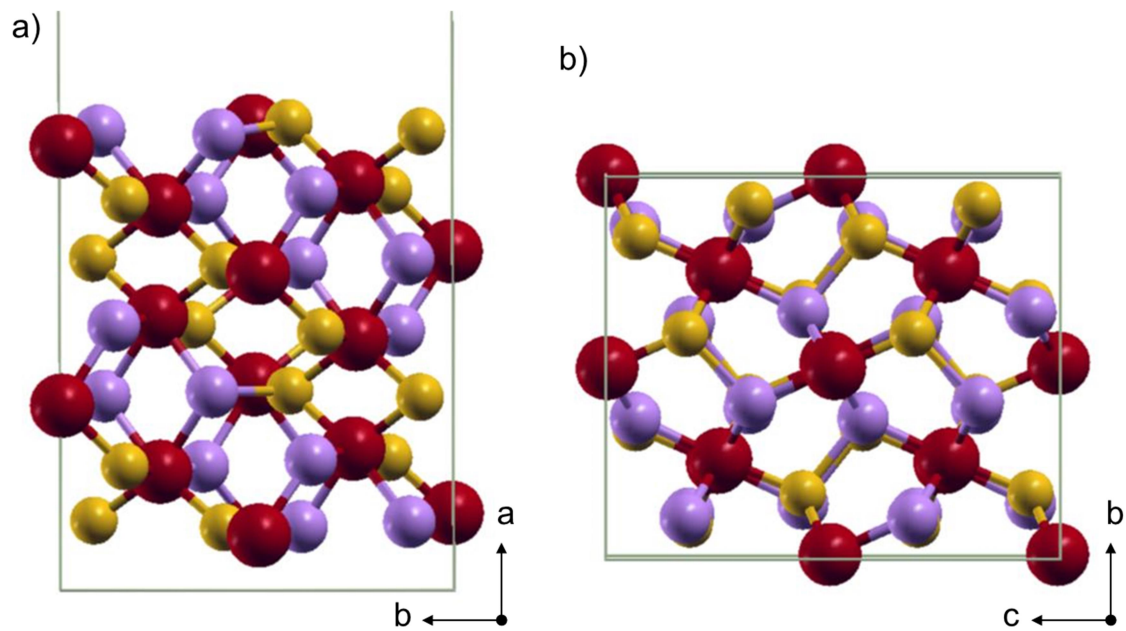


Figure 4.1: Arsenopyrite (101) surface. a) Side view and b) Top view. Brown is iron, purple is arsenic and yellow is sulfur.

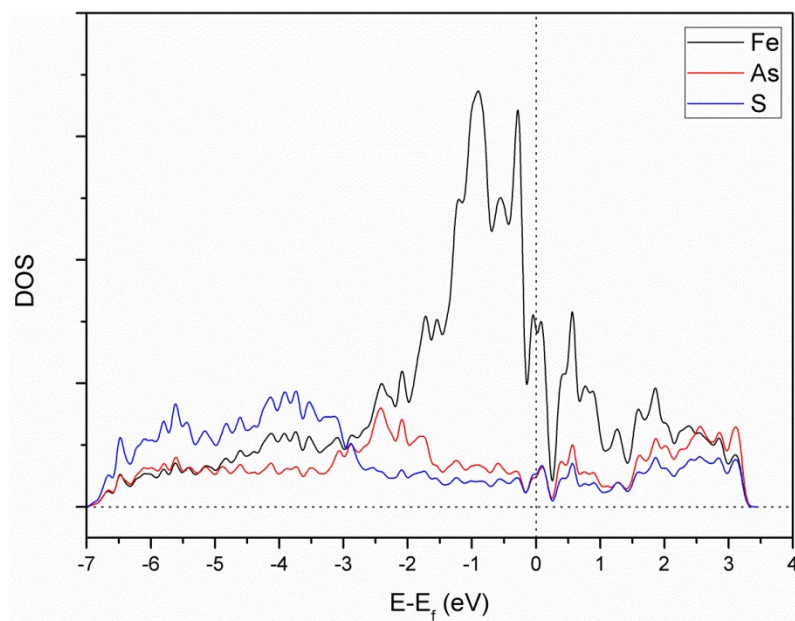


Figure 4.2: DOS projected over the (101) surface atoms.

The performed calculations indicate that the water molecule adsorbs onto the Fe site with Fe–O distance of 2.10 Å, as shown in Figure 4.3. The attempt of adsorption on the second iron site led to a dissociative final product, in which an OH<sup>-</sup> ion attached to an As atom with 1.83 Å distance and an H<sup>+</sup> ion attached to another As with distance 1.72 Å (Figure 4.4). The water molecule did not adsorb molecularly on top of the arsenic atom, leading to a structure with As–O distance equal to 2.97 Å (Figure 4.5). The same happened to the sulfur site, in which the S–H distance found was 2.64 Å (Figure 4.6), forming what could be a non-conventional hydrogen bond, although no evidence of bond formation was investigated [18].

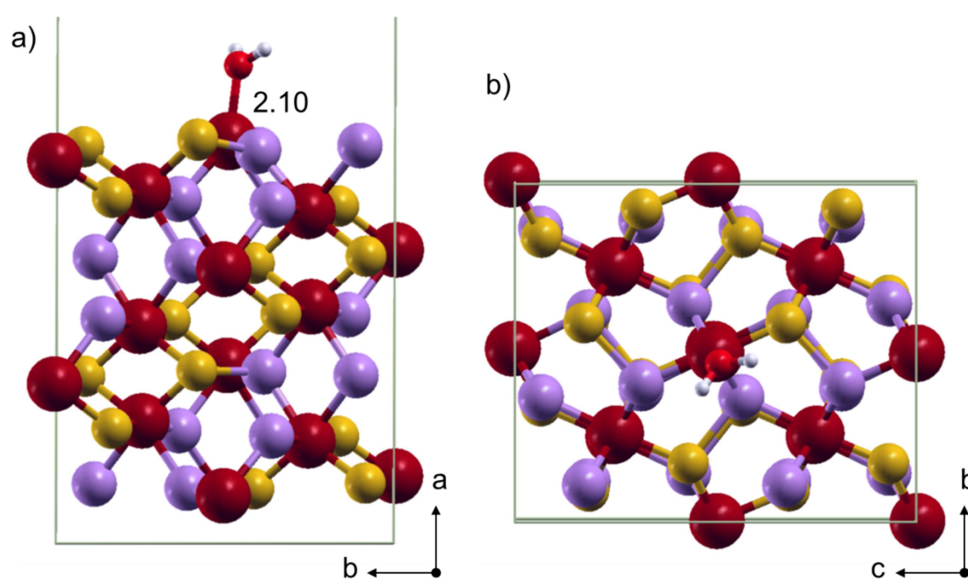


Figure 4.3: Adsorption of a water molecule to the iron site on arsenopyrite (101) surface. a) Side view and b) Top view. Brown is iron, purple is arsenic, yellow is sulfur, red is oxygen and white hydrogen.

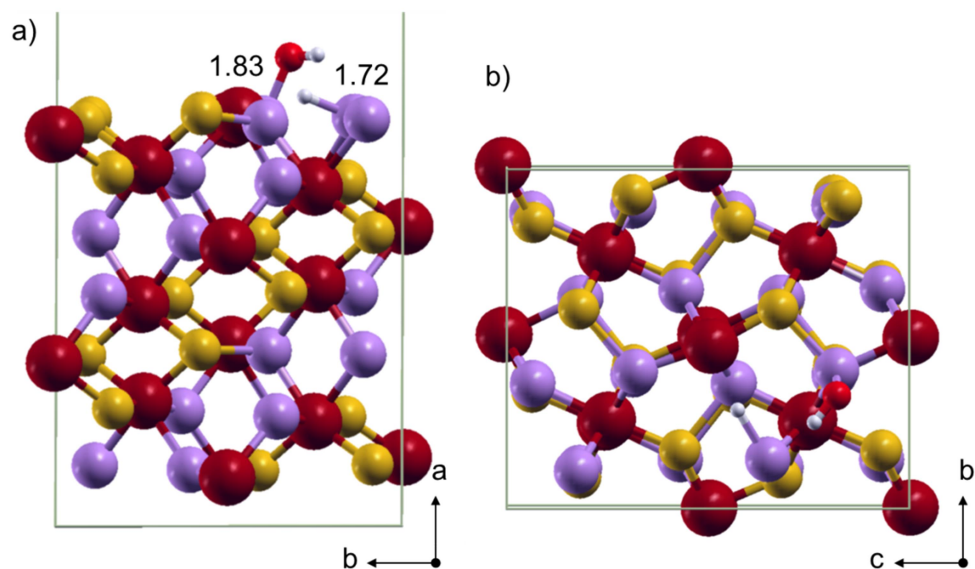


Figure 4.4: Dissociative adsorption of a water molecule on arsenopyrite (101) surface. a) Side view and b) Top view. Brown is iron, purple is arsenic, yellow is sulfur, red is oxygen and white hydrogen.

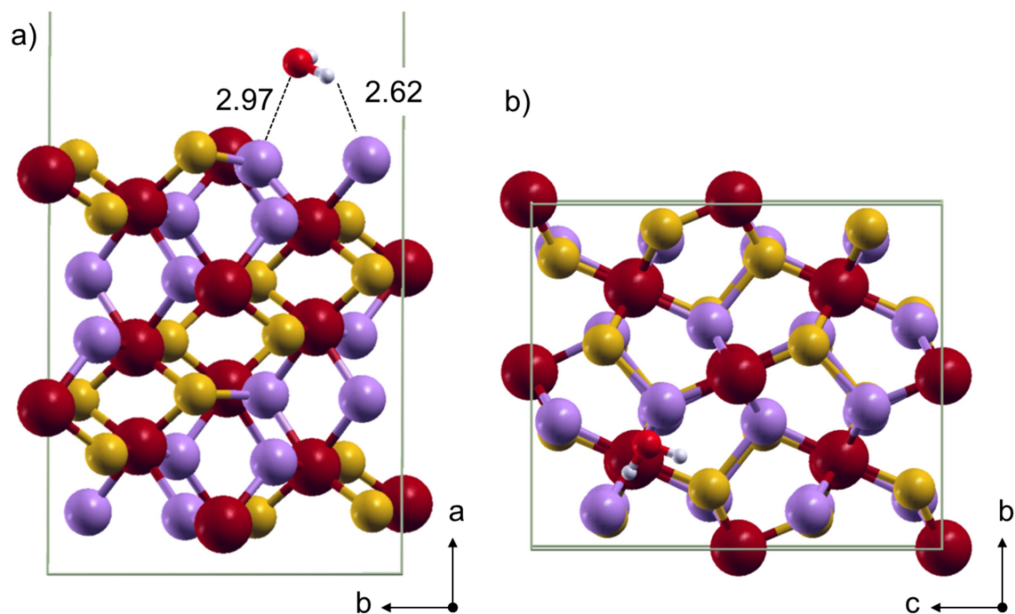


Figure 4.5: Adsorption of a water molecule to the arsenic site on arsenopyrite (101) surface. a) Side view and b) Top view. Brown is iron, purple is arsenic, yellow is sulfur, red is oxygen and white hydrogen.

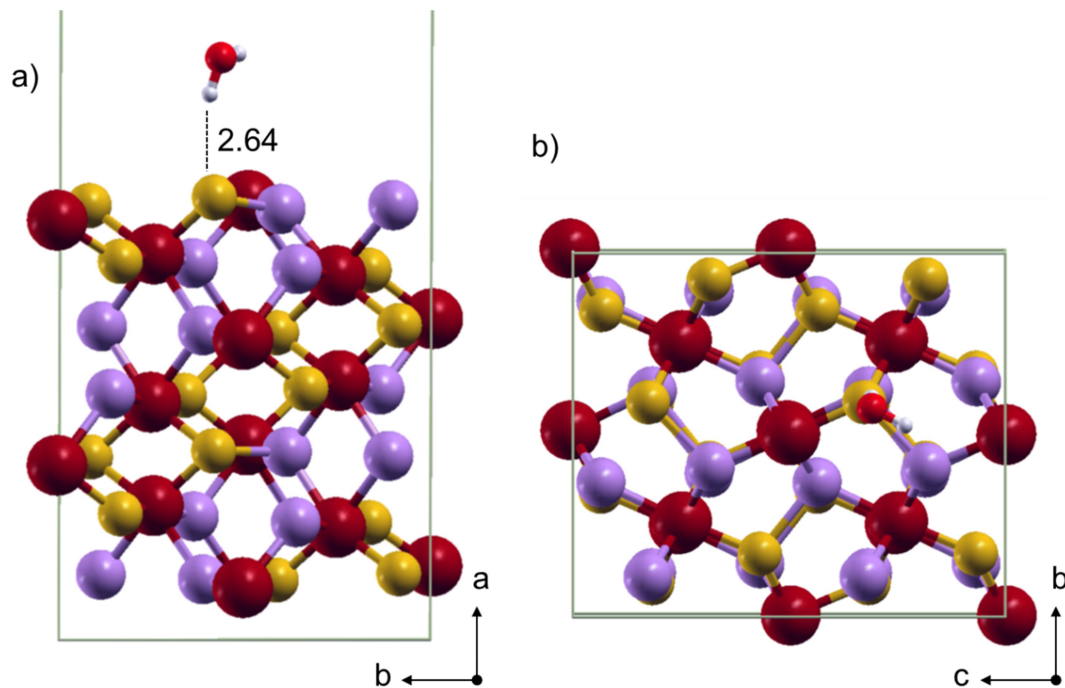


Figure 4.6: Adsorption of a water molecule to the sulfur site on arsenopyrite (101) surface. a) Side view and b) Top view. Brown is iron, purple is arsenic, yellow is sulfur, red is oxygen and white hydrogen.

Another form of water adsorption studied was it making hydrogen bond in a bridge between two neighbor arsenic atoms. The calculated As–H distances were 2.71 and 3.03 Å, shown in Figure 4.7. Similarly the water molecule was also adsorbed between two neighbor sulfur atoms (Figure 4.8) with S–H distances equal to 2.62 and 2.66 Å.

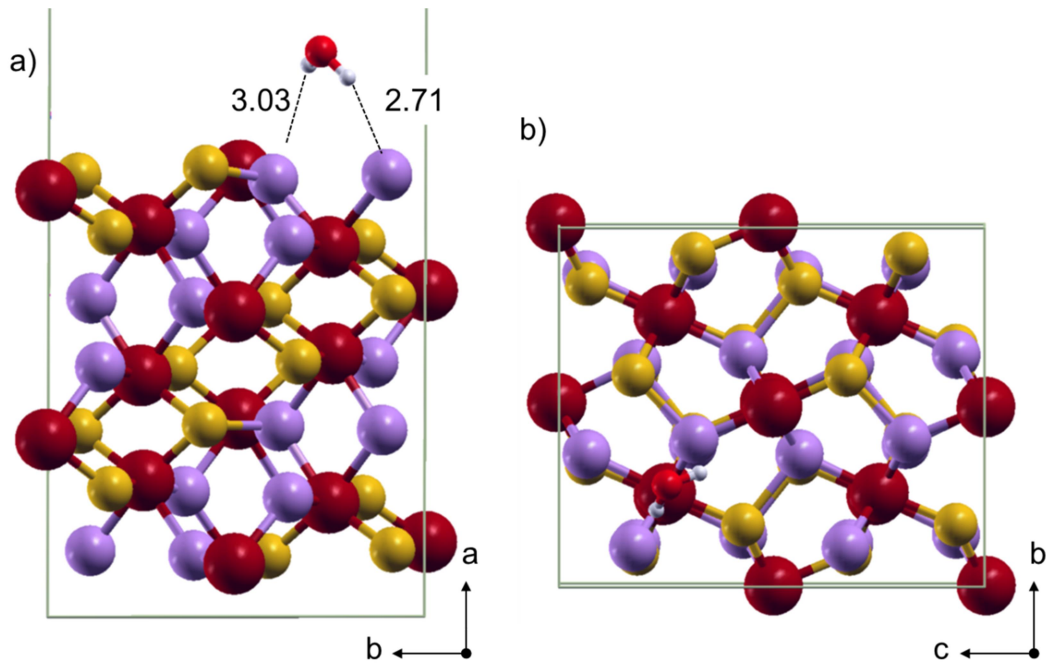


Figure 4.7: Adsorption of a water molecule to two neighbor arsenic atoms on arsenopyrite (101) surface. a) Side view and b) Top view. Brown is iron, purple is arsenic, yellow is sulfur, red is oxygen and white hydrogen.

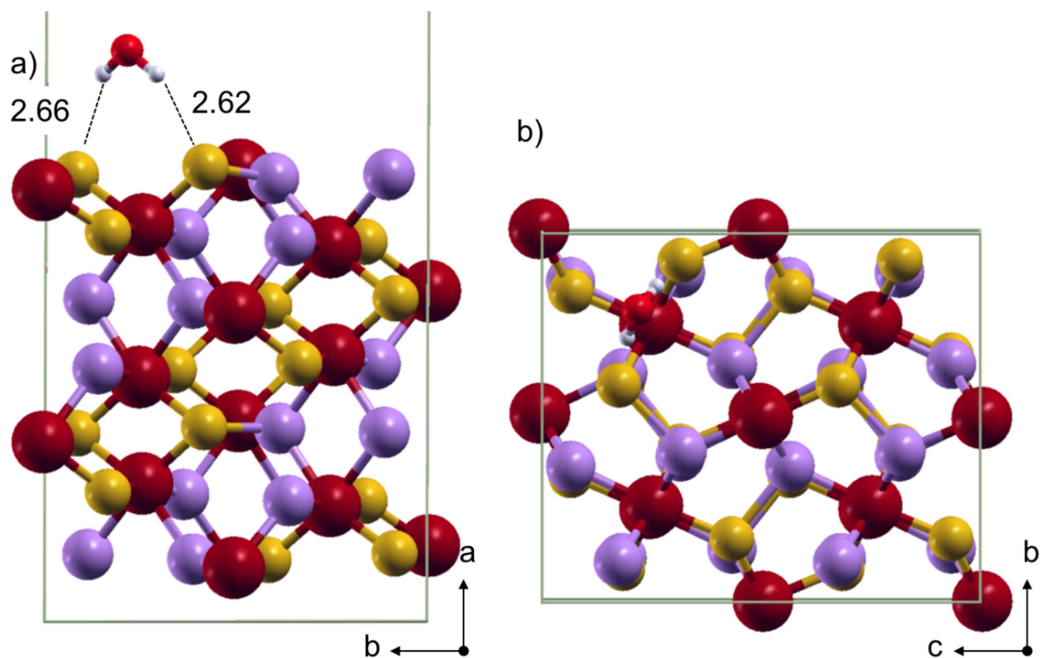


Figure 4.8: Adsorption of a water molecule to two neighbor sulfur atoms on arsenopyrite (101) surface. a) Side view and b) Top view. Brown is iron, purple is arsenic, yellow is sulfur, red is oxygen and white hydrogen.

The possibility of adsorption of a water molecule between an arsenic and a sulfur atom was also investigated. In Figure 4.9, the distances found were: 3.14 Å for As–H and 2.63 Å for S–H distances. The As–S bond increased slightly from 2.37 Å to 2.38 Å.

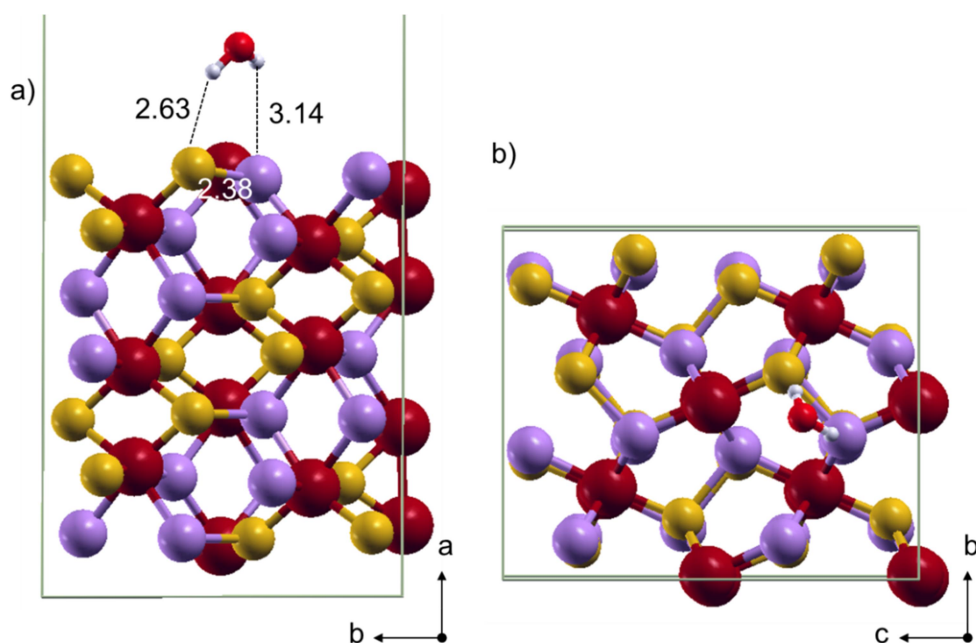


Figure 4.9: Adsorption of a water molecule to two neighbor arsenic and sulfur atoms on arsenopyrite (101) surface. a) Side view and b) Top view. Brown is iron, purple is arsenic, yellow is sulfur, red is oxygen and white hydrogen.

The adsorption energy calculated for water on the iron site was  $-12.1 \text{ kcal mol}^{-1}$ , more favorable than the adsorption energy on the As site,  $-2.8 \text{ kcal mol}^{-1}$  and the S site  $-1.9 \text{ kcal mol}^{-1}$ . For the other positions, similar values of adsorption energy were found:  $-2.3 \text{ kcal mol}^{-1}$  for the bridge between the As atoms,  $-3.0 \text{ kcal mol}^{-1}$  for the bridge between the S atoms and  $-1.7 \text{ kcal mol}^{-1}$  for the bridge between the As and S atoms. The dissociative adsorption investigated was unfavorable, with adsorption energy of  $13.4 \text{ kcal mol}^{-1}$ .

#### 4.1.2 Water adsorption on (001) Surface

Arsenopyrite (001) surface was shown in the previous chapter to be the most favorable cleavage surface. It is formed by breaking Fe–As and Fe–S axial bonds,

exposing all three types of atoms, as shown in Figure 4.10. In this surface formation, there is a small relaxation changing the initial bulk atomic positions, in which the largest bond change was 0.14 Å in a surface Fe–As bond. Different from pyrite, FeS<sub>2</sub>, the Fe sites on this surface are not all equivalents. There are two different iron sites on the surface: Fe1, more exposed and more distant from the next Fe atom, and Fe2, less exposed and closer to the next Fe atom, as shown in Figure 4.11. All Fe1 sites have similar chemical environment, as well as all Fe2 sites.

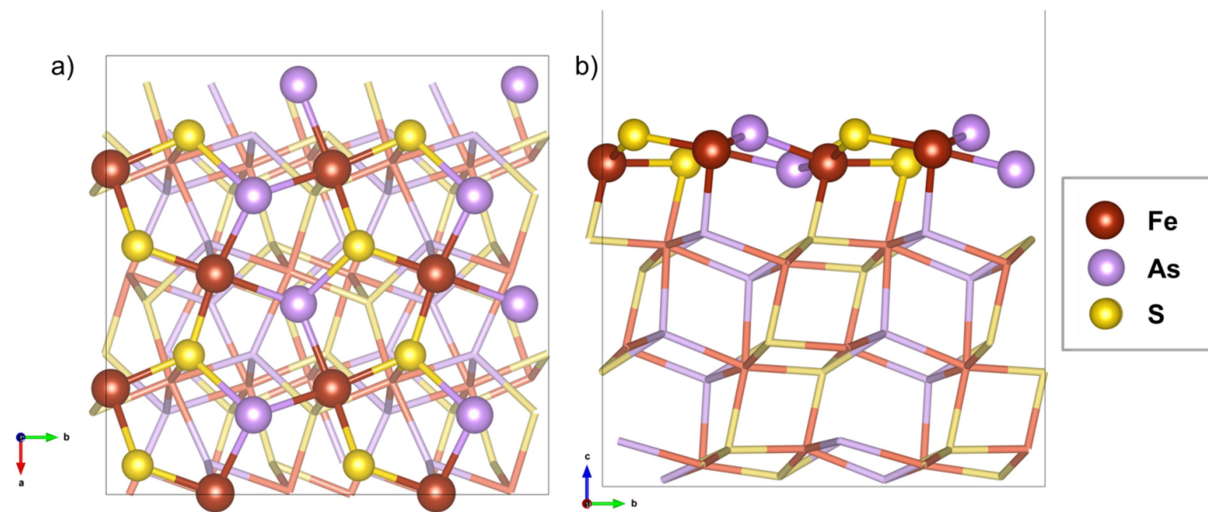


Figure 4.10: Arsenopyrite (001) surface: a) top view; b) side view.

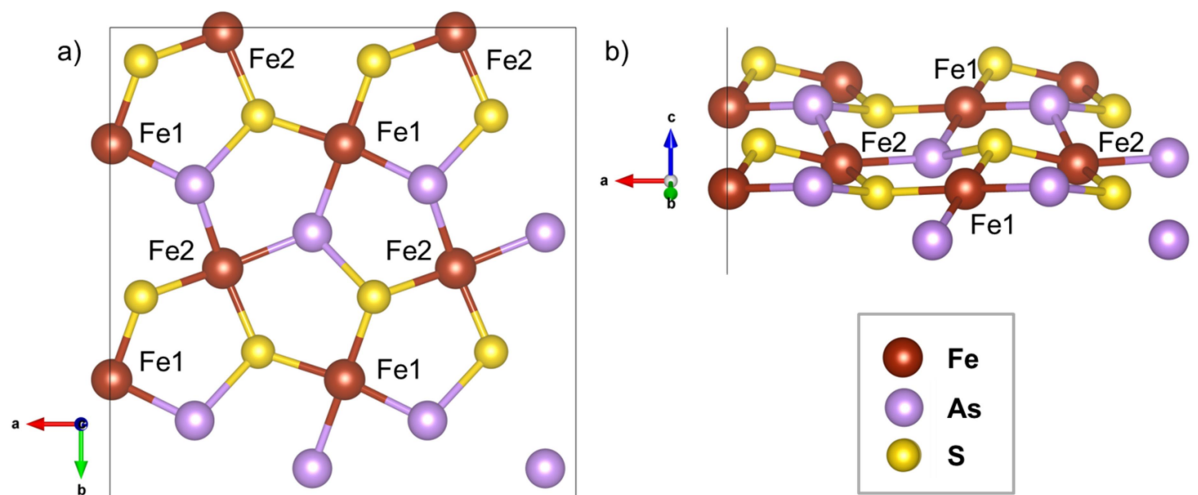


Figure 4.11: First layer of atoms in arsenopyrite (001) surface showing the two different Fe sites: Fe1, more exposed, and Fe2, less exposed. a) top view; b) side view.

According to Figure 3.22, page 70, the Fe atom is the most favorable site to adsorb a water molecule on arsenopyrite (001) surface, whereas the valence and conduction bands are dominated by this atom. Therefore a lone pair of electrons from an oxygen atom can be received by the iron atom, which acts as a Lewis acid. Since there are two different iron sites on the surface, the adsorption of one water molecule was tested on both.

After optimization of the water molecule in different starting positions, the most stable structures obtained are shown in Figure 4.12. In Figures 4.12a and 4.12b the water molecule is attached to a Fe1 adsorption site with estimated adsorption energy of  $-10.8 \text{ kcal mol}^{-1}$  and Fe–O distance of  $2.16 \text{ \AA}$ . This energy value is slightly higher than the  $-13 \text{ kcal mol}^{-1}$  adsorption energy and the Fe–O distance longer than the  $2.12 \text{ \AA}$  calculated by Stirling *et al.* [1] for pyrite using Car-Parrinello Molecular Dynamics (CPMD). This difference might be due to different methodology used or to a stronger interaction between pyrite and water. In fact, calculations for water adsorption on pyrite using the same methodology applied for FeAsS, in which  $E_{\text{ad}} = -16.1 \text{ kcal mol}^{-1}$  present in Table 4.8, page 105, show that a water molecule adsorbs stronger on pyrite surface than on arsenopyrite. For chalcopyrite [10], the adsorption is even stronger,  $-22.8 \text{ kcal mol}^{-1}$ , although the Fe–O distance is longer,  $2.38 \text{ \AA}$ . A hydrogen bond of  $2.62 \text{ \AA}$  was formed between one H atom of the water molecule and an As atom of the surface, similar to the longest hydrogen bond calculated for pyrite,  $2.698 \text{ \AA}$  [1]. The effect of this adsorption on arsenopyrite surface is presented in Table 4.1, where the bond lengths are analyzed compared to the pristine surface. On the As–S bonds, which are the strongest ones in the system, the changes are negligible. However it increases the distances of Fe–As and Fe–S bonds, especially on the Fe–As axial bond, which happens between the first and second layers of the mineral surface. The reason is the reception of a lone electron pair from the oxygen by the iron atom, probably in an anti-bonding orbital, that weakens all the other bonds, especially the one related to the water by an inversion operation. The effect of the adsorption on the water molecule is an O–H bond  $0.014 \text{ \AA}$  longer in the direction of the hydrogen bond with As, compared to the molecule calculated in vacuum, and a  $1.9^\circ$  wider  $\angle \text{H–O–H}$  angle. In Figures 4.12c and d, the adsorption energy on the Fe2 site was less favorable,  $-5.0 \text{ kcal mol}^{-1}$ , and

Fe–O distance longer, 2.22 Å. The hydrogen bond with an As atom is also longer compared to the adsorption on Fe1 site, 2.64 Å.

Table 4.1: Atomic distances on arsenopyrite (001) surface as effect of water adsorption. All distances are in Å.

	Pristine surface	Molecular	Dissociative	Full coverage
Fe – As*	2.323	2.376	2.416	2.372
Fe – S*	2.202	2.222	2.242	2.226
Fe – As axial	2.308	2.387	2.520	2.384*
As – S*	2.374	2.377	2.373	2.379
Fe – O	-	2.155	1.811	2.195*

\*Average of the bonds around the adsorbed atom.

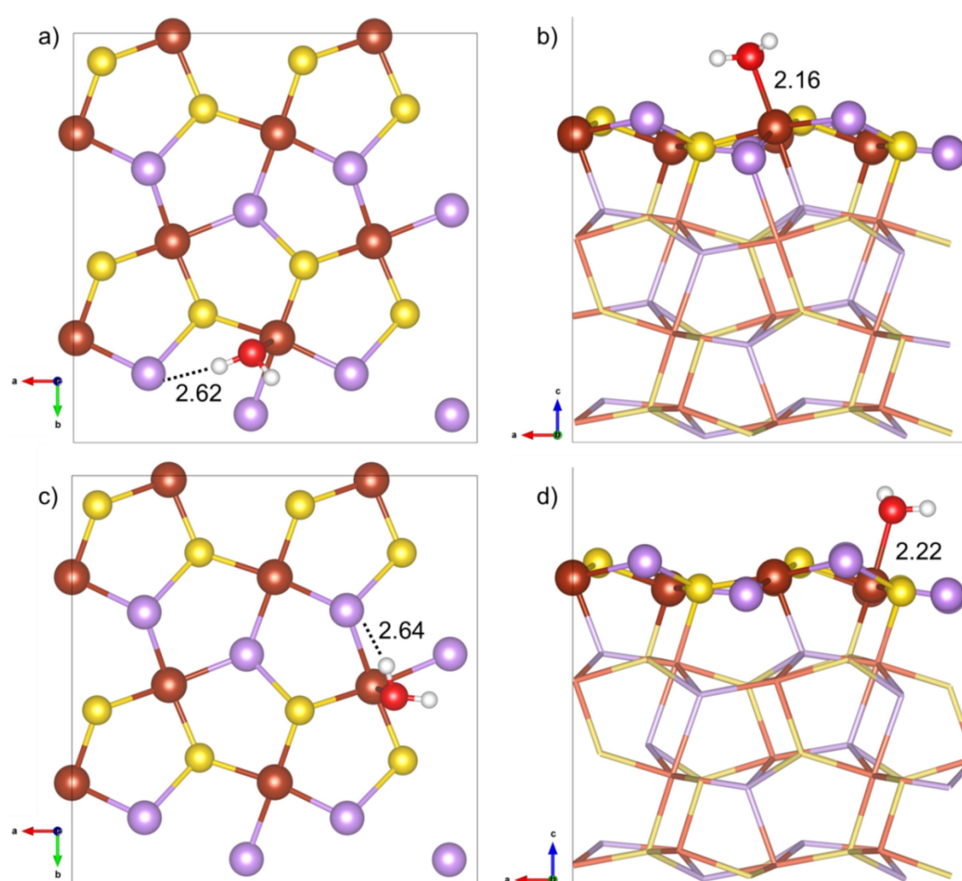


Figure 4.12: Adsorption of one water molecule on two different Fe sites on the (001) arsenopyrite surface: a) Fe1 top view; b) Fe1 side view; c) Fe2 top view; Fe2 side view. Yellow atoms are sulfur, purple are arsenic, brown are iron, red are oxygen and white are hydrogen.

For the sake of comparison, a water molecule was also adsorbed on a Fe site on the other reported cleavage (100), (110) and (101) surfaces, as shown in Figure 4.13. On (100) surface, the adsorption energy was  $-7.7 \text{ kcal mol}^{-1}$  and the Fe–O distance  $2.19 \text{ \AA}$ . On (110) the adsorption energy was  $-17.4 \text{ kcal mol}^{-1}$  and the Fe–O distance  $2.11 \text{ \AA}$ . On (101) surface, the adsorption energy was  $-14.6 \text{ kcal mol}^{-1}$ , more stable than the value of  $-12.1 \text{ kcal mol}^{-1}$  obtained in the previous spin compensated calculations, and the Fe–O distance also  $2.11 \text{ \AA}$ . The lower energies and bond lengths of the water adsorption on the (110) and (101) surfaces compared to (001) can be explained by the fact that these surfaces are less stable, therefore, more reactive than the (001) surface. These calculations indicated that the adsorption energy can vary up to  $7 \text{ kcal mol}^{-1}$  depending on the surface exposed and, in a natural sample, more than one surface can be exposed. However in this work we concentrated on (001), which is predicted to be the most stable one, consequently, expected to be the most available surface in the mineral.

The water adsorption was also tested on As and S sites, shown in Figure 4.14, page 88. The molecule kept a distance of around  $3 \text{ \AA}$  from the surface and very low adsorption energies were found: As site:  $-1.5 \text{ kcal mol}^{-1}$ ; As and S sites:  $-2.2 \text{ kcal mol}^{-1}$ ; S site:  $-1.2 \text{ kcal mol}^{-1}$ . The H–As or H–S distances are long and require an investigation of its nature in order to be considered as a hydrogen bond [18]. These results show that this type of adsorption is not favorable, as expected.

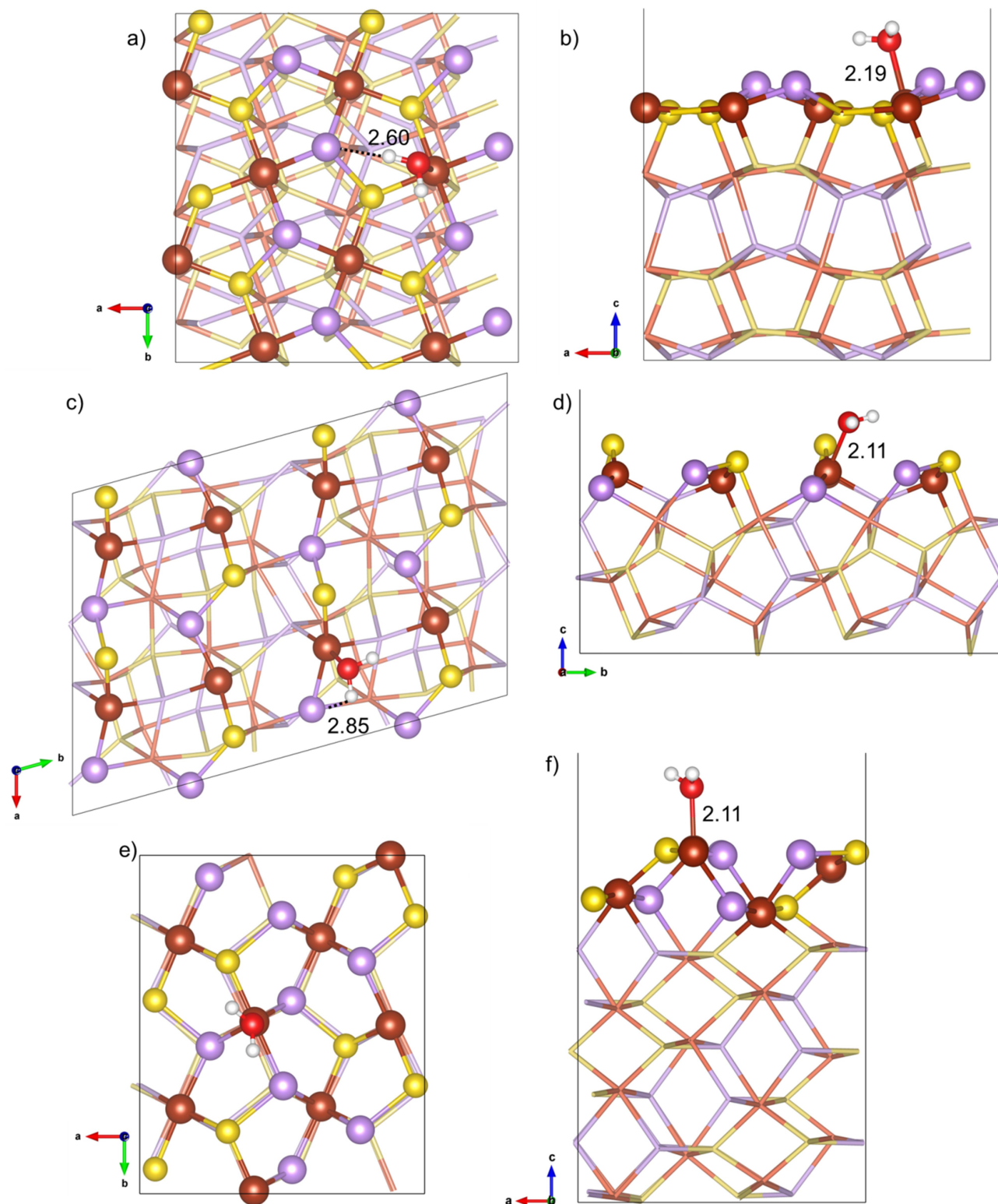


Figure 4.13: Adsorption of one water molecule on Fe sites on (100), (110) and (101) arsenopyrite surfaces: a) (100) top view; b) (100) side view; c) (110) top view; d) (110) side view; e) (101) top view; (101) side view. Yellow atoms are sulfur, purple are arsenic, brown are iron, red are oxygen and white are hydrogen.

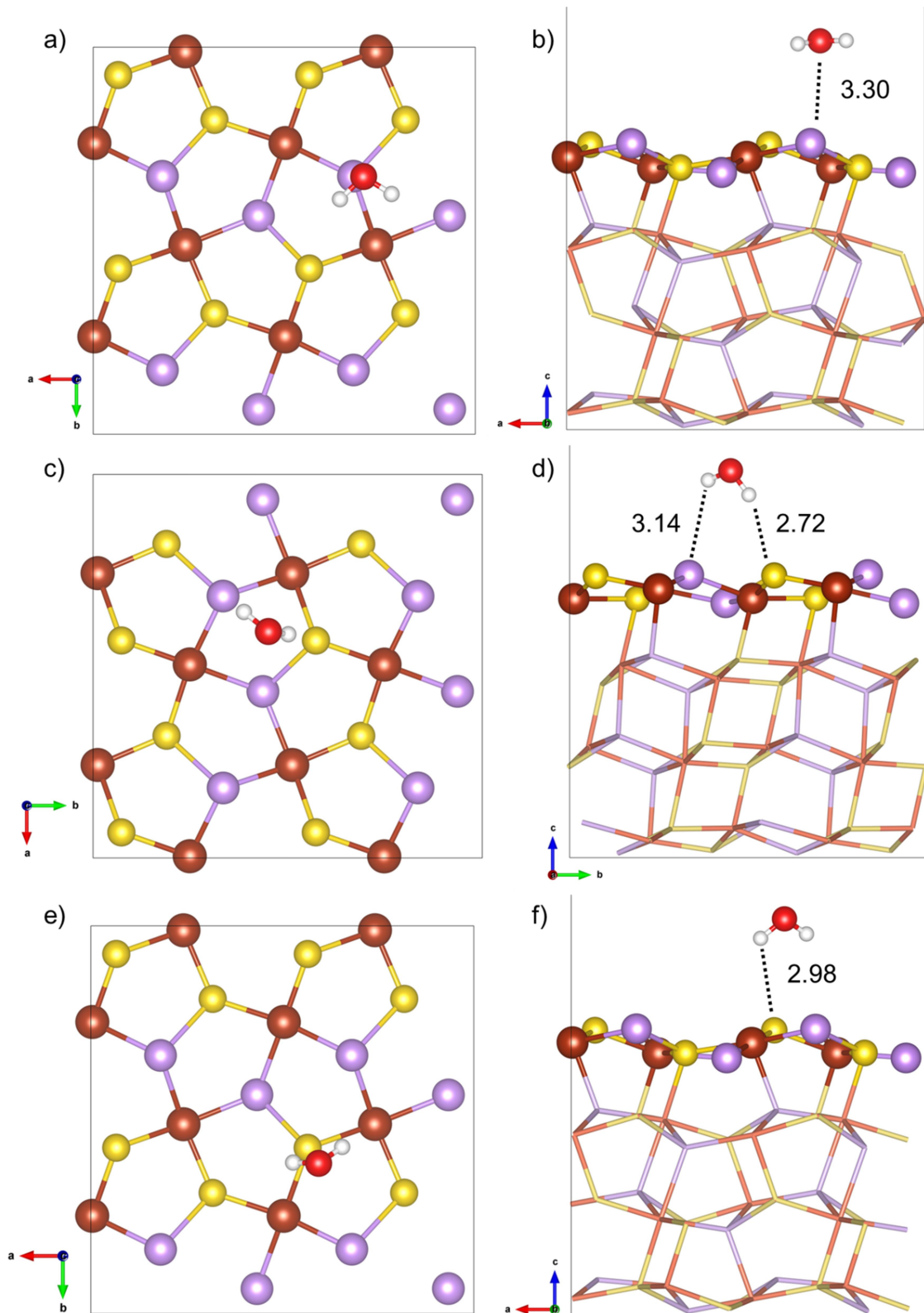


Figure 4.14: Adsorption of one water molecule on the As and S sites of (001) arsenopyrite surface: a) and b) As site; c) and d) As and S sites; e) and f) S site. Yellow atoms are sulfur, purple are arsenic, brown are iron, red are oxygen and white are hydrogen.

The dissociative adsorption of one water molecule on the surface resulted in a positive adsorption energy structure, i.e., not stable. The reason is that in this process a strong O–H bond is broken in order to form weaker S–H or As–H bonds. Figures 4.15a and 4.15b show the dissociation of a water molecule in which the OH is adsorbed on the Fe site and the hydrogen is adsorbed on the As site, yielding 4.8 kcal mol<sup>-1</sup> of adsorption energy. This value is lower than the one calculated by Stirling *et al.* [1] for pyrite, 19 kcal mol<sup>-1</sup>, which might mean that the S–H bond is weaker than the As–H. The Fe–O distance found in this case for arsenopyrite, 1.81 Å was also smaller than for pyrite, 2.01 Å. The effect of this kind of adsorption on the surface was also analyzed and the results are present on Table 4.1, page 85. As in the case of molecular adsorption, the dissociative adsorption does not lead to significant changes on the As–S bonds, but increases the distances between Fe and the other atoms, more effectively than in the case of molecular adsorption. Figures 4.15c and 4.15d show a similar situation, in which the H atom is adsorbed on the S site, yielding 10.4 kcal mol<sup>-1</sup> of adsorption energy. This higher value is expected since the calculated dissociated water adsorption energy at FeS<sub>2</sub> is also higher. In both cases of arsenopyrite, the adsorbed H atoms do not make hydrogen bond with the adsorbed O, due to the long distance between these atoms. Other sites for the H adsorption were tested, but they were even less favorable, as shown in Table 4.2 and Figures 4.16 and 4.17. The adsorption of OH on the Fe2 site was even less favorable, requiring 17.2 kcal mol<sup>-1</sup> of energy, see Figure 4.18. Therefore the dissociative adsorption of water on arsenopyrite surface, as well as on pyrite, is unlikely to happen. For chalcopyrite [10], DFT calculations using numerical basis sets indicated that this adsorption was possible, yielding up to -8.97 kcal mol<sup>-1</sup> of adsorption energy, although the calculated Fe–O distance was longer (about 1.94 Å) than for arsenopyrite.

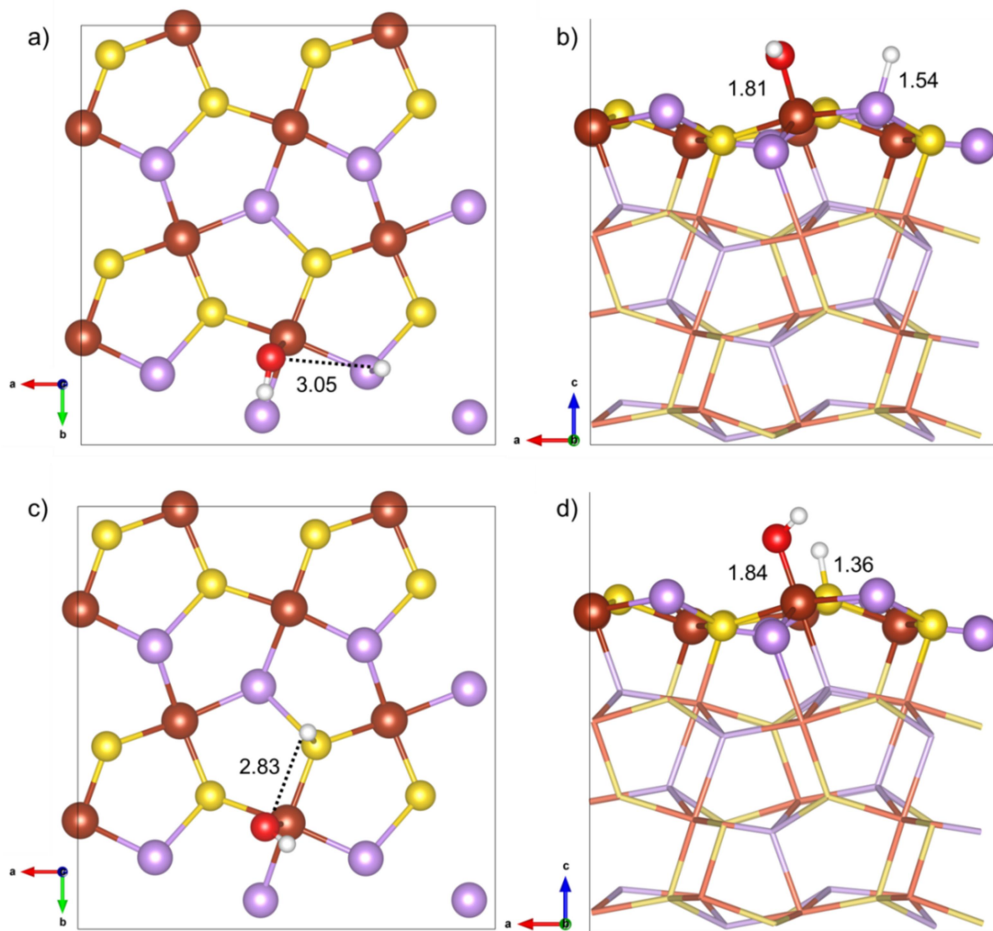


Figure 4.15: Dissociative adsorption of one water molecule, in which the OH group bounds to an Fe1 site and the H atom bounds to a) As and b) S and c) Fe1 and d) S. Yellow atoms are sulfur, purple are arsenic, brown are iron, red are oxygen and white are hydrogen.

Table 4.2: Dissociative adsorption of water on arsenopyrite surface. All energies are in kcal mol<sup>-1</sup>.

Structure	Adsorption Energy	Site of H adsorption
Figure 4.16a	6.8	As
Figure 4.16c	5.8	As
Figure 4.16e	5.2	As
Figure 4.17a	13.1	S
Figure 4.17c	13.5	S
Figure 4.17e	13.0	S
Figure 4.17g	34.1	S

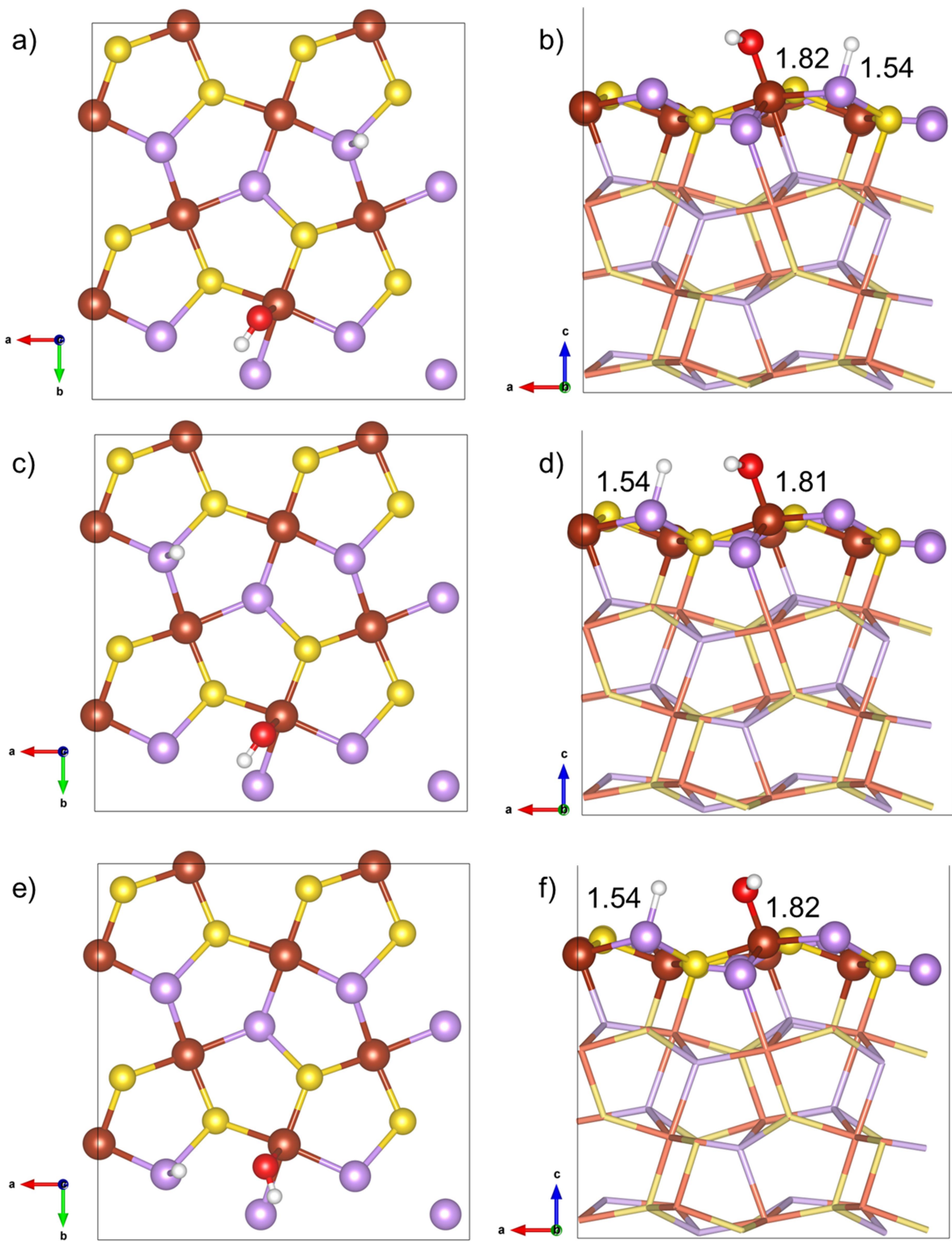


Figure 4.16 Dissociative adsorption of one water molecule, in which the OH group bounds to an Fe1 site and the H atom bounds to an As atom. Yellow atoms are sulfur, purple are arsenic, brown are iron, red are oxygen and white are hydrogen.

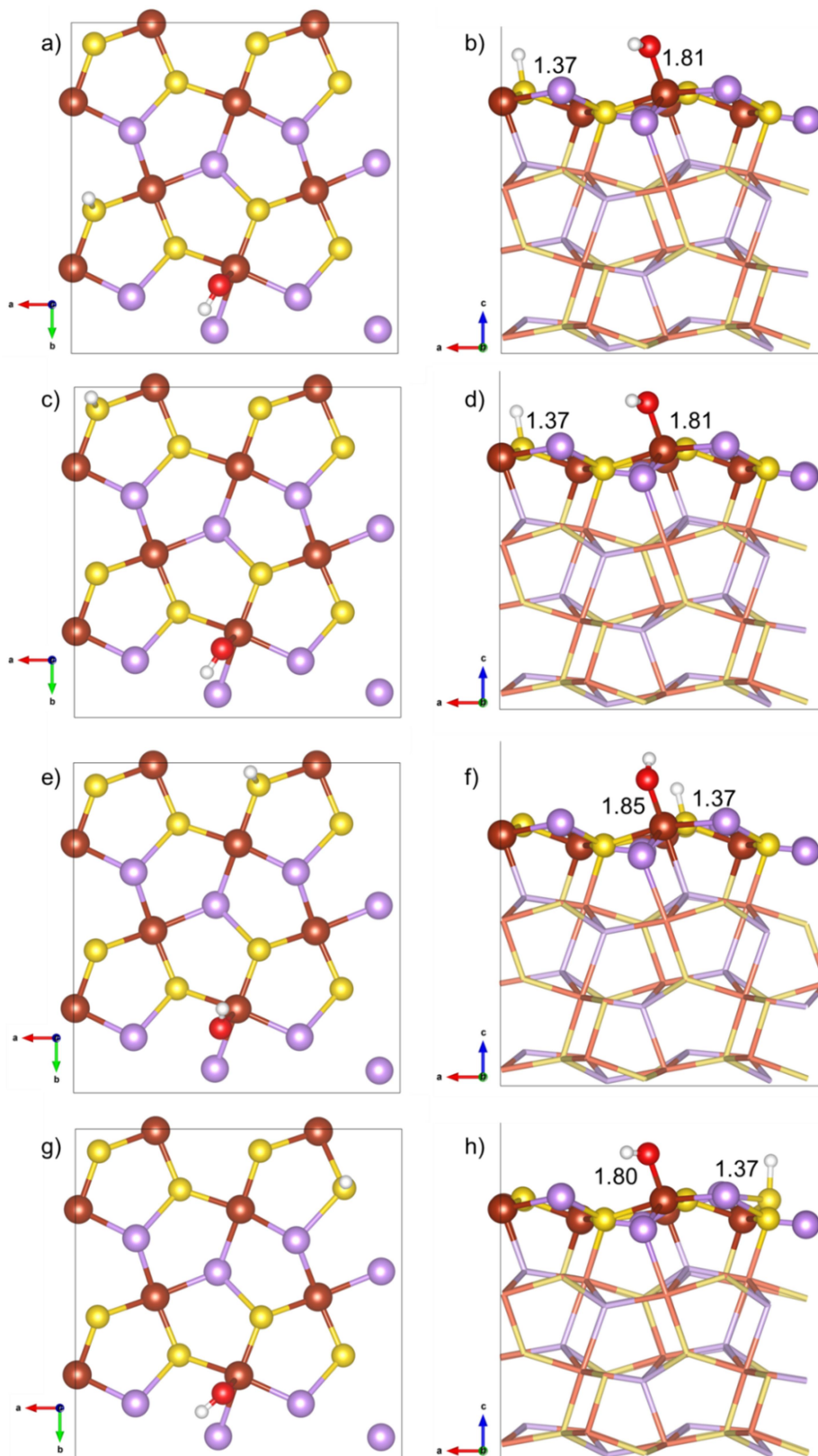


Figure 4.17: Dissociative adsorption of one water molecule, in which the OH group bounds to a Fe1 site and the H atom bounds to a S atom. Yellow atoms are sulfur, purple are arsenic, brown are iron, red are oxygen and white are hydrogen.

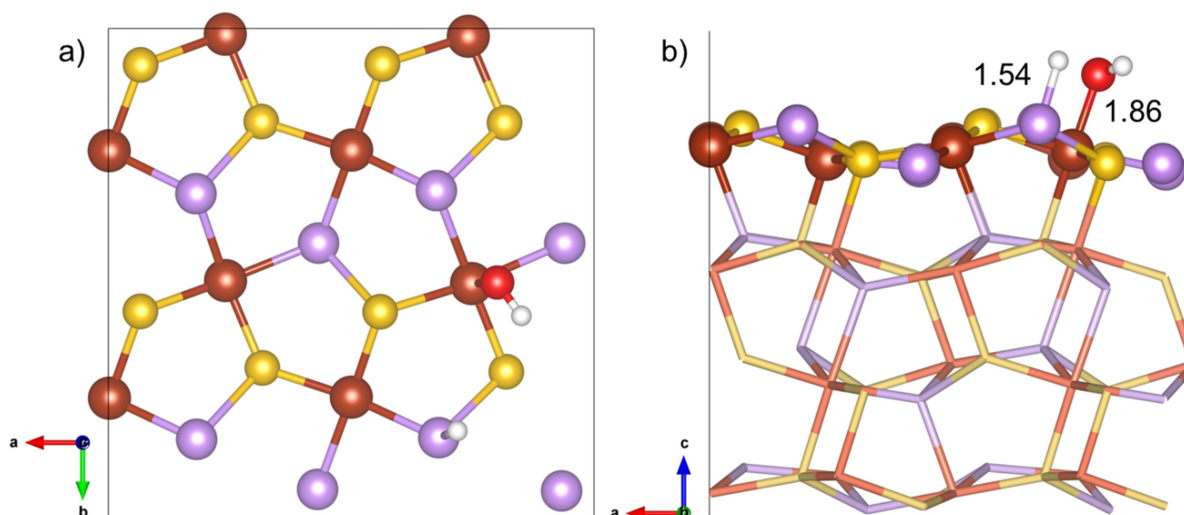


Figure 4.18: Dissociative adsorption of one water molecule, in which the OH group bounds to a Fe2 site and the H atom bounds to a As atom. Yellow atoms are sulfur, purple are arsenic, brown are iron, red are oxygen and white are hydrogen.

The model considered for the (001) arsenopyrite surface has 8 Fe sites (4Fe1 and 4Fe2), that could adsorb up to 8 water molecules in a full surface coverage. This adsorption structure was optimized using the optimal geometry of one water molecule repeated on the other Fe adsorption sites on the surface as starting point. After relaxation, only 4 molecules could keep adsorbed to the Fe surface atoms, while the other 4 molecules preferred to bind to the first ones through hydrogen bonds, forming a second solvation layer, as shown in Figure 4.19. This modification was also reported for the full water adsorption on chalcopyrite surfaces [10]. But in the case of arsenopyrite it is due to the existence of two different Fe sites. The full water coverage on the surface led to an adsorption energy per molecule not much different from that of a single molecule. The adsorption energy per water molecule is slightly lower ( $-0.6 \text{ kcal mol}^{-1}$ ) to that case:  $-11.4 \text{ kcal mol}^{-1}$ . For pyrite [19], the full coverage adsorption energy was higher than that for a single molecule, although more hydrogen bonds are formed. Nevertheless, de Leeuw *et al.* [20], using model potential, predicted a lower energy for the full monolayer water adsorption, which agrees with our results. For chalcopyrite, the most stable configuration of the full covered surface was  $2 \text{ kcal mol}^{-1}$  lower in energy than the adsorption of a single molecule, similar to our calculations. However, the Fe–O distance in chalcopyrite was shorter for the full coverage than for the single molecule adsorption, in slight

disagreement with our results, which was 0.03 Å longer. The effect of the full water coverage adsorption on FeAsS surface bonds is similar to the situation of a single molecule adsorption, see Table 4.1, page 85. If only 4 water molecules are adsorbed on all Fe1 sites, the adsorption energy per molecule is practically the value of a single molecule:  $-10.7 \text{ kcal mol}^{-1}$  (Figure 4.20).

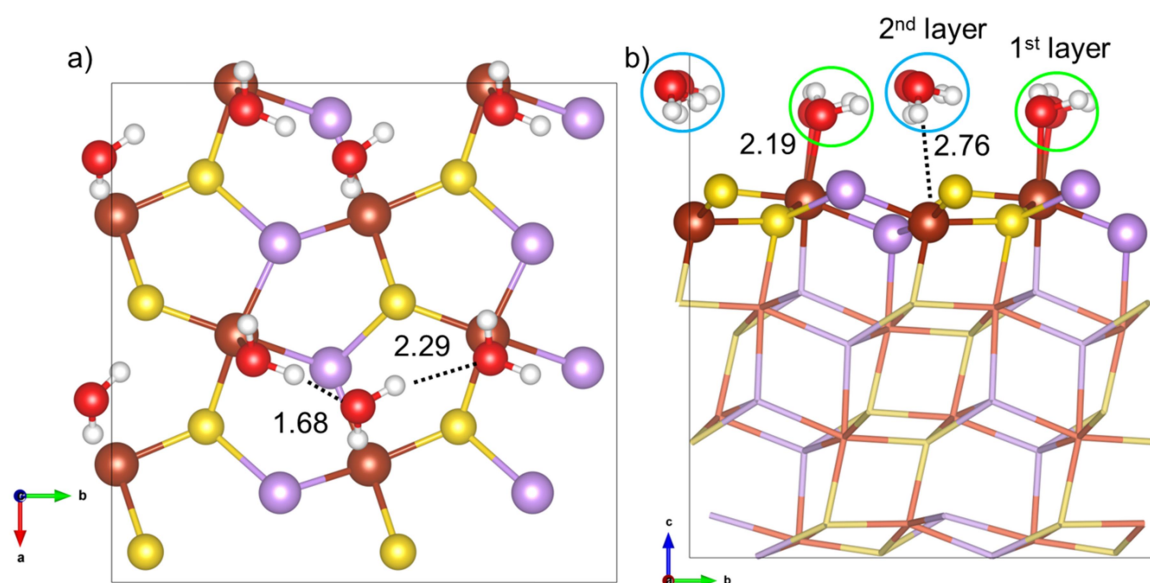


Figure 4.19: Optimized structure of 8 water molecules adsorbed on arsenopyrite (001) surface forming two solvation layers. Yellow atoms are sulfur, purple are arsenic, brown are iron, red are oxygen and white are hydrogen.

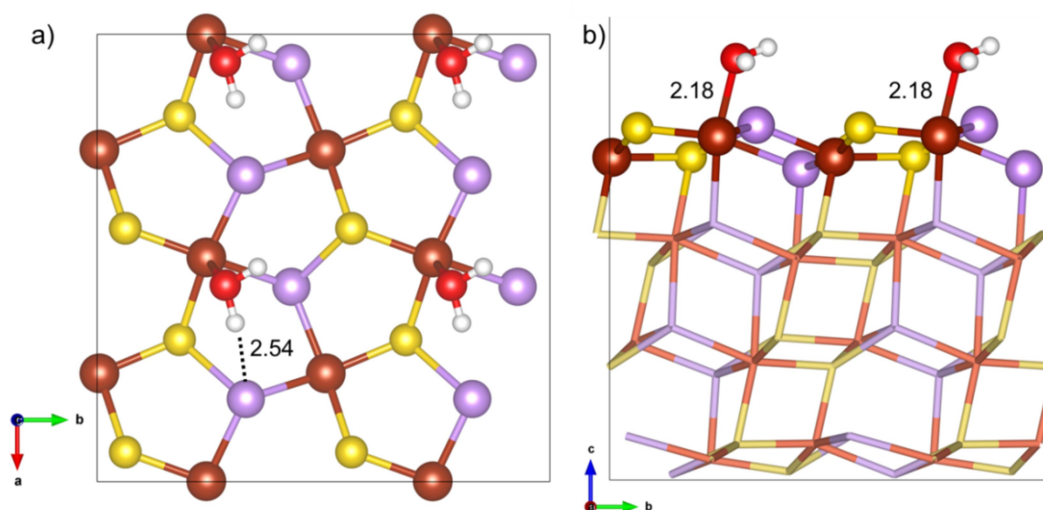


Figure 4.20: Optimized structure of 4 water molecules adsorbed on arsenopyrite (001) surface. Yellow atoms are sulfur, purple are arsenic, brown are iron, red are oxygen and white are hydrogen.

Table 4.3 presents the results of water adsorption compared for different sulfides in different studies. Rosso *et al.* [21] used atomic clusters and localized basis functions for pyrite. Steele *et al.* [22] used DFT/PW approach for ZnS. Chen *et al.* [8] also used DFT/PW for FeS<sub>2</sub> and PbS. Zhao *et al.* [6] DFT/PW for FeS<sub>2</sub>, ZnS, PbS and MoS<sub>2</sub>. All sulfides analyzed, except molybdenite, could adsorb a water molecule in a higher or lower degree, although Chen *et al.* [8] also argument that water prefers to bind to another water molecule than to the PbS surface. This table shows how the methodology choice might change the results; therefore it is a very important aspect of the study.

Table 4.3: Adsorption Energy of water calculated for different sulfide surfaces.

Sulfide	Adsorption Energy/ kcal mol <sup>-1</sup>
FeS <sub>2</sub> [1]	-12.9
FeS <sub>2</sub> [21]	-50.8, -57.8
FeS <sub>2</sub> [6]	-17.0
FeS <sub>2</sub> [8]	-13.4
ZnS [6]	-5.8
ZnS [22]	-17.8
PbS [6]	-2.1
PbS [8]	-7.0
MoS <sub>2</sub> [6]	0.48
CuFeS <sub>2</sub> [10]	-22.8
FeAsS	-10.8

## 4.2 Adsorption of HCl

Other leaching agents were also tested according to the adsorption on arsenopyrite (001) surface. HCl is a strong acid, which means that it will be dissociated in H<sup>+</sup> and Cl<sup>-</sup> in aqueous solution. Therefore it is expected that these ions will adsorb dissociatively to the arsenopyrite surface, which is in agreement with our results, as shown in Figure 4.21. The adsorption energy is -11.3 kcal mol<sup>-1</sup> when the

$\text{H}^+$  ion binds to an As and  $-6.5 \text{ kcal mol}^{-1}$  when the  $\text{H}^+$  binds to a S atom. The Fe–Cl distances are similar to Fe–O distances in adsorbed water. Again, even though the adsorption energy of HCl on chalcopyrite surface [10] was lower ( $-21.2 \text{ kcal mol}^{-1}$ ) than on arsenopyrite, the Fe–Cl distance was longer ( $2.34 \text{ \AA}$ ). The adsorption of this species causes an elongation of the bonds on arsenopyrite surface, especially the Fe–As axial (Table 4.4). Probably the  $\text{Cl}^-$  ion donates electron density to the Fe atom, weakening the bonds related to this atom. On the As–S bond again the effect is small. The adsorption of  $\text{Cl}^-$  on Fe2 site was less stable than on Fe1, as expected, yielding  $-7.3 \text{ kcal mol}^{-1}$ , and the Fe–O distance  $0.12 \text{ \AA}$  longer (Figure 4.22).

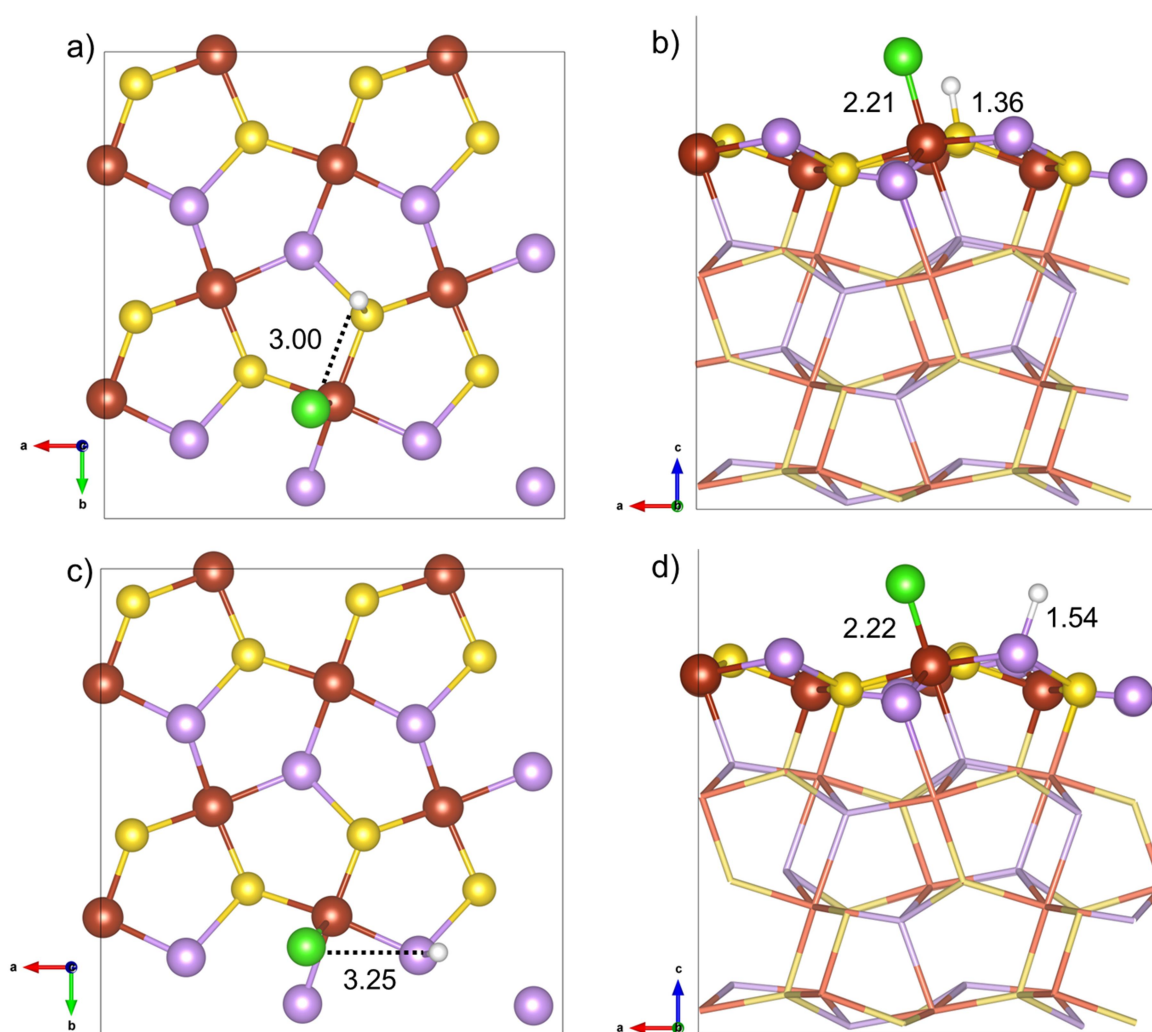


Figure 4.21: Dissociative adsorption of HCl on arsenopyrite (001) surface: a), b) on Fe1 and S sites c), d) on Fe1 and As sites. Yellow atoms are sulfur, purple are arsenic, brown are iron, green are chlorine and white are hydrogen.

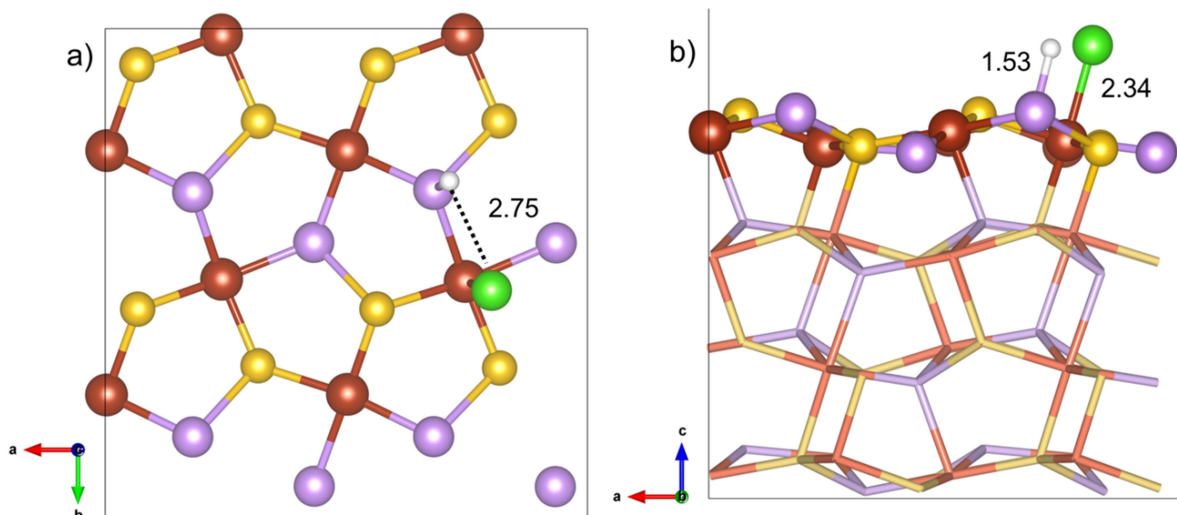


Figure 4.22: Figure 9: Dissociative adsorption of HCl on Fe2 site of arsenopyrite (001) surface. Yellow atoms are sulfur, purple are arsenic, brown are iron, green are chlorine and white are hydrogen.

Table 4.4: Atomic distances on arsenopyrite (001) surface as effect of HCl adsorption. All distances are in Å.

	Pristine surface	Dissociative As	Dissociative S
Fe – As*	2.323	2.396	2.382
Fe – S*	2.202	2.194	2.285
Fe – As axial	2.308	2.439	2.472
As – S*	2.374	2.374	2.397
Fe – Cl	-	2.215	2.211

\*Average of the bonds around the adsorbed atom.

## 1.6 Adsorption of $H_2SO_4$

In computational chemistry the consideration of the pH is a challenge, since it is hard to treat the aqueous medium, especially as an interface with a solid surface. In this way, the pH can be considered in simulation studies when adsorbing the species available at the pH of interest. Sulfuric acid,  $H_2SO_4$ , is also a strong acid, which means that it will be dissociated in aqueous solution. However, differently from

HCl, it has two protons, and its dissociation leads to two species: bisulfate ( $\text{HSO}_4^-$ ) and sulfate ( $\text{SO}_4^{2-}$ ). Since the  $\text{p}K_{a2}$  at 25°C is 1.99 [23],  $\text{SO}_4^{2-}$  is predominant in pH above this value, and  $\text{HSO}_4^-$  is predominant in pH below it.  $\text{H}_2\text{SO}_4$  is in equilibrium with bisulfate only in very low pH. However, for the completeness of the work and also due to the fact that in some extreme situation, such a pH can be observed, we decided to investigate all three species. And for these species there are three types of coordination modes: monodentate mononuclear (MM), in which an oxygen atom from the sulfate molecule binds to one Fe site, bidentate mononuclear (BM), in which two oxygen atoms from the sulfate molecule binds to one Fe site, and bidentate binuclear (BB), in which two oxygen atoms from the sulfate molecule binds to two neighbor Fe sites each. Monodentate binuclear (MB) coordination is not possible for arsenopyrite surface due to the fact that the distance between the Fe sites is about 4 Å, leading to strength in the bonding. All possibilities were investigated for the three species and the results are reported on Table 4.5.

$\text{H}_2\text{SO}_4$  preferred to adsorb on Fe1 site in MM coordination, with adsorption energy of  $-13.5 \text{ kcal mol}^{-1}$  (Figures 4.23a and 4.23b). On Fe2 site, this adsorption was not stable. The species  $\text{H}^+$  and  $\text{HSO}_4^-$  are best adsorbed in BB coordination to Fe1 and Fe2 sites with  $-10.7 \text{ kcal mol}^{-1}$  of energy (Figures 4.23c and 4.23d). A similar BB structure, in which two O atoms bind to two Fe surface atoms, was also found by Blanchard *et al.* [3] in the adsorption of  $\text{As}(\text{OH})_3$  on pyrite. Sulfate is predicted to have adsorption energy of at least  $1.4 \text{ kcal mol}^{-1}$  in a BB coordination between a Fe and a neighbor As atom (Figures 4.23g and 4.23h), therefore not favorable. In an adsorption between two neighbor Fe atoms, the energy is even higher,  $9.8 \text{ kcal mol}^{-1}$  (Figures 4.23e and 4.23f). For chalcopyrite [10], the most stable adsorption structures were also the BB coordination modes. In this case, the adsorption of  $\text{SO}_4^{2-}$  was less stable than of  $\text{HSO}_4^-$  too, but the latter was also favorable, with  $-34$  and  $-25.5 \text{ kcal mol}^{-1}$  energies respectively. The Fe–O distances were similar on both sulfide surfaces, but for chalcopyrite they were equal on both sides [10], while for arsenopyrite, the bond is longer on Fe2 site. The bonds between the surface atoms get longer, as the adsorbed sulfate is deprotonated, according to Table 4.6. Again this effect is larger on axial bonds and is little on As–S bonds.

Other positions of the H atom in sulfate and bisulfate adsorption were also investigated and are reported on Table 4.7.

Table 4.5: Adsorption energies of aqueous H<sub>2</sub>SO<sub>4</sub> species in different positions on arsenopyrite (001) surface in kcal mol<sup>-1</sup>.

	H <sub>2</sub> SO <sub>4</sub>	HSO <sub>4</sub> <sup>-</sup>	SO <sub>4</sub> <sup>2-</sup>
MM	-13.5	-5.0	BB*
BM	MM*	MM*	23.7
BB	MM*	-10.7	9.8, 1.4**

\* These structures converged to another coordination mode.

\*\* Coordination between Fe and As atoms.

Table 4.6: Atomic distances on arsenopyrite (001) surface as effect of H<sub>2</sub>SO<sub>4</sub> adsorption. All distances are in Å.

	Pristine surface	H <sub>2</sub> SO <sub>4</sub>	HSO <sub>4</sub> <sup>-</sup>	SO <sub>4</sub> <sup>2-</sup>
Fe – As*	2.323	2.369	2.368	2.382
Fe – S*	2.202	2.236	2.256	2.268
Fe1 – As axial	2.308	2.386	2.443	2.530
Fe2 – S axial	2.124	2.117	2.210	2.213
As – S*	2.374	2.378	2.376	2.366
Fe1 – O	-	2.198	2.032	1.841
Fe2 – O	-	-	2.121	2.059

\*Average of the bonds around the adsorbed atom.

Table 4.7: Dissociative adsorption of SO<sub>4</sub><sup>2-</sup> and HSO<sub>4</sub><sup>-</sup> on arsenopyrite surface. All energies are in kcal mol<sup>-1</sup>.

Structure	Adsorption Energy	Site of H adsorption
Figure 4.24a	23.7	As and As
Figure 4.24c	-5.0	As
Figure 4.25a	13.4	As and As
Figure 4.25c	-3.9	As
Figure 4.26a	-1.4	S
Figure 4.26c	-2.3	S
Figure 4.27a	27.6	As and S
Figure 4.27c	-0.95	S

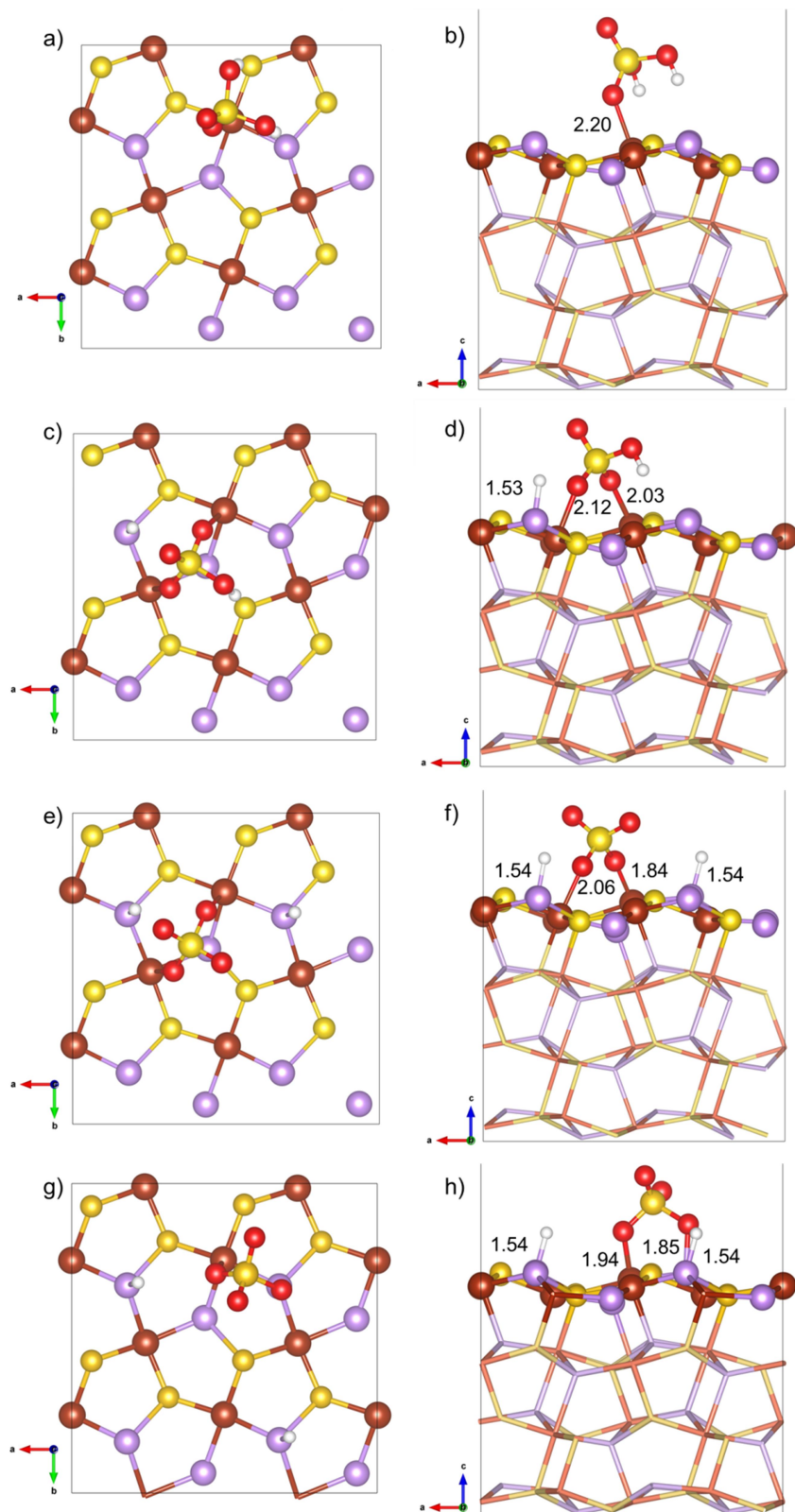


Figure 4.23: Most stable structures for adsorption of  $\text{H}_2\text{SO}_4$  on arsenopyrite (001) surface: a),b)  $\text{H}_2\text{SO}_4$  MM; c),d)  $\text{H}^+$ ,  $\text{HSO}_4^-$  BB, e), f)  $2\text{H}^+$ ,  $\text{SO}_4^{2-}$  BB on Fe sites; g), h)  $2\text{H}^+$ ,  $\text{SO}_4^{2-}$  BB on Fe and As sites. Yellow atoms are sulfur, purple are arsenic, brown are iron, red are oxygen and white are hydrogen.

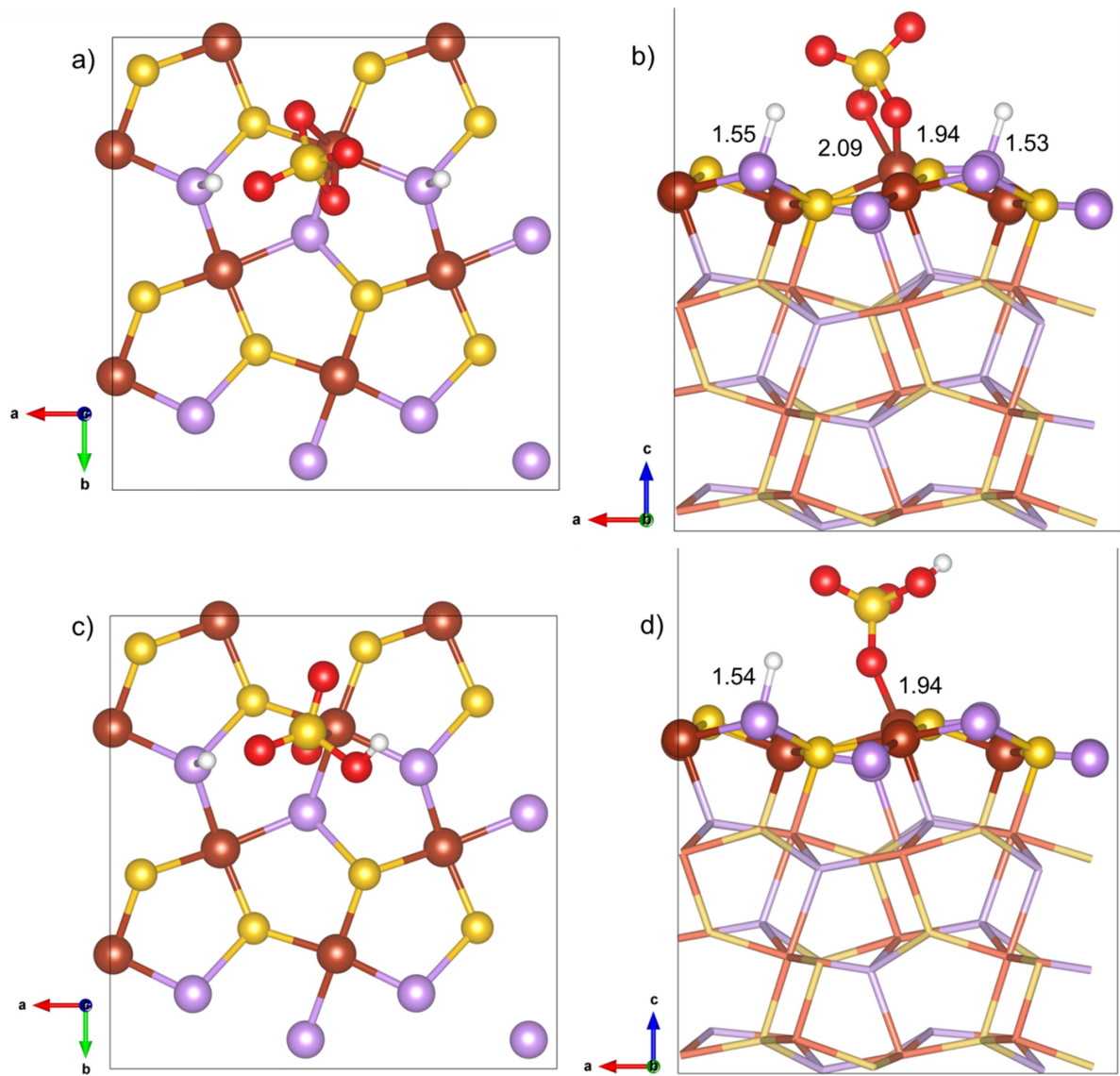


Figure 4.24: Adsorption of  $\text{H}_2\text{SO}_4$  on arsenopyrite (001) surface: a), b)  $2\text{H}^+$ ,  $\text{SO}_4^{2-}$  BM; c), d)  $\text{H}^+$ ,  $\text{HSO}_4^-$  MM. Yellow atoms are sulfur, purple are arsenic, brown are iron, red are oxygen and white are hydrogen.

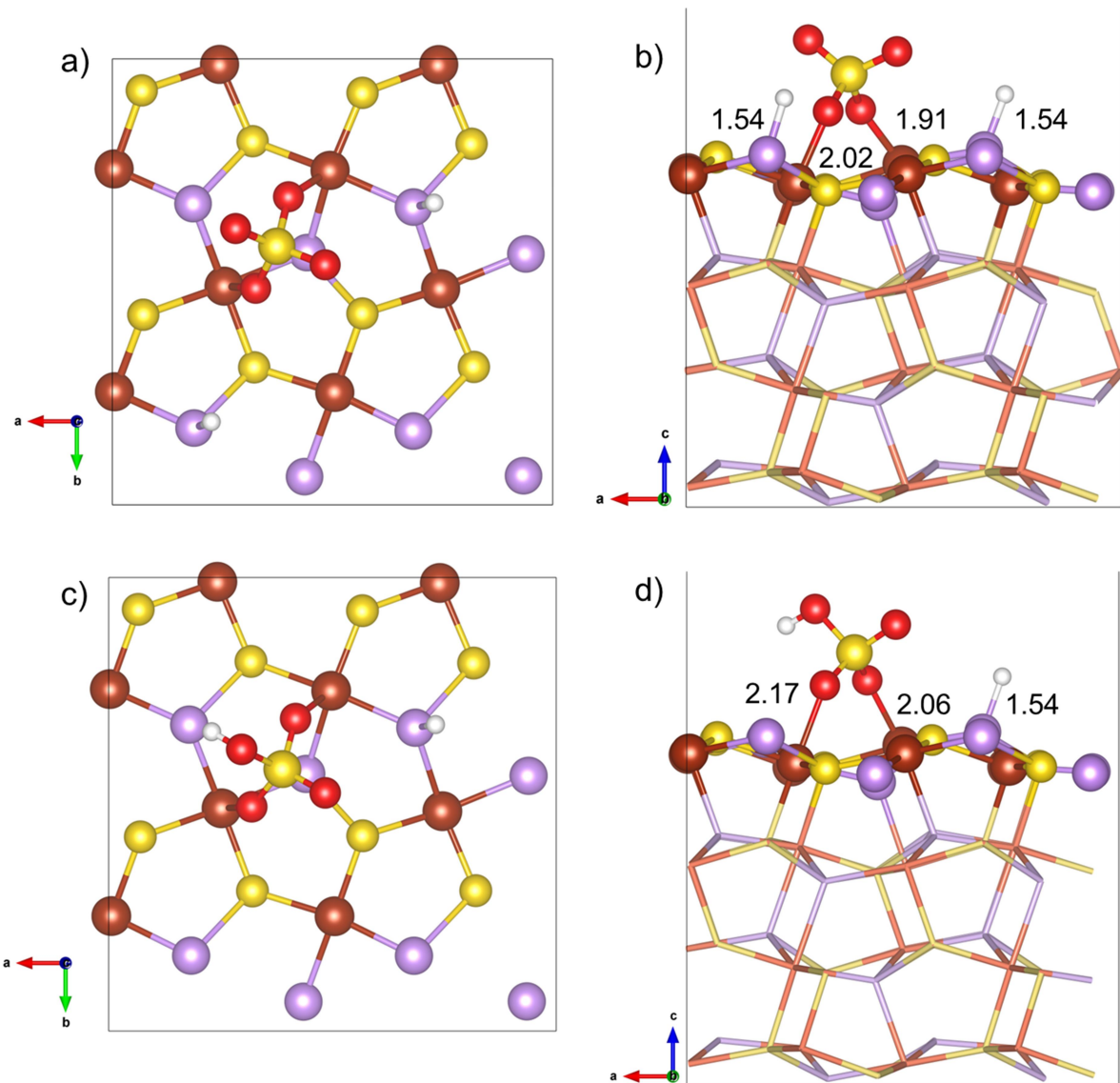


Figure 4.25: Adsorption of  $\text{H}_2\text{SO}_4$  on Fe and As atom of arsenopyrite (001) surface: a), b)  $2\text{H}^+$ ,  $\text{SO}_4^{2-}$ ; c), d)  $\text{H}^+$ ,  $\text{HSO}_4^-$ . Yellow atoms are sulfur, purple are arsenic, brown are iron, red are oxygen and white are hydrogen.

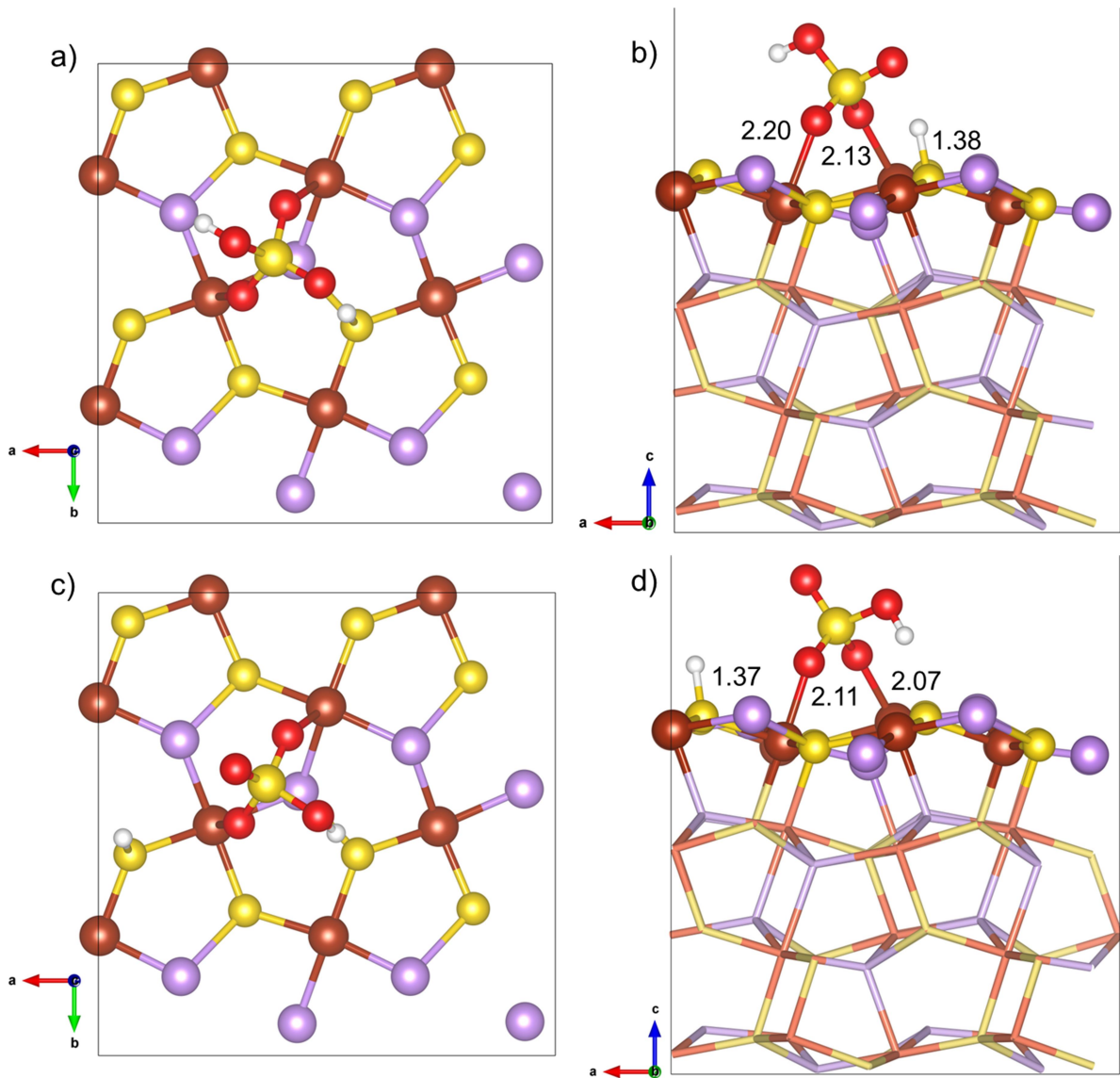


Figure 4.26: Figure S7: Adsorption of  $\text{HSO}_4^-$  on Fe and S atom of arsenopyrite (001) surface: a), b) S1; c), d) S2. Yellow atoms are sulfur, purple are arsenic, brown are iron, red are oxygen and white are hydrogen.

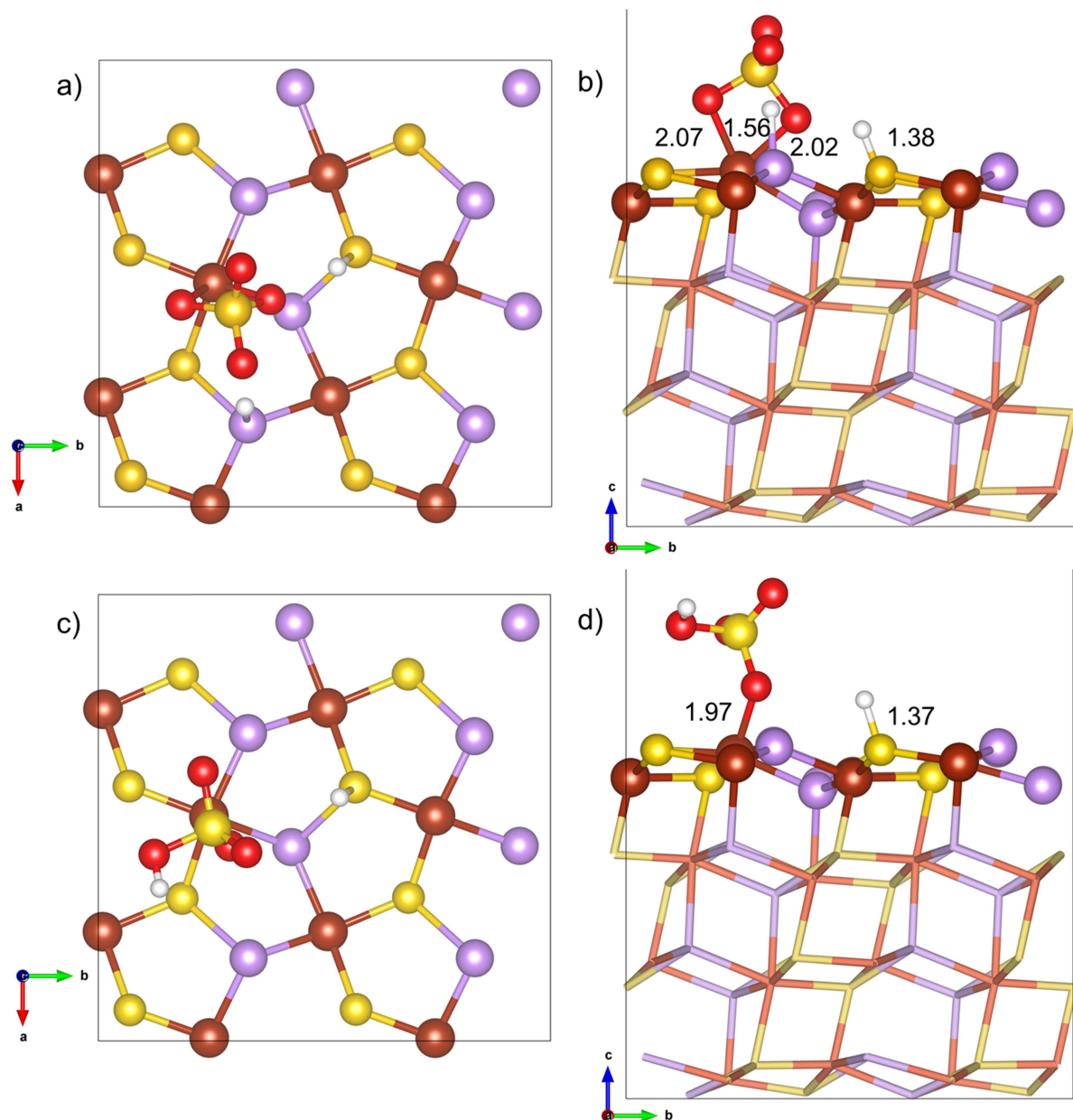


Figure 4.27: Adsorption of  $\text{H}_2\text{SO}_4$  on arsenopyrite (001) surface: a), b)  $\text{SO}_4^{2-}$  BB; c),d)  $\text{HSO}_4^-$  MM. Yellow atoms are sulfur, purple are arsenic, brown are iron, red are oxygen and white are hydrogen.

Comparing the adsorption energy of leaching agents on top of arsenopyrite (001) surface with other sulfides, presented on Table 4.8, one realizes that the behavior of arsenopyrite is similar to pyrite and all analyzed sulfides, although other computation methods were used in different studies. Stirling *et al.* [1] used CPMD/GGA to investigate the adsorption of water on pyrite and De Lima *et al.* [10, 12] used DFT/numerical basis sets for the study on chalcopyrite. In order to have a

complete comparison between the mineral sulfides we decided to calculate the adsorption energy of the sulfate, chloride and water on pyrite. The same methodology used for the FeAsS calculations was used for pyrite and the structures are shown in Figures 4.28 to 4.30. The sulfide that most adsorbs leaching agents among the ones listed is chalcopyrite.

Table 4.8: Adsorption Energy of leaching agents calculated for different sulfide surfaces.

Species	Adsorption Energy/ kcal mol <sup>-1</sup>				
	FeS <sub>2</sub> [1]	FeS <sub>2</sub> *	CuFeS <sub>2</sub> [10, 12]	FeAsS	
				Fe1	Fe2
H <sub>2</sub> O	-12.9	-16.1	-22.8	-10.8	-5.0
H <sup>+</sup> , OH <sup>-</sup>	19.4	17.4	-9.0	4.8	17.2
H <sup>+</sup> , Cl <sup>-</sup>	-	-4.2	-21.2	-11.3	-7.3
H <sub>2</sub> SO <sub>4</sub>	-	-16.2	-	-13.5	-
H <sup>+</sup> , HSO <sub>4</sub> <sup>-</sup>	-	-13.0	-34.0	-10.7	
2H <sup>+</sup> , SO <sub>4</sub> <sup>2-</sup>	-	21.4	-25.5	9.8	

\* calculated in this work using the same level of theory of FeAsS calculations.

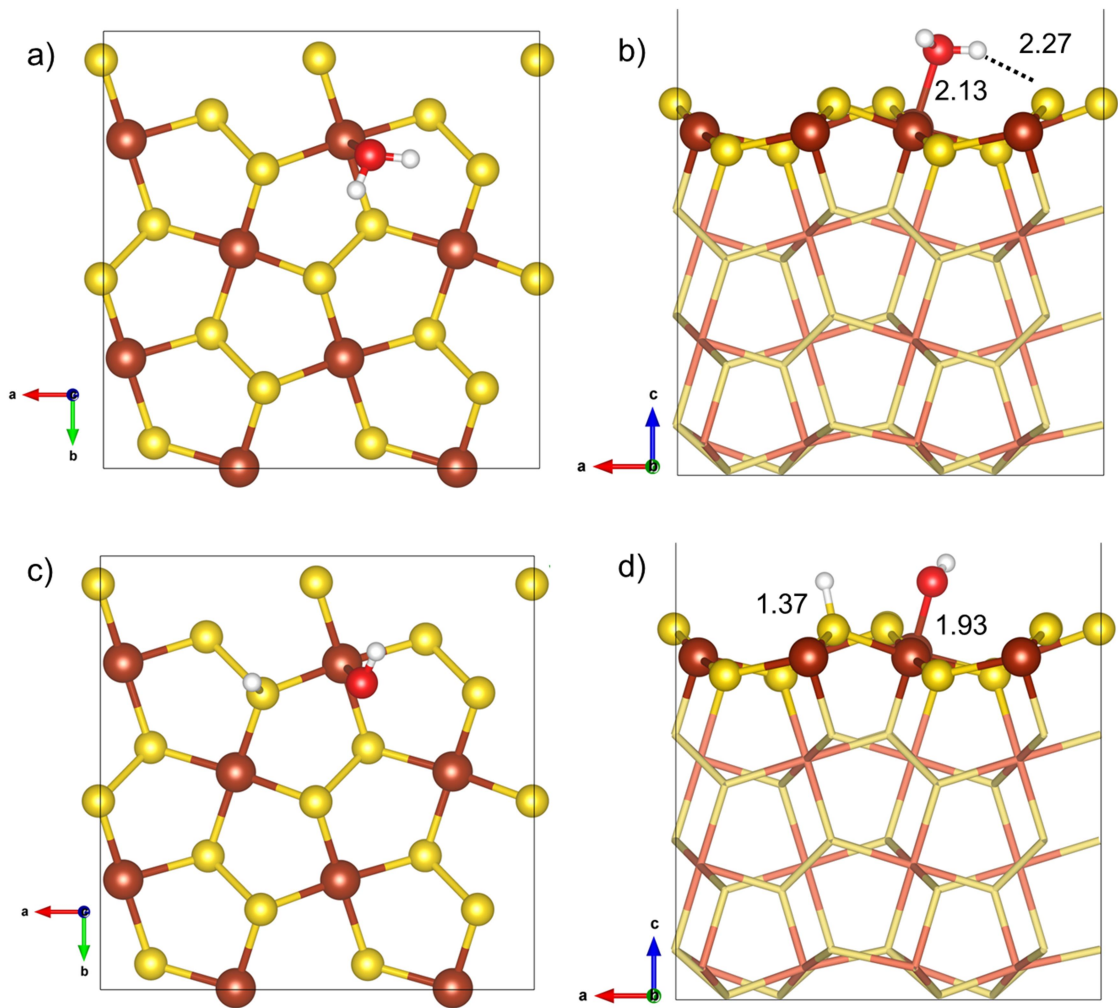


Figure 4.28: Adsorption of  $\text{H}_2\text{O}$  on pyrite (001) surface. a),b) molecular adsorption; c),d) dissociate adsorption. Yellow atoms are sulfur, brown are iron, red are oxygen and white are hydrogen.

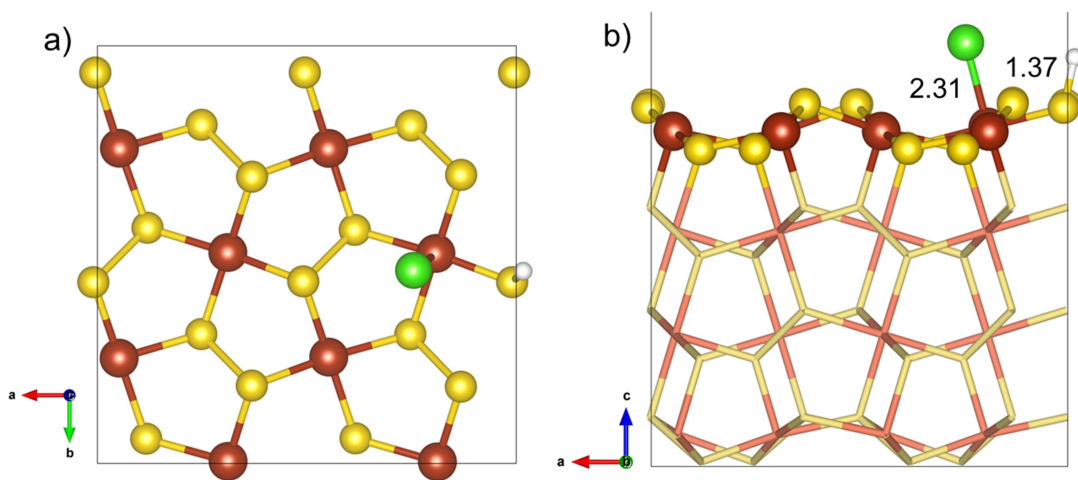


Figure 4.29: Dissociative adsorption of  $\text{HCl}$  on pyrite (001) surface. Yellow atoms are sulfur, brown are iron, green are chlorine and white are hydrogen.

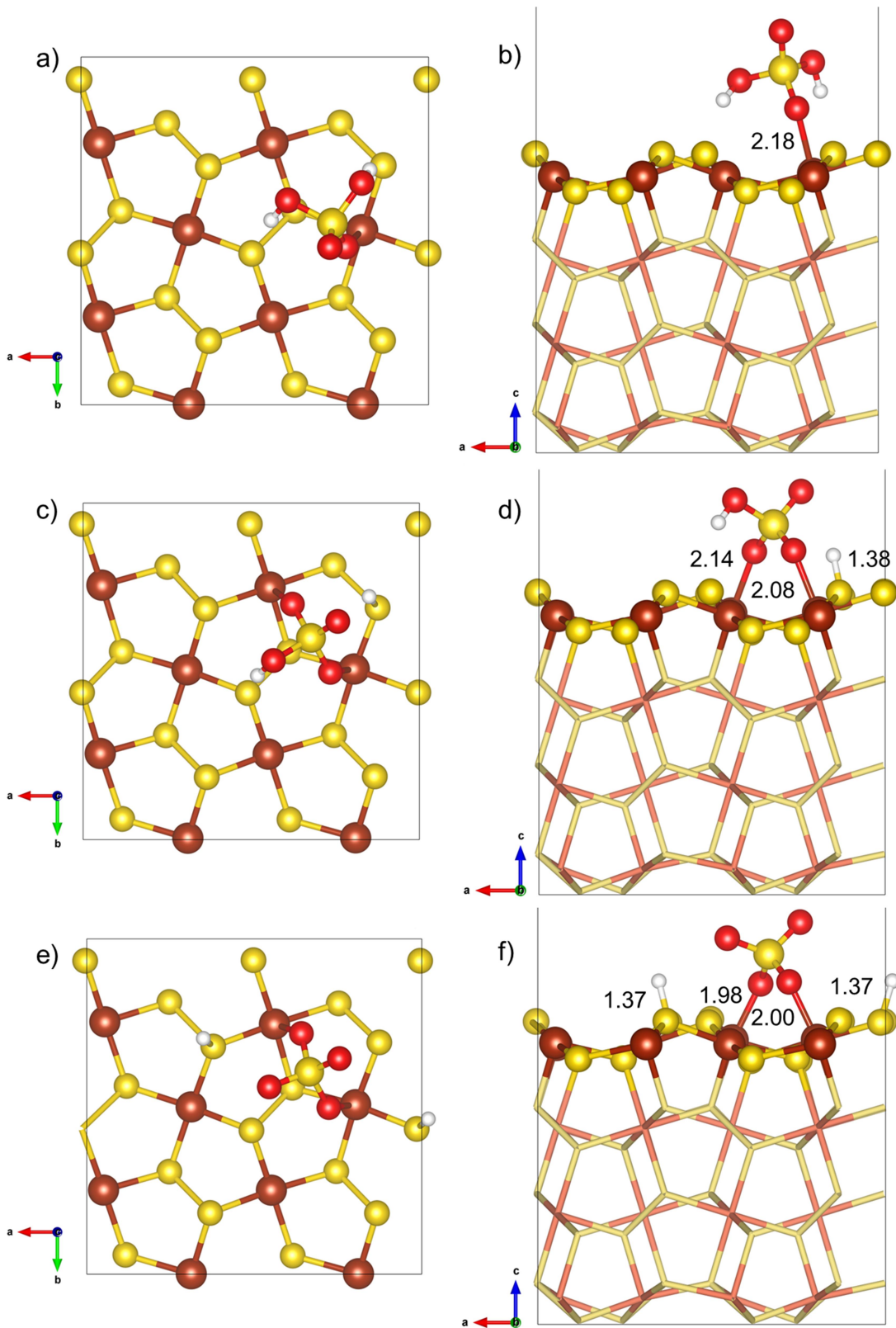


Figure 4.30: Adsorption of  $\text{H}_2\text{SO}_4$  on pyrite (001) surface: a), b)  $\text{H}_2\text{SO}_4$ , c), d)  $\text{H}^+$ ,  $\text{HSO}_4^-$  e), f)  $2\text{H}^+$ ,  $\text{SO}_4^{2-}$ . Yellow atoms are sulfur, brown are iron, red are oxygen and white are hydrogen.

### 4.3 Final Considerations

The different adsorption energy values for different sulfides indicate that the study of the interface solid/water is still a challenge for theoretical chemistry. The localized numerical basis set used by De Lima *et al.* [12] are truncated and confined in a way that the results can be overestimated, while in CPMD, used by Stirling *et al.* [1], the solvent influence is better considered. Nevertheless, the geometric structures calculated in different sulfides using different methods are similar and the relative order of stability is in agreement. Experimental values for the adsorption energy are scarce and generally obtained in condensed phase, which makes it harder to compare with calculated values.

The adsorption of leaching agents such as water, hydrochloric acid, and sulfuric acid on this surface was investigated using DFT/plane waves methods. Water adsorbs molecularly on the surface preferentially on Fe1 site. On less stable surfaces, the adsorption of water is stronger. In a full coverage of water on the (001) surface, only the top surface iron atoms will adsorb a water molecule, and the other molecules should connect to the first ones through hydrogen bonds, forming a second solvation layer. Water dissociative adsorption is unlikely to happen. Hydrochloric acid adsorbs dissociatively, but sulfuric acid prefers molecular adsorption in vacuum, although in water it would be dissociated. Bisulfate adsorbs preferentially in a bidentate binuclear coordination and sulfate adsorption was not favorable in the conditions of the calculations. Since the equilibrium of these species in water is dependent on the pH, a molecular dynamics with acids and water molecules would give more information about the behavior of the surface in acidic media. However, this is beyond of the present stage of the computational development. Arsenic is more basic, i.e., has more affinity for protons than sulfur in both water and acid media, then it could be more reactive than the latter element, in agreement with the observations of Nesbitt *et al.* [24] and Corkhill *et al.* [16]. The adsorption of leaching agents on arsenopyrite surface is similar to pyrite surface, although the adsorption energies may vary.

Table 4.8, page 105 provides a comparison of the adsorption energies between the different sulfide minerals. Chalcopyrite seems to be able to interact stronger with water, chloride and sulfates than the other minerals. This is an

indication that the products formed (hydroxides, sulfates and chlorides) will stick to the surface of chalcopyrite, preventing its oxidation. This is coherent to the fact that chalcopyrite has a slow kinetics of leaching. Actually, efforts are being made to improve the leaching process for copper extraction from chalcopyrite using hydrometallurgical routes. The ARD phenomena, on the other side, leads to the formation of sulfates on the pyrite and arsenopyrite surfaces. However, the sulfate adsorption is not favorable, remobilizing the products to the water medium and exposing more surface for oxidation. Only in low pH, the bisulfate ( $\text{HSO}_4^-$ ) will be favorably adsorbed. Furthermore, the adsorption of water on pyrite is more favored than on arsenopyrite, this means that the first layer of water molecules in contact to the surface is more strongly bound in pyrite. Therefore, it is expected that the diffusion of this layer from the water medium to the surface is slower in pyrite than in arsenopyrite, preventing the oxidant agents such as molecular oxygen to arrive at the surface of the former.

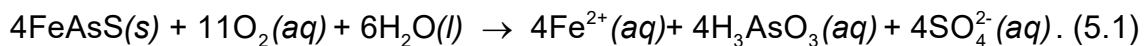
#### 4.4 References:

1. Stirling, A., M. Bernasconi, and M. Parrinello, *Ab initio simulation of water interaction with the (100) surface of pyrite*. Journal of Chemical Physics, 2003. **118**(19): p. 8917-8926.
2. Stirling, A., M. Bernasconi, and M. Parrinello, *Ab initio simulation of  $\text{H}_2\text{S}$  adsorption on the (100) surface of pyrite*. The Journal of Chemical Physics, 2003. **119**(9): p. 4934-4939.
3. Blanchard, M., et al., *Adsorption of  $\text{As}(\text{OH})_3$  on the (001) Surface of  $\text{FeS}_2$  Pyrite: A Quantum-mechanical DFT Study*. The Journal of Physical Chemistry C, 2007. **111**(30): p. 11390-11396.
4. Sit, P.H.L., M.H. Cohen, and A. Selloni, *Interaction of Oxygen and Water with the (100) Surface of Pyrite: Mechanism of Sulfur Oxidation*. Journal of Physical Chemistry Letters, 2012. **3**(17): p. 2409-2414.
5. Dos Santos, E.C., J.C. de Mendonça Silva, and H.A. Duarte, *Pyrite Oxidation Mechanism by Oxygen in Aqueous Medium*. The Journal of Physical Chemistry C, 2016. **120**(5): p. 2760-2768.
6. Zhao, C., et al., *Study of  $\text{H}_2\text{O}$  adsorption on sulfides surfaces and thermokinetic analysis*. Journal of Industrial and Engineering Chemistry, 2014. **20**(2): p. 605-609.
7. Chen, J.-h., et al., *DFT calculation on relaxation and electronic structure of sulfide minerals surfaces in presence of  $\text{H}_2\text{O}$  molecule*. Journal of Central South University, 2014. **21**(10): p. 3945-3954.

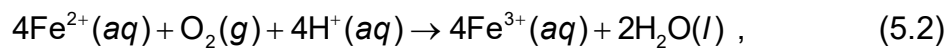
8. Chen, J., X. Long, and Y. Chen, *Comparison of Multilayer Water Adsorption on the Hydrophobic Galena (PbS) and Hydrophilic Pyrite (FeS<sub>2</sub>) Surfaces: A DFT Study*. The Journal of Physical Chemistry C, 2014. **118**(22): p. 11657-11665.
9. de Oliveira, C. and H.A. Duarte, *Disulphide and metal sulphide formation on the reconstructed (001) surface of chalcopyrite: A DFT study*. Applied Surface Science, 2010. **257**(4): p. 1319-1324.
10. de Lima, G.F., et al., *Water Adsorption on the Reconstructed (001) Chalcopyrite Surfaces*. The Journal of Physical Chemistry C, 2011. **115**(21): p. 10709-10717.
11. de Oliveira, C., et al., *Reconstruction of the Chalcopyrite Surfaces—A DFT Study*. The Journal of Physical Chemistry C, 2012. **116**(10): p. 6357-6366.
12. de Lima, G.F., et al., *Sulfuric and hydrochloric acid adsorption on the reconstructed sulfur terminated (001) chalcopyrite surface*. International Journal of Quantum Chemistry, 2012. **112**(19): p. 3216-3222.
13. Wolff, G.A. and J.D. Broder, *Cleavage and the Identification of Minerals*. American Mineralogist, 1960. **45**(11-2): p. 1230-1242.
14. Klein, C., C.S. Hurlbut, and J.D. Dana, *Manual of mineralogy : (after James D. Dana)*. 21st ed. 1999, New York: J. Wiley.
15. Dana, E.S. and W.E. Ford, *A Text-book of Mineralogy: With an Extended Treatise on Crystallography and Physical Mineralogy*. 4 ed. 1966, New York: Wiley.
16. Corkhill, C.L., et al., *The oxidative dissolution of arsenopyrite (FeAsS) and enargite (Cu<sub>3</sub>AsS<sub>4</sub>) by Leptospirillum ferrooxidans*. Geochimica et Cosmochimica Acta, 2008. **72**(23): p. 5616-5633.
17. Ford, M. and C.C. Ferguson, *Cleavage Strain in the Variscan Fold Belt, County Cork, Ireland, Estimated from Stretched Arsenopyrite Rosettes*. Journal of Structural Geology, 1985. **7**(2): p. 217-223.
18. Arunan, E., et al., *Defining the hydrogen bond: An account (IUPAC Technical Report)*, in *Pure and Applied Chemistry*. 2011. p. 1619.
19. Stirling, A., M. Bernasconi, and M. Parrinello, *Defective pyrite (100) surface: An ab initio study*. Physical Review B, 2007. **75**(16): p. 165406.
20. de Leeuw, N.H., et al., *Modeling the Surface Structure and Reactivity of Pyrite: Introducing a Potential Model for FeS<sub>2</sub>*. The Journal of Physical Chemistry B, 2000. **104**(33): p. 7969-7976.
21. Rosso, K.M., U. Becker, and M.F. Hochella, *The interaction of pyrite {100} surfaces with O<sub>2</sub> and H<sub>2</sub>O; fundamental oxidation mechanisms*. American Mineralogist, 1999. **84**(10): p. 1549-1561.
22. Steele, M.H., K. Wright, and H.I. Hillier, *A quantum-mechanical study of the (110) surface of sphalerite (ZnS) and its interaction with Pb<sup>2+</sup> species*. Physics and Chemistry of Minerals, 2003. **30**(2): p. 69-75.
23. Rankin, D.W.H., *CRC handbook of chemistry and physics, 89th edition, edited by David R. Lide*. Crystallography Reviews, 2009. **15**(3).
24. Nesbitt, H.W., I.J. Muir, and A.R. Prarr, *Oxidation of arsenopyrite by air and air-saturated, distilled water, and implications for mechanism of oxidation*. Geochimica et Cosmochimica Acta, 1995. **59**(9): p. 1773-1786.

## 5 Oxidation of Arsenopyrite

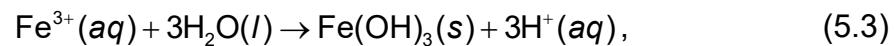
Molecular oxygen and the  $\text{Fe}^{3+}$  species are two agents responsible for arsenopyrite oxidation in natural environment. But the  $\text{Fe}^{3+}$  ion can oxidize arsenopyrite at least one order of magnitude faster than dissolved oxygen [1]. The reactions caused by these two oxidant agents are described by the equations below [2, 3]. The overall equation of the first step in arsenopyrite oxidation by  $\text{O}_2$  is



In oxidant conditions and pH above 5,  $\text{Fe}^{2+}$  can rapidly oxidize to  $\text{Fe}^{3+}$ , according to

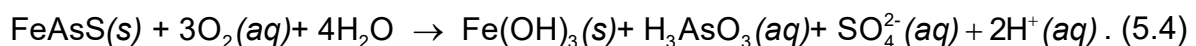


and the latter can precipitate as hydroxide,

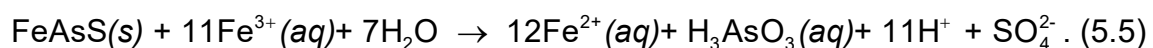


leaving the medium more acidic.

The overall oxidation reaction then becomes



If  $\text{Fe}^{3+}$  does not precipitate, it can also oxidize arsenopyrite according to



Walker *et al.* [2] did not find a dependence of the arsenopyrite oxidation rate on the concentration of  $\text{O}_2$ , in disagreement with the results of Yu *et al.* [3]. This difference might be due to the different pH used in the previous studies. In fact, Yu *et*

a/. [3] found a decrease in the release rate of As in pH above 6.5, reaching a minimum between pH 7 and 8.

DFT/Plane wave calculations have been performed using the same protocol used in the previous sections. The Activation Energies were calculated using the NEB (Nudged Elastic Band) method with CI (climbing image) option. These calculations have been performed at the gamma ( $\Gamma$ ) point, using 14 images converged until the norms of the forces orthogonal to the path were under  $0.05 \text{ eV}\cdot\text{\AA}^{-1}$ .

## ***5.1 Adsorption of Oxygen***

According to equations 5.1 to 5.5, molecular oxygen should be involved in the oxidation of arsenopyrite. For this reason, the adsorption of this molecule on the arsenopyrite (001) surface was investigated in different possibilities. The oxygen molecule can be adsorbed in two orientations: end-on, bound to the surface by only one atom of the molecule, and side-on, bound to the surface by both atoms. As noticed in chapter 4, iron is the best site for adsorption on the arsenopyrite (001) surface, which has two different possible iron sites. Figure 5.1 shows these possible adsorption sites on the FeAsS surface. Fe1 and Fe3 are more sterically exposed, and Fe2 and Fe4 less exposed, as can be noticed in Figure 5.1b. Although the distance between Fe3 and Fe4 is the shortest one, and possibly the best for side-on oxygen adsorption, it is blocked by the S2 surface atom, which is in between and in a higher position than the two iron centers. The same happens for the As2 atom in the oxygen adsorption between Fe1 and Fe4. The S2 and As2 are also more reactive than the other anion sites, since they have one dangling bond due to the bond breaking in the surface cleavage. Since the atoms Fe2 and Fe3 are connected by the subsurface atom S1, and the distance between them is the second shortest, it should be the best site for a side-on oxygen adsorption.

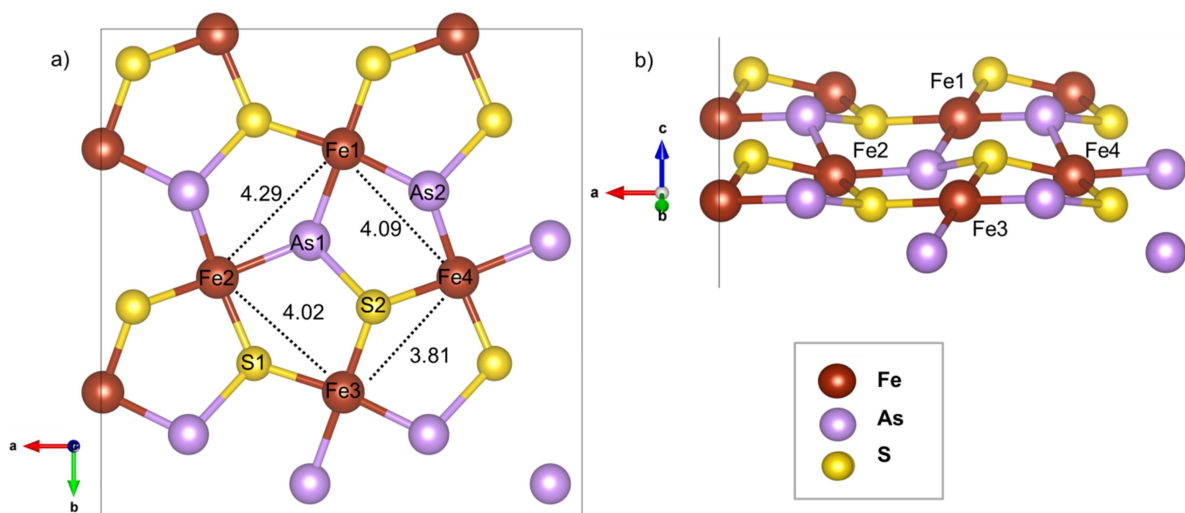


Figure 5.1: First layer of atoms of the arsenopyrite (001) surface showing the different Fe sites: Fe1 and Fe3, more exposed, and Fe2 and Fe4, less exposed. a) top view; b) side view.

Figure 5.2 shows the end-on adsorption on the Fe1 and Fe2 sites. The calculated adsorption energy ( $E_{ad}$ ) on the Fe1 site, Figures 5.2a and 5.2b, is  $-16.6 \text{ kcal mol}^{-1}$ , the same value calculated by Rozgonyi and Stirling [4] for pyrite, and similar to the values calculated for pyrite by Sit *et al.* [5] ( $-14.1 \text{ kcal mol}^{-1}$ ), by Dos Santos *et al.* [6] ( $-14.9 \text{ kcal mol}^{-1}$ ), and by Sacchi *et al.* [7] ( $-13.1 \text{ kcal mol}^{-1}$ ). The Fe–O distance of  $1.78 \text{ \AA}$  is slightly shorter than the one calculated by Dos Santos *et al.* [6] for pyrite,  $1.87 \text{ \AA}$ , and the O–O distance is the same,  $1.30 \text{ \AA}$ . This is the same O–O distance as in the superoxide ion,  $\text{O}_2^-$ , according to Table 5.1, which was calculated in the same conditions as the adsorbed surface. So it is possible that a radical ( $\text{Fe-O-O}\cdot$ ) is formed in a similar way of a Fenton reaction. The longer length of the O–O bond indicates that the  $\pi$  antibonding orbitals of the oxygen molecule are being populated in the adsorption. Therefore, the bonded oxygen receives an electron from the iron atom of the surface. The molecule axis is tilted in a  $50^\circ$  angle from the surface normal. This is  $5^\circ$  more than the same molecule on the surface of pyrite [7]. The end-on adsorption on Fe2 site is less stable,  $-3.6 \text{ kcal mol}^{-1}$ , shown in Figures 5.2c and 5.2d.

Table 5.1: O–O distances calculated for different O<sub>2</sub> bond types in gas phase.

Species	Distance/Å
Oxygen	1.2319
Superoxide Ion	1.3034
Peroxide Ion	1.3164
Hydrogen Peroxide	1.4876

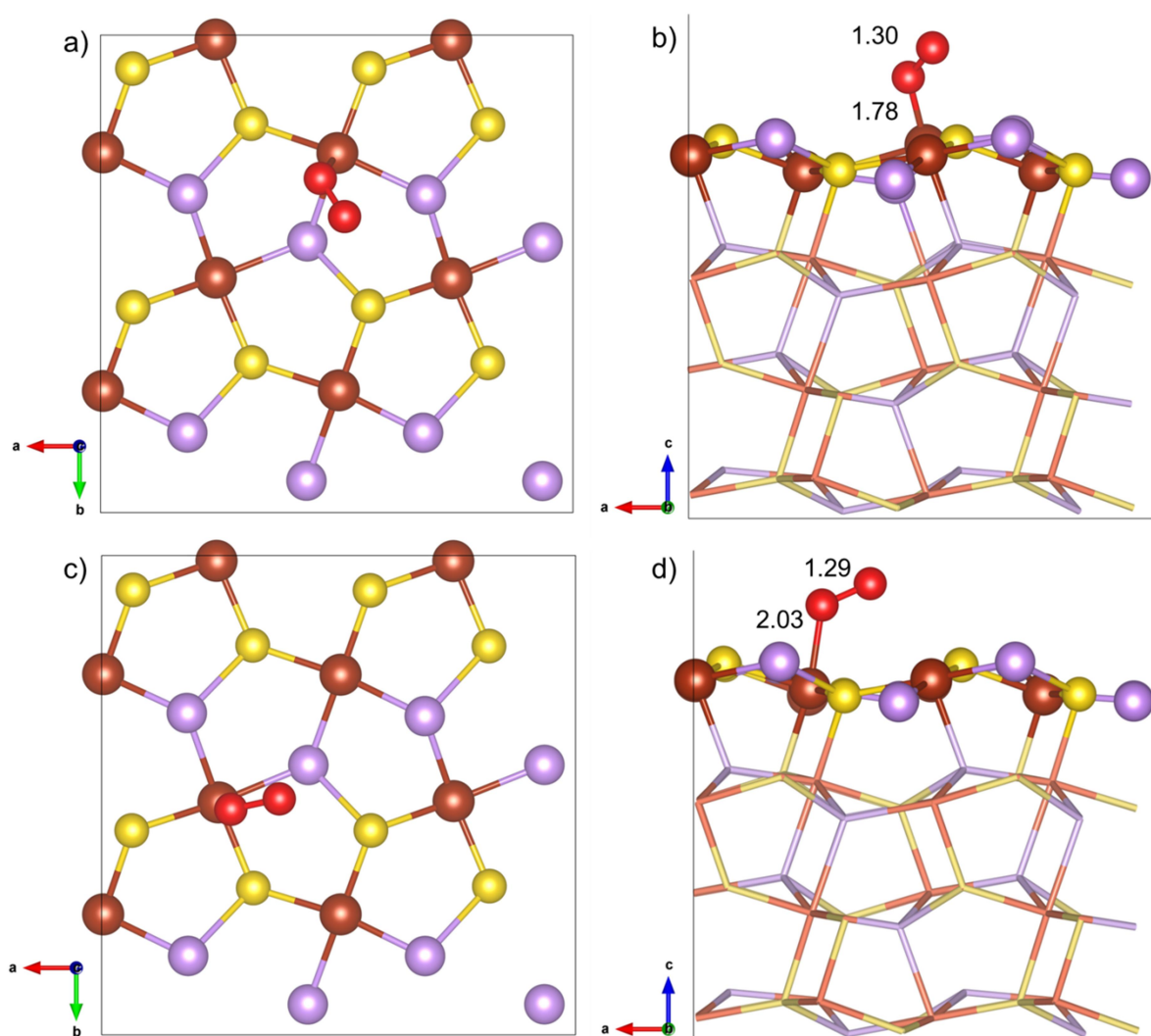


Figure 5.2: End-on adsorption of O<sub>2</sub> on the (001) arsenopyrite surface: a) Fe1 top view, b) Fe1 side view ( $E_{\text{ad}} = -16.6 \text{ kcal mol}^{-1}$ ); c) Fe2 top view, d) Fe2 side view ( $E_{\text{ad}} = -3.6 \text{ kcal mol}^{-1}$ ). Yellow atoms are sulfur, brown are iron, red are oxygen and white are hydrogen.

For the side-on adsorption two structures were obtained: one involving the Fe1 site and a neighboring As and one involving the Fe2 and Fe3 sites (Figure 5.3). A structure with the side-on oxygen adsorption on sites Fe1 and Fe2 is not stable and immediately breaks the O–O bond, as well as for the other Fe sites. The calculated adsorption energy for the first structure shown in Figures 5.3a and 5.3b is  $-29.2 \text{ kcal mol}^{-1}$ . For the second structure, shown in Figures 5.3c and 5.3d, the calculated adsorption energy is less stable,  $-6.2 \text{ kcal mol}^{-1}$ ,  $10.4 \text{ kcal mol}^{-1}$  higher than the one calculated for pyrite by Sit *et al.* [5],  $10.1 \text{ kcal mol}^{-1}$  higher than Dos Santos' *et al.* [6], and  $14.3 \text{ kcal mol}^{-1}$  higher than Rozgonyi and Stirling's [4]. These deviations are probably due to the differences in the mineral structure. However, the Fe–O distances of  $1.90 \text{ \AA}$  and  $1.94 \text{ \AA}$  are shorter on arsenopyrite than the ones on pyrite [6] ( $1.96 \text{ \AA}$  and  $2.02 \text{ \AA}$ ) and the O–O distance is longer:  $1.40 \text{ \AA}$ , compared to  $1.37 \text{ \AA}$ . This is not the most stable structure, but it is more important than the first structure due to the interest in a reaction mechanism in which the O atoms bound to Fe atoms. In this case, the O–O distance stays between the distances in the peroxide ion ( $\text{O}_2^{2-}$ ) and hydrogen peroxide ( $\text{H}_2\text{O}_2$ ), as presented in Table 5.1. This means that both oxygen atoms must receive an electron from each iron atom, oxidizing them to  $\text{Fe}^{3+}$ .

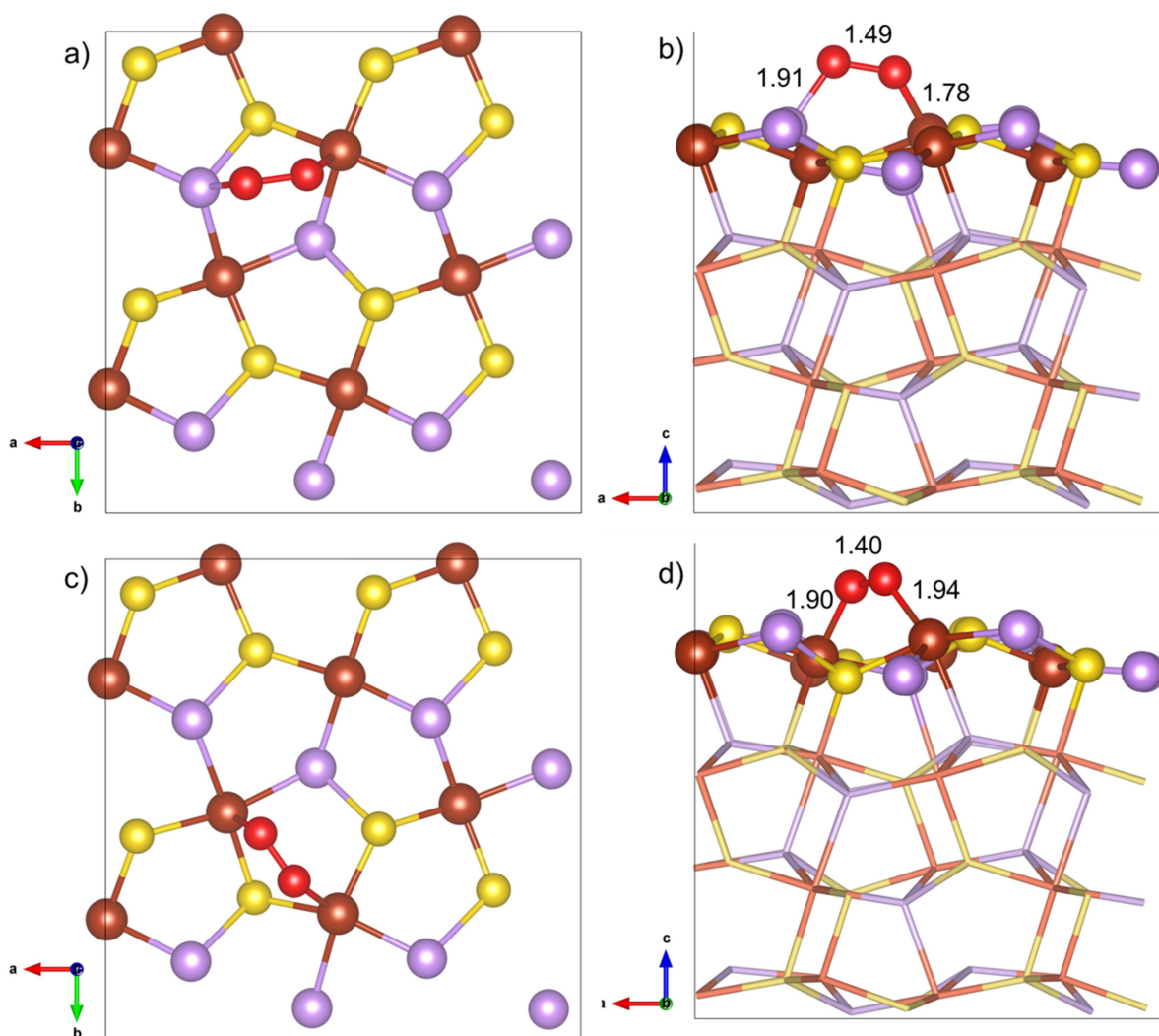


Figure 5.3: Side-on adsorption of  $O_2$  on the (001) arsenopyrite surface: a) Fe1 and As sites top view, b) Fe1 and As sites side view ( $E_{ad} = -29.2 \text{ kcal mol}^{-1}$ ); c) Fe2 and Fe3 sites top view, d) Fe2 and Fe3 sites side view ( $E_{ad} = -6.2 \text{ kcal mol}^{-1}$ ). Yellow atoms are sulfur, brown are iron, red are oxygen and white are hydrogen.

The O–O bond can break to form atomic oxygen adsorbed on the surface, as shown in Figure 5.4. In this case the iron atom must again be oxidized, giving origin to the species  $Fe^{4+}=O^{2-}$ . This species has been studied by Sit *et al.* [5] in pyrite oxidation. However, we have also investigated this system and our calculations indicated that it should not exist or its lifetime must be very short in aqueous media [6]. Still, in this theoretical study, these species are more stable than the side-on adsorption structure by  $14.4 \text{ kcal mol}^{-1}$  ( $E_{ad} = -43.6 \text{ kcal mol}^{-1}$ ), shown in Figures 5.4a and 5.4b, and by  $24.9 \text{ kcal mol}^{-1}$  ( $E_{ad} = -31.1 \text{ kcal mol}^{-1}$ ), shown in Figures 5.4c and

5.4d. It is important to highlight that these calculations do not include any solvent effects. Rozgonyi and Stirling [4] also observed that O<sub>2</sub> dissociation adsorption on pyrite is more stable than molecular adsorption. The case in which one O atom adsorbs to a Fe atom and the other one to an As atom (see Figures 5.4 a and 5.4b) was observed by Li *et al.* [8] for pyrite using DFT/PW91. Their estimated adsorption energy was -58.2 kcal mol<sup>-1</sup> for the pure surface and -59.3 kcal mol<sup>-1</sup> for the surface doped with As, compared to -43.6 kcal mol<sup>-1</sup> for arsenopyrite calculated in the present work. The Fe–O distance of 1.78 Å and the As–O distance of 1.91 Å are shorter than the ones calculated by Li *et al.* [8] of 1.674 and 1.657 Å, respectively.

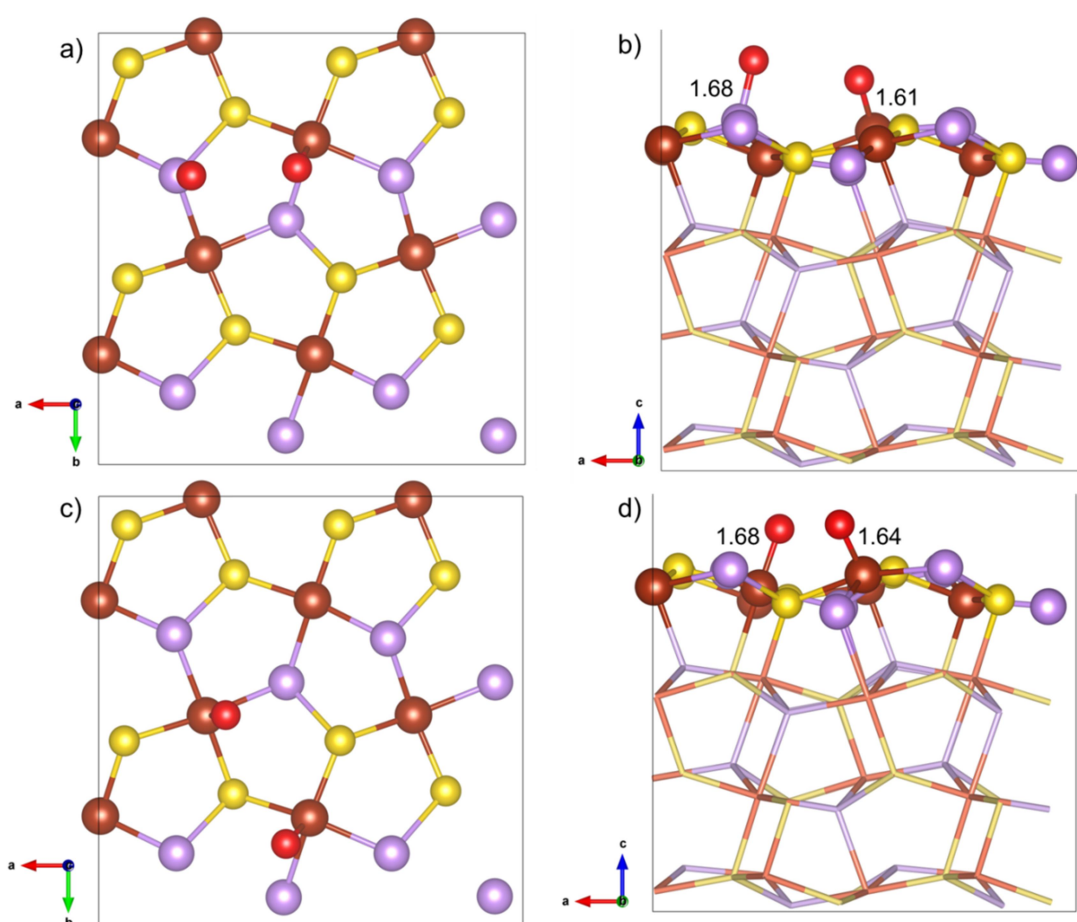


Figure 5.4: Dissociative adsorption of O<sub>2</sub> on the arsenopyrite (001) surface: a) Fe1 and As sites top view, b) Fe1 and As sites side view ( $E_{ad} = -43.6$  kcal mol<sup>-1</sup>); c) Fe2 and Fe3 sites top view, d) Fe2 and Fe3 sites side view ( $E_{ad} = -31.1$  kcal mol<sup>-1</sup>). Yellow atoms are sulfur, brown are iron, red are oxygen and white are hydrogen.

The oxygen atom adsorbed to the Fe2 and Fe4 sites can also easily form a second bond with a neighbor anion in the geometry optimization, as presented in Figure 5.5 for different situations, yielding structures more stable than the ones shown in Figure 5.4. The respective adsorption energies in these cases are according to Figure 5.5: a,b)  $-53.2 \text{ kcal mol}^{-1}$ , c,d)  $-56.0 \text{ kcal mol}^{-1}$ , e,f)  $-34.6 \text{ kcal mol}^{-1}$ , and g,h)  $-55.9 \text{ kcal mol}^{-1}$ . The least stable of these structures is the one in which the O binds to a Fe and a S atom (Figures 5.5e and 5.5f). Therefore, the Fe–O–As bonds are stronger than Fe–O–S ones and the former must be involved in O<sub>2</sub> adsorption on arsenopyrite. Although the side-on adsorption on iron sites, shown in Figures 5.3c and 5.3d, is favored, the dissociative adsorption (Figures 5.5c and 5.5d) leads to much more stable structures. Therefore, the side-on adsorption mode must be seen as a precursor of its dissociation on the surface.

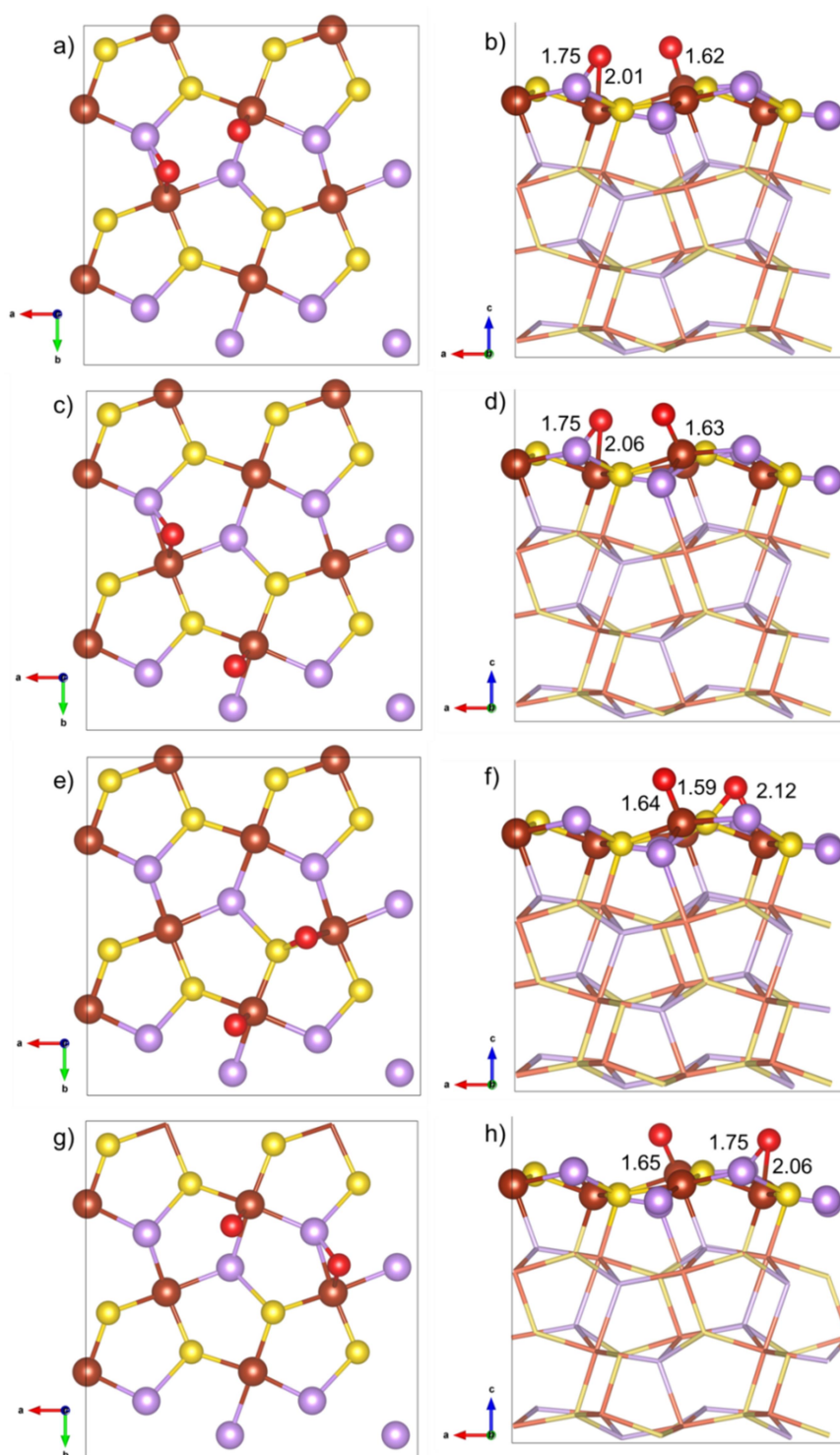


Figure 5.5: Dissociative adsorption of  $O_2$  on the arsenopyrite (001) surface: a) Fe1 and Fe2 sites top view, b) Fe1 and Fe2 sites side view ( $E_{ad} = -53.2 \text{ kcal mol}^{-1}$ ); c) Fe2 and Fe3 sites top view, d) Fe2 and Fe3 sites side view ( $E_{ad} = -56.0 \text{ kcal mol}^{-1}$ ); e) Fe3 and Fe4 sites top view, f) Fe3 and Fe4 sites side view ( $E_{ad} = -34.6 \text{ kcal mol}^{-1}$ ); g) Fe4 and Fe1 sites top view, h) Fe4 and Fe1 sites side view ( $E_{ad} = -55.9 \text{ kcal mol}^{-1}$ ). Yellow atoms are sulfur, brown are iron, red are oxygen and white are hydrogen.

Analyzing the results one could argue that the oxygen molecule will adsorb in a dissociative mechanism and the atomic oxygen will prefer the bridge sites between the Fe and As centers. In fact, our calculations show that the O bound to the Fe1 and Fe3 sites also connects to the neighbor arsenic anion, as shown in Figure 5.6. The calculated adsorption energies are  $-58.5 \text{ kcal mol}^{-1}$  for Figures 5.6a and 5.6b and  $-59.1 \text{ kcal mol}^{-1}$  for Figures 5.6c and 5.6d. The oxygen adsorbed to the Fe–As bridge sites will lead to the oxidation of both Fe and As to form the  $\text{O}^{2-}$  adsorbed species.

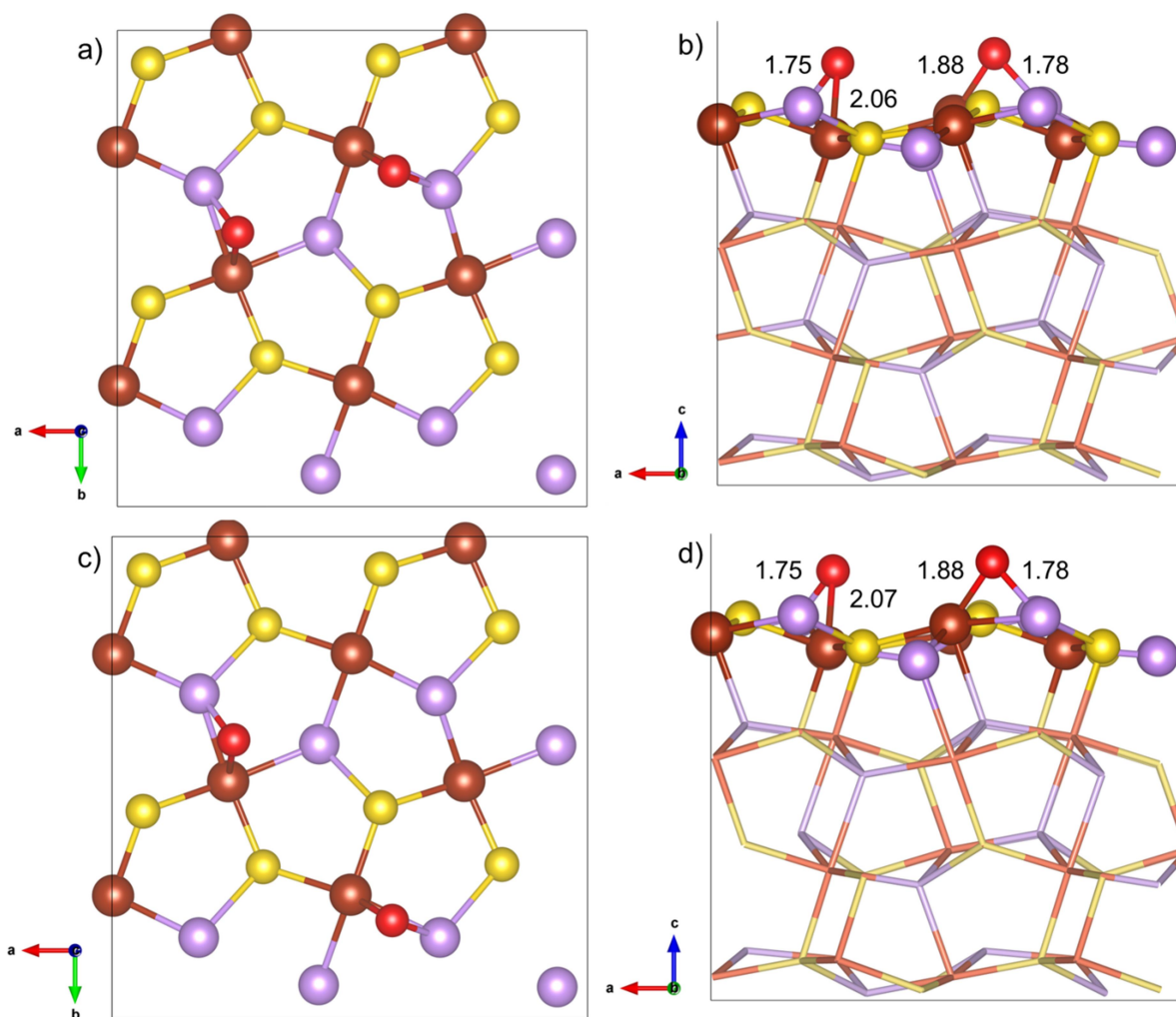


Figure 5.6: Dissociative adsorption of  $\text{O}_2$  on the arsenopyrite (001) surface: a) Fe1 and Fe2 sites top view, b) Fe1 and Fe2 sites side view ( $E_{\text{ad}} = -58.5 \text{ kcal mol}^{-1}$ ); c) Fe2 and Fe3 sites top view, d) Fe2 and Fe3 sites side view ( $E_{\text{ad}} = -59.1 \text{ kcal mol}^{-1}$ ). Yellow atoms are sulfur, brown are iron, red are oxygen and white are hydrogen.

Other positions for O<sub>2</sub> dissociate adsorption on the FeAsS surface forming Fe–O–S bonds were also investigated and are presented at Figure 5.7. The adsorption energies in these cases are -29.7, -35.7 and -39.9 kcal mol<sup>-1</sup> for the arrangements shown in Figure 5.7a, 5.7c and 5.7e, respectively. These structures are less stable since they involve weaker Fe–O–S bonds.

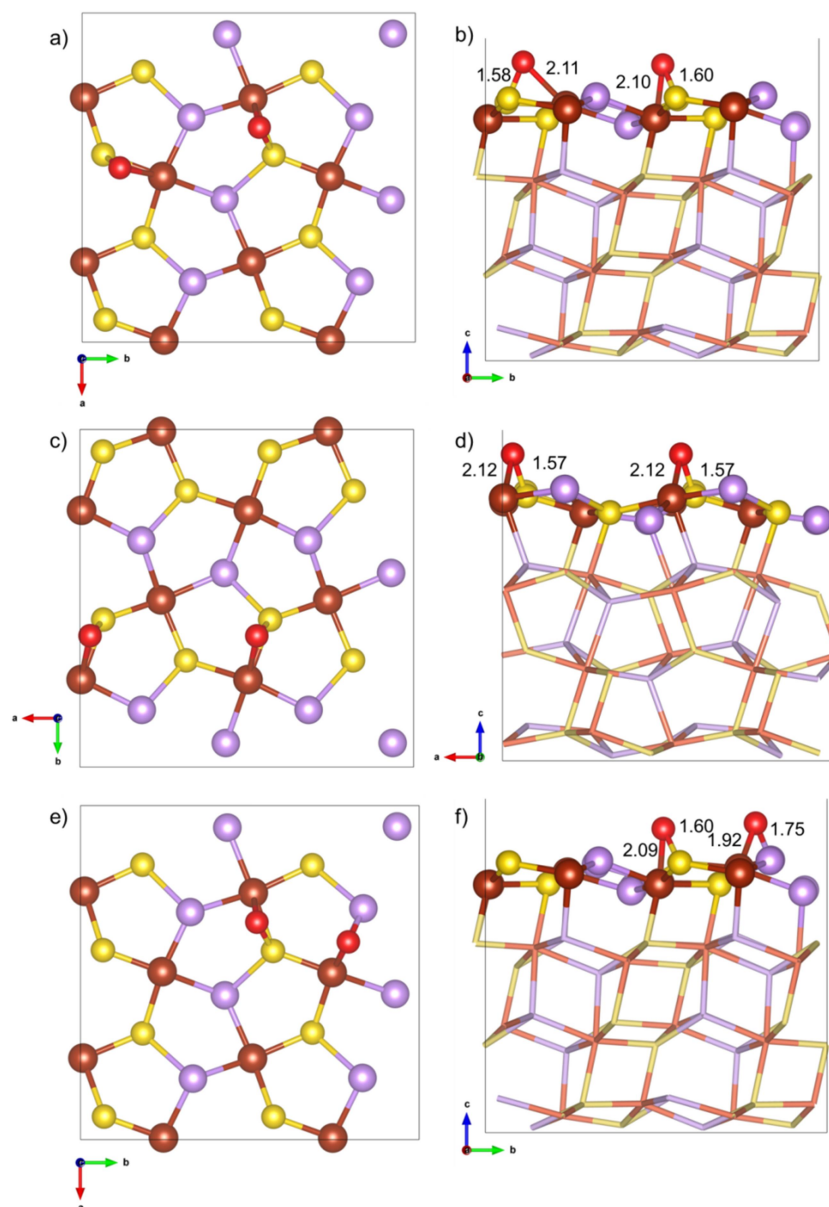


Figure 5.7: Dissociative adsorption of O<sub>2</sub> on the arsenopyrite (001) surface: a) Fe1 and Fe4 sites top view, b) Fe1 and Fe4 sites side view ( $E_{ad} = -29.7$  kcal mol<sup>-1</sup>); c) equivalent Fe3 sites top view, d) equivalent Fe3 sites side view ( $E_{ad} = -35.7$  kcal mol<sup>-1</sup>); e) Fe3 and Fe4 sites top view, f) Fe3 and Fe4 sites side view ( $E_{ad} = -39.9$  kcal mol<sup>-1</sup>). Yellow atoms are sulfur, brown are iron, red are oxygen and white are hydrogen.

The dissociative oxygen adsorption process could also lead to the structure in which the O atoms adsorb on top of the arsenic atoms, as shown in Figure 5.8, with  $E_{ad} = -40.2 \text{ kcal mol}^{-1}$ . It is more stable than the structure in Figure 5.4c and 5.4d ( $E_{ad} = -31.1 \text{ kcal mol}^{-1}$ ), where each O atom adsorbs to a Fe surface atom. Therefore the adsorption of an oxygen atom is more stable on an As than on a Fe surface atom. Rozgonyi and Stirling [4], Sacchi *et al.* [7], and Dos Santos *et al.* [6] observed the same for pyrite. The dissociative  $O_2$  adsorption prefers sulfur over iron atoms. But the adsorption energy in this case is higher (less stable) than for the bridge structure shown in Figures 5.6c and 5.6d. The dissociative  $O_2$  adsorption on sulfur atoms in the arsenopyrite surface is less favorable than on arsenic atoms, with  $E_{ad} = -26.3 \text{ kcal mol}^{-1}$ , as shown in Figure 5.9.

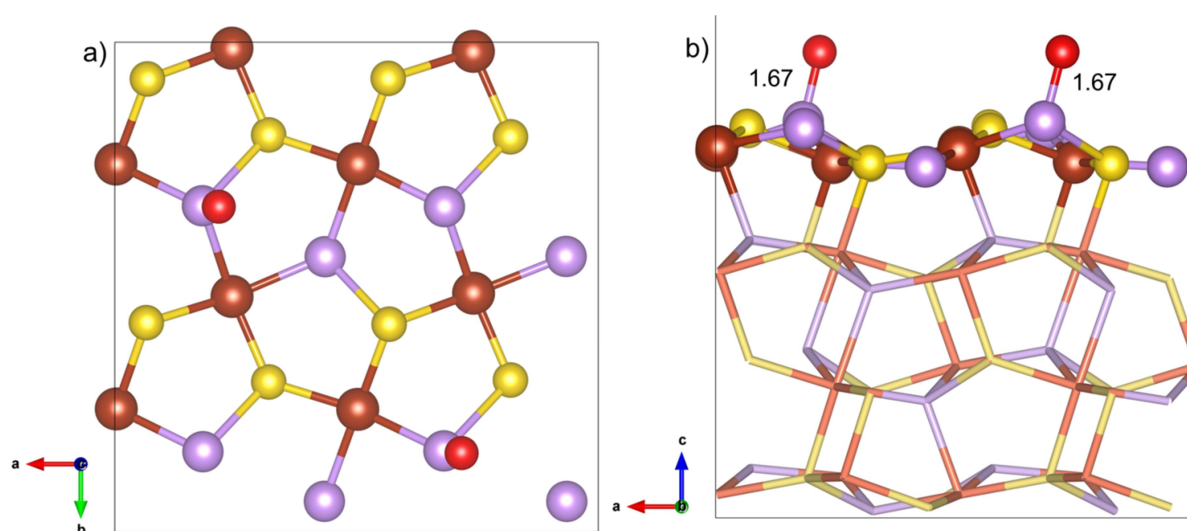


Figure 5.8: Dissociative adsorption of  $O_2$  on the arsenopyrite (001) surface on As atoms: a) top view, b) side view ( $E_{ad} = -40.2 \text{ kcal mol}^{-1}$ ). Yellow atoms are sulfur, brown are iron, red are oxygen and white are hydrogen.

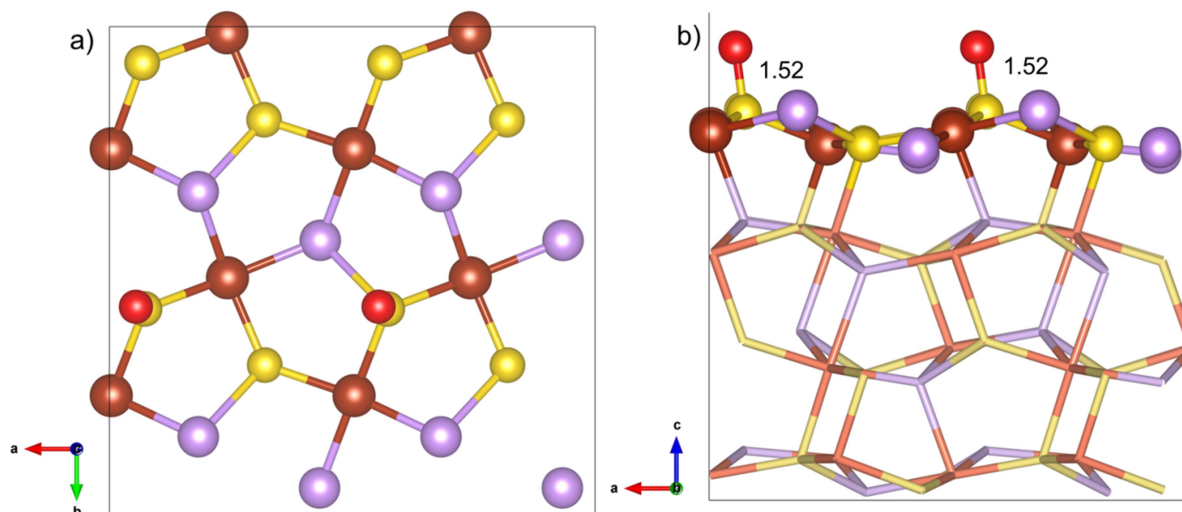


Figure 5.9: Dissociative adsorption of  $O_2$  on the arsenopyrite (001) surface on S atoms: a) top view, b) side view ( $E_{ad} = -26.3 \text{ kcal mol}^{-1}$ ). Yellow atoms are sulfur, brown are iron, red are oxygen and white are hydrogen.

Table 5.2 lists the adsorption energies and iron-oxygen distances of the most stable structures obtained in the study of  $O_2$  adsorption on arsenopyrite surface. It shows that the most stable structure is formed in the dissociative adsorption, where the O atom binds to Fe and As atoms forming a bridge (Figures 5.6c and 5.6d). In general the adsorption of oxygen on FeAsS surface is stronger than that of water or the other leaching agents probably due to the  $\pi$ -backdonation from the antibonding electron of the oxygen molecule to the iron atom.

Table 5.2: Adsorption energies and M–O distances for the  $O_2$  adsorption on the arsenopyrite (001) surface. M = Fe or As.

Species	Type	Sites	Adsorption Energy/kcal mol <sup>-1</sup>	M–O distance/Å
$O_2$	End-on	On top Fe1	-16.6	1.78
	Side-on	Bridge Fe2, Fe3	-6.2	1.90, 1.94
	Dissociative	On top Fe2, Fe3	-31.1	1.68, 1.64
	Dissociative	On top As, As	-40.2	1.67, 1.67
	Dissociative	On top S, S	-26.3	1.52, 1.52
	Dissociative	Bridge Fe2-As, Fe3-As	-59.1	2.07, 1.75; 1.88, 1.78

To summarize, initially the end-on adsorption is more favorable on the Fe1 site. Although the side-on adsorption between the Fe2 and Fe3 sites is less favorable than between the Fe1 and As sites, the dissociative energy of the side-on structure is  $-52.9 \text{ kcal mol}^{-1}$ , which makes the total process more favorable ( $E_{\text{ad}} = -59.1 \text{ kcal mol}^{-1}$ ) when the end-on adsorption is followed by the molecule dissociation (Figure 5.10). The breakage of the O–O bond is energetically favorable, yielding  $24.9 \text{ kcal mol}^{-1}$  of energy, with a low energy barrier of  $4.5 \text{ kcal mol}^{-1}$  (see Figure 5.11). Sit *et al.* [5] found a higher barrier of  $6.1 \text{ kcal mol}^{-1}$  for the dissociation of  $\text{O}_2$  on the pyrite surface, and a more favorable energy change of  $-26.2 \text{ kcal mol}^{-1}$ . Dos Santos *et al.* [6] found a barrier of  $5.4 \text{ kcal mol}^{-1}$  for the dissociation of  $\text{O}_2$  on the pyrite surface, comparable to our result, and an energy change of  $-23.9 \text{ kcal mol}^{-1}$ . Rozgonyi and Stirling [4] found a similar barrier of  $6.9 \text{ kcal mol}^{-1}$  for pyrite, and observed that the migration of the O atoms to sulfur sites leads to more stable structures with an energy barrier of  $13.4 \text{ kcal mol}^{-1}$ . Therefore the O migration was considered as the determining step in this dissociation.

The intermediate structure in Figure 5.10b presents a  $\text{Fe}^{4+}=\text{O}^{2-}$  species, which was used in the oxidation study of pyrite [5]. On pyrite [6], this type of adsorption has an energy of  $-40.2 \text{ kcal mol}^{-1}$ , while on arsenopyrite, it is  $-31.1 \text{ kcal mol}^{-1}$ . However, in the case of FeAsS, the O atoms can bind to neighboring As atoms, yielding a Fe–O–As bridge adsorption site, shown in Figure 5.10c. This bond formation brings great stability to this structure. It forms by an oxidation of both Fe and As to  $\text{Fe}^{3+}$  and  $\text{As}^0$  and a reduction of the O atoms to  $\text{O}^{2-}$ . The calculated  $\angle \text{Fe–O–As}$  angle is  $80.7^\circ$  on the Fe1 site and  $74.2^\circ$  on the Fe2 site. The presence of softer arsenic atom center in the arsenopyrite structure leads to a crucial difference in the adsorption of oxygen, which leads to the oxidation of both Fe and arsenic centers. This is completely distinct from what has been observed in our studies of pyrite oxidation [6]. The structure of Figure 5.10c is therefore the most stable structure found and it was considered in the next reaction steps of the oxidation of arsenopyrite.

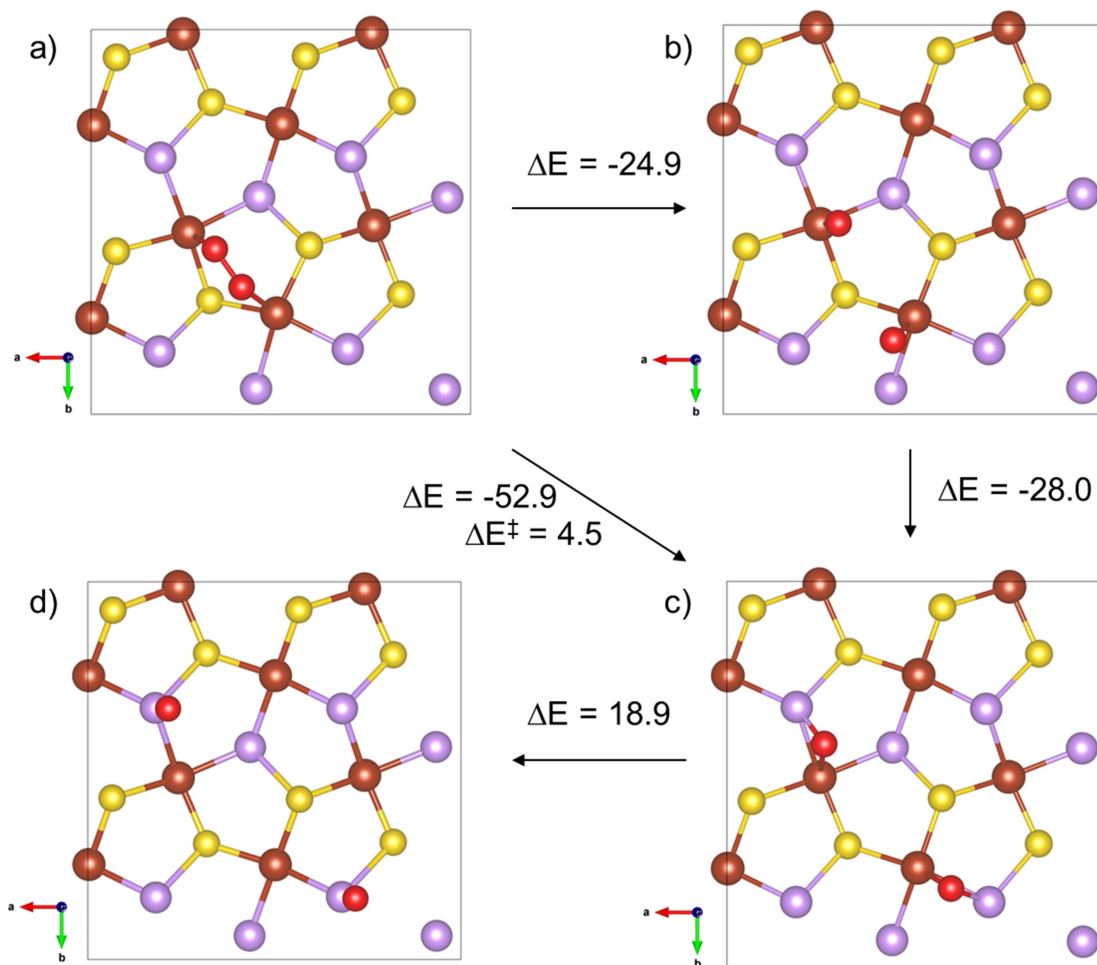


Figure 5.10: Dissociation of the  $O_2$  molecule on the arsenopyrite (001) surface. Yellow atoms are sulfur, brown are iron, red are oxygen and white are hydrogen. Energy values are in  $\text{kcal mol}^{-1}$ .

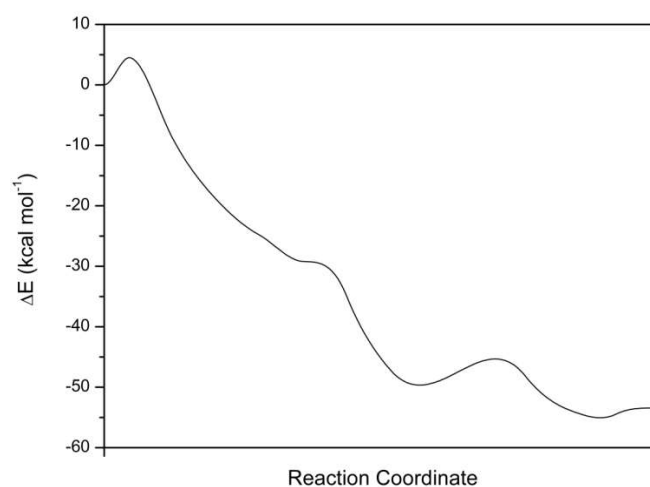


Figure 5.11: Energy barrier graph for the  $O_2$  dissociation on the arsenopyrite (001) surface.

Table 5.3 shows the effect of oxygen adsorption on the surface bonds in arsenopyrite. In general the bonds are elongated due to oxygen adsorption, either molecular or dissociative, except for the As–S bond, which keeps almost the same length since it is the strongest bond in the surface. This was also observed in the adsorption of other leaching agents in the previous chapter.

Table 5.3: Atomic distances on the arsenopyrite (001) surface as effect of oxygen adsorption. All distances are in Å.

	Pristine surface	Molecular	Dissociative
Fe – As*	2.323	2.360	2.372
Fe – S*	2.202	2.220	2.227
Fe – As axial	2.308	2.464	2.450
Fe – S axial	2.123	2.119	2.143
As – S*	2.374	2.375	2.372
Fe – O	-	1.783	2.065; 1.882

\*Average of the bonds around the adsorbed atom.

## 5.2 Adsorption of Oxygen and Water

Nesbitt *et al.* [9] observed that the oxidation of FeAsS proceeds to a greater extent in water than in air. The co-adsorption of water and oxygen on the arsenopyrite surface is also very favorable. The adsorption of one water molecule between two adsorbed oxygen atoms in hydrogen bonds has an energy of  $-7.1 \text{ kcal mol}^{-1}$  (see Figure 5.12a). When the water molecule adsorbs to a neighbor iron, it is  $-23.3 \text{ kcal mol}^{-1}$  (see Figure 5.12b), compared to the value of  $-32.3 \text{ kcal mol}^{-1}$  calculated by Sit *et al.* [5] in a similar structure for pyrite. The adsorption energy of two water molecules on the same surface, in which one molecule adsorbs to a Fe atom and the other one forms hydrogen bonding is  $-28.3 \text{ kcal mol}^{-1}$  (see Figure 5.12c). Therefore, these species must act together in a surface oxidation process. If the water molecules from the bulk water are considered interacting through hydrogen bonds to the adsorbed oxygen, the adsorption energy is higher,  $-10.7 \text{ kcal mol}^{-1}$  (see Figure 5.12d).

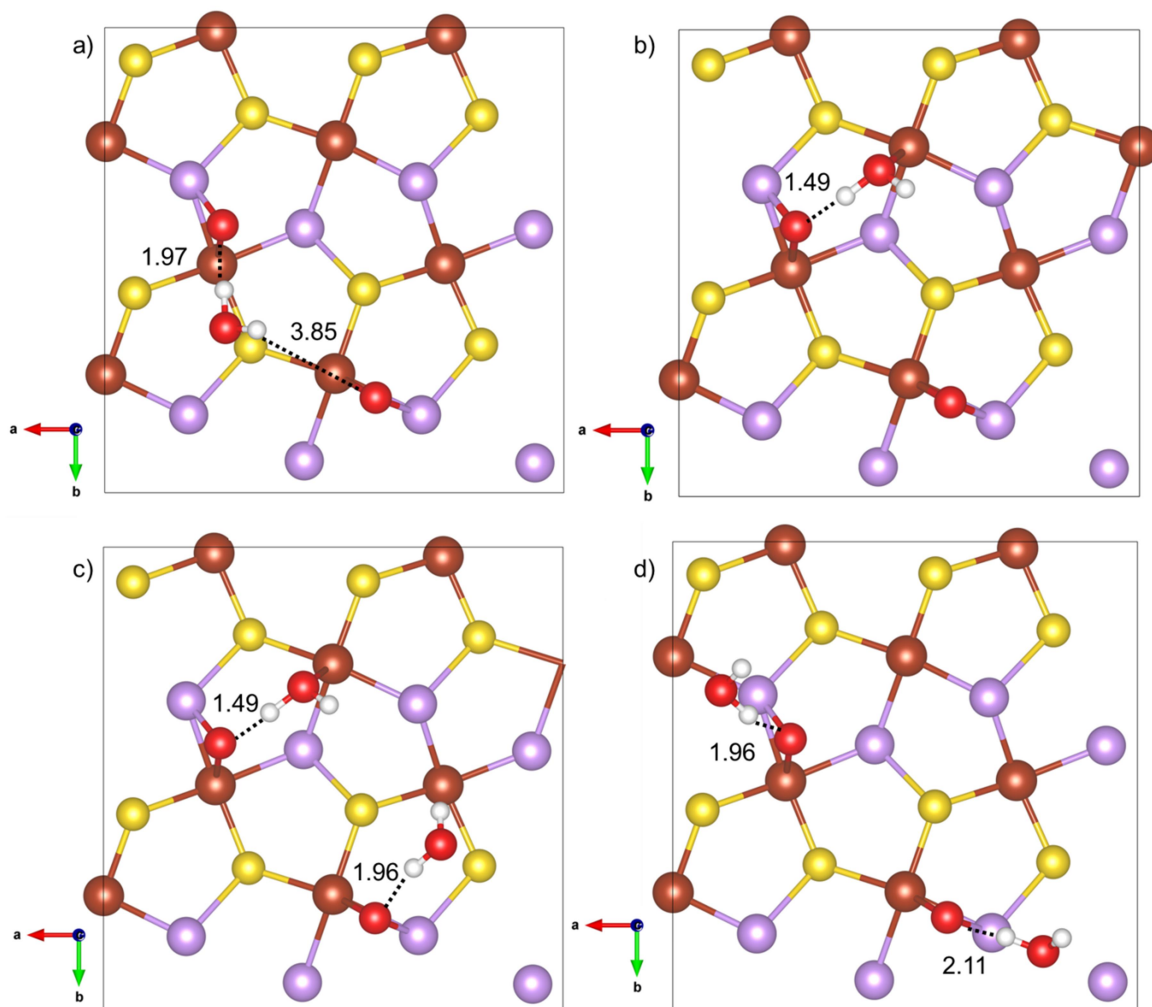


Figure 5.12: Co-adsorption of water and dissociated oxygen to the arsenopyrite (001) surface. Yellow atoms are sulfur, brown are iron, red are oxygen and white are hydrogen.

Nesbitt *et al.* [9] found the species  $O^{2-}$ ,  $OH^-$ ,  $H_2O$  and  $FeOOH$  on an oxidized arsenopyrite surface, besides the arsenic and sulfur compounds. An attempt to investigate the formation of the oxyhydroxide species is presented in Figure 5.13, where a water molecule is adsorbed in a dissociative mechanism to the oxygen end-on structure of Figure 5.2a in a stable compound. The adsorption energy is  $-30.8 \text{ kcal mol}^{-1}$ , a difference of  $\Delta E = -24.6 \text{ kcal mol}^{-1}$  compared to the end-on adsorbed oxygen. This value is close to the adsorption energy of pyrite [6] for the same species ( $-33.5 \text{ kcal mol}^{-1}$ ). Then this type of adsorption structure is favorable. This species is involved in an oxidation path proposed by De Lima *et al.* [10] for pyrite.

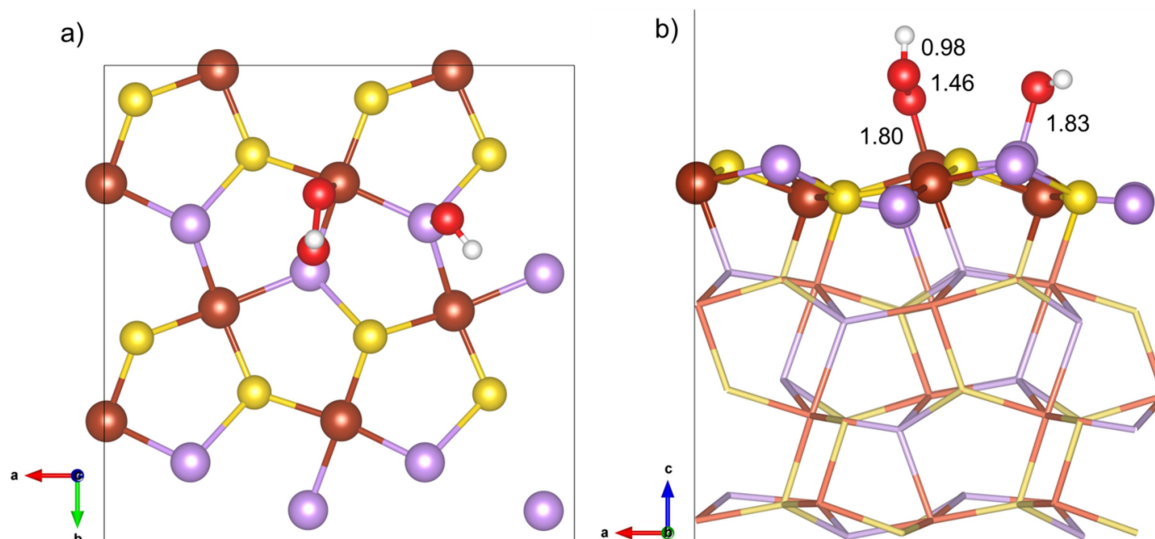


Figure 5.13: Co-adsorption of water and oxygen end-on to the arsenopyrite (001) surface. Yellow atoms are sulfur, brown are iron, red are oxygen and white are hydrogen.

Table 5.4 summarizes the different structures obtained for the co-adsorption of oxygen and water on arsenopyrite (001) surface. The most stable structures are the ones in which a water molecule adsorbed to an iron atom makes hydrogen bonds with an oxygen adsorbed in a bridge of the Fe–O–As type.

Table 5.4: Adsorption energies and Fe–O distances in O<sub>2</sub> and H<sub>2</sub>O adsorption on the arsenopyrite (001) surface.

Species	Type	Sites	Adsorption Energy/kcal mol <sup>-1</sup>	Fe–O distance/Å
O <sub>2</sub> + H <sub>2</sub> O	O <sub>2</sub> bridge, H <sub>2</sub> O H bond	Fe2, Fe3	-66.2	2.09, 1.88
	O <sub>2</sub> bridge, H <sub>2</sub> O adsorbed on Fe1	Fe2, Fe3	-82.4	2.13, 1.89
	O <sub>2</sub> end-on, H <sub>2</sub> O dissociative	Fe1	-30.8	1.80
O <sub>2</sub> + 2H <sub>2</sub> O	O <sub>2</sub> bridge, H <sub>2</sub> O adsorbed on Fe1	Fe2, Fe3	-87.4	2.13, 1.92
	O <sub>2</sub> bridge, H <sub>2</sub> O H bond	Fe2, Fe3	-69.8	2.10, 1.92

If the surface is fully covered by water, it is also possible to adsorb oxygen substituting the water molecules, as shown in Figures 5.14 and 5.15. In the first case, the oxygen end-on adsorption is capable of substituting a water molecule and release  $-6.0 \text{ kcal mol}^{-1}$  of energy. In the second case, the dissociative oxygen adsorption is capable of substituting two water molecules bound to the surface with and energy of  $-43.8 \text{ kcal mol}^{-1}$ .

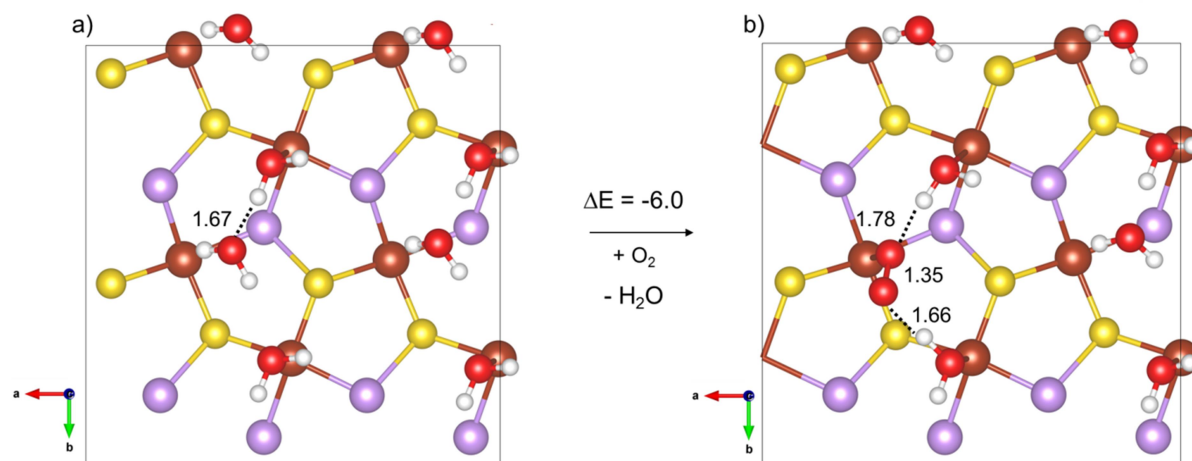


Figure 5.14: Substitution of one water molecule for an  $\text{O}_2$  molecule on the arsenopyrite (001) surface. Yellow atoms are sulfur, brown are iron, red are oxygen and white are hydrogen.

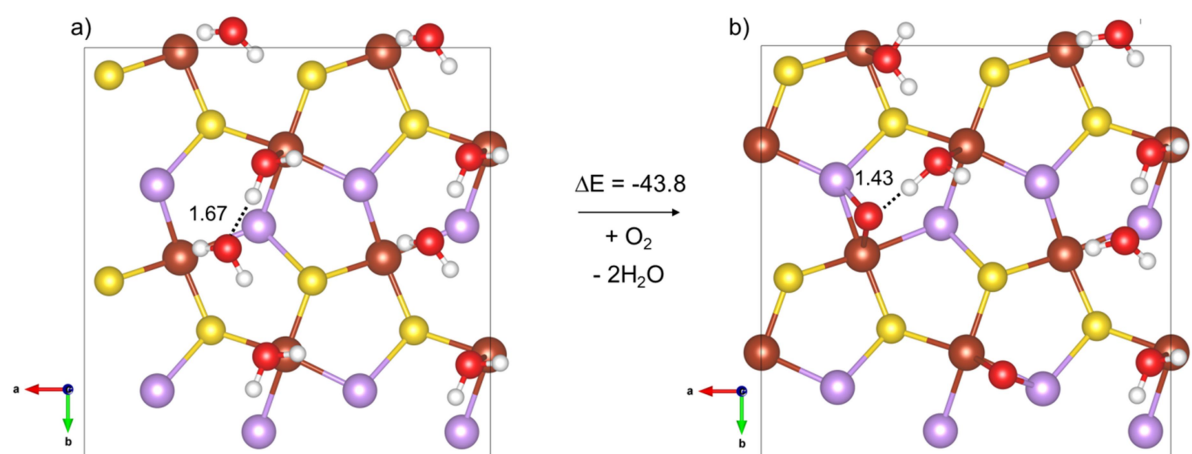


Figure 5.15: Substitution of two water molecules for an  $\text{O}_2$  molecule on the arsenopyrite (001) surface. Yellow atoms are sulfur, brown are iron, red are oxygen and white are hydrogen.

A molecular dynamics study could give further information about the co-adsorption of water and oxygen on the arsenopyrite surface; however, this is beyond the present stage of our computer capability.

### 5.3 Oxidation Reaction

After having investigated the adsorption of water and O<sub>2</sub> on the arsenopyrite (001) surface, we are now able to propose a reaction path for its oxidation. One possibility is the donation of a H<sup>+</sup> or H radical from water molecules to the adsorbed O atoms on the surface, as considered by Dos Santos *et al.* [6] and by Sit *et al.* [5] for pyrite. The same mechanism was investigated for arsenopyrite, leading to the results shown in Figure 5.16. The process starts with the dissociative adsorption of an O<sub>2</sub> molecule on the arsenopyrite surface. By this, the Fe and As atoms are oxidized to Fe<sup>3+</sup> and As<sup>0</sup>. Subsequently, a water molecule approaches the O adsorbed, with  $\Delta E = -1.2 \text{ kcal mol}^{-1}$ . This water molecule donates a radical H to the O adsorbed and the OH· group binds to the neighbor As, which keeps the oxidation state 0 because the As–O bond is substituted by an As–OH bond. The energy change is  $\Delta E = -15.2 \text{ kcal mol}^{-1}$  and the energy barrier  $12.0 \text{ kcal mol}^{-1}$  (Figure 5.17a). This step is similar to the one calculated by Dos Santos *et al.* [6] for pyrite, in which the OH group binds instead to a Fe atom, with energy barrier of  $5.0 \text{ kcal mol}^{-1}$  and  $\Delta E = -5.3 \text{ kcal mol}^{-1}$ . Sit *et al.* [5] found values of  $\Delta E = 0.6 \text{ kcal mol}^{-1}$  and a barrier of  $2.9 \text{ kcal mol}^{-1}$  in a similar H donation. In the oxidation of arsenopyrite, the previous step is repeated with the second O adsorbed, with a water adsorption energy of  $-5.5 \text{ kcal mol}^{-1}$ . The donation of H yields  $-9.1 \text{ kcal mol}^{-1}$  of energy and has an energy barrier of  $22.0 \text{ kcal mol}^{-1}$  (Figure 5.17b). Compared to pyrite [6], the energy changes are more favorable in the last steps, but the barriers are higher.

Next, another water molecule adsorbs to a neighbor Fe atom, with  $-22.6 \text{ kcal mol}^{-1}$  of energy and donates a radical H to the adsorbed OH group, forming water and reducing the initial oxidized Fe again to Fe<sup>2+</sup>. This process yields  $-1.3 \text{ kcal mol}^{-1}$  of energy, with a very low barrier of  $0.2 \text{ kcal mol}^{-1}$  (Figure 5.17c). Again another water molecule approaches, yielding  $-9.6 \text{ kcal mol}^{-1}$  of energy and donates a H to the other OH group with an energy barrier of  $5.0 \text{ kcal mol}^{-1}$

(Figure 5.17d) and  $\Delta E = -11.6 \text{ kcal mol}^{-1}$ . In this process a new surface As atom is oxidized to  $\text{As}^0$ . Compared to pyrite [6], this second H donation is less favorable, but with lower energy barriers. All the steps investigated for FeAsS oxidation are energetically favorable, and preliminary results for the energy barrier indicate that this reaction mechanism is relatively low compared to the pyrite oxidation mechanism. The values of energy barriers are still in process of calculation, which takes a long time to converge, but the preliminary results shows that they are not larger than  $22.0 \text{ kcal.mol}^{-1}$ . These results are not yet converged due to the complexity and difficulty of these NEB calculations.

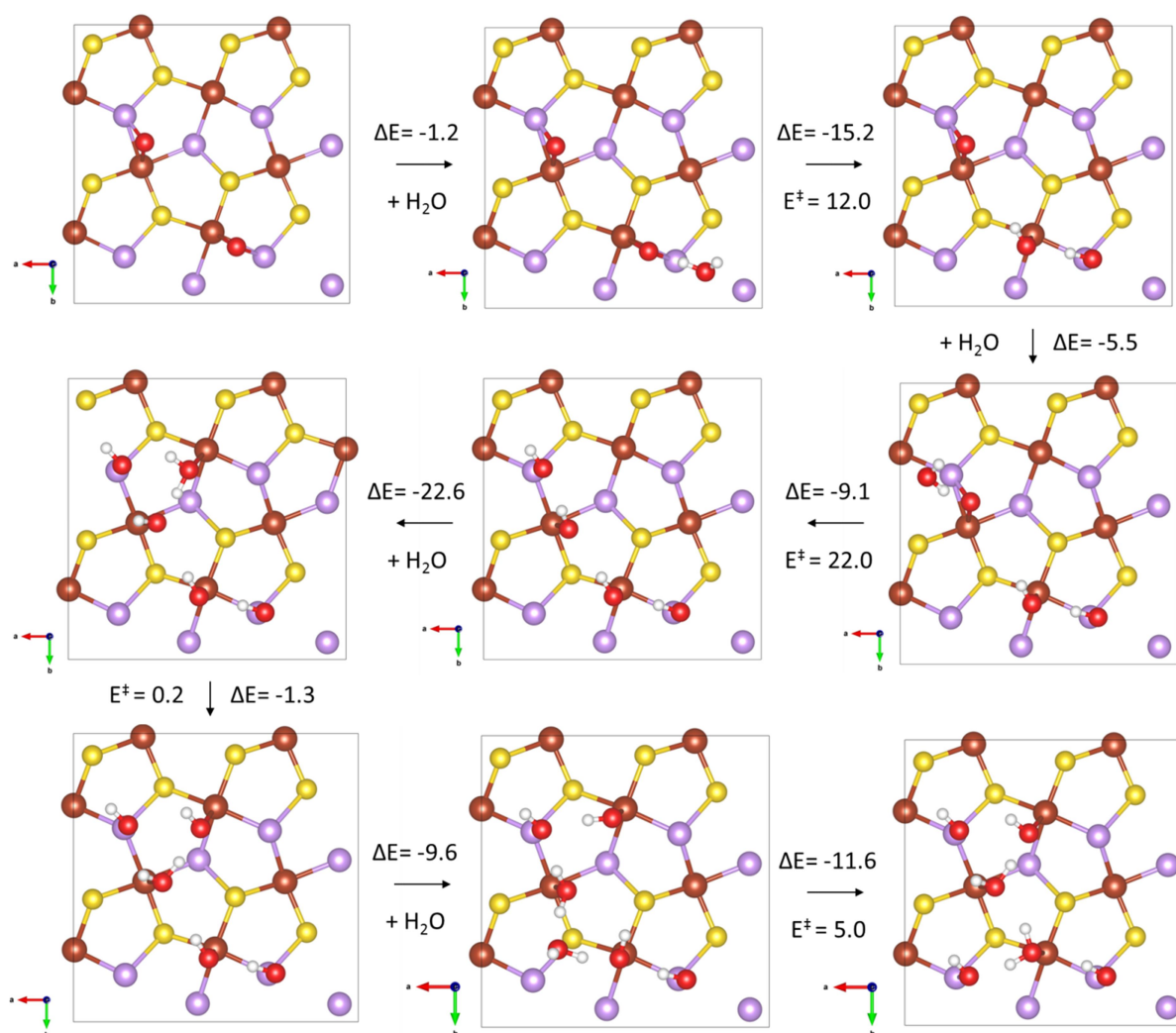


Figure 5.16: Proposed oxidation reaction for the arsenopyrite (001) surface. All energies are in  $\text{kcal mol}^{-1}$ . Yellow atoms are sulfur, brown are iron, red are oxygen and white are hydrogen.

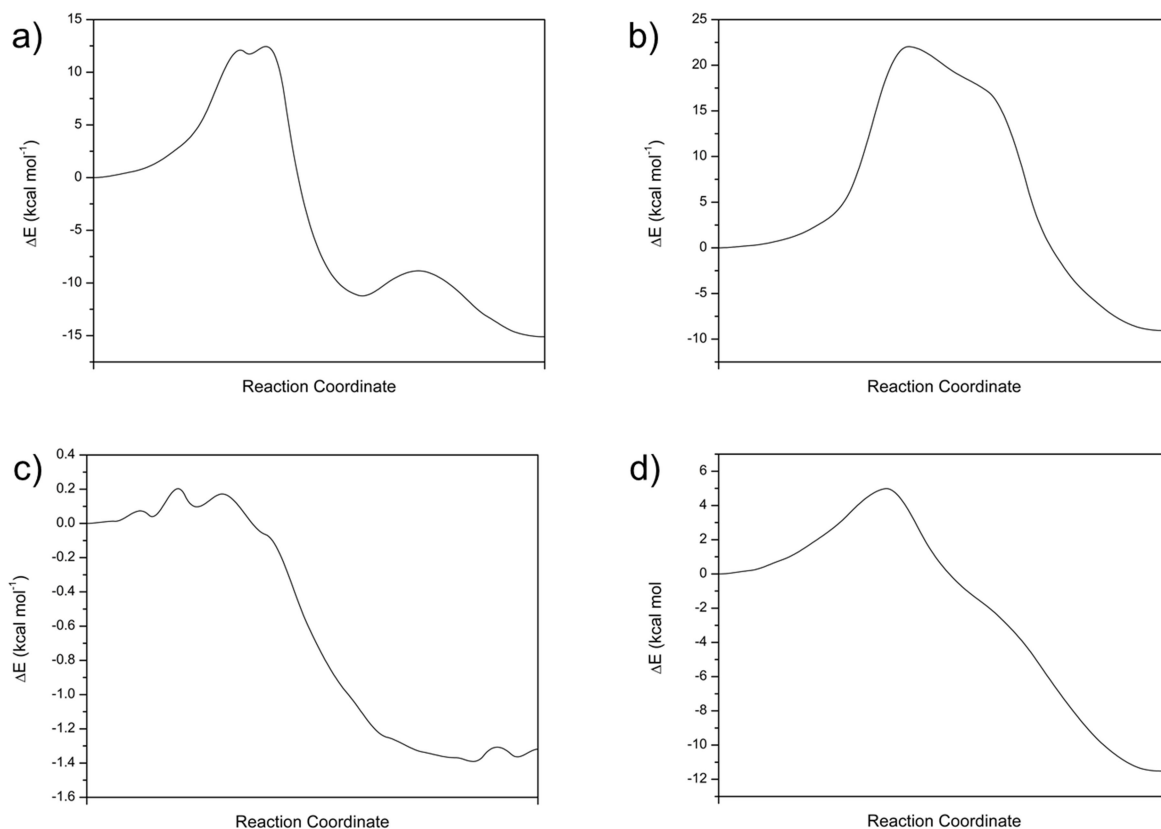


Figure 5.17: Minimum Energy Paths for the H donation reactions in the oxidation of arsenopyrite.

A variation of the previous mechanism includes the bonding of the OH groups to the S atom instead of the As atom (see Figure 5.18a). As expected, this situation is less stable than the previous one, by  $17.8 \text{ kcal mol}^{-1}$ . The situation where two OH groups are bonded to S atoms is  $47.8 \text{ kcal mol}^{-1}$  less stable than in the case of As bond (Figure 5.18b). In an attempt to form OH groups that are only connected to the Fe and S atoms was unsuccessful (Figure 5.18c). One of the OH groups donates a H atom to form water on top of Fe. The energy involved is estimated to be  $30.8 \text{ kcal mol}^{-1}$ , higher than for the structure involving As, i.e., it is less stable. Therefore the first steps in the arsenopyrite oxidation must involve the reaction of the As rather than the S atom.

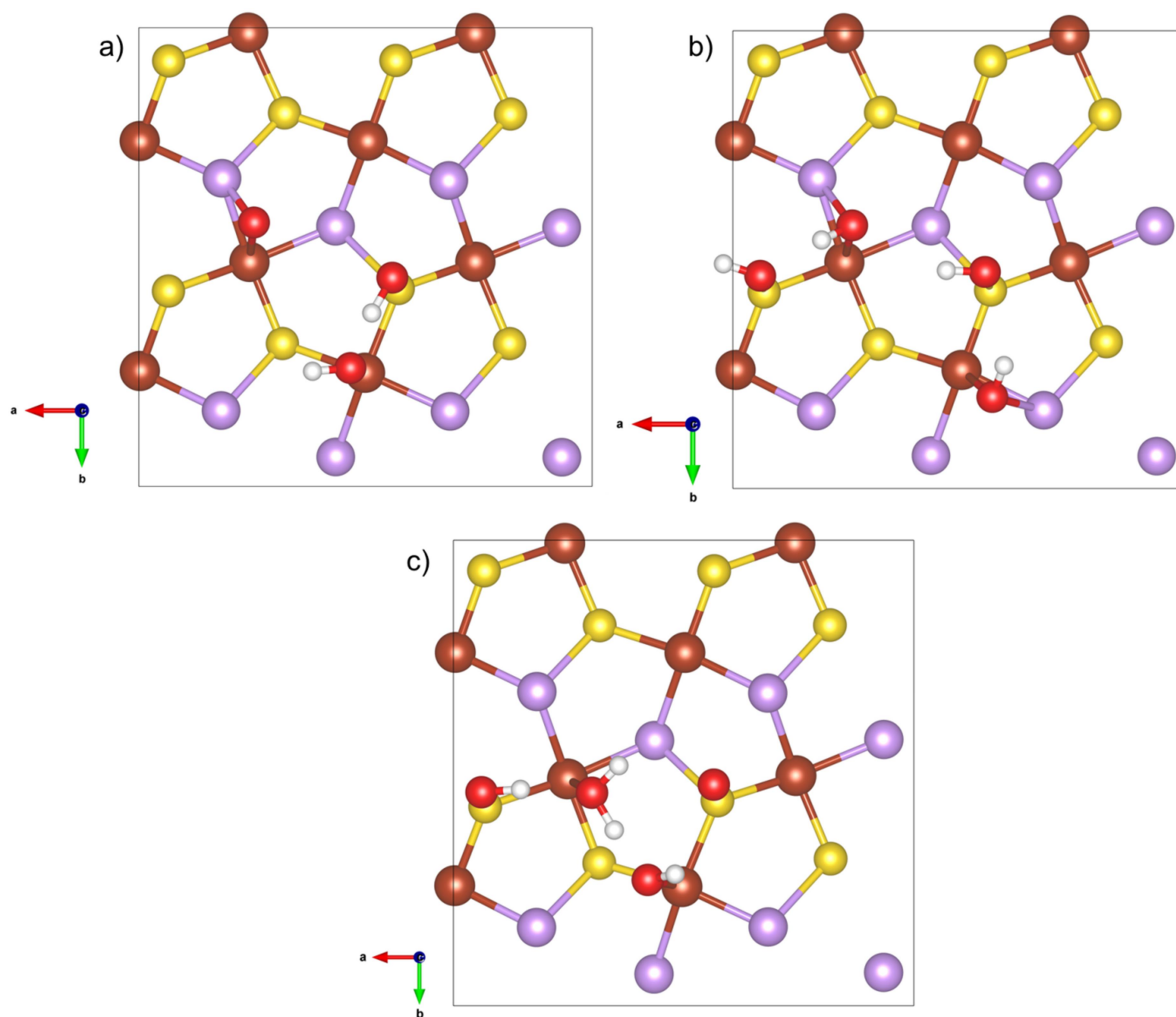


Figure 5.18: OH groups bound to S atoms in the oxidation reaction of the arsenopyrite (001) surface. Yellow atoms are sulfur, brown are iron, red are oxygen and white are hydrogen.

If the OH group bound to the Fe atom in the last structure of Figure 5.16 is moved to an As atom, thereby oxidizing it and reducing the Fe, the structure is  $5.0 \text{ kcal mol}^{-1}$  more stable than the previous one (see Figure 5.19). This shows that in the beginning of the oxidation process in arsenopyrite, the surface Fe atoms are oxidized and then recovered to  $\text{Fe}^{2+}$ , in accordance with equation 5.1.

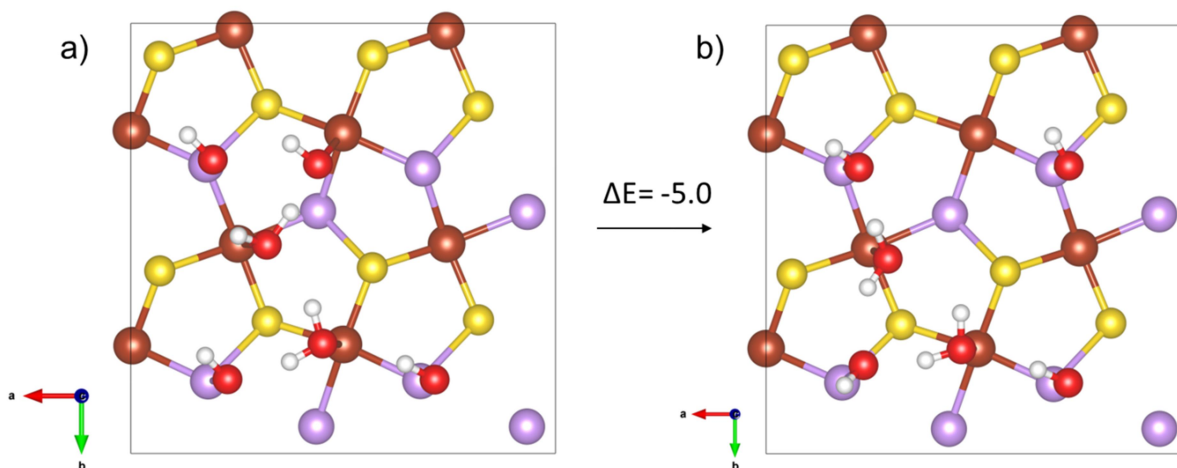


Figure 5.19: Migration of the OH group from an Fe atom to an As atom on the arsenopyrite surface. Yellow atoms are sulfur, brown are iron, red are oxygen and white are hydrogen.

The highest energy barrier observed in the previous reaction steps was  $22.0 \text{ kcal mol}^{-1}$  for the donation of one H from water to the adsorbed O and the adsorption of OH to As. This value is in the range of the ones found by Sit *et al.* [5] for the oxidation of the surface of pyrite. As discussed by these authors, this value of the energy barrier makes the reaction process slow, but it is still possible at room temperature. It should be noted that the method used in this study considers the system as a perfect crystal at 0K. Finite temperature and defects on the surface can decrease this value. Experimentally Yu *et al.* [3] found a value of  $13.6 \text{ kcal mol}^{-1}$  for the activation energy of arsenopyrite in the reaction with  $\text{O}_2$  at pH 5.9.

In an attempt similar to the one of Sit *et al.* [5] for pyrite, the formation of  $\text{AsO}_4^{3-}$  was investigated in the oxidation reaction of arsenopyrite. The structure shown in Figures 5.5c and 5.5d is the most readily obtained by geometry optimization and it was used here to compare with the results of Sit *et al.* [5] for pyrite. Figure 5.20 shows the structures obtained with the respective energies. In the first reaction, water and oxygen adsorb to the FeAsS (001) surface yielding  $-64.2 \text{ kcal mol}^{-1}$ . Then, the water molecule donates both hydrogens to the adsorbed oxygens, and the remaining oxygen adsorbs to arsenic with  $\Delta E = -8.3 \text{ kcal mol}^{-1}$ . This process is less favorable than the corresponding one in pyrite ( $-23.8 \text{ kcal mol}^{-1}$ ) [5]. The As atom is oxidized to  $\text{As}^{+1}$ . A second water molecule approaches, yielding  $-17.6 \text{ kcal mol}^{-1}$  of energy, which is more favorable

than the process in pyrite, with  $-5.6 \text{ kcal mol}^{-1}$  [5]. This water molecule donates again both hydrogens to the formed OH groups and again the remaining second oxygen is bound to the same arsenic atom. The last step is not favorable, since its energy is positive ( $0.58 \text{ kcal mol}^{-1}$ ). However, the value is small, under  $1 \text{ kcal mol}^{-1}$ , and it can easily become favorable at higher temperature or near a surface defect. A similar energy was found by Sit *et al.* [5] for pyrite in the same reaction step. In the following, the water molecules formed are desorbed and a new set of oxygen and water molecules adsorb to the iron sites on the surface with  $-50.1 \text{ kcal mol}^{-1}$  energy, which is much more favorable than the same process in pyrite ( $-8.4 \text{ kcal mol}^{-1}$ ) [5]. Again the water molecule donates both hydrogens to the adsorbed oxygen atoms and the remaining third oxygen is bound to the As, forming  $\text{AsO}_3^{3-}$  and yielding  $-3.9 \text{ kcal mol}^{-1}$ , which is much less favorable than the same step in pyrite ( $-32.1 \text{ kcal mol}^{-1}$ ) [5].

A last water molecule adsorbs with  $-17.1 \text{ kcal mol}^{-1}$  and donates both hydrogens to the OH groups on the surface and the fourth oxygen atom binds to the As atom. This last step is not favorable, requiring  $11.6 \text{ kcal mol}^{-1}$  of energy, but all the other previous steps are exothermic. In the reaction of pyrite, this last step is favorable with  $\Delta E = -48.6 \text{ kcal mol}^{-1}$  [5]. But the species formed is different in the case of pyrite,  $\text{SO}_4^{2-}$ . Therefore, in arsenopyrite, the formation of  $\text{As(III)O}_3^{3-}$  is energetically more favorable than the species  $\text{As(V)O}_4^{3-}$ , in agreement with the experimental observations of Yu *et al.* [3], in which As(III) was determined as the dominant redox species. The formation of  $\text{AsO}_4^{3-}$  might be more favorable in solution than on the surface.

Compared to pyrite, the structures involving water adsorption are more stable in the FeAsS reaction, while the proton donation was more favorable in the  $\text{FeS}_2$  reaction. The energy barriers for each of the proposed steps still need to be calculated in order to confirm that this reaction path is favorable. However, Table 5.5 shows a comparison of the  $\text{p}K_a$  and standard electrochemical potentials  $\Delta E^\circ(\text{V})$  of arsenic and sulfur aqueous species. It is clear that at pH about 7 the predominant species are  $\text{SO}_4^{2-}$  and  $\text{HSO}_3^-$ ,  $\text{HAsO}_4^{2-}$  and  $\text{H}_3\text{AsO}_3$ . Therefore, it is expected that the formation of this species adsorbed on the surface will be followed by their partial protonation. Furthermore, the standard electrochemical potential of reduction of these species indicates that the oxidation of  $\text{H}_3\text{AsO}_3$  is less favorable than  $\text{H}_2\text{SO}_3$ , in

agreement with our estimates that arsenite must be the preferential product in the arsenopyrite oxidation, while sulfate must be the preferential product in the pyrite reaction.

Table 5.5:  $pK_a$  and standard electrochemical potentials for arsenic and sulfur aqueous species [11].

Species	$pK_a$	$\Delta E^\circ(V)(red)$
$H_2SO_3$	1.85; 7.2	S(VI)/S(IV) = +0.172
$H_2SO_4$	Strong, 1.99	
$H_3AsO_3$	9.29	As(V)/As(III) = +0.56
$H_3AsO_4$	2,26; 6.76; 11.29	

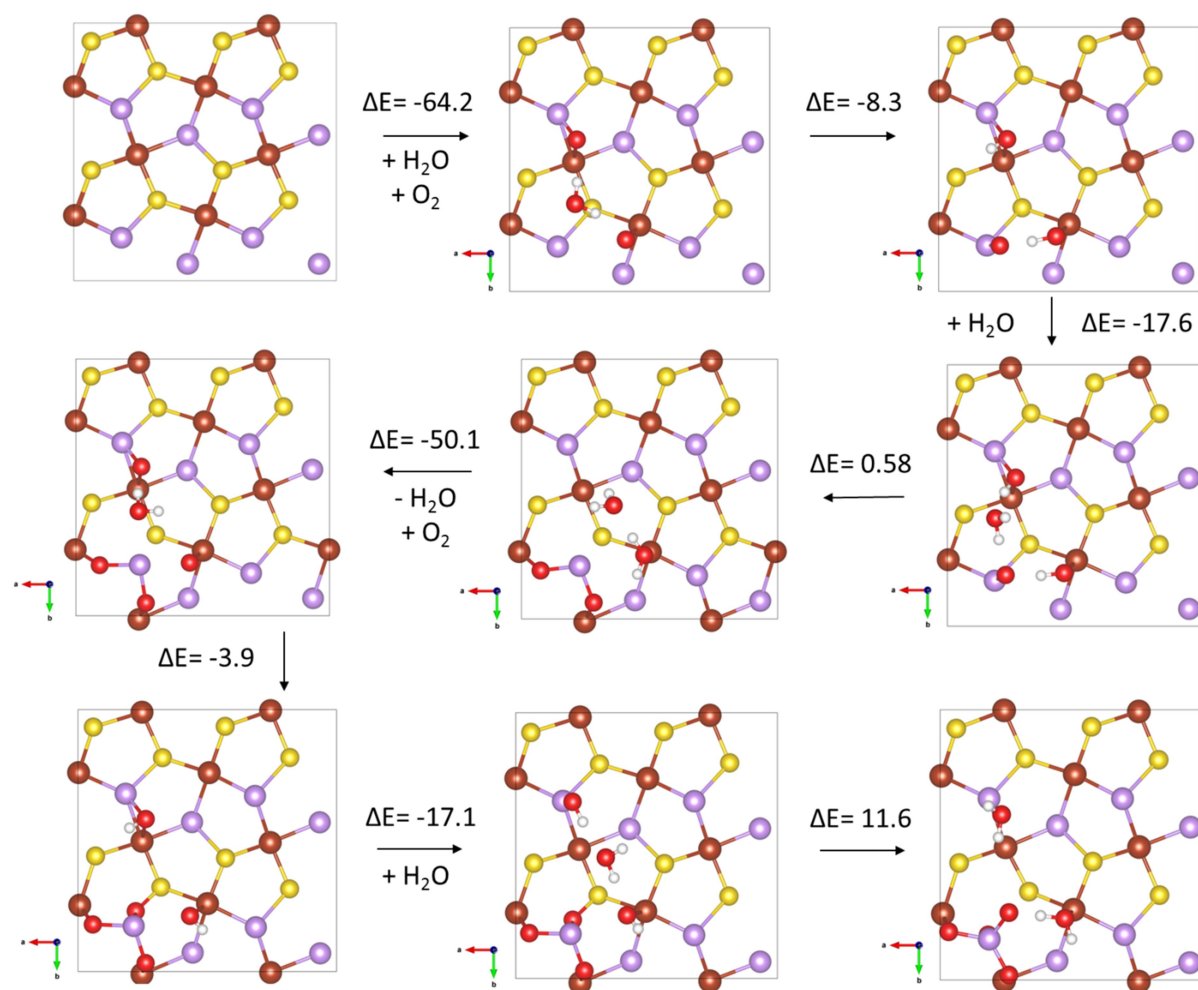


Figure 5.20: Reaction steps for the formation of  $AsO_4^{3-}$  on the FeAsS (001) surface. Yellow atoms are sulfur, brown are iron, red are oxygen and white are hydrogen.

## 5.4 Final Considerations

Molecular oxygen is strongly adsorbed to FeAsS (001) surface, especially in dissociative form. The energy barrier for this dissociation is low and the adsorbed structure forms are very stable, mainly the ones that form a Fe–O–As bridge, not yet observed for pyrite. Co-adsorption of oxygen and water, necessary for the oxidation of arsenopyrite, is also favorable. One oxygen molecule is able to replace adsorbed water molecules on the surface.

Two possible mechanisms for the initial steps in the oxidation of FeAsS are proposed: one involving the donation of H radicals from water to the adsorbed O atoms on the surface, and one involving the formation of As(III)O<sub>3</sub><sup>3-</sup>. Both mechanisms are energetically possible and are in agreement with isotopic labeling experiments on pyrite [12] that suggested the oxygens from the sulfur oxide are derived from water and those from oxyhydroxide from O<sub>2</sub>. The results are in agreement with Corkhill *et al.* [13], Nesbitt *et al.* [9] and Schaufuss *et al.* [14], who observed that As is more readily oxidized than Fe and S. Our results also agree with Walker *et al.* [2], who proposed that the rate-determining step of FeAsS oxidation reaction is the attachment of oxygen from water to the As and S species. The lower energy barriers in the oxidation of arsenopyrite compared to pyrite suggest that the oxidation of the former mineral is faster than the latter, in accordance with the observations of McKibben *et al.* [1].

## 5.5 References

1. McKibben, M.A., B.A. Tallant, and J.K. del Angel, *Kinetics of inorganic arsenopyrite oxidation in acidic aqueous solutions*. Applied Geochemistry, 2008. **23**(2): p. 121-135.
2. Walker, F.P., M.E. Schreiber, and J.D. Rimstidt, *Kinetics of arsenopyrite oxidative dissolution by oxygen*. Geochimica et Cosmochimica Acta, 2006. **70**(7): p. 1668-1676.
3. Yu, Y., et al., *Rates of Arsenopyrite Oxidation by Oxygen and Fe(III) at pH 1.8–12.6 and 15–45 °C*. Environmental Science & Technology, 2007. **41**(18): p. 6460-6464.
4. Rozgonyi, T. and A. Stirling, *DFT Study of Oxidation States on Pyrite Surface Sites*. The Journal of Physical Chemistry C, 2015. **119**(14): p. 7704-7710.

5. Sit, P.H.L., M.H. Cohen, and A. Selloni, *Interaction of Oxygen and Water with the (100) Surface of Pyrite: Mechanism of Sulfur Oxidation*. Journal of Physical Chemistry Letters, 2012. **3**(17): p. 2409-2414.
6. Dos Santos, E.C., J.C. de Mendonça Silva, and H.A. Duarte, *Pyrite Oxidation Mechanism by Oxygen in Aqueous Medium*. The Journal of Physical Chemistry C, 2016. **120**(5): p. 2760-2768.
7. Sacchi, M., M.C.E. Galbraith, and S.J. Jenkins, *The interaction of iron pyrite with oxygen, nitrogen and nitrogen oxides: a first-principles study*. Physical Chemistry Chemical Physics, 2012. **14**(10): p. 3627-3633.
8. Li, Y.-Q., J.-H. Chen, and J. Guo, *DFT study of influences of As, Co and Ni impurities on pyrite (100) surface oxidation by O<sub>2</sub> molecule*. Chemical Physics Letters, 2011. **511**(4-6): p. 389-392.
9. Nesbitt, H.W., I.J. Muir, and A.R. Prarr, *Oxidation of arsenopyrite by air and air-saturated, distilled water, and implications for mechanism of oxidation*. Geochimica et Cosmochimica Acta, 1995. **59**(9): p. 1773-1786.
10. de Lima, G.F., H. Avelino de Abreu, and H. Anderson Duarte, *Chapter 6 Surface reactivity of the sulfide minerals*, in *Chemical Modelling: Volume 10*. 2014, The Royal Society of Chemistry. p. 153-182.
11. Rankin, D.W.H., *CRC handbook of chemistry and physics, 89th edition, edited by David R. Lide*. Crystallography Reviews, 2009. **15**(3).
12. Usher, C.R., et al., *Mechanistic Aspects of Pyrite Oxidation in an Oxidizing Gaseous Environment: An in Situ HATR-IR Isotope Study*. Environmental Science & Technology, 2005. **39**(19): p. 7576-7584.
13. Corkhill, C.L., et al., *The oxidative dissolution of arsenopyrite (FeAsS) and enargite (Cu<sub>3</sub>AsS<sub>4</sub>) by Leptospirillum ferrooxidans*. Geochimica et Cosmochimica Acta, 2008. **72**(23): p. 5616-5633.
14. Schaufuss, A.G., et al., *Reactivity of surface sites on fractured arsenopyrite (FeAsS) toward oxygen*. American Mineralogist, 2000. **85**(11-12): p. 1754-1766.

## 6 Concluding Remarks and Perspectives

Investigation of the sulfides reactions involved in the acid rock drainage process is a challenge to engineers and chemists because of their complexity. Chemistry can contribute in this area with information about the surface structure, the species formed and the reaction mechanism. In this way, theoretical calculations can help with information at a molecular level based on chemical models. However, the computer simulation of sulfides, especially in contact with an aqueous medium, can be a challenge due to the size of the system, the choice of a proper method and of a realistic model able to describe it.

In order to investigate the bonding nature of arsenopyrite (FeAsS) and, consequently, its reactivity towards the oxidation, different methods of chemical bond analysis, such as quantum theory of atom in molecules (QTAIM), electron localization function (ELF), density of states (DOS) and band structure have been used. The main concepts supporting these methods have been reviewed in this thesis. Structural and mechanical properties have also been calculated and the values estimated based on the DFT/PW method.

The calculated structural parameters of arsenopyrite bulk are in good agreement with the available experimental data. The results based on QTAIM and ELF indicate that iron centers have an oxidation state equal to +2, and no Fe–Fe bond was found in the FeAsS in spite of its short distance of 2.67 Å. Based on QTAIM analysis, the Fe–As and Fe–S bonds have ionic character, while the As–S bonds have covalent character and are the strongest bonds in the crystal. In fact, one should propose that arsenopyrite is coherent with the formula  $\text{Fe}^{2+}(\text{AsS})^{2-}$ . This strong As–S bond is unlike to be broken during the surface formation.

In the development of this work some difficulties were found inherent to the fact that the experimental results reported in the literature are scarce and, from the viewpoint of crystallography, partly ambiguous. There is no consensus among authors regarding the preferential cleavage surface of arsenopyrite, and crystallographic definitions can lead to wrong conclusions. We unveiled this unclear aspect of the literature and tried to make a clear analysis of the structure and an adequate crystallographic analysis [1]. Therefore, we started the study of the surface reactivity investigating the water adsorption on the (101) surface of arsenopyrite. To

realize the incongruity of the published results, we decided to conduct a detailed study on the cleavage energy of arsenopyrite, leading us to conclude that the (001), (010) and (100) planes are the preferential cleavage surfaces because they have the lowest surface energies. Surface (001) has been chosen for adsorption and oxidation studies because it has the lowest surface energy ( $1.05 \text{ J m}^{-2}$ ) and exposes all elements of arsenopyrite to the surface. Therefore it is considered the best model to study the oxidation of arsenopyrite. The exposition of the iron centers on the surface lead the system to present partial spin polarization, which has to be adequately treated. The other (010) and (100) surface energies are at maximum  $0.04 \text{ J m}^{-2}$  higher in energy.

The first step for the oxidation of arsenopyrite is the adsorption of the leaching agents on its surface. Therefore, we have investigated the adsorption of water, hydrochloric acid (HCl) and sulfuric acid ( $\text{H}_2\text{SO}_4$ ) on the (001) surface. The DOS analysis shows that the iron atom is the preferred site for adsorption on this surface, which presents two different iron sites: Fe1, more sterically exposed, and Fe2, less exposed. Water is adsorbed molecularly on the Fe1 sites with  $E_{\text{ad}} = -10.8 \text{ kcal mol}^{-1}$ . On less stable surfaces, the water molecule adsorbs stronger because these surfaces are expected to be more reactive. Dissociative adsorption of water is not stable. In a full coverage of water on this surface, each Fe1 site adsorbs one molecule. The molecules that could be adsorbed at Fe2 sites prefer to form a second solvation layer. Hydrochloric acid adsorbs dissociatively on the surface, with  $E_{\text{ad}} = -11.3 \text{ kcal mol}^{-1}$  when the  $\text{H}^+$  binds to an As atom. Sulfuric acid presented the most stable structure as protonated, in monodentate mononuclear coordination, with  $E_{\text{ad}} = -13.5 \text{ kcal mol}^{-1}$ . However it is present only in pH close to zero, which is not achieved in the environment. Bisulfate ( $\text{HSO}_4^-$ ) can adsorb in bidentate binuclear coordination with  $E_{\text{ad}} = -10.7 \text{ kcal mol}^{-1}$ , while sulfate ( $\text{SO}_4^{2-}$ ) adsorption is not stable. Arsenic turns out to be a stronger Lewis base, i.e., a better site for adsorption of  $\text{H}^+$  than sulfur.

This study also contributed to understanding the leaching kinetics of different sulfides. We have also calculated the adsorption energies of water, chloride and sulfate species on the (001) surface of pyrite, which has similar structure to that of arsenopyrite, with one sulfur atom replaced by an arsenic atom. The adsorption energies are of the same magnitude as found for arsenopyrite, indicating that its

surface reactivity must be similar, but water adsorbs stronger to pyrite. Therefore arsenopyrite should be more reactive than pyrite in aqueous media. Hydrochloric acid and bisulfate present similar low values of adsorption energies on both minerals, indicating that these species are easily displaced from the surface, facilitating the exposition of the surface to the oxidant agents. Chalcopyrite is the sulfide that most adsorbs leaching agents, therefore it has the slowest leaching kinetics, since the oxidation products bind strongly to its surface, not allowing contact with oxidants. In the case of chalcopyrite, the larger adsorption energy of the sulfate explains the formation of jarosites and the decrease of its leaching kinetics.

The adsorption of molecular oxygen on arsenopyrite was also investigated in order to understand its oxidation mechanism. This molecule adsorbs strongly to the iron sites, especially in a dissociative way, making a Fe–O–As bridge ( $E_{ad} = -59.1 \text{ kcal mol}^{-1}$ ). Co-adsorption of water and oxygen is also favorable. Oxygen can also easily replace water molecules adsorbed on the surface since the adsorption energy of the latter is only  $-10.8 \text{ kcal mol}^{-1}$ .

The oxidation mechanism of pyrite by oxygen in the presence of water has intensely been investigated. However, the oxidation mechanism of arsenopyrite has not received attention commensurate with its environmental and technological importance. Two reaction paths have been proposed in this work for the oxidation reaction of arsenopyrite with molecular oxygen based on our recent study about the oxidation mechanism of pyrite [2]. The first path involves the adsorption of oxygen and water, in which water donates a hydrogen radical to the adsorbed O atoms in order to reduce the Fe atom oxidized previously by the oxygen. In this process the arsenic atoms are also oxidized. All the steps in this mechanism are exothermic and the highest activation energy is  $22.0 \text{ kcal mol}^{-1}$ , which is possible to occur in environmental conditions. The fact that the oxygen adsorbs dissociatively on arsenopyrite, leading to the oxidation of the iron and arsenic centers, is the main difference with respect to pyrite, in which the  $O_2$  is molecularly adsorbed on the iron center and a water molecule is necessary to approach in order to transfer a hydrogen atom to the adsorbed  $O_2^-$  species, leading to the oxidation of the iron centers. The oxidation of sulfur in pyrite occurs only in a second step. In the case of arsenopyrite, the atomic oxygen is readily adsorbed in a bridge site of Fe–As, leading to the oxidation of both atoms to Fe(III) and As(0). The approach of water will

lead to the reduction of the iron center and the oxidation of the arsenic center. Therefore, the oxidation of arsenopyrite is favored by a more straightforward mechanism.

The second mechanism involves the formation of  $\text{As(III)O}_3^{3-}$ , similar to the mechanism proposed by Sit *et al.* [3] for the formation of  $\text{SO}_4^{2-}$  in pyrite. First, one oxygen molecule adsorbs to two iron surface sites. Then a water molecule donates both H atoms to the adsorbed O atoms and the left oxygen from water binds to an As surface atom. A new water molecule approaches, the process repeats and the O atom left from the water molecule binds to the same As atom. Two water molecules are formed on top of the iron atoms, which can desorb and permit a new oxygen molecule to be adsorbed. Again a water molecule donates its H atoms to the adsorbed O and the left oxygen binds to the same As atom. All the steps in this process are exothermic or slightly endothermic. The formation of  $\text{As(V)O}_4^{3-}$  is unlikely to happen on the FeAsS surface, in agreement with the experimental study of Yu *et al.* [4], that detected As(III) as the dominant redox species in arsenopyrite oxidation. In both mechanisms, the arsenic atom is the one that oxidizes more readily, in agreement with the experimental observations of Nesbitt *et al.* [5] and Schaufuss *et al.* [6]. The results found in the present work can contribute strongly to help understanding the reaction of arsenopyrite in order to prevent acid rock drainage.

Although the proposed mechanism can explain most of the experimental data available and is reasonable based on the calculated values, it is clear that a more complex process in an abiotic medium is occurring. After the initial stages, the Fe(II) is mobilized to the environment, which is promptly oxidized by the dissolved oxygen. The Fe(III) species in an aqueous medium is a strong oxidant and catalyzes the oxidation of pyrite and arsenopyrite. The investigation of a mechanism involving the Fe(III) species is a challenge and has already deserved some consideration in our group. The chemical speciation of Fe(III) and Fe(II) in aqueous solution is not easy to be adequately described [7, 8]. The inner sphere mechanism involving the Fe(III) species seems to be the most important for the arsenopyrite oxidation and, consequently, to the ARD phenomenon.

As a perspective of this work, an attempt of adsorption of  $\text{Fe}^{3+}$  has been carried out (Figure 6.1). If the  $\text{Fe(H}_2\text{O)}_6^{3+}$  ion is the oxidant approaching arsenopyrite

surface, it could release two water molecules to the solution and adsorb to the surface as  $\text{Fe}(\text{H}_2\text{O})_4^{3+}$ . The adsorption energy in this process is estimated to be  $\Delta E = -687.9 \text{ kcal mol}^{-1}$ . The energy barrier for the oxidation of arsenopyrite by  $\text{Fe}^{3+}$  obtained experimentally [4] was  $3.8 \text{ kcal mol}^{-1}$ , much lower than the process with  $\text{O}_2$ .

Furthermore, most of the natural arsenopyrite is incrustated in pyrite, forming an agglomerate that can influence the oxidation mechanism. In fact, the electrochemical potential is different for the two minerals leading to the formation of an electrochemical cell. One of the phases must be considered as cathode and the other as anode. Understanding the nature of the interface between these two minerals, the effect on the band structure, energy gap, and the reactivity of the surfaces and interfaces is crucial. This is an important challenge which one should boldly go in order to bring a breakthrough to the area.

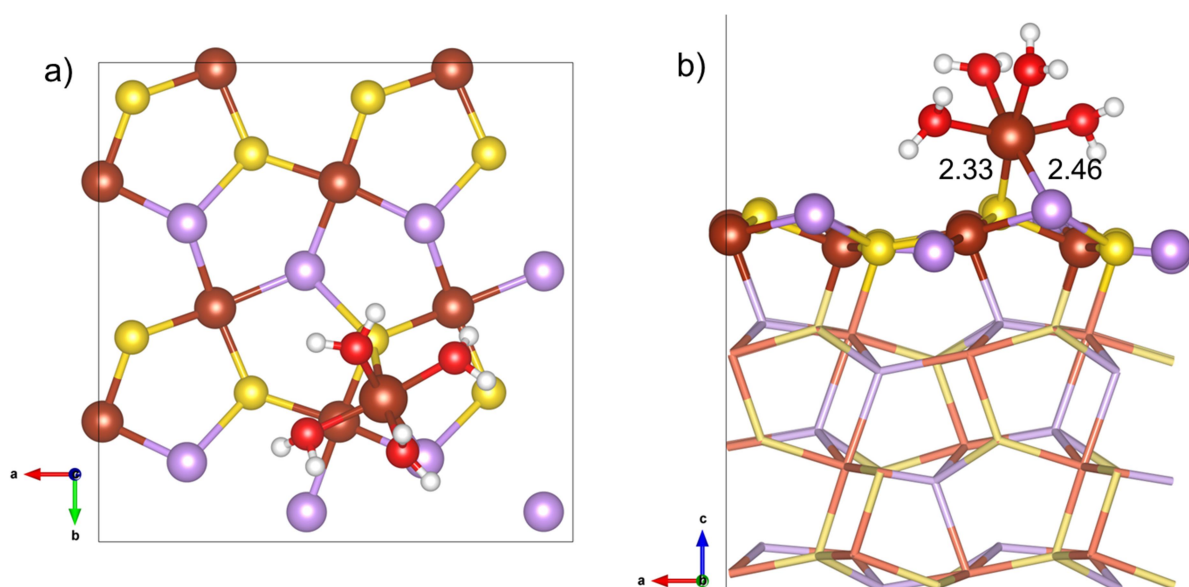


Figure 6.1: Adsorption of  $\text{Fe}(\text{H}_2\text{O})_4^{3+}$  on the  $\text{FeAsS}$  (001) surface. Yellow atoms are sulfur, brown are iron, red are oxygen and white are hydrogen.

## 6.1 References

1. Silva, J.C.M., H.A. De Abreu, and H.A. Duarte, *Electronic and structural properties of bulk arsenopyrite and its cleavage surfaces - a DFT study*. RSC Advances, 2015. **5**(3): p. 2013-2023.

2. Dos Santos, E.C., J.C. de Mendonça Silva, and H.A. Duarte, *Pyrite Oxidation Mechanism by Oxygen in Aqueous Medium*. The Journal of Physical Chemistry C, 2016. **120**(5): p. 2760-2768.
3. Sit, P.H.L., M.H. Cohen, and A. Selloni, *Interaction of Oxygen and Water with the (100) Surface of Pyrite: Mechanism of Sulfur Oxidation*. Journal of Physical Chemistry Letters, 2012. **3**(17): p. 2409-2414.
4. Yu, Y., et al., *Rates of Arsenopyrite Oxidation by Oxygen and Fe(III) at pH 1.8–12.6 and 15–45 °C*. Environmental Science & Technology, 2007. **41**(18): p. 6460-6464.
5. Nesbitt, H.W., I.J. Muir, and A.R. Prarr, *Oxidation of arsenopyrite by air and air-saturated, distilled water, and implications for mechanism of oxidation*. Geochimica et Cosmochimica Acta, 1995. **59**(9): p. 1773-1786.
6. Schaufuss, A.G., et al., *Reactivity of surface sites on fractured arsenopyrite (FeAsS) toward oxygen*. American Mineralogist, 2000. **85**(11-12): p. 1754-1766.
7. De Abreu, H.A., L. Guimarães, and H.A. Duarte, *Density-Functional Theory Study of Iron(III) Hydrolysis in Aqueous Solution*. The Journal of Physical Chemistry A, 2006. **110**(24): p. 7713-7718.
8. Guimarães, L., H.A. de Abreu, and H.A. Duarte, *Fe(II) hydrolysis in aqueous solution: A DFT study*. Chemical Physics, 2007. **333**(1): p. 10-17.

## 7 Curriculum Vitae

Name: Juliana Cecília de Mendonça Silva

Birth: 31/05/1986 in Belo Horizonte/MG, Brazil

### Formal Education

#### **2012-2016 Doctorate in Chemistry.**

Universidade Federal de Minas Gerais, UFMG, Belo Horizonte, Brazil with one year period in Jacobs University Bremen (Advisor: Thomas Heine)

Title: Estudo DFT das propriedades da arsenopirita e sua interação com agentes lixiviantes

Advisor: Hélio Anderson Duarte

Co-advisor: Heitor Avelino de Abreu

Scholarship from: Conselho Nacional de Desenvolvimento Científico e Tecnológico (CNPq)

#### **2010 - 2012 Master in Chemistry.**

Universidade Federal de Minas Gerais, UFMG, Belo Horizonte, Brazil

Title: Estudo teórico da desidratação do etanol catalisada por hematita

Advisor: Wagner Batista de Almeida

Co-advisor: Juliana Fedoce Lopes

Scholarship from : Coordenação de Aperfeiçoamento de Pessoal de Nível Superior (CAPES)

#### **2005 - 2010 Graduation in Chemistry.**

Universidade Federal de Minas Gerais, UFMG, Belo Horizonte, Brazil

#### **2001 - 2006 Technical Education in Industrial Chemistry.**

Centro Federal de Educação Tecnológica de Minas Gerais, CEFET/MG, Belo Horizonte, Brazil

## **Complementary Education**

2013 - 2013 Short Term Course in Theoretical Chemistry. (4h).

Universidade Federal de São João Del-Rei, UFSJ, Sao Joao Del Rei, Brazil

2012 - 2012 Short Term Course in Reaction Mechanisms Determination Techniques (6h). Universidade Federal de Minas Gerais, UFMG, Belo Horizonte, Brazil

2012 - 2012 Short Term Course in Mechanism of Heterogeneous Reactions. (4h). Instituto Militar de Engenharia, IME, Rio De Janeiro, Brazil

2009 - 2009 Short Term Course in Chemical Modification of Carbon Nanocompounds. (4h). Universidade Federal de Juiz de Fora, UFJF, Juiz De Fora, Brazil

## **Professional Experience**

### **1. Universidade Federal de Minas Gerais - UFMG**

2013 - 2013 Volunteer Professor, Working hours (weekly): 2, Schemes of job: Part-time. Disciplines Taught: General Chemistry – Experimental.

2012 - 2016 Position: PhD Student, Working hours (weekly): 40, Schemes of job: Full-time and exclusiveness

2010 - 2012 Position: Master Student, Working hours (weekly): 40, Schemes of job: Full-time

2005 - 2005 Position: Undergraduate Student, Working hours (weekly): 20, Schemes of job: Part-time

### **2. Fundação Centro Tecnológico de Minas Gerais - CETEC**

2005 - 2006 Position: Intern, Working hours (weekly): 20

## Complete articles published in journals

1. FEDOCE LOPES, J.; SILVA, J. C. M.; CRUZ, M. T. M.; DE M. CARNEIRO, J. W.; DE ALMEIDA, W. B., DFT Study of Ethanol Dehydration Catalysed by Hematite. RSC Advances: an international journal to further the chemical sciences, v. 6, p. 40408-40417, 2016.
2. DOS SANTOS, E. C.; DE MENDONÇA SILVA, J. C.; DUARTE, H. A., Pyrite Oxidation Mechanism by Oxygen in Aqueous Medium. Journal of Physical Chemistry. C, v.120, p.2760 - 2768, 2016.
3. SILVA, J. C. M.; DE ABREU, H. A.; DUARTE, H. A., Electronic and structural properties of bulk arsenopyrite and its cleavage surfaces - a DFT study. RSC Advances: an international journal to further the chemical sciences, v.5, p.2013 - 2023, 2014.

## Events

1. Presentation of Poster on Congresso de Químicos Teóricos de Expressão Latina, 2015. Adsorption of Water and Oxygen on Arsenopyrite (001) Surface.
2. Presentation of Poster on XVIII Simpósio Brasileiro de Química Teórica, 2015. Adsorption of Water and Oxygen on Arsenopyrite (001) Surface.
3. 2º Simpósio Temático do Programa de Pós-Graduação em Química da UFMG, 2013.
4. VI Encontro da Rede Mineira de Química, 2013.
5. Workshop: Química Teórica, 2013.
6. Oral Presentation on XXVII ERSBQ-MG, 2013. Estrutura e propriedades da Arsenopirita: um estudo teórico.
7. Theoretical Chemistry in Rio: a meeting to honor the 65th birthday of Professor Marco Antonio Chaer Nascimento, 2012.
8. Oral Presentation on Winterschool: Nanotechnology for the design of functional materials: Theory, experiments, and developments NDFM 2012, 2012. Theoretical Study of Ethanol Dehydration Catalyzed by Hematite.

9. Presentation of Poster on XXXVIII Congresso de Químicos Teóricos de Expressão Latina, 2012. Theoretical Study of Ethanol Dehydration Catalyzed by Hematite.
10. Presentation of Poster on no XVI Simpósio Brasileiro de Química Teórica, 2011. Theoretical Study of Ethanol Oxidation Catalyzed by Hematite.
11. Presentation of Poster on 23º Encontro Regional da Sociedade Brasileira de Química, 2009. Modificação de rejeito de aciaria para sua utilização na oxidação com  $H_2O_2$  de corantes e efluentes.